



Investigations of Spin Dynamics in Magnetic Systems and Development of Novel Probes

Daniel Margineda de Godos

PhD Thesis submitted for the degree of

Doctor of Philosophy in Physical Science

Led by:

Sean Giblin, PhD Thesis Director

Cardiff University

September 2017

© Copyright 2017
by
Daniel Margineda de Godos
All Rights Reserved

Abstract

This thesis presents the development of the first SQUID-based ac-magnetometer built in a dry dilution fridge. The possibility of expanding the frequency response from tens of kHz of a commercial magnetometer to the bandwidth of muon-spin relaxation μ SR (MHz), an indirect magnetic probe, which measures magnetic dynamics from the depolarisation of fundamental particles, is demonstrated. It opens a new scenario to investigate classical and quantum magnetic fluctuations by a direct probe in a range of frequencies that have an important role in exotic magnetic phases. Geometrical spin ices, frustrated magnets where magnetic excitations can be deconfined forming monopoles are good candidates to investigate. The study of magnetic fluctuations will help to understand the magnetic dynamics of these elementary excitations. Quantum spin liquids, frustrated systems without long-range order but with spins highly correlated that still fluctuate down to zero Kelvin are also interesting systems. The temperature dependence of their quantum fluctuations investigated by μ SR have shown a dynamical plateau that might be corroborated by susceptibility measurements.

The fabrication of the magnetometer has been combined with μ SR investigations of the ground state of NbFe_2 and CeRhIn_5 . The magnetic ground state of the ferromagnetic quantum critical point induced by growing around 1% Nb-rich $\text{Nb}_{1-y}\text{Fe}_{2+y}$ is claimed to be reached in this kind of clean itinerant systems by a long-range spin density wave (SDW), although several attempts to identify the ground state by neutron scattering were unsuccessful. The μ SR measurements

prove that the ground state of the stoichiometric compound is governed by static and short-range correlations or by an incommensurate and helical SDW.

The heavy fermion CeRhIn_5 was investigated at ambient pressure due to the coexistence of antiferromagnetic and superconducting order in an intermediate region of pressures. The filamentary or bulk nature of the superconducting phase is still until debate and the onset of superconductivity at ambient pressure reported in some works may shed some light into the nature of the ground state. μSR and resistivity measurements were carried out to investigate the antiferromagnetic and helical phase without any signature of a superconducting transition.

Acknowledgements

I am indebted to my advisor Sean Giblin who opened the doors of superconductivity and low temperature magnetism for me. His broad knowledge and passion for physics were always a source of inspiration and our discussions always useful and motivational, although tone were sometimes beyond the standards. He also gave me the opportunity to work in unique facilities. That is the reason I also want to thank ISIS and PSI people. Every visit to a Muon Source triggered a spark of curiosity that kept the flame of knowledge alive and helped me to escape from the lab routine. I definitely have to thank Rob Tucker and Andrew Harrison from the electronic workshop since they were always available to discuss about filtering, grounding and shielding and willing to design and fabricate any kind of electronic circuit that I thought could be useful. I want to thank people from Cardiff University that were always organising events to keep our minds free of madness. Thanks to Maxime Fays for his support and company in my first steps in Cardiff, a unique host, Valeriu Predoi, he was always available/pushing for a quick chat and a long visit to the pub, Greg Leighton, your endless stories about crusades were always a satisfying experience, no one show me Hemingway like you. I also want to thank Kane Essien, a priceless source of sci-fi authors and ideal for sharing soup-based meals. Thanks to the Bro League for our time in pubs and gardens. No thanks for your puppy GIFs. I also want to acknowledge my father. His meticulousness, perseverance and scientific rigour is an example of life that took me time to appreciate. I want to thank my mother for her empathy, patience and unconditional love. I always felt their support and love.

Publications

- [1] D. Margineda, C. Stock and S. Giblin, *Ground state of CeRhIn₅ at ambient pressure*, – (in progress)
- [2] P. Freeman, D. Margineda and S. Giblin, *μ SR study of the charge-stripe ordered LaNiO_{4.11}*, – (in progress)
- [3] D. Margineda and S. Giblin, *Novel SQUID-based AC and DC magnetometer in a dilution refrigerator*, Rev. Sci. Instrum. (in progress)
- [4] D. Margineda, J. Duffy, J. Taylor and S. Giblin, *μ SR study of stoichiometric NbFe₂*, Physica B: Condens. Matter 504, p. 121 (2017)
- [5] M. J. Graf, S. M. Disseler, C. Dhital, T. Hogan, M. Bojko, A. Amato, H. Luetkens, C. Baines, D. Margineda, S. R. Giblin, M. Jura and S. D. Wilson, *Magnetism and magnetic order in the pyrochlore iridates in the insulator-to-metal crossover region*, J. Phys. Conf. Ser. 551 (1), p. 012020 (2014)

CONTENTS

Abstract	iii
Acknowledgements	v
Publications	vii
List of Tables	xiii
List of Figures	xv
1. Introduction	1
2. Theory	5
2.1 Magnetism in insulators	5
2.1.1 Atomic magnetism	7
2.1.2 Langevin Diamagnetism and Van Vleck paramagnetism	12
2.1.3 Paramagnetism	13
2.2 Magnetic interactions	15
2.2.1 Magnetic dipolar interaction	15
2.2.2 Exchange interaction	16
2.2.3 Types of exchange interaction	19
2.3 Magnetic frustration	20
2.3.1 Dipolar spin ice	22
2.4 Magnetism in metals	27
2.5 Landau-Fermi liquid theory	29
2.6 Heavy fermion systems	30
2.6.1 Kondo effect	30
2.6.2 RKKY interaction	32

2.6.3	Kondo lattice	34
2.7	Quantum criticality	36
2.8	Spin density waves	38
2.9	Superconductivity	38
2.9.1	London equations	40
2.9.2	Ginzburg-Landau equations	41
2.9.3	Electron-phonon interactions	42
2.9.4	Flux quantisation	44
2.9.5	Josephson Junctions	45
2.9.6	RCSJ model	47
2.9.7	dc SQUID	50
3.	Muon-spin relaxation and rotation	63
3.1	Muon properties	64
3.2	μ SR: experimental aspects	65
3.2.1	Muon production	65
3.2.2	Polarized muons	67
3.2.3	Muon implantation, thermalisation and localization	68
3.2.4	Muon decay and its anisotropy	69
3.2.5	Experiment geometry	70
3.2.6	Data acquisition and statistical uncertainties	73
3.3	μ SR capabilities and muon sources	75
3.4	Relaxation functions	77
3.4.1	Zero-field μ SR	79
3.4.2	Longitudinal-field μ SR	82
3.4.3	Transverse-field μ SR	83
3.4.4	Magnetic fluctuations	83
3.5	μ SR in superconductors	85
4.	Low temperature DC and AC magnetometer in a dry dilution refrigerator .	93
4.1	Introduction	93
4.2	Magnetometer	98
4.2.1	Magnetic flux detection method	98
4.2.2	Flux transformer and gradiometers	103
4.2.3	Sources of poor SQUID magnetometer performance	108

4.3	First Prototypes	109
4.3.1	Gradiometers response and discussion	112
4.3.2	Noise measurements	119
4.4	Final Design	121
4.4.1	Motion	121
4.4.2	Detection and excitation coils	125
4.4.3	dc-SQUID and flux transformers	127
4.4.4	Materials and shielding	128
4.4.5	Heaters	131
4.4.6	Thermalisation at 4K	132
4.4.7	Sample holder: thermalisation, issues and improvements . . .	133
4.4.8	Automotion	137
4.5	DC Calibration	140
4.6	AC Calibration	145
4.7	Inductive magnetometer	151
4.8	Conclusions and future work	153
5.	μ SR study of stoichiometric NbFe ₂	161
5.1	Introduction	161
5.2	Bulk magnetization	166
5.3	Muon spin relaxation	169
5.4	Conclusions	178
6.	Ground state of CeRhIn ₅ at ambient pressure	185
6.1	Introduction	185
6.2	Muon spin relaxation	193
6.2.1	Longitudinal field configuration	194
6.2.2	Transverse field configuration	205
6.3	Resistivity	209
6.3.1	Sample preparation	212
6.3.2	Experimental setup	213
6.3.3	Results	214
6.4	Conclusions	217

7. Conclusions and further work 225

APPENDICES

A. Appendices 229

A.1 Refrigerators 229

A.1.1 Cryocoolers 230

A.1.2 Cooling below 4 K 231

A.1.2.1 Sorption refrigerators 232

A.1.2.2 Adiabatic demagnetization refrigerator 234

A.1.3 Dilution refrigerators 235

A.2 SQUID electronics 237

A.2.1 Flux-locked loop circuit (FLL) 237

A.2.2 Two-stage SQUID amplifier 238

List of Tables

3.1	Main muon propertiesas.	65
4.1	List of the gradiometers tested in the Helium Dewar and their main features. It includes the mutual inductance and the FT flux-transfer functions, f_i	112
4.2	Measured and calculated transfer functions, moment to flux coefficients (according to Eqs: 4.12 and 4.13) and low and high frequency dynamic ranges for the tested gradiometers. Errors in the measured and calculated transfer functions explained in text.	115
4.3	Thermal conductivity at 1 K, resistivity and volume susceptibility of some insulators and metals used in the setup at 4 K. <i>Depends on purity¹ or grade²</i> . Data taken from [24, 25].	129
4.4	Critical temperature and field of superconductors used in this work. . . .	130
4.5	Magnetic flux density at 10 Oe and maximum permeability of the high-permeability materials used.	130
4.6	Moment to voltage coefficients, measured and calculated losses and ratios for the calibration sample and the sample coil with the FT in two different positions.	144
6.1	Fitting parameters of the TF20 measurements above and below T_N for the muons stopped in the sample. Fitting errors in parentheses.	198
6.2	Fitting parameters of the ZF- μ SR from Eq. 6.3 for s1 at 65 mK. Same parameters were found for s2 with different f_i (last column). The silver contribution was fixed to $f_{bg}=a_0 \cdot (1 - V_f)$. Ratio of muons that contribute to the relaxation is $(1 - f_{no})/V_f \simeq 48\%$ and 45% for $s1$ and $s2$ respectively. Fitting errors in parentheses.	201
6.3	Fitting parameters of the temperature dependence of the frequencies. The lowest frequencies is not fitted. Fitting errors in parentheses. . . .	202

6.4	Fitting parameters of the TF- μ SR experiments at T= 50 mK. Fitting errors in parentheses.	207
-----	--	-----

List of Figures

2.1	(a) Sketch of the temperature dependence of the susceptibility. Frustration is characterised by a large frustrated ratio, f . (b) Sketch of the correlation function. Frustrated paramagnets present an anisotropic $S(\mathbf{Q},\omega)$ with respect to the vector \mathbf{Q}	22
2.2	(a) Triangular and (b) kagomé lattice with antiferromagnetic coupling. (c) Ferromagnetic pyrochlore lattice taken from [2].	23
2.3	Scans of χ' and χ'' on $\text{Dy}_2\text{Ti}_2\text{O}_7$ measured along the [110] axis taken from [18].	26
2.4	Temperature dependence of resistivity for metal with magnetic impurities that introduce a logarithmic contribution to the phonon scattering T^5 term. Minimum is given at the so-called Kondo temperature, T_K . . .	31
2.5	RKKY exchange interaction, J_{RKKY} produced by a magnetic atom at $r=0$. The antiferromagnetic Kondo exchange, J_K polarises the conduction electron (blue arrows) and a long range magnetic interaction with either ferromagnetic and antiferromagnetic coupling are possible.	33
2.6	Doniach's phase diagram.	34
2.7	Critical field H_c and London penetration depth λ_L as a function of the temperature.	39
2.8	Scheme of a Josephson junction.	45
2.9	(a) RCSJ equivalent circuit. (b) The tilted washboard potential U_J as a function of the phase difference, δ in a bias current below and (c) above the critical current. Taken from ref. [69].	47
2.10	(a) Josephson junction with a non-hysteretic I-V characteristic curve, ($\beta_c \ll 1$) and (b) hysteretic I-V curve as a function of β_c	49

2.11	(a) dc-SQUID scheme. (b) Equivalent circuit of a dc-SQUID in the RCSJ model.	50
2.12	(a) dc-SQUID I-V characteristic curve for different magnetic flux. (b) The periodic V-flux curve.	53
3.1	Scheme of muon production.	67
3.2	Parity violation of pion π^+ decay at rest frame into a muon μ^+ and a muonic neutrino ν_μ	68
3.3	Schematic representation of the processes of implantation and thermalisation of a muon within a sample. Dissociation of thermal muonium does not always occur in the final stage. Taken from Ref. [1].	69
3.4	Angular distribution of emitted positrons with respect to the initial muon-spin direction (horizontal arrow) for a fixed energy. Positrons are preferentially emitted along the muon spin.	70
3.5	Sketch of a μ SR experiment in a continuous muon source taken from Muon Training Course notes.	71
3.6	Backward (black squares), forward (red circles) and resulting asymmetry (green triangles) in a TF20 experiment. 16 ns raw bin is averaged with a bunching factor of 8	74
3.7	Muon spin polarization rotating around a magnetic field of arbitrary orientation.	78
3.8	(a) Superposition of GKT functions delayed by the fluctuation rate ν for which the relaxation envelope is well described by an exponential decay. (b) Polarisation function for different ratios between the fluctuation rate and internal field of a GKT polarisation function.	84
3.9	(a) Magnetic field suppression within a superconductor and the resulting μ SR depolarisation for three muon stopping sites. (b) Field distribution for the three muon sites. Data taken from [12] and scheme from [13].	86
3.10	Field distribution inside a superconductor with magnetic vortices and the corresponding TF- μ SR function for three cases: (a) the normal state, (b) the superconducting state, (c) as (b) with a shorter penetration depth taken from [4].	88
3.11	Field distribution lineshape, $p(B)$, produces by an ideal vortex line lattice taken from [1] with general features explained in text.	89
4.1	Frequency and time response of the most common techniques used to investigate magnetic fluctuations.	95

4.2	(a) Equivalent circuit used for the High Frequency Inductive Magnetometer without and with (b) the resistance network that removes the circuit self-resonance.	99
4.3	(a) Induced voltage in a first-order gradiometer for different magnetic moments and the frequency response of the circuit with and without the network resistance. (b) Circuit effects in the induced voltage. Red lines define the limiting factors. More details in text.	101
4.4	Estimations of the detectable magnetic moments of the High Frequency Inductive Magnetometer.	102
4.5	Input SQUID voltage-to-flux response with the final gradiometer attached. Transfer coefficient, V_{Φ} , obtained from the maximum slope (red line) at the working point (WP-blue circle) and locked by the FLL.	104
4.6	Flux per magnetic moment induced in a first-order (bottom-green) and a second-order (upper-red) gradiometer with loop radius $a=5\text{mm}$, according to the reciprocity principle (Eqs. 4.6 and 4.7).	105
4.7	Scheme of the SQUID magnetometer. Flux is induced in the gradiometer and transferred through a set of flux transformers. Flux is coupled to the SQUID by an internal coil with a self, L_{sq} , and mutual inductance, M_{sq} . Transfer functions are explained in text.	107
4.8	Design of the probe used to test the first prototypes. It includes an internal rod to fit the SQUID at the bottom and a KF-25 flange to fit the probe to the Helium dewar.	110
4.9	Scheme of 5 gradiometers tested in the Helium dewar. Description in text.	111
4.10	Frequency response of the bare SQUID and some of the gradiometers tested. A Copper coil is used to produce an input magnetic flux, according to Eq. 4.4. The voltage-to-flux coefficient relates the readout voltage to the SQUID flux, Φ_{sq}	113
4.11	DC linear response of the gradiometers. Φ_{sq} higher than $5\Phi_0$ are obtained changing the SQUID sensitivity via the FLL circuit. Linearity changes for output fluxes lower than $0.1\Phi_0$ and higher than $5\Phi_0$	114
4.12	Measured (black filled square) and calculated flux loss (empty red circles) for the tested gradiometers. Green stars are the ratio between both values. Calculation method and propagation of the systematic errors are explained in text.	117

4.13	Effects of a bad balanced primary coil. CsMgCrF ₆ paramagnetic response using a 25 mm long solenoid onto the 1st cylindrical gradiometer and a background signal when the sample is removed.	118
4.14	Test of a 60 Ω heater resistor located over the superconducting twisted pairs with 50 mA (a) and 100 mA (b) applied current. t_0 and t_1 are the time when the heater is turned on and switched off, respectively. Δt is a few seconds lapse.	119
4.15	(a) Magnetic noise floor spectral density for two testing gradiometers (green and red) and the final design. (b) Effects of the Pulse Tube in the SQUID noise floor in the planar gradiometer (red-magenta) and the final design (black-grey). Bare SQUID noise is included (blue) with the reference noise given by the SQUID manufacturer highlighted by a green circle.	120
4.16	Sketch of a magnetic field spectrum consisting of a measurable signal in the order of nT in a noise spectrum of pT \sqrt{Hz}	120
4.17	Picture of the magnetometer. It includes the Cu rods to thermalise it to the still plate, the dc-SQUID, the FT box and the coils shielded by the Lead can. Coils are thermalised by Cu thermal wires and the magnet wires shielded by Pb/Sn solder.	122
4.18	Attocube piezomotor performance in a dilution refrigerator taken from [7]. Distance per step, velocity and heat generated for several frequencies and voltages of the saw-tooth profile. The heat generated is measured for a 1 μ m s ⁻¹ velocity.	123
4.19	(a) Scheme of the dilution fridge with the stepper motor, the stainless Steel shaft is linked to the coils setup at the bottom. Copper clamps are used to thermalise the shaft. (b) Scheme of the magnetometer, thermally linked to the Still Plate. It includes the SQUID, a box with the flux transformers, heaters and thermometers and the coils setup. . .	124
4.20	Sample movement effects on the sample (full dots) and MXC temperature (empty dots) for three different velocities.	125
4.21	From left to right, pictures of the second-order gradiometer (a), the solenoid magnet (b), the primary and secondary coil mounted together and attached to the Cu clamp (c), and the setup with the two magnetic shields (d).	126
4.22	(a) Scheme of the flux transformers (FT), including the heaters, the thermometers and the thermalisation wires. (b) Picture of a FT with the heater. (c) Picture of the FT inside the shielding box. (d) A zoomed image of the heater. Details in text.	127

4.23	Calculation of the axial component of an external field B_0 inside a cylinder shield of diameter a and distance z from the edge. Input flux is calculated for $B_0 = 0.5G$ and pickup coil with 5 mm radius. The blue line is the flux-transfer function. In green, the approximated gradiometer position at $z \simeq 85$ mm.	131
4.24	(a) SQUID response as a function of time when 2 mA (blue vertical line) and 1 mA (purple vertical line) currents are applied to the coil heaters located in the pickup and the flux transformer circuit. (b) No thermal effects on the SQUID and the FT BOX temperature when the current is applied.	133
4.25	(a) Thermalisation to 4 K of the SQUID plate, the flux transformers and the coils holder. (b) Thermalisation after adding high-purity Copper wires to the setup. The Bluefors plates temperatures are added.	134
4.26	(Left) Copper sample holder. It includes the RuO ₂ thermometer, the sample and Copper stripes that link it to the MXC. (Right) Stainless Steel shaft to transfer the movement from outside and Torlon rod connected to the sample holder. Details of the Teflon separators at the bottom of the coil holder is included.	135
4.27	Position scan of the sample coil for different fields showing evidences of a faulty shielding. (a) Voltage drift in the SQUID readout. (b) Electromagnetic coupling to the SQUID when field is turned on.	136
4.28	(a) Position scan for different setups. Background effects depending on the way to link the SS tube to the sample holder. (b) Sample and MXC base temperature reached by the PhBr and the Torlon rod setup. To the final design, high purity Cu strips were added to improve the sample thermalisation. More details in text.	137
4.29	Sample temperature when the position is scanned without a teflon separator. A touch between the sample holder and the coils dramatically increased the sample base temperature.	138
4.30	Flowchart of the scalable Labview projects to carry out measurements in the Bluefors fridge.	139
4.31	Screenshot of a DC (a), and AC (b) data acquisition GUI. DC protocol includes field and temperature scan option and gain calibration. AC protocol includes frequency and temperature scan in the extraction mode.	140
4.32	Sample coil position scan for different current-magnetic moment at 4K. Fits to the expected second-order gradiometer are included.	141

4.33	(a) Temperature dependence of the DC field cooled and low frequency susceptibility in $\text{Dy}_2\text{Ti}_2\text{O}_7$ taken from the supplementary information of Paulen et al. work [3]. (b) Magnetometer calibration. SQUID voltage in the same sample is measured by cooling in zero field.	142
4.34	$\text{Dy}_2\text{Ti}_2\text{O}_7$ and $\text{Gd}_2\text{Zr}_2\text{O}_7$ position scan at different temperatures. Fits to the expected second-order gradiometer are included.	143
4.35	Magnetometer calibration using a sample coil and the spin-ice $\text{Dy}_2\text{Ti}_2\text{O}_7$ as described in text.	144
4.36	Frequency scan of χ' and χ'' of the spin-ice $\text{Dy}_2\text{Ti}_2\text{O}_7$ from 2 K (black squares) to 15 K (purple pentagons).	146
4.37	Frequency scan of χ' and χ'' of the spin-ice $\text{Dy}_2\text{Ti}_2\text{O}_7$ taken in the Bluefors magnetometer below 1K. Peak extrapolation from reference [3] at the studied temperatures are depicted by vertical lines. High temperature (4.3 K) plot is compared with 4 and 5 K PPMS results.	147
4.38	Temperature scan of χ' and χ'' of the spin-ice $\text{Dy}_2\text{Ti}_2\text{O}_7$ at 1 Hz (red circles) and 3.1 Hz (green triangles) and the DC susceptibility (black squares). Vertical lines are the expected transitions $\delta T \simeq 15$ mK. . . .	149
4.39	Temperature dependence of χ'' peak in $\text{Dy}_2\text{Ti}_2\text{O}_7$ from references 1 [3] and 2 [31] and the PPMS and the magnetometer measurements. Gaussian fits give the errors in the magnetometer data.	150
4.40	RuO_2 sample thermometer vs MXC thermometer.	150
4.41	High frequency inductive magnetometer.	151
4.42	(a) Position scan of $\text{Ho}_2\text{Ti}_2\text{O}_7$ susceptibility at 1 MHz at room temperature. (b) χ' and χ'' high frequency scan taken by Edward Riordan at 11.5 and 12.5 K.	152
4.43	Frequency scan of χ' and χ'' $\text{Dy}_2\text{Ti}_2\text{O}_7$ using one or two coils. Eddy currents at high frequencies due to the diamagnetic sample holder are removed by using the extraction mode.	155
5.1	Magnetic phase diagram of $\text{Nb}_{1-y}\text{Fe}_{2+y}$ with the apparent ground states as a function of doping. Ref [6].	162
5.2	(a) NbFe_2 C14 Hexagonal Laves with the Fe atoms at the 6h sites (pink) separated by the 2a sites Fe atoms (red) and the Nb atoms at the interstitial sites. (b) Planar triangular kagomé lattices formed by the Fe atoms at the 6h sites.	163

5.3	Zero-field μ SR asymmetry spectrum of $\text{Nb}_{1-y}\text{Fe}_{2+y}$ for $y= +0.016$ (FM) (a), 0.0 (b) and $= -0.004$ (c) (SDW?) from [13]. Oscillations are only observed in the FM phase.	165
5.4	Neutron Laue diffraction along the c axis.	165
5.5	(a) Temperature dependence of the field-cooled (black squares), zero field-cooled (green circles) susceptibility and inverse susceptibility (red triangles) showing a peak at $T_N \sim 10$ K. The inverse susceptibility displays approximately linear Curie-Weiss like behaviour, commonly observed in weak itinerant magnets [35]. (b) ZFC-FC susceptibility as a function of the field. The transition disappears at $B = 1\text{T}$	166
5.6	(a) Magnetic isotherms. (b) Susceptibility $\frac{dM}{dH}$ at different temperatures. Inset. Critical field as a function of the temperature. Error bars are given from data precision in the susceptibility.	167
5.7	Temperature scan of χ' and χ'' for different frequencies. No frequency-dependent behaviour is observed. Data are distorted by eddy currents above 1000 Hz.	168
5.8	Zero field- μ SR run above T_N fitted with 1 muon site or 2 muon sites without any background contribution.	171
5.9	(a) Zero-field muon spectra above and below T_N fitted to a GbG form. The 1/3 tail is emphasised by the red line. (b) Muon repolarisation in LF- μ SR confirms the quasi-static nature of the internal fields. High time spectra in right panel. Statistical errors are given by the number of events ≈ 15 MeV and the binning length 10 ns. For visualization binning factor of 80 and 40 was chosen for the high-time ZF-and LF- μ SR spectra.	172
5.10	(a) Short time muon spectra at 2 K fitted to different models. The monotonic decay of the asymmetry was reasonable well-fitted to the GbG model described in text (and its discretisation in 17 GKT) and two gaussian functions with a weight ratio 1:3. (b) Residual analysis of both models. χ^2 for a fitting range up to 8 μs	174
5.11	Gaussian weight function at 2 K and after redefining it by Eq. 5.5. (b) Distribution of the Gaussian weight function of internal fields as a function of temperature that spreads homogeneously from 0 to beyond Δ_{eff}	176

5.12	(a) Temperature dependence of the effective local fields and the maximum of the Gaussian weight function fitted to a critical exponent Eq. 5.6. (b) Fluctuations as a function of temperature (black squares) and field at 2 K (red circles) which remain below the slow fluctuation limit $\nu < \Delta_{eff}$. Values and errors are extracted from fitting data to Eq. 5.4.	177
6.1	Schematic plot of the CeRhIn ₅ tetragonal crystal structure. The interstitial muon sites suggested by [20] 1a(red), 2g (yellow) and 2f (green) are flagged in the unit cell. Ce magnetic moments (m) are confined in the ab plane aligned antiferromagnetically. They propagate in spiral along the c axis forming an incommensurate helical structure with propagation vector q [16].	187
6.2	CeRhIn ₅ T-P phase diagram at zero field determined by specific heat (filled symbols) and resistivity (crosses) from [11]. SC onset at P _x \simeq 0.9 GPa coincides with the maximum T_N . AFM phase vanishes at P1 although a field-induced QCP can be reached at P2. Inset. Different behaviour has been found at low pressures. The updated phase diagram proposed by [13] is shown in the inset figure. T_c from ac susceptibility (filled symbols) coincides with bulk SC from previous measurements (color symbols) under pressure, but a new SC transition was also reported at low and ambient pressure.	189
6.3	(a) $\chi'(T)$ for different pressures. (b) Powdering and polishing effects in χ at P_{amb} taken from [13].	191
6.4	Scheme of LF- and TF- configurations of the MUSR spectrometer. 64 detectors are grouped in 8 detector clusters. The red and the yellow arrow specify the muon beam (antiparallel to the muon spin polarisation, \vec{S}_μ) and the field direction.	193
6.5	Samples mounted in a Silver holder.	194
6.6	(a) ZF- μ SR at T=4.2 K (above T_N) for sample1. Silver background and then the volume fraction V_f is calculated from the GKT fits.	195
6.7	(a) Fourier transform of TF- μ SR by applying $H \simeq 20$ Oe for s1 above T_N and below for s1 and s2. $B_p^{s1}(4K)=19.6$ G, $B_p^{s1}(1K)=19.1$ G and $B_p^{s2}(1K)=18.7$ G. (b) TF- μ SR in the time domain. The volume fraction V_f is estimated to be $V_f \simeq 90\%$ for s2 from fitting parameters. A variable binning parameter was used to reduce error bars at large times.	196

6.8	(a) ZF- μ SR at different orientations from ref. [20]. (b) ZF- μ SR for sample 1 (black squares) and sample 2 (red circles) with a non-relaxing signal equivalent to the U orientation in (a). Non-relaxing signal is due to internal fields at muon sites parallel to the detectors or muons stopped at the silver holder, which are reduced in sample 2. The raw bin size 16 ns is increased for visualisation by a variable bunching factor. Fits described in text.	198
6.9	(a) Shifted Fourier transform (FT) of ZF- μ SR at different temperatures. (Top) FT derivative at 65 mK and 1 K. (b) ZF- μ SR at 0.065, 0.7 and 1 K. (Bottom) shifted curves. No relevant change in the frequency and time spectra from 1 K to the base temperature.	199
6.10	Temperature dependence of the four precession frequencies fitted to a critical exponent described in text (line). The lowest frequency remains unaltered in the paramagnetic phase suggesting that the AFM arrangement does cancel out the magnetic field at the muon sites.	202
6.11	(a) Temperature dependence of the normalised fractions, f_i/V_f , and the non-oscillating signal, f_{no}/V_f , (b) and the relaxation rate, σ_i for s1 (empty dots and s2 (full dots). Standard errors on parameters given by the χ^2 method.	203
6.12	TF- μ SR asymmetry for a specific detector cluster in the PM phase (T = 4K), the AFM phase (T = 0.5 K) and at the base temperature (T = 0.05 K) for three applied fields. N=2 on fits to Eq. 6.7 is only observed for B= 150G. At the lowest field, depolarisation is too fast for the spectrometer resolution $\sigma_2^{75G} \rightarrow \infty$. For the highest field, not a second depolarisation is observed $f_2^{400G} = 0$	206
6.13	Temperature dependence of the Eq. 6.7 fitting parameters for three TF- μ SR experiments (black, red, green dots). Empty (full) dots correspond to i = 1(2), respectively. f_2 (400 G) = 0 and σ_2 (75 G) = ∞	208
6.14	Probability distribution of the internal flux density at different temperatures for 75 (a) and 150 G (b) applied fields.	209
6.15	Four-lead arrangement for measuring transport properties.	210
6.16	Scheme of the sample used in resistivity measurements with an axis of symmetry, dimensions and contact nomenclature.	212
6.17	(a) Picture of the PPMS resistive sample puck. (b) Scheme of the setup for low temperature transport measurements in the dilution refrigerator. It includes a pure Cu holder to improve sample thermalisation, the RuO ₂ thermometer and superconducting Pb pads and Al contact wires to avoid heating effects due to the applied current.	213

6.18	CeRhIn ₅ resistivity and resistance temperature dependence in two perpendicular directions of the ab plane with and without an applied field $H = 1\text{T}$. ρ_{\parallel} (black and red lines) and ρ_{\perp} (green and blue lines) are defined as $\rho_{\parallel,\perp} \equiv \frac{\pi t}{ln2} R_{\parallel,\perp}$. Axial symmetry results in an average total resistivity ρ for a sample thickness = 320 μm (cyan line).	215
6.19	(a). Temperature dependence of in-plane (a) and out-plane (b) resistivity of CeRhIn ₅ taken from [36]. (b) Resistivity and resistance of 1 cm and 70 μm Gold wires [37] and Aluminium wires with two residual resistivity, ρ_0 [38].	216
6.20	Low temperature in-plane (ρ_{\parallel}) resistivity of CeRhIn ₅ for two different currents. Al wires superconducting transition is seen at 1.2 K (inset). .	217
A.1	(a) Two stage PT scheme. (b) Drawing of the Cryomech PT-415 used in the Bluefors dilution refrigerator.	231
A.2	(a) ³ He and ⁴ He vapour pressure as a function of temperature. (b) ³ He- ⁴ He mixture phase diagram from [2].	232
A.3	Modified ³ He - ⁴ He sorption cooler scheme from [3].	233
A.4	(a) Bluefors DR Helium cycle. (b) DR Bluefors picture [2].	235
A.5	Scheme of a Flux-Locked Loop circuit taken from Thomas Schurig work [7].	238
A.6	Schematic diagram of a typical two-stage SQUID amplifier from Star Cryoelectronics SA632s user's manual.	239

1

Introduction

Since the English physicist William Thomson conceived in 1848 a scale of absolute temperature defining absolute zero as a state in which particles had ceased all forms of motion and hence a complete absence of heat and temperature, a race to reach the lowest possible temperature and liquefy the existing gases began. The Helium liquefaction by Kammerlingh Onnes for the first time in 1908 was a milestone in condensed matter physics. The development of cryogenic techniques, most of them based on the unique properties of Helium and their isotopes provided access to temperature of a few milliKelvins. Reducing thermal vibrations together with the development of methods for making high-quality crystals new exotic states of matter emerged and a new area of research arose. Superconductivity but also other phenomena destroyed by thermal effects such as weak magnetic interactions or quantum mechanical properties that occurs at the atomic level were then open to experimental investigation. Non-Fermi liquid behaviours, coexistence of magnetism

and superconductivity in heavy fermions, quantum transitions at zero absolute or frustrated magnetic systems that behave as cooperative paramagnets in fluid-like states of matter are only a few examples of the exciting time in condensed matter. In this range of temperatures, magnetic fluctuations seems to play a crucial role in the mechanism to stabilise the magnetic interactions and their interplay. This thesis concentrates on providing new tools to investigate magnetic fluctuations at very low temperature. The development of a novel magnetometer in a dry dilution refrigerator and efforts to expand the ac-susceptibility bandwidth are presented here, but also two magnetic materials with unusual and still controversial ground state were investigated using muon-spin relaxation known as μ SR. Muons are short-lived particles with non-zero magnetic moment that can be used as local magnetic probes. Fully spin-polarised muons embedded within the material relax by the effect of the local fields providing insight into the magnetic interactions. This thesis is organised as follows:

Chapter 2, Theory: Introduction to magnetism and superconductivity. Physics phenomena necessary to understand the systems used to calibrate the magnetometer and the metal compounds investigated during this thesis are detailed.

Chapter 3, Muon-spin relaxation and rotation: The μ SR technique is described. Experimental aspects of the muon instrumentation and the muon spin relaxation functions are provided. Emphasis was put on those that were used to analyse the systems presented in this thesis.

Chapter 4, Low temperature DC and AC magnetometer in a dry dilution refrigerator: The development of the magnetometer is described in detail. The magnetometer construction, issues involved in the fabrication, different prototypes tested and first results are given here.

Chapter 5, μ SR study of stoichiometric NbFe₂: The magnetic ground state of NbFe₂ is explored with μ SR and supported by bulk magnetisation measurements. The sensitivity of muons to the field distribution and fluctuations in the vicinity of the quantum critical point is demonstrated and new insights to the claimed long-range ordered ground state provided.

Chapter 6, Ground state of CeRhIn₅ at ambient pressure: The onset of superconductivity in CeRhIn₅ has been reported in some works at ambient pressure. They suggest that superconductivity, which unambiguously emerges in a region of pressure, coexists with antiferromagnetic order and has a bulk character. No signature of superconductivity was found by using transverse- and zero-field μ SR together with resistivity measurements below the expected transition.

Chapter 7, Conclusions and further work: The most relevant findings are summarised. Further work to improve the magnetometer capabilities and new experiments in the investigated magnetic systems are suggested.

This thesis encompasses an extensive experimental work supported by theoretical insights. Many notions were required to understand and carry out all the experiments from condensed matter physics involved in the investigated systems, to those related with materials and electrical engineering for the magnetometer construction. A rigorous mathematical study is beyond the scope of this work, but an effort was done to introduce all the concepts with consistent mathematical notations. Bold fonts are used for vector notation although arrow notation are applied in some figures for clarity.

2

Theory

2.1 Magnetism in insulators

The theory of atomic magnetism in the independent electron approximation is a good starting point to introduce the magnetism in solids. At a first approximation, insulating solids can be described based on the properties of separated atoms or ions, although the crystalline structure will introduce some modifications. Crystal field perturbation will take into account the interaction of the ions with the crystalline lattice that will affect the magnetic properties of the solids, the quenching of the orbital momentum in d-electron ions is an example of the lattice effects. However, electronic interactions have dramatic effects in the magnetism of some solids. One can think in the interactions of the electron magnetic moments with each other (dipolar interactions) or with the electrostatic field created by the nuclei (spin-orbit coupling) as the responsible of these effects instead, spontaneous magnetic order and other phenomena are originated by the electrostatic entanglement of the electron

orbitals in form of a exchange interaction by far, larger than the former interactions. It requires, in most of the cases, to go beyond the independent electron approximation. The complexity of the electronic structures in solids hinder the possibility to give a full picture of the magnetic interactions. However, the direct exchange coupling will be briefly introduced for the simple case of two-electron system together with some of the most common case of indirect exchange interaction.

The magnetization density of a quantum system of volume V in the presence of a magnetic field B is ruled by statistical mechanics. In thermal equilibrium at temperature T classical Maxwell-Boltzmann statistics may describe the magnetic density for each excited state of energy $E_n(B)$ by

$$M(B, T) = \frac{\sum_n M_n(B) e^{-E_n/k_B T}}{\sum_n e^{-E_n/k_B T}} \quad (2.1)$$

where the magnetization of each state of energy is defined as

$$M_n(B, T) = -\frac{1}{V} \frac{\partial E_n(B)}{\partial B} \quad (2.2)$$

In thermodynamics, the Helmholtz free energy F is the useful potential to investigate a system at a constant temperature and volume. In equilibrium F is minimised and the total magnetization can be defined as

$$M(B, T) = -\frac{1}{V} \frac{\partial F(B)}{\partial B} \quad (2.3)$$

where F is given by the partition function Z

$$F = -k_B T \ln Z = -k_B T \ln \left(\sum_n e^{-E_n/k_B T} \right) \quad (2.4)$$

$k_B = 8.617 \times 10^{-5} eV/K$ is the Boltzmann constant.

The magnetic susceptibility is then

$$\chi = \mu_0 \frac{\partial M}{\partial B} = -\mu_0 \frac{1}{V} \frac{\partial^2 F}{\partial B^2} \quad (2.5)$$

where μ_0 is the vacuum permeability. It indicates the orientation of the magnetic moments under the presence of a magnetic field but also gives information of structural properties providing insight into bonding and energy levels. Substances with negative susceptibility are classified as diamagnetic whilst positive susceptibility characterise paramagnetic substance. Electrostatic interactions may give rise to ordered arrays of magnetic moments in form of different sort of magnetism such as ferromagnetism, antiferromagnetism, ferrimagnetism, helical or more complex magnetic structures.

2.1.1 Atomic magnetism

In quantum mechanics, quantum states are described by a set of eigenfunctions $\Psi(\mathbf{r}, t)$ of the Hamiltonian operator defined in the so-called Schroedinger equation

$$\hat{\mathcal{H}}\Psi(\mathbf{r}, t) = -i\hbar \frac{\partial}{\partial t} \Psi(\mathbf{r}, t) \quad (2.6)$$

For a time-independent Hamiltonian, solutions have the form $\Psi(\mathbf{r}, t) = e^{-\frac{E_n}{i\hbar}t} \psi(\mathbf{r}) \bar{\chi}$ resulting in the time-independent Schroedinger equation

$$\hat{\mathcal{H}}\psi(\mathbf{r}) \bar{\chi} = E_n \psi(\mathbf{r}) \bar{\chi} \quad (2.7)$$

where the quantized energy levels E_n are the eigenvalues of the Hamiltonian. Eigenfunctions may be described by a spatial eigenfunction $\Psi(\mathbf{r})$ and an eigienspinor $\bar{\chi}$ that takes into account the spin state of the system. Note that a bar is included in the spinor notation to differentiate from the magnetic susceptibility.

To understand the atomic magnetism is then necessary to investigate the Hamiltonian of the quantum system in the presence of a magnetic field B . The classical and non-relativistic Hamiltonian may be derived from the classical Lagrangian L . To determine classical equations of motion the Hamiltonian \mathcal{H} must be expressed in terms of coordinates \mathbf{r}_i and canonical momenta $\mathbf{p}_i \equiv \partial_{\mathbf{r}_i} L = m\mathbf{v}_i - e\mathbf{A}(\mathbf{r}_i)$

$$\mathcal{H} = \sum_i \frac{1}{2m} \left[\mathbf{p}_i + e\mathbf{A}(\mathbf{r}_i) \right]^2 - e\varphi(\mathbf{r}_i) = \mathcal{H}_0 + \mathcal{H}_M \quad (2.8)$$

that can be split into a field-independent term \mathcal{H}_0 that deals with the electronic kinetic energy $\sum_i \frac{\mathbf{p}_i^2}{2m}$ and the scalar potential $\varphi(\mathbf{r}_i)$ and a field-dependent term \mathcal{H}_M , the magnetic Hamiltonian from now on.

In quantum mechanics any quantity, so-called observable, which can be measured in a physical experiment is associated to a Hermitian operator in such a way than the possible quantum states will be an eigenvector of those operators and their eigenvalues must be real as they can be the result of the experiment. The linear momentum operator for each electron $\hat{p}_i = -i\hbar\nabla_i$ gives the magnetic Hamiltonian operator as

$$\hat{\mathcal{H}}_M = - \sum_i \frac{ie\hbar}{m} \mathbf{A}_i \cdot \nabla_i + \sum_i \frac{e^2}{2m} \mathbf{A}_i^2 \quad (2.9)$$

in the Coulomb gauge ($\nabla \cdot \mathbf{A} = 0$). The first term can be given as a function of the angular momentum operator

$$\hat{\mathbf{L}} = \sum_i [\mathbf{r}_i \times (-i\hbar\nabla_i)] \quad (2.10)$$

since the vector potential of a stationary and uniform magnetic field is $\mathbf{A}(\mathbf{r}_i) = -\frac{1}{2}\mathbf{r}_i \times \mathbf{B}$. For a magnetic field oriented along z the operator of the magnetic Hamiltonian can be written as

$$\hat{\mathcal{H}}_M = \frac{\mu_B}{\hbar}(\hat{L}_z + g_0\hat{S}_z)B + \frac{e^2}{8m}B^2 \sum_i (x^2 + y^2) \quad (2.11)$$

as a magnetic moment, the spin degrees of freedom will be also lifted by the magnetic field. Thus, another term of the z component of the total spin operator is added. g_0 is the gyromagnetic ratio or g-factor for electronic systems that is $g_0 \approx 2$ for the electron spin.

The electron spin operator is defined by the Pauli matrices

$$\hat{s}_j = \frac{\hbar}{2}\hat{\sigma}_j \quad j = x, y, z \quad (2.12)$$

and the total momentum operator of a system of i particles is given by the sum of each particle spin operator. The z component of the total spin operator is then $\hat{S}_z = \sum_i \hat{s}_z^i$.

It is always possible to form a basis of orthonormal eigenvectors of Hermitian operators. Furthermore, a set of operators that commute by pairs form a complete set of commuting observables (C.S.C.O.) if specifying the eigenvalues a unique common eigenvector describe the quantum state, fulfilling the Pauli exclusion principle. It states that two identical electrons cannot occupy the same quantum state. Then, \hat{H}_0 , whose eigenvalue is the energy of the field-independent Hamiltonian, commute with \hat{L}^2 , \hat{S}^2 , \hat{L}_z and \hat{S}_z . forming a suitable C.S.C.O. Their eigenvalues for single-electron atoms are

$$\hat{\mathbf{L}}^2 \psi(\mathbf{r}) = l(l+1) \hbar^2 \psi(\mathbf{r}) \quad l = 0, 1, \dots, n-1 \quad (2.13)$$

$$\hat{L}_z \psi(\mathbf{r}) = m_l \hbar \psi(\mathbf{r}) \quad m_l = -l, -l+1, \dots, l-1, l \quad (2.14)$$

$$\hat{\mathbf{S}}^2 \psi(\mathbf{r}) = s(s+1) \hbar^2 \bar{\chi} \quad s = 1/2 \quad (2.15)$$

$$\hat{S}_z \psi(\mathbf{r}) = m_s \hbar \bar{\chi} \quad m_s = -s, -s+1, \dots, s-1, s \quad (2.16)$$

known as the quantum numbers.

For multi-electron atoms, the individual electron momenta are not constant of motion and their operators do not commute with the Hamiltonian, thus a new basis has to be written as a function of the total momentum operators with eigenvalues:

$$L = \left| \sum_i m_l \right| \quad \text{and} \quad S = \left| \sum_i m_s \right| \quad (2.17)$$

In the Dirac notation, the quantum states given by the eigenvalues of the C.S.C.O are written as $|E_n, L, S, m_L, m_S\rangle$. Single-electron atoms in a central potential form a degenerate quantum state as its energy only depends on the principal quantum number, n . For multi-electron atoms, the degeneracy will be lifted by the electron-electron Coulomb interactions and the relativistic corrections introduced by the Dirac equation. These atoms are mostly formed by ‘core electrons’. As the charge distribution in closed shells display spherical symmetry, the electron interaction will contain large spherically components and the central field approximation can be applied to the Hamiltonian. The lowest-lying levels after the degeneracy is lifted can be, to a good approximation, described by a simple set of rules ,.

The degeneracy is partially lifted to $(2L+1)(2S+1)$ possible states or multiplets according to the Hund’s first and second rule. The value of S is as large as possible with the limitations of the Pauli exclusion principle. On the other hand, for a given S , electrons occupy states such the value of L is maximum. Therefore, the previous C.S.C.O is still valid for light atoms in absence of applied field .

Corrections introduced by the relativistic treatment, known as the fine structure, break the degeneracy of the multiplets. The energy shift of the fine structure is strongly dependent on the atomic number. It varies from $\sim 10^{-4} - 10^{-5}$ eV for light atoms to 10^{-2} eV in rare-earth ions. Since energy levels of the non-relativistic Hamiltonian is in the order of eV, the fine structure can be computed by ordinary perturbation theory for light atoms (Russel-Saunders coupling). Its principal contri-

bution to the Hamiltonian is the coupling between the spin and orbital momentum. Moving electrons interact with the electrostatic field created by the protons by the so-called spin-orbit coupling

$$\hat{\mathcal{H}}_{SO} = \sum_i \xi_i(\mathbf{r}_i) \hat{\mathbf{L}}_i \cdot \hat{\mathbf{S}}_i \quad (2.18)$$

If the spin-orbit term is not negligible, $|E_n LS J m_J\rangle$.C.S.C.O is a better choice as the Hamiltonian commutes with the total angular momentum $\hat{\mathbf{J}} = \hat{\mathbf{L}} + \hat{\mathbf{S}}$ and its z component. A new energy term is obtained from the perturbation treatment

$$\langle E_0 LS J m_J | \sum_i \xi_i(\mathbf{r}_i) \hat{\mathbf{L}}_i \cdot \hat{\mathbf{S}}_i | E_0 LS J m_J \rangle = \zeta(L, S) \langle E_0 LS J m_J | \hat{\mathbf{L}} \cdot \hat{\mathbf{S}} | E_0 LS J m_J \rangle \quad (2.19)$$

The third Hund's rule is established by the sign of $\zeta(L, S)$. Positive values for subshells that are less than half filled will favor ground states with minimum J and negative values for subshells that are more than half filled will produce maximum J . Thus, the ground state will have a J value

$$\begin{aligned} J &= |L - S| & n \leq (2l + 1) \\ J &= L + S & n \geq (2l + 1) \end{aligned} \quad (2.20)$$

for n the number of electrons in the subshell and the energy degeneracy will be lifted to $2J + 1$ states known as J-multiplet.

The magnetic susceptibility is obtained by computing Eq. 2.11 in the new basis $|E_n LS J m_J\rangle \equiv |SJ\rangle$. The result of second-order perturbation theory is

$$\begin{aligned} \Delta E_M &= \mu_B B \langle J | (\hat{L}_z + g_0 \hat{S}_z) | J \rangle + \sum_{n' \neq n} \frac{\langle J | \mu_B B (\hat{L}_z + g_0 \hat{S}_z) | J' \rangle}{E_J - E_{J'}} \\ &+ \frac{e^2}{8m} B^2 \langle J | \sum_i (x^2 + y^2) | J \rangle \end{aligned} \quad (2.21)$$

The energy of the first and largest term of the magnetic Hamiltonian is given by the Bohr magneton $\mu_B = \frac{e\hbar}{2m} = 5.79 \times 10^{-5} \text{ eV/T}$.

It is worth noting that for weak magnetic fields, effects of the nuclear spin known as the hyperfine structure ($10^{-7} - 10^{-8} \text{ eV}$) might play a relevant role in the energy of the ground state.

2.1.2 Langevin Diamagnetism and Van Vleck paramagnetism

In insulators with all shells filled such as noble gases or simple ionic crystals the angular, the spin and the total angular momentum is zero. Hence, the dominant term known as the Zeeman energy vanishes. The ground state is degenerate and there is negligible probability of ion being in any but its ground state in thermal equilibrium. The susceptibility of a solid composed of N of those ions with Z the total number of electron per ion is given by the third term in Eq. 2.21

$$\chi_L = -\mu_0 \frac{N}{V} \frac{\partial^2 E_1}{\partial B^2} = -\frac{\mu_0 N Z e^2}{6mV} \langle r^2 \rangle \quad (2.22)$$

known as the Larmor diamagnetic susceptibility, since it induces a moment opposite to the applied field. The same result is obtained by the classical treatment of Langevin diamagnetism where electrons of filled shells precess around the central nuclei with the Larmor frequency $\omega = \mu_B B / \hbar$. Larmor diamagnetism is found in all kind of atoms due to the core electrons with typical values in the order of $\chi_L \sim 10^{-5}$.

In insulators with shells that are one electron short of being half filled, the linear term still vanishes but the ground state is non-degenerate as \mathbf{L} and \mathbf{S} are not zero. Excited states with $J' \neq 0$ can be thermally populated giving rise to a non-zero second term. Since the energy of any excited state will be higher than the ground state energy, it will give a paramagnetic contribution known as Van Vleck paramagnetism. The balance between the diamagnetic and the paramagnetic contributions will determine the magnetic behaviour since they are both small.

2.1.3 Paramagnetism

For all other cases, i.e., $J \neq 0$, the energy shift arises from the much larger first term known as Zeeman energy. The consequence of the applied field is the removal of the degeneracy in the $(2J+1)$ -fold degenerate ground state. The calculation of the eigenvalues of the Zeeman term involves a non-diagonal matrix whose diagonalization is given by the Wigner-Eckart theorem

$$\langle E_0LSJm_J | (\hat{L}_z + g_0\hat{S}_z) | E_0LSJm'_J \rangle = g(LSJ) \langle E_0LSJm_J | \hat{J}_z | E_0LSJm'_J \rangle \quad (2.23)$$

with the Landé factor

$$g(LSJ) = \frac{3}{2} + \frac{1}{2} \left[\frac{S(S+1) - L(L+1)}{J(J+1)} \right] \equiv g \quad (2.24)$$

independent of the \hat{J}_z eigenvalues. Hence, the $(2J+1)$ -fold degenerate ground state split into states with different energies $g\mu_B m_J B$.

Although the degeneracy is lifted by the applied field, the $(2J+1)$ lowest-lying states will contribute to the total magnetic density in Eq. 2.1 because $k_B T \gg g\mu_B B$ except at the lowest temperatures and highest fields. .

On the assumption that only the $2J+1$ states per ion contribute to the magnetic state, the magnetization given by Eq. 2.3 can be computed by means of the Brillouin function B_J for N of such ions in a volume V

$$M = \frac{N}{V} g J \mu_B B_J \left(\frac{g \mu_B J B}{k_B T} \right) \quad (2.25)$$

In most cases, the argument in Brillouin function is $x \ll 1$ as $x \cdot T \simeq 1\text{K}$ for $B = 1T$, hence it can be expanded as

$$B_J(x) = \frac{J+1}{3J} x + O(x^3) \quad (2.26)$$

It results in the well-known Curie's law in paramagnetic solids. The susceptibility varies inversely with the temperature as

$$\chi = \frac{N}{V} \frac{J(J+1)g^2\mu_B^2}{3K_B T} = \frac{N}{V} \frac{\mu_{eff}^2\mu_B^2}{3K_B T} = \frac{C}{T} \quad (2.27)$$

where C is the Curie constant and $\mu_{eff} = g[J(J+1)]$ the effective number of Bohr magnetons or effective moment per ion.

The theory of the atomic paramagnetism can be evaluated when they are part of a solid. Rare-earth insulators are found to obey Curie's law. In fact, the agreement between the calculated and the measured μ_{eff} is reasonable good if $J \neq 0$. The agreement fails in crystals based on elements with $J = 0$. In this case, the first J-multiplet lying just above the ground state is close enough in energy to have an important contribution to the second term in the magnetic Hamiltonian. At a first approximation, it may be concluded that the magnetism of rare earth ions in an insulating solid is well described by the $(2J+1)$ -fold degenerate ground state of the isolated ions.

On the other hand, insulators based on transition metal ions obeys a Curie's law if only the spin momentum is computed in the effective moment. The quenching of the angular orbital momentum ($L = 0$) is an effect of the crystal field on the outermost electronic shells.

The crystal field is an electric field derived from neighbouring atoms in the crystal. The electrons in the partially d-shells are affected by asymmetric crystal fields invalidating the Hund's rules. The crystal field splitting, that depends of the crystalline structure is often larger than the spin-orbit coupling in transition metals, hence it is computed as a perturbation of the $(2S+1)(2L+1)$ -fold degenerate ground state. In cases with low spin-orbit coupling (3d shells), the prevailing crystal field interaction lift the orbital degeneracy. If the crystalline structure is asymmetric enough a ground state where $\hat{\mathbf{L}}$ vanishes emerges. This is known as the quenching

of the orbital momentum.

Rare-earth ions can be considered the other limiting case where the crystal field splitting is irrelevant because f shells responsible for paramagnetism lies deep inside the ions. For heavier transition metals, the crystal field and the spin-orbit may be comparable resulting in more complex system where the ground-state will be driven by the competition of both interactions. Sometimes, the interactions are in the opposite way and the magnetic ions modify the crystalline symmetry by distorting the local environment known as Jahn-Teller effect.

2.2 Magnetic interactions

Until now, the magnetic properties of the materials have been described under the picture of atomic magnetism of non-interacting electrons. Although it successfully describes the magnetism in most of the insulators, magnetic interactions have obvious consequences in some solids such as the spontaneous alignment of the magnetic moments in ferromagnets. Without the presence of these interactions, the magnetic moment will be thermally disordered if no magnetic field is applied. Antiferromagnetism is another common case of magnetic order where the magnetic interactions favors antiparallel alignment between the magnetic moments resulting in a zero net magnetization. Ferrimagnetism, is a special case of antiferromagnetic coupling of local moments with different magnitude. The complexity of possible magnetic structures is large and other configurations such as spin density waves or helimagnetism have been also found in the nature. In this section, a simple introduction of the physics of the magnetic interaction is given.

2.2.1 Magnetic dipolar interaction

Against one's intuition, the dominant source of the magnetic interaction is not the dipolar or the spin-orbit interactions, but the Coulombic electron-electron interaction. In fact, the energy of the dipole-dipole interaction, relevant in some frustrated magnets known as spin ices (Sec. 2.3.1), depends on their separation and

their degree of mutual alignment

$$\mathcal{H}_{dipolar} = \frac{\mu_0}{4\pi} \left[\frac{\boldsymbol{\mu}_1 \cdot \boldsymbol{\mu}_2}{|\mathbf{r}|^3} - \frac{3(\boldsymbol{\mu}_1 \cdot \mathbf{r})(\boldsymbol{\mu}_2 \cdot \mathbf{r})}{|\mathbf{r}|^5} \right] \quad (2.28)$$

where $\boldsymbol{\mu}_i$ are magnetic moments with a relative position \mathbf{r} . It can be estimated for two moments each of $\mu \approx 1\mu_B$ separated by $r \approx 1\text{\AA}$ to be equivalent to about 1 K in temperature, values much lower than standard electrostatic energies between atomic states or the energy due to the electrostatic repulsion in magnetically ordered systems.

2.2.2 Exchange interaction

Exchange interactions are by far the main reason to have long range magnetic order. They are Coulombic interactions between electrons arising by the energy cost of keeping electrons close together. They are a consequence of the symmetrization postulate of quantum mechanics. It states that a system of several identical particles described by a set of eigenvectors of a C.S.C.O must be antisymmetric with respect to permutation of these particles if they are fermions.

The exchange interaction may be explained by a simple model of two electrons. This system has two possible total wavefunctions, one with a singlet state $\bar{\chi}_S$ ($S = 0$) and another with a triplet state $\bar{\chi}_T$ ($S = 1$). In the former case $\bar{\chi}$ is antisymmetric since spins are antiparallel, hence it must have a symmetric spatial part. On the other hand, the triplet must have a spatial part which is antisymmetric under exchange of the two electrons.

The independent electron approximation solves the problem by using the two wavefunctions with lowest energy solutions of the one-electron problem to form symmetric and antisymmetric space wavefunctions. It results a bad approximation when the protons are far apart. Instead, the tight-binding method takes linear combinations of atomic stationary-state wavefunctions centered at the lattice points

where protons are fixed (a and b).

$$\begin{aligned}\psi_0 &= \psi_a(\mathbf{r}) + \psi_b(\mathbf{r}) \\ \psi_1 &= \psi_a(\mathbf{r}) - \psi_b(\mathbf{r})\end{aligned}\tag{2.29}$$

Then, the two-electron symmetric spatial wavefunction can be built as $\psi_S(\mathbf{r}_1, \mathbf{r}_2) = \psi_0(\mathbf{r}_1)\psi_1(\mathbf{r}_2)$ and the antisymmetric as $\psi_T(\mathbf{r}_1, \mathbf{r}_2) = \psi_0(\mathbf{r}_1)\psi_1(\mathbf{r}_2) - \psi_1(\mathbf{r}_1)\psi_0(\mathbf{r}_2)$ resulting in

$$\begin{aligned}\Psi_S &= \frac{1}{\sqrt{2}} [\psi_a(\mathbf{r}_1)\psi_b(\mathbf{r}_2) + \psi_a(\mathbf{r}_2)\psi_b(\mathbf{r}_1)] \bar{\chi}_S \\ \Psi_T &= \frac{1}{\sqrt{2}} [\psi_a(\mathbf{r}_1)\psi_b(\mathbf{r}_2) - \psi_a(\mathbf{r}_2)\psi_b(\mathbf{r}_1)] \bar{\chi}_T\end{aligned}\tag{2.30}$$

Note, that terms in the singlet wavefunction which entails both electrons centred on the same proton are not considered here. This is known as the Heitler-London approximation that is valid for widely separated protons.

The singlet-triplet splitting can be estimated as

$$E_S - E_T = \langle \Psi_S^* | \hat{\mathcal{H}} | \Psi_S \rangle - \langle \Psi_T^* | \hat{\mathcal{H}} | \Psi_T \rangle\tag{2.31}$$

that results in the exchange integral or exchange interaction J

$$J = \frac{E_S - E_T}{2} = \int \psi_a^*(\mathbf{r}_1)\psi_b^*(\mathbf{r}_2)\hat{\mathcal{V}}\psi_a(\mathbf{r}_2)\psi_b(\mathbf{r}_1) d\mathbf{r}_1 d\mathbf{r}_2\tag{2.32}$$

that is related to the overlap of the charge distributions of the atom a and b in an effective potential, $\hat{\mathcal{V}}$.

The analysis of the two-electron problem can be simplified by consider a four-fold degenerate ground state when atoms are far apart that is lifted when atoms get closer as $E_S \neq E_T$. The quantum system can be represented as a simple four-level system where the difference between the singlet and triplet states can

be parametrized by the $\hat{\mathbf{S}}_1 \cdot \hat{\mathbf{S}}_2$ operator. Hence, the effective Hamiltonian will include a spin-dependent term that can be written as

$$\hat{\mathcal{H}}_{spin} = -2J\hat{\mathbf{S}}_1 \cdot \hat{\mathbf{S}}_2 \quad (2.33)$$

The spin Hamiltonian will favor the triplet state or parallel alignment of the spins if $J > 0$ and the singlet state or antiparallel alignment if $J < 0$.

The generalization to a many-body system is not trivial but for many cases the spin Hamiltonian can be written as the sum over all pairs of ions

$$\hat{\mathcal{H}}_{spin} = - \sum_{\langle i,j \rangle} J_{i,j} \hat{\mathbf{S}}_1 \cdot \hat{\mathbf{S}}_2 \quad (2.34)$$

known as the Heisenberg Hamiltonian. The calculation of the exchange integral is complicated but there are some general results that can be useful. First Hund's rule is consistent with a positive exchange integral for two electrons on the same atom. In the case of interatomic electrons, $J_{i,j}$ is sometimes considered constant for nearest neighbour spins and to be 0 otherwise.

The Ising model is a specific case of the Heisenberg Hamiltonian in which the spins are only allowed to point to one direction. In this case the Hamiltonian is written as

$$\hat{\mathcal{H}}_{spin} = - \sum_{\langle i,j \rangle} J_{i,j} \hat{S}_1^z \cdot \hat{S}_2^z \quad (2.35)$$

Although, there is no a complete formulation of the zero-field susceptibility in the Heisenberg model. The high-temperature expansion of the susceptibility results in a modified Curie's law

$$\chi = \frac{N}{V} \frac{g^2 \mu_B^2}{3K_B T} S(S+1) \left[1 + \frac{\theta}{T} \right] = \frac{C}{T} \left(1 + \frac{\theta}{T} \right) \quad (2.36)$$

where $\theta = \frac{S(S+1)}{3} \frac{J_0}{k_B}$ with J_0 the sum of the exchange interactions. Therefore, $\theta > 0$ ($\theta < 0$) when the predominant coupling is ferromagnetic (antiferromagnetic). The above equation is the Taylor expansion, for $\theta \ll T$ of

$$\chi = \frac{C}{T - \theta} \quad (2.37)$$

θ is usually called the Curie-Weiss parameter due to the Weiss model of ferromagnetism and antiferromagnetism based on the mean field approximation that arrives to the same formula with $\theta = T_C$ or $\theta = -T_N$, the Curie and Neel transition temperatures of ferromagnets and antiferromagnets, respectively. Experimentally, there are large discrepancies between the Curie-Weiss parameter and the transition temperatures due to the mean field assumptions.

2.2.3 Types of exchange interaction

The model above described is known as direct exchange. This is because it arises from the Coulombic interaction between electrons on neighbouring magnetic atoms without any intermediary. It is common that there is not enough direct overlap between neighbouring magnetic orbitals and direct exchange cannot be the important exchange mechanism. This is the case of rare-earths where the f-electrons are strongly localized and lie very close to the nucleus. Magnetic properties are even hard to justify by direct exchange in transition metals that have delocalized d orbitals.

Instead, indirect exchange mechanisms become relevant. Superexchange is an indirect exchange found in some ionic solids. The two magnetic atoms are separated by a nonmagnetic ion which mediates the interaction. In a simple case two magnetic atoms with an unpaired electron in a d orbital are separated by an oxygen atom with two p electrons in the unfilled shell. The antiferromagnetic coupling will

lower the energy of the system by allowing the electrons become delocalized. The coupling is strongly dependent upon the bond direction. Ferromagnetic coupling, although possible, are less common and weak.

In rare-earth systems, the direct exchange is weak and magnetic atoms are coupled through their interactions with the conduction electrons. This exchange interaction will be more detailed in Sec 2.6. Itinerant exchange, an important exchange mechanism among the conduction electrons in metals or the double exchange between ions in different oxidation states are other possible cases.

2.3 Magnetic frustration

Magnetic frustration takes place in materials where the local magnetic moments cannot simultaneously satisfied all the pairwise exchange interactions so there is no an unique ground state. Therefore, a large landscape of energetically equivalent states, separated by low energy barriers which can be crossed by thermal or quantum processes, with a macroscopic degeneracy emerges. From the early 60s to the late 80s the interest for magnetic frustration were focused on spin glasses, systems where both frustration and disorder act together down to a freezing temperature at which point the quenched disorder produces a degenerate ground state whose explanation is not fully understood due to the complex role of the disorder in their properties [1]. Frustrated magnetism has become an extremely active field of research in the last 20 years in systems with clean and periodic lattices but still geometrically frustrated, motivated by the discovering of new states and new properties of matter. Under certain conditions, frustration leads to exotic ground states, normally described as cooperative paramagnets, characterised by the lack of long-range order and spins that remain highly correlated down to a temperature of absolute zero. They form a fluid-like state of matter, so-called spin liquids. In spin ice, a classical spin liquid, thermal fluctuations and/or magnetic field can produce collective phenomena like fractionalised elementary excitations or monopoles. In some cases, the uncertainty principle allows quantum fluctuations that persist

down to zero Kelvin, resulting in a quantum spin liquids, which is a superposition state in which the spins simultaneously point in many different directions [2]. New properties and/or alternatives to long-range order such as residual entropy, dipolar correlations, gapped or gapless spin liquids, spin nematics or the frustration role in multiferroics encouraged scientists to study frustrated magnets. Recently, the constraints imposed by the limited frustrated magnets found in nature have been overcome by fabricating artificial frustrated lattice with a spin ice-like behaviour [3].

There are several ways to distinguish between normal and cooperative paramagnets in periodic lattices. One of the most revealing evidence of frustration is observed in the magnetic susceptibility. Both follow a Curie-Weiss law temperature dependence, where the Curie-Weiss parameter θ_{CW} is proportional to the spin interactions and its sign determines if the coupling is antiferromagnetic or ferromagnetic, but whereas a normal parameter usually order at $T \sim \theta_{CW}$, observed by a cusp in χ , the frustrated magnet behaves as a cooperative paramagnet until temperatures much lower than the Curie-Weiss parameter. They sometimes magnetically order or freeze the spins out at lower temperatures T_c and frustration is revealed by a large ratio $f \equiv |\theta_{CW}|/T_c \gg 1$ [4]. Long-range magnetic order is then avoided in the frustrated regime $T_c < T < |\theta_{CW}|$, see Fig. 2.1 (a). Although frustration is manifested in other bulk properties such as anomalously large specific heat or residual entropy in spin ice, the distinction from conventional paramagnets and useful information are better obtained by local magnetic probes as neutron scattering which easily differentiate spin ordered phases. The periodic spin correlation is observed in the form of Bragg peaks, while the decreasing spin correlation in a paramagnet gives rise to diffuse scattering, Fig. 2.1 (b). The diffuse neutron scattering in the reciprocal space is characterised by the correlation function $S(\mathbf{Q})$ with vector \mathbf{Q} that presents different symmetries with respect to a Brillouin zone centre. Ideal or conventional paramagnetic phases have an homogeneous and/or isotropic correlation function, frustrated systems have an anisotropic spin-spin correlation function with respect to the vector \mathbf{Q} [5].

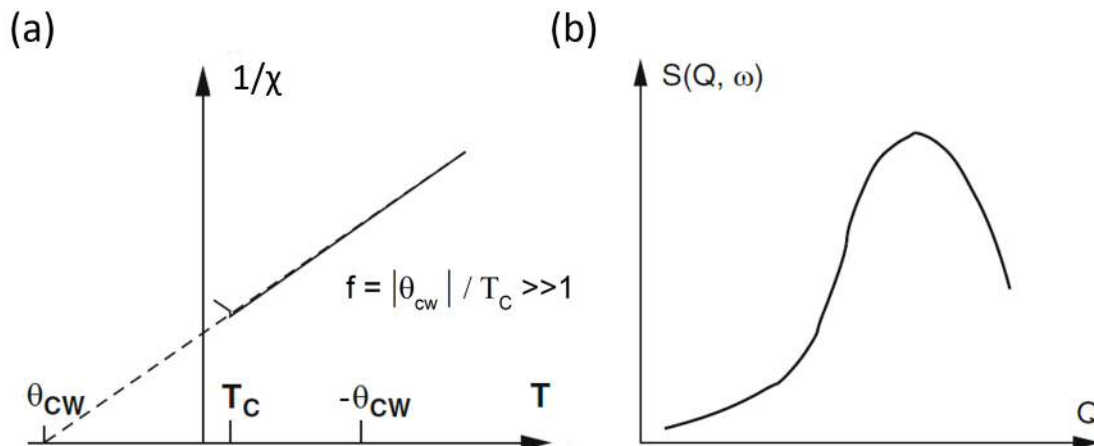


Figure 2.1: (a) Sketch of the temperature dependence of the susceptibility. Frustration is characterised by a large frustrated ratio, f . (b) Sketch of the correlation function. Frustrated paramagnets present an anisotropic $S(Q, \omega)$ with respect to the vector Q .

The most ubiquitous path to obtain frustrated magnets is the geometric frustration. Some families of compounds with inherent frustrated geometries are triangular and kagomé (formed by corner-sharing triangles) antiferromagnets in 2D or spinel and pyrochlore lattice in 3D. Examples are shown in Fig. 2.2. In this work, the interest will be focused on the magnetic family of $A_2B_2O_7$ pyrochlore oxides formed by a rare-earth element A and a transition metal B such as Ti, Sn, Mo or Mn that have a wide range of low temperature thermodynamic and magnetic exotic properties. A review can be found here [6].

2.3.1 Dipolar spin ice

Unlike systems with antiferromagnetic coupling between the magnetic moments located on the sites of triangular, kagomé or tetrahedral lattices, spin ices constitute a less-known systems of pyrochlore oxides with large magnetic moment (Dy^{3+} , Ho^{3+}) coupled ferromagnetically in a lattice with a strong, single-ion and Ising-like anisotropy. Geometrically frustrated antiferromagnets are interesting due to the novel quantum ground states with exotic properties like no long-range order and quantum bonds at temperatures close to zero that arise from quantum fluc-

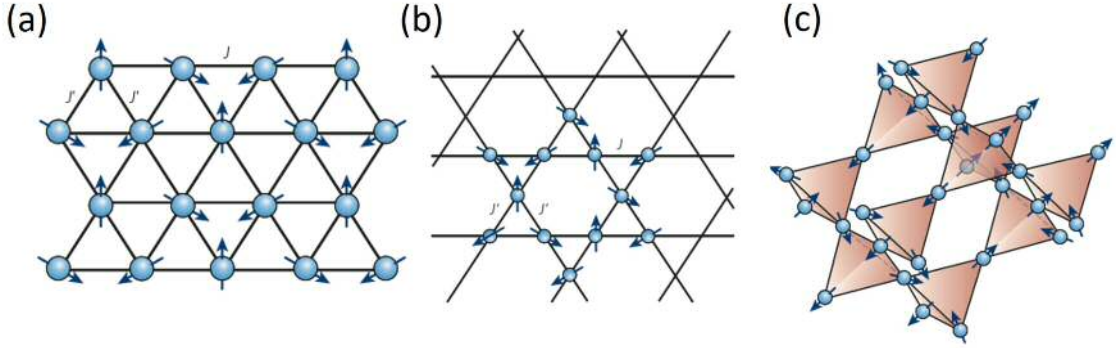


Figure 2.2: (a) Triangular and (b) kagomé lattice with antiferromagnetic coupling. (c) Ferromagnetic pyrochlore lattice taken from [2].

tuations [2, 5]. In spin ice, the frozen ground state is apparently not influenced by quantum fluctuations and some controversial studies reveal that magnetic excitations might be deconfined and fractionalised forming elementary excitations or magnetic monopoles [7]. They get their name from the large degenerate ground state that displays an extensive low-temperature entropy analogous to the proton-disorder entropy in water ice.

The large number of possible configurations, Ω of degenerate ground states in geometrically frustrated magnetic systems results in a macroscopic residual ground state entropy, $S_o = k_B \ln(\Omega)$ that was earlier found in water ice and explained by Pauling [8]. The tetrahedrally coordinated O^{2-} framework constrains the protons to be only one per O-O bond with two equivalent positions that states the “ice rules”: for each oxygen anion two protons must be “near” and two “far”. This configuration gives six equivalent configurations, whose entropy Pauling calculated, $S = N_0 k_B \ln(3/2)$, being N_0 the number of oxygen anions.

Pyrochlore oxides form a crystal structure of two independent and interpenetrating pyrochlore sublattices of A^{3+} and B^{4+} ions respectively. They are face-centered cubic lattice with a tetrahedral basis cell of four sites occupied by the ions. Alternating “upward” and “downward” corner-sharing tetrahedra constitute the pyrochlore lattice that is shown only for the rare earth sublattices in Fig. 2.2

(c). The energetic study of the ground-state leads to a magnetic ion configuration that behave as a classical Ising-like doublets aligned with the local $\langle 111 \rangle$ axis that connects the centres of the two tetrahedra in such a way that the ground state has two spins pointing towards the centre and two away, in analogy with the local proton coordination in water ice.

The magnetic properties of pyrochlore oxides are characterised by the exchange and dipolar interactions of mainly the nearest-neighbour spins. If the exchange interaction is antiferromagnetic and stronger than the dipolar interactions unusual magnetic states flourish in the frustrated lattices, such as quantum spin liquids [2], otherwise long-range order emerges. Spin ice are a special case where exchange and dipolar interaction have a comparable energy scales. To date, spin ice features have been widely investigated in series with Dy and Ho, being the insulating $\text{Dy}_2\text{Ti}_2\text{O}_7$ and $\text{Ho}_2\text{Ti}_2\text{O}_7$ considered the canonical spin ice.

The isolated electronic ground state of rare-earth atoms is normally given by the total angular momentum, \mathbf{J} . When it is studied in a lattice, the $(2J+1)$ -fold degeneracy is lifted by the crystal-field interaction. In the system of interest, the energy levels can be studied by a Hamiltonian given by the crystal-field of the non-interacting ions (single-ion) plus the Zeeman effect and another term that describes the ionic interactions. The crystal-field ground-state doublet have a large energy gap ~ 300 K to the first excited state and the Zeeman excited state at 20 T is around 10 K, so it is safe to consider that below 10 K the Dy- and Ho- spin ice have a ground-state doublet where the accessible states are given by the ionic interactions. Then, an effective low-temperature Hamiltonian that describes the ionic interactions may be developed using the perturbation theory on the basis of the single-ion, crystal-field ground state. As a result, only two eigenstates of the total angular momentum operator have a significant weight $\langle \hat{J}_z \rangle = \pm J$ in the tetrahedra basis along one of the four cubic $\langle 111 \rangle$ directions. It means, that the magnetic moments behave as classical spins aligned parallel or antiparallel to the local $\langle 111 \rangle$ axis. It gives an

effective, classical and Ising-like Hamiltonian in the dipolar spin-ice model

$$\mathcal{H}_{SI} = -J \sum_{\langle i,j \rangle} \mathbf{S}_i \cdot \mathbf{S}_j + D \sum_{i,j} \left[\frac{\mathbf{S}_i \cdot \mathbf{S}_j}{|\mathbf{r}_{ij}|^3} - \frac{3(\mathbf{S}_i \cdot \mathbf{r}_{ij})(\mathbf{S}_j \cdot \mathbf{r}_{ij})}{|\mathbf{r}_{ij}|^5} \right] \quad (2.38)$$

governed by the nearest-neighbour exchange coupling, J and the long-ranged magnetostatic dipole-dipole interaction D between the electronic spins \mathbf{S}_i and \mathbf{S}_j separated a distance \mathbf{r}_{ij} and magnitude $|\mathbf{S}| = 1$, ($\mathbf{S}_i \cdot \mathbf{S}_j = -1/3$ for $i \neq j$) in the local Ising frame. This Hamiltonian is justified in the Ho^{3+} , Dy^{3+} - insulating rare-earth oxides, with a large total angular momentum $\mathbf{J} = 8$ and $15/2$ respectively, by the antiferromagnetic exchange interaction J and dipolar energy D much smaller than the crystal-field that lie on the same range of energy for $Ho_2Ti_2O_7$ [9] and $Dy_2Ti_2O_7$ [10].

The first experimental evidence of geometrical magnetic frustration in these systems was found in $Ho_2Ti_2O_7$ [11, 12]. No long-range order was observed down to 350 mK in the neutron scattering results and to 50 mK with μ SR. A ferromagnetic interaction was deduced from the positive Curie-Weiss parameter ($\theta_{CW} = 1.9$ K). A ferromagnetic interaction is required to cause frustration. The antiferromagnetic coupling $J < 0$ in $Ho_2Ti_2O_7$ and $Dy_2Ti_2O_7$ should lead to a long-range order (all-in or all-out) but combined with a positive long-range dipolar interaction ($1/r_{ij}^3$) results in an effective ferromagnetic coupling and a frustrated ground state in the ‘‘dipolar spin ice model’’. The proposed ground state is characterised by a simple and six-fold degenerate spin arrangement with two spins ‘‘in’’ and two spins ‘‘out’’ on each tetrahedron which fulfils the ice condition

$$\sum_{tetra} \mathbf{S}_i = 0 \quad (2.39)$$

Dipolar spin-ice ground state depends on the weak equilibrium of the long-range dipolar interaction with the antiferromagnetic exchange interaction in a system with single-ion anisotropy. The large magnetic moments of both Dy^{3+} and Ho^{3+} , about $10 \mu_B$, lead to a strong dipolar interaction that gives them a critical role in the spin-ice states. Spin ice features have been observed in other pyrochlore

oxides such as stannates $(\text{Ho,Dy})_2\text{Sn}_2\text{O}_7$ [6] and germanates $(\text{Ho,Dy})_2\text{Ge}_2\text{O}_7$ [13–15], or the dynamical spin-ice state reported in $\text{Pr}_2\text{Sn}_2\text{O}_7$ [16], but also in other structures as the CdEr_2Se_4 [17] spinel that opens the investigations to a new family of compounds. Other pyrochlore oxides like the Tb-based have a lower energy gap separating the ground doublet that hinders the application of the dipolar spin-ice model.

The canonical spin ices, $\text{Ho}_2\text{Ti}_2\text{O}_7$ and $\text{Dy}_2\text{Ti}_2\text{O}_7$ have been chosen for the calibration and the first measurements in the novel magnetometer because they have a freezing temperature that depends dramatically with the frequency at mK temperatures as can be seen in Fig. 2.3. This dependency will help to detect thermalisation issues at those temperatures.

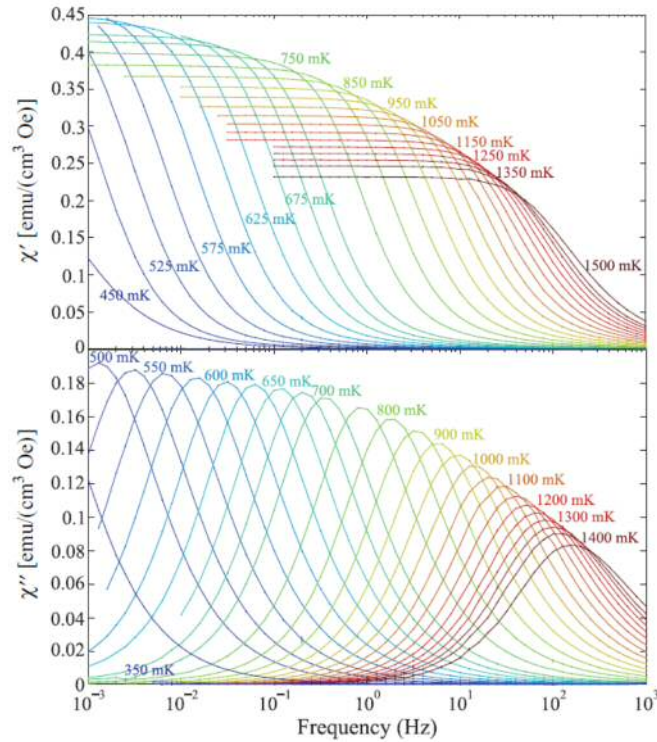


Figure 2.3: Scans of χ' and χ'' on $\text{Dy}_2\text{Ti}_2\text{O}_7$ measured along the $[110]$ axis taken from [18].

2.4 Magnetism in metals

Previous section has been focused in the atomic magnetic properties and their application in solids with spatially localized magnetic moments. The extrapolation to insulating solids is possible thanks to the exclusion principle. The constraint makes the atomic electrons to behave similarly to electrons localized on different ions. In metals, the magnetic moments can be associated to the localized magnetic moments but also to the strongly delocalized conduction electrons or itinerant electrons. The study of the magnetism in the free or non-interacting electron model gives rise to the weak Pauli paramagnetism and Landau diamagnetism. This simple approximation is inadequate to the problem of magnetism in real metals, where electron-electron interactions have a dominant role in the magnetic properties but the magnetism of free electron gas is a good starting point to investigate the intricate magnetism in metals.

Non-interacting fermions are treated, in the Fermi gas model, as quantum particles that occupy the available energy states according to the Pauli exclusion principle. At $T = 0$ K, without thermal excitations, electrons with mass m fill up the states up to the Fermi energy

$$\epsilon_F = \frac{\hbar k_F^2}{2m} \quad (2.40)$$

with a characteristic Fermi surface represented by the Fermi wave vector k_F .

Each electron contributes $-\mu_B/V$ to the magnetization density if its spin is parallel to the applied field and μ_B/V if it is antiparallel to the field, for the g-factor of an electron $g_0 = 2$. Therefore the magnetization density will be

$$M = -\mu_B(n_+ - n_-) \quad (2.41)$$

as quantum particles, electrons obey Fermi Dirac statistics and the density of

electrons with spin parallel or antiparallel to the field, n_{\pm} is given by

$$n_{\pm} = \int f(\epsilon, \mu) g_{\pm}(\epsilon) d\epsilon \quad (2.42)$$

where $g_{\pm}(\epsilon)d\epsilon$ is the density of states for each kind of spin in the energy range $\epsilon + d\epsilon$ and f is the Fermi function that governed the occupancy of each state at a specific temperature. The chemical potential μ can be written as a function of the Fermi energy being $\mu = E_F$ at $T=0$ K.

In metals, the density of states is on the scale of Fermi energy. Since the $\mu_B B$ is much smaller than ϵ_F , the density of each spin state can be expanded as a function of the density of states at zero field

$$g_{\pm}(\epsilon) = \frac{1}{2}g(\epsilon) \pm \frac{1}{2} \frac{dg(\epsilon)}{d\epsilon} \mu_B B \quad (2.43)$$

In conjunction with Eq. 2.42 the magnetic density results in

$$M = \mu_B^2 B \int g(\epsilon) \left(-\frac{\partial f}{\partial \epsilon} \right) d\epsilon \quad (2.44)$$

In the degenerate limit at $T=0$ K, $-\frac{\partial f}{\partial \epsilon} = \delta(\epsilon - \epsilon_F)$. It results in a paramagnetic susceptibility

$$\chi = \mu_B^2 g(\epsilon_F) = \frac{2n\mu_0\mu_B^2}{2\epsilon_F} \quad (2.45)$$

known as the Pauli paramagnetic susceptibility. The susceptibility of conduction electrons is a weak effect $\chi_P \sim 10^{-6}$ much smaller than the paramagnetism observed in insulators and independent of the temperature. This is because only electrons close to the Fermi surface contributes to the magnetism.

2.5 Landau-Fermi liquid theory

Landau successfully addressed the inherent complexity of strongly interacting fermion systems in the limiting case of low temperatures and low-excitation energies in the Landau-Fermi Liquid (LFL) Theory [19]. It describes the normal state of most metals but also some extremes cases of strong correlated systems such as some heavy fermions [20, 21] and cuprate superconductors [22].

From the Fermi gas model of non-interacting fermions Landau considered that the scattering of an extra fermion in the Fermi surface is constrained by the occupied states and the Pauli exclusion principle, so he considered a Fermi gas of non-interacting fermions where the interactions were adiabatically turned on. The single-particle excitation so-called “quasiparticle” that corresponds one-to-one to the non-interacting fermion contains information of the interaction by renormalising the bare electron mass ($m \rightarrow m^*$)

$$\frac{m^*}{m} = 1 + \frac{F_1^s}{3} \quad (2.46)$$

The main thermodynamic and transport properties in the LFL are renormalised to

$$C_p/T = \gamma = \frac{m^* k_F k_B^2}{3\hbar^2} \quad (2.47)$$

$$\chi = \frac{\mu_0 \mu_B m^* k_F}{\pi^2 \hbar^2} \frac{1}{1 + F_0^a} \quad (2.48)$$

$$\rho = \rho_0 + AT^2 \quad (2.49)$$

given a linear specific heat renormalised by the Sommerfield coefficient, γ , a constant magnetic susceptibility and the resistivity that depends quadratically on temperature. F_0^a and F_1^s are Landau parameters, k_B the Boltzmann constant, μ the Bohr magneton, ρ the residual resistivity and A , a coefficient proportional to the square of the renormalised density of states at the Fermi level.

$$N(E_F) = \frac{m^* k_F}{\pi^2 \hbar^2} \quad (2.50)$$

Qualitatively, LFL retain the non-interacting Fermi gas properties but enhanced by the quasiparticle mass m^* . The fact that LFL is applicable at low temperatures and excitations close to the Fermi surface is due to the required long lifetime τ of the quasiparticle that is inversely proportional to the energy difference $(E - E_F)$.

2.6 Heavy fermion systems

Heavy fermion systems (HF) are intermetallic compounds with unfilled f-electron bands with strong interactions. Since they were firstly discovered by Andres et al. [23] in CeAl_3 , systems where the f-electrons are entangled with the conduction band electrons below a characteristic temperature have given rise to a new family to study magnetic interactions in strongly correlated compounds with a diversity of ground states [24]. They are characterised by the formation of quasiparticles with effective masses 100s to 1000s times larger than the bare electron mass. The physics of heavy fermions is described by the Kondo lattice model [25] as an expansion of the well-known single-ion Kondo effect. Experimental review of f-electron metals can be found in Stewart work [26].

2.6.1 Kondo effect

The minimum in the resistivity curve at low temperature of systems with magnetic impurities embedded in a metallic and non-magnetic host shown in Fig. 2.4 was solved by Kondo [27] by adding a perturbation term, H_K to the Hamiltonian. In the dilute regime where the magnetic impurities interaction can be neglected, the Hamiltonian proposed by Kondo is the sum of an unperturbed term that takes into account the kinetic energy of the itinerant electrons and H_K that deals with the scattering off the sea of conduction electrons with spin moments $\mathbf{s}(\mathbf{r})$ and the localised magnetic impurity, \mathbf{S} , through the Kondo exchange interaction, J_K .

$$\mathcal{H}_K = -J_K \mathbf{S} \cdot \mathbf{s}(\mathbf{r}) \quad (2.51)$$

The Kondo perturbation explained the upturn of the electric resistivity and the resistance minimum at low temperatures in metals. The spin scattering off individual

magnetic impurities results in a logarithmic contribution to the resistivity that combined with the T^5 term, due to the phonon scattering or lattice resistivity, explains the observed minimum at low temperatures

$$\rho = aT^5 + c\rho_0 - c\rho_1 \log T \quad (2.52)$$

where ρ_0 is a residual resistivity which involves many causes. a, c, ρ_1 are material constants.

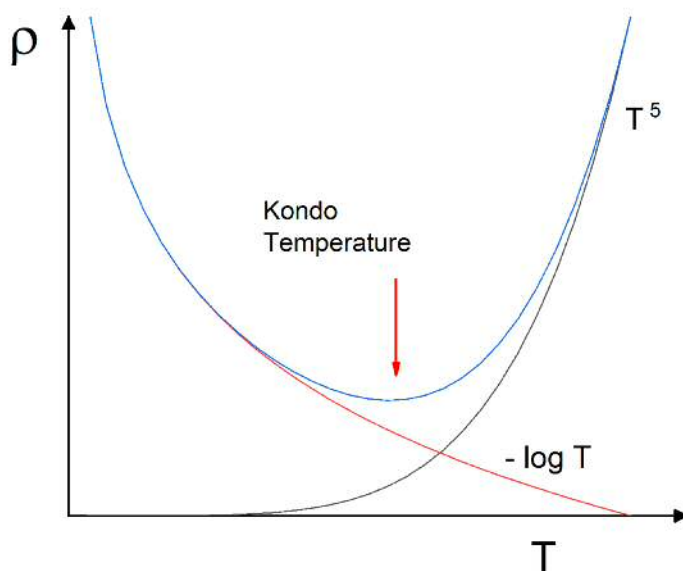


Figure 2.4: Temperature dependence of resistivity for metal with magnetic impurities that introduce a logarithmic contribution to the phonon scattering T^5 term. Minimum is given at the so-called Kondo temperature, T_K .

Kondo's calculations gave rise to a resistivity divergence for temperatures approaching zero Kelvin in the case of antiferromagnetic exchange interaction constituted the so-called Kondo problem. The unphysical result was solved by using renormalisation group by Wilson et al. [28] in terms of a singlet bound state ($S=0$) between the conduction electrons and a localized spin [29], that also explained other

experimental results such as the saturation of the magnetic susceptibility. The polarised conduction electrons form an electronic cloud around the localised spin that screens the magnetic moment resulting in a non-magnetic ground state. The antiferromagnetic hybridization of the conduction electrons with f-impurities and the formation of the singlet state due to the Kondo effect induces a peak in the density of states, $N(E_F)$, at the Fermi energy whose characteristic energy is given by the Kondo temperature

$$K_B T_K \propto \exp\left(-\frac{1}{N(E_F)J_K}\right) \quad (2.53)$$

At sufficiently low temperature, $T \ll T_K$, the system with the magnetic impurities behaves in the Fermi liquid framework of heavy quasiparticles with a large effective mass. It means, a temperature-independent Pauli susceptibility, a large linear specific heat and a saturated residual resistivity. At $T \gg T_K$ systems exhibit a Curie-like susceptibility due to the non-interacting magnetic moments as a normal metal with free magnetic moments.

2.6.2 RKKY interaction

In contrast to the well-understood impurity limit, when a periodic array of Kondo atoms are distributed in the lattice an effective spin-spin interaction between the localised magnetic moments cannot be neglected. It is well known that the electronic spin density of a sea of itinerant electrons are polarised by the localised magnetic moment via the antiferromagnetic Kondo exchange J_K . In densely-packed magnetic moments, although the direct interaction is rather weak and insignificant due to the screening effect, the polarisation of the conduction cloud leads to a strong and long-range indirect exchange interaction. The so-called Ruderman, Kittel, Kasuya, Yosida (RKKY) interaction [30] is given by a Hamiltonian

$$\mathcal{H}_{RKKY} = J_{RKKY}(\mathbf{r}) \mathbf{S}_i \cdot \mathbf{S}_j \quad (2.54)$$

that describes the coupling between local spins \mathbf{S}_i and \mathbf{S}_j separated by a distance r in terms of the RKKY exchange interaction J_{RKKY} . As only electrons within a limited wavelength range near to the Fermi surface participate in the scattering process, the polarisation of the conduction electrons is modulated by the momentum of the Fermi surface, $2k_F$, and decays as $1/(k_F r)^3$ (Friedel oscillations). The exchange interaction with a second local moment reduces at large distance to

$$J_{RKKY} \sim -J_K^2 N(E_F) \frac{\cos(2k_F r + \phi)}{(2k_F r)^3} \quad (2.55)$$

assuming a spherical Fermi surface of momentum k_F and density of states $N(E_F)$. The phase factor ϕ takes into account the charge difference between the impurity and the host. The oscillatory coupling determined by the itinerant electrons on the Fermi surface may be then ferromagnetic or antiferromagnetic depending on the f-electrons distance as shown Fig. 2.5.

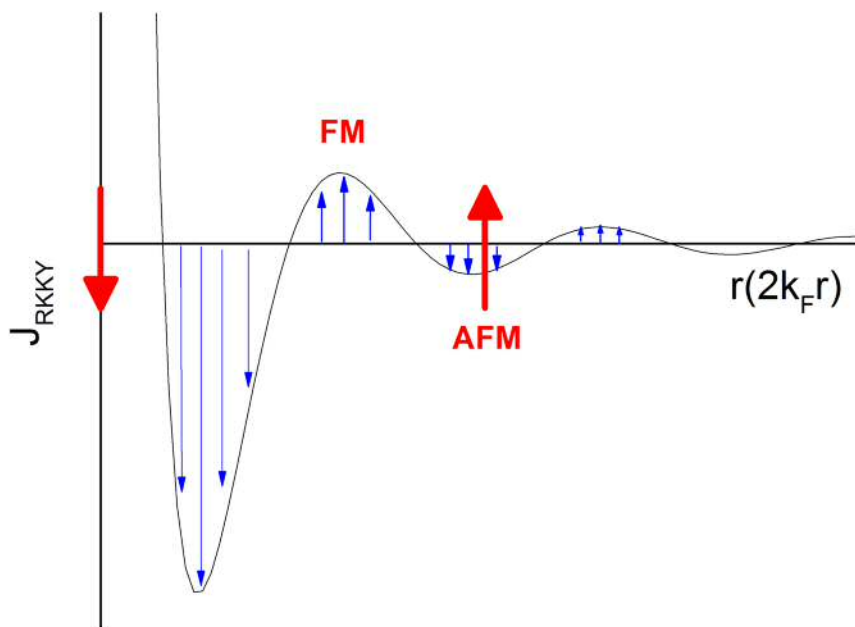


Figure 2.5: RKKY exchange interaction, J_{RKKY} produced by a magnetic atom at $r=0$. The antiferromagnetic Kondo exchange, J_K polarises the conduction electron (blue arrows) and a long range magnetic interaction with either ferromagnetic and antiferromagnetic coupling are possible.

The characteristic energy of the RKKY interaction is

$$k_B T_{RKKY} \sim J_K^2 N(E_F) \quad (2.56)$$

In contrast to the Kondo interaction, where the conduction electrons weaken the magnetic atoms interaction, the RKKY interaction favours a ground state in which the atoms are magnetically ordered.

2.6.3 Kondo lattice

The complex interplay between long-range magnetic order (RKKY interaction) and the non-magnetic singlet bound state (Kondo interaction), that depends on J_K , is described by, the still unsolved, Kondo lattice model [31]. The competition is often represented by the Doniach's phase diagram [32] in Fig. 2.6.

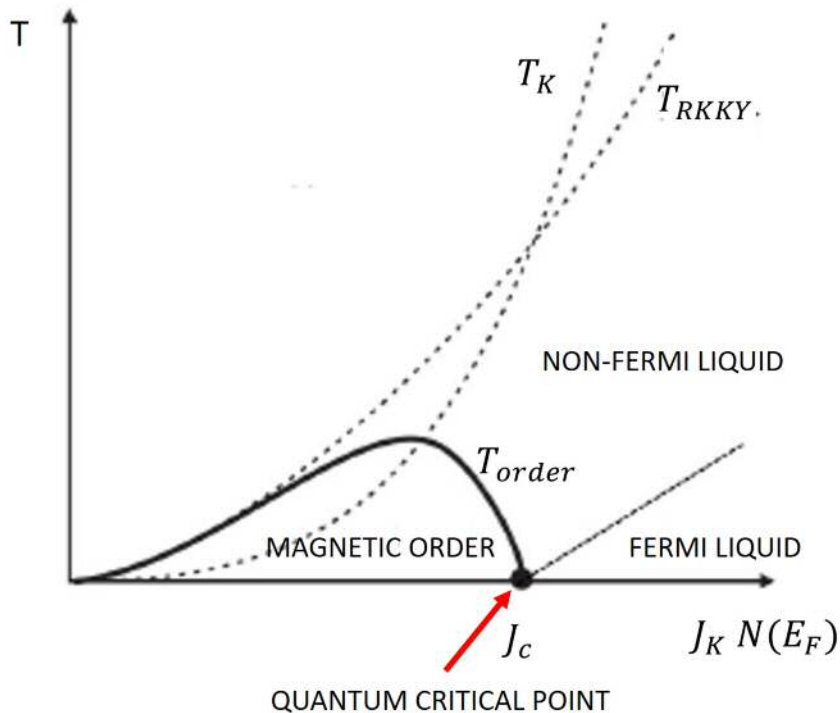


Figure 2.6: Doniach's phase diagram.

For weak couplings $J_K < J_c$ the interaction between the local moments dom-

inates and magnetic order, normally antiferromagnetic, emerges in a small Fermi volume. In the localised limit, CeCu_2Ge_2 is an archetypal antiferromagnet whose localised 4f electrons order at $T_N \approx 4\text{K}$ [33] in a well-defined crystal field-doublet manifold [34]. On the other hand, if Kondo screening dominates, $J_K > J_c$, the Fermi volume, containing both itinerant electrons and the local moments, will be large [35], the non-magnetic singlet formation and heavy-electron band with highly renormalized quasiparticles will emerge. In the first heavy fermion discovered, CeAl_3 , a 4f virtual-bound-state formation gives rise to a non-magnetic singlet. The linear heat capacity, constant paramagnetic susceptibility and quadratic resistivity is an example of a Fermi Liquid ground state with strongly renormalised masses [23].

Doniach's picture is only a comparison of energy scales and does not provide information of the mechanism that connects the antiferromagnetic state to the heavy-fermion phase. In fact, the surface of large Fermi volume is susceptible to instability that leads to a large variety of phenomena such as superconductivity, commensurate and incommensurate magnetic order or even Kondo insulators [36]. CeCu_2Si_2 was the first heavy-fermion superconductor to be discovered [37]. It demonstrates that superconductivity can exist in a metal in which many-body interactions strongly renormalised the properties of the conduction-electron gas.

According to that, the itinerant or the localised nature of electrons is believed to be behind the superconducting or the magnetic order ground state [38]. However, magnetism and superconductivity may coexist carried by deeply localised 4f electrons and itinerant s,p or d orbitals, respectively. Examples can be found in RRh_4B_4 compounds where R is a rare earth element [39]. However, the distinction between localised magnetic phases and itinerant HF or superconductors is not always straightforward. For instance, the U-based heavy-fermion compound, UPd_2Al_3 displays a division of the 5f-quasiparticle states into two nearly separate subsystems with local-moment and heavy-mass itinerant behaviour. Two electrons are localised 5f electrons responsible of the magnetic order, while the remaining 5f electron is itinerant and the origin of superconductivity [40, 41]. The exponential

dependence of T_K makes the equilibrium between the competing interactions unstable and a tuning parameter such as hydrostatic or chemical (doping) pressure or magnetic field may modify the ground state. The prototypical heavy-fermion superconductor CeCu_2Si_2 is an example of a complicated ternary phase diagram where slight changes in stoichiometry or sample preparation give rise to unconventional superconductivity, SDW or both [42], or field may induce magnetic instability and quantum criticality [43]. Examples of high-pressure induced superconductivity are CeCu_2Ge_2 [44] and CeRhIn_5 [45].

What is of particular interest is the breakdown of the Fermi Liquid picture. The generic phase diagram of heavy fermions presents a quantum critical point when T_{RKKY} approaches T_K if the order parameter is tuned to zero temperature by some external parameter. The non-Fermi Liquid behaviour around criticality, including unconventional superconductivity seems to be dominated by quantum fluctuations. Unlike the formation of Cooper pairs through an interaction mediated by phonon-vibrations of the crystal lattice described by the BCS theory, antiferromagnetic fluctuations have been suggested as the pairing mechanism that produces the attractive spin-spin interaction [46, 47]. They might be also implicated in the superconductivity that emerges in the proximity of a quantum critical point in high- T_c cuprates [48].

2.7 Quantum criticality

A quantum critical point (QCP) is a singular feature in the phase diagram of matter at zero temperature [49]. It occurs at the point of the phase diagram, where the transition temperature of an ordered phase is driven to zero by a tuning parameter. Classical phase transitions occur at finite temperatures where thermal fluctuations drive the system into a lower symmetry phase, as temperature approaches zero Kelvin the fluctuations disappear. However, the uncertainty principle permits that quantum fluctuations drive the system into a new phase at $T=0$ K in a quantum phase transition. In both transitions, fluctuations are correlated over a characteristic length scale ξ that diverges at the critical temperature.

Although one can only access the behaviour at finite temperatures, the influence of a QCP expands over a wide region of the phase diagram and the critical scaling of various quantities at experimentally accessible temperatures can be observed. In the vicinity of a QCP, either thermal or quantum fluctuations may drive the transition, but there is a quantum critical region where the thermal energy $k_B T$ is lower than a correlation time that characterises the quantum fluctuations. In this region, quantum fluctuations lead the compound properties far away of the FL behaviour [26]. In Kondo lattices, the magnetic instability of the surface of large Fermi volume is described in the Doniach diagram by $T_{RKKY}=T_K$ where the Neel temperature is leaded to zero absolute by the tuning parameter. In the quantum critical region, deviations from the temperature dependence of the experimental properties given by Eqs. 2.47, 2.48 and 2.49 such as weak power laws or logarithmic conduct emerges in the so-called non-Fermi Liquids (NFL).

QCP are not only presented in heavy fermions, some intermetallic transition-metal compounds exhibit critical behaviour close to ferromagnetic instability explained by the Self-Consistent Renormalisation (SCR) or Hertz-Millis-Moriya (HMM) theory of spin fluctuations [50]. QCPs have been reported in some weak itinerant ferromagnets emerging intermediate escape routes to quantum criticality such as second to first order transition in MnSi [51, 52], ZrZn₂ under hydrostatic pressure [53], incommensurate order [54], spin density wave (SDW) in NbFe₂ [55] or even superconductivity in MnP [56].

Although a lot of experimental and theoretical work has been done in heavy fermions and transition-metal compounds at low temperature and near quantum criticality, QCP physics is not fully understood and some question are still unsolved. For instance experimental work to obtain a detailed analysis of energy- and momentum-resolved magnetic fluctuations or the influence of disorder on the critical properties would be instructive [35].

2.8 Spin density waves

Spin density waves (SDW) consist of an antiferromagnetically ordered phase with spatial oscillations of the spins with a wave vector \vec{q} . If the spin periodicity is a rational fraction or multiple of the lattice constant it is called a commensurate density wave, otherwise is incommensurate. Whereas some metals and alloys with a high density of states at the Fermi volume become superconductor, the sinusoidal amplitude modulation of the spin density are associated to the existence of nesting vectors in the Fermi surfaces. Chromium and its alloys are the best known cases [57, 58], although SDW fluctuations in the high- T_c superconducting cuprates are very similar to these seen in Chromium close to T_N [59]. SDW have been also reported in organic conductors [60].

SDW is explained in terms of nesting of the Fermi surface that allows electrons in one band to form bound states with holes in another nested band [61]. The nesting wavevector \vec{q} in the reciprocal space results in a real-space periodicity of the SDW with wavelength $2\pi/q$. The spatial modulation of the electron spin density leads to a superstructure with an energy gap $2\Delta(T)$ at the Fermi energy that increases with decreasing temperature.

2.9 Superconductivity

Superconductivity is an exotic state of matter that has intrigued scientists ever since Kammerlingh Onnes observed the resistance of mercury dropping to zero in 1911 [62]. Superconductivity has become an exciting area to study with hundreds of discovered superconductors. The mechanism behind conventional superconductors is based on the electron-phonon interaction. However, the source of interactions that governs high temperature superconductors and the unconventional superconductivity around QCP are likely different and the mechanism leading to superconductivity is not known yet [63].

At the early stages, macroscopic effects were observed in superconductors.

Thermal fluctuations, large magnetic fields and/or large electrical currents destroy the superconductivity. For instance, the critical field H_c that moves the metal to its normal state is well described by:

$$H_c(T) = H_c(0) \left[1 - \left(\frac{T}{T_c} \right)^2 \right] \quad (2.57)$$

where T_c is the critical temperature. The Meissner effect describes the magnetic field expulsion from inside a superconductor during its transition to the superconducting state. When an external field is applied, a superconducting current appears at the surface producing an opposite field that cancels out the magnetic field inside the superconductor. As a consequence the superconductor exhibits perfect diamagnetism with magnetic susceptibility $\chi = -1$ (SI units). The magnetic field B drop at the superconductors surface is not spontaneous. It gradually diminishes with a characteristic London penetration depth λ_L of few hundreds of nm. Penetration depth decreases with the temperature according to:

$$\lambda_L = \frac{\lambda_L(0)}{[1 - (T/T_c)^4]^{1/2}} \quad (2.58)$$

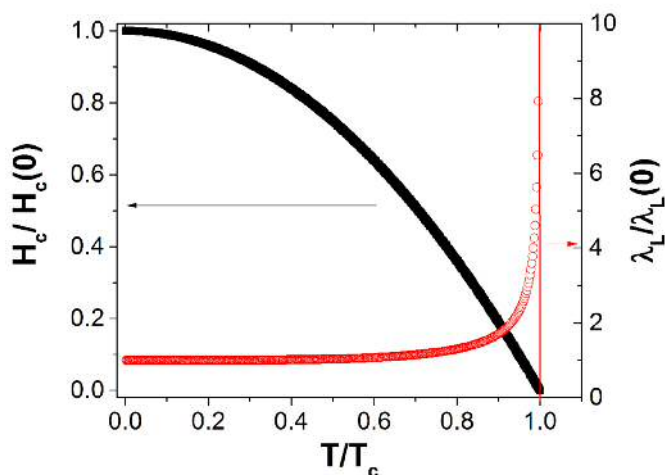


Figure 2.7: Critical field H_c and London penetration depth λ_L as a function of the temperature.

2.9.1 London equations

The constitutive equation relating the superconducting current to the electric field was given in 1935 by London [64]. A few years later, a phenomenological theory introduced in 1950 by Landau [65] put together a macroscopic description of the superconductivity before Bardeen, Cooper and Schrieffer [66] published their microscopic theory of superconductivity (BCS). The London equations are

$$\frac{\partial (\Lambda \mathbf{J}_s)}{\partial t} = \mathbf{E} \quad (2.59)$$

$$\nabla \times (\Lambda \mathbf{J}_s) + \mathbf{B} = 0 \quad (2.60)$$

\mathbf{J}_s is the superconducting current density. \mathbf{E} and \mathbf{B} are the electrical and magnetic field, respectively. The parameter Λ is related with the penetration depth by

$$\Lambda = \mu_0 \lambda_L^2 = \frac{m_p}{n_p e_p^2} = \frac{m}{2n_p e^2} \quad (2.61)$$

where μ_0 is the permeability of free space, n_p the number of Cooper pairs and $m_p = 2m$ and $e_p = -2e$ its mass and charge forming by two electrons. The first London equation shows the non-linear relationship between the current and the electrical field. It is deduced from the Bloch's theorem that states a ground state with zero canonical momentum \mathbf{p} . In the microscopic quantum theory of superconductivity, the superconducting state is considered the ground state of the system which results in the following superconducting current

$$\mathbf{J}_s = n_p e_p \mathbf{v}_p = \frac{n_p e_p}{m_p} (\mathbf{p} - e_p \mathbf{A}) = -\frac{\mathbf{A}}{\Lambda} \quad (2.62)$$

with \mathbf{v}_p the average velocity of Cooper pairs and \mathbf{A} the magnetic vector potential. From the definition of \mathbf{A} , the current derivative gives the First London equation since the electric potential inside the superconductor is constant. If the curl is applied to Eq. 2.59; $\nabla \times \mathbf{E} = -\frac{\partial \mathbf{B}}{\partial t}$

$$\frac{\partial [\mathbf{B} + \nabla \times (\Lambda \mathbf{J})]}{\partial t} = 0 \quad (2.63)$$

where constant and exponentially decaying solutions are possible for the magnetic field. Since the Meissner effect forbids constant solution, the Second London equation 2.60 must be right.

The decay solution and the physical meaning of the London penetration depth is found when Ampere's Law $\nabla \times \mathbf{H} = \mathbf{J}$ is applied to the Second London equation.

$$\nabla^2 \mathbf{B} = \frac{\mu_0}{\Lambda} \mathbf{B} = \frac{1}{\lambda_L^2} \mathbf{B} \quad (2.64)$$

Then, the magnetic field decays exponentially over a distance λ_L .

2.9.2 Ginzburg-Landau equations

Later, Ginzburg and Landau conceived an intuitive theory that is widely used to describe macroscopic phenomena in superconductors, but it is not adequate for microscopic processes. They introduced a wave function for each Cooper pair

$$\Psi_i(\mathbf{r}, t) = \Psi_{i,0}(\mathbf{r}, t) \exp [i\phi_i(\mathbf{r}, t)] \quad (2.65)$$

whose average or density is the order parameter $|\Psi(\mathbf{r}, t)|^2$ of the superconducting condensate. The average of the wave functions will be non-zero if the phases ϕ_i of each Copper pairs are close enough. A coherence between the Copper pairs is then needed. Ψ_0^2 is identified as the density of Cooper pairs $\Psi_0^2 = n_p$.

Ginzburg-Landau (G-L) equations are obtained from the Landau theory of phase transitions. It assumed that the wave function is small near the transition and the free energy can be expanded in powers of the wave function. If the free energy is minimized with respect to the order parameter and to the magnetic vector potential the two G-L equations are respectively obtained. The second G-L equation defines the superconducting current by minimizing the free energy with respect to

the vector potential

$$\mathbf{J} = \frac{e_p}{m_p} |\Psi(\mathbf{r}, t)|^2 [\hbar \nabla \phi - e_p \mathbf{A}(\mathbf{r}, t)] = e_p n_p \mathbf{v}_p(\mathbf{r}) \quad (2.66)$$

2.9.3 Electron-phonon interactions

The first evidence of the role of the interactions between the electrons and the lattice in superconductivity was found at the beginning of the 1950s. The critical temperature of mercury was inversely proportional to the atomic mass of different isotopes [67].

The idea behind the formation of Cooper pairs is explained by the much greater inertia of the lattice ions than the electrons. The Coulomb interaction attracts the lattice ion to the electron, when the electron moves forward to the next ions the previous ion takes longer to come back to the equilibrium position. An excess of positive charges is created around the electron position that is occupied by a second electrons, hence two electrons move across the lattice correlated over a distance ξ_0 , known as BCS coherence length. The two electrons are attracted by the electron-induced lattice deformations known as the electron-phonon interaction. The coherence lengths are $10^2 - 10^3$ nm, that can be considered the average size of a Cooper pair in weak-coupling superconductors.

A minimum attractive interaction is needed to create a bound state. Normally, the Fermi energy is three order of magnitude higher than the binding energy, $E \propto T_c$, but, at low temperature, the electron kinetic energy is approximately linear and then the bound state is possible. The Cooper pairs binding energy can be estimated for weakly coupled superconductors from the Hamiltonian of two electrons in an electron-phonon potential. $\hat{\mathcal{H}} = \frac{\hat{p}_1^2}{2m} + \frac{\hat{p}_2^2}{2m} + U_{e-p}$. The eigenstates of the Cooper pairs are a linear combination of two electron eigenstates for all the possible wave vectors \mathbf{k} and eigenenergies $|\xi(\mathbf{k})|$ with amplitudes $b_{\mathbf{k}}$. For a S-wave

superconductor, the spatial wavefunction is symmetric, and hence, the spin wavefunction is antisymmetric. Consequently, the singlet state of the Cooper pair gives the following eigenstate:

$$2|\xi(\mathbf{k})| + \sum_{\mathbf{k}'} U_{\mathbf{k}\mathbf{k}'} b_{\mathbf{k}'} = E b_{\mathbf{k}}, \quad (2.67)$$

with a binding energy $E = -2\Delta$. The electrons that form the Cooper pair have the same wave vector $|\xi_1(\mathbf{k})| = |\xi_2(\mathbf{k})|$. The amplitudes $b_{\mathbf{k}}$ can be obtained approximating the electron-phonon interaction to a constant $U_{\mathbf{k}\mathbf{k}'} = -U$ within a sphere centred at the Fermi wave vector, k_F , and radius ω_D/v_F . If the $b_{\mathbf{k}}$ amplitudes are summed, an equation for the binding energy is obtained:

$$1 = \frac{U}{2} = \sum_{k_{min} < |\mathbf{k}| < k_{max}} \frac{1}{|\xi(\mathbf{k})| + \Delta} \approx \frac{N(E_F)U}{2} \ln \left(\frac{\hbar\omega_D}{\Delta} \right) \quad (2.68)$$

where ω_D is the Debye frequency of the crystal and v_F and $N(E_F)$ the velocity and the density of states at the Fermi level. The approximation is given by replacing the sum over the wave vector by and integral over the range $\pm\hbar\omega_D$ in the vicinity of the Fermi level. The resulting binding energy

$$2\Delta = 2\hbar\omega_D \exp \left(\frac{-2}{N(\varepsilon_F)U} \right) \quad (2.69)$$

only differs to the BCS theory [66] by the factor 2 in the exponent.

The binding energy is required to break a Cooper pair, but the simplest excitation in a superconductor is to add a quasi-particle, an electron or a hole by applying an energy Δ . At non-zero temperatures, quasi-particles are thermally activated but well below T_C are relatively small. The temperature enlarges the Fermi surface and the density of states, $N(E_F)$, therefore, the higher the temperature, the lower the binding energy is, according to Eq. 2.69. When temperature approaches T_c , the density of quasi-particles become relevant until Δ goes to zero at T_c . For d-wave superconductors, quasi-particles can be created with no energy cost along the Ψ nodes. The proportionality of the binding energy with T_c is given by the BCS

theory, $2\Delta/k_B T_c \sim 3.5$, for weak-coupling superconductors.

The previous results are only valid on the weak-coupling regime $N(\varepsilon_F)U \ll 1$. [68]. In superconductors with a strong electron-phonon coupling, the effect of electrons on phonons also has to be taken into account. This is modelled by introducing a gap function $\Delta(\omega)$ where phonon frequencies are renormalized due to the electrons.

The isotope effect displays the relationship between the critical temperature and the atomic mass M as $T_c M^\alpha = \text{constant}$. Predicted to be $\alpha = 0.5$ in the strong-coupling limit, the BCS theory is unable to explain the experimental results of some superconductors and to predict which materials become superconductors.

2.9.4 Flux quantisation

One of the consequences of the macroscopic wavefunction, Eq. 2.65, is the persistent supercurrent in closed superconducting circuits. The Cooper pair condensate moves with the same center of mass velocity for all pairs and loss of energy by inelastic scattering would require to slow down the system as a whole, which means a large amount of energy. Another consequence, relevant to the SQUID operation, is the magnetic flux quantisation. The total magnetic flux that threads a superconducting closed path must be an integer multiple of the flux quantum, Φ_0 , if the superconductor is thicker than the penetration depth. From the second G-L Eq. 2.66, the path integral of the wavefunction phase over a closed path is an integer multiple of 2π to guarantee the single value of the wavefunction

$$2\pi n = \oint \nabla\phi \cdot d\mathbf{l} = \frac{m_p}{e_p n_p \hbar} \oint \mathbf{J} \cdot d\mathbf{l} + \frac{e_p}{\hbar} \oint \mathbf{A} \cdot d\mathbf{l} \quad (2.70)$$

The second integral on the right hand is the magnetic flux through the closed contour Φ . The penetration depth identity (Eq.2.61) and the flux quantum definition $\Phi_0 = h/e_p = h/2e$ lead to the flux quantisation condition

$$n\Phi_0 = \mu_0 \lambda_L^2 \oint \mathbf{J} \cdot d\mathbf{l} + \Phi \quad (2.71)$$

If the thickness of the superconductor is larger than the penetration depth, deep inside the superconductor $\mathbf{J} = 0$ and , then the total flux inside a closed path in a superconductor should be an integer multiple of a flux quantum $\Phi = n\Phi_0$.

2.9.5 Josephson Junctions

SQUID operation may not be understood without the Josephson Tunneling effect that takes place in the junction of two superconductors separated by an insulating thin barrier. The Josephson tunneling effect is explained by the first Josephson equation. It correlates the superconducting current across the insulator barrier with the phase difference of the superconductors. The supercurrent $|\mathbf{J}| = j_s$ in Eq. 2.66 can be rewritten as a function of the gauge invariant phase difference or Josephson phase difference δ , Φ_0 and the mass and charge of the electron

$$j_s = \frac{en_p\hbar}{m} \left[\frac{1}{d\mathbf{l}} \left(\int_C \nabla\phi \cdot d\mathbf{l} - \frac{2\pi}{\Phi_0} \int_C \mathbf{A} \cdot d\mathbf{l} \right) \right] = \frac{en_p\hbar}{m} \cdot \frac{d\delta}{d\mathbf{l}} \quad (2.72)$$

$$\phi_2 - \phi_1 = \frac{m}{en_p\hbar} \int_C j_s \cdot d\mathbf{l} + \frac{2\pi}{\Phi_0} \int_C \mathbf{A} \cdot d\mathbf{l} \quad (2.73)$$

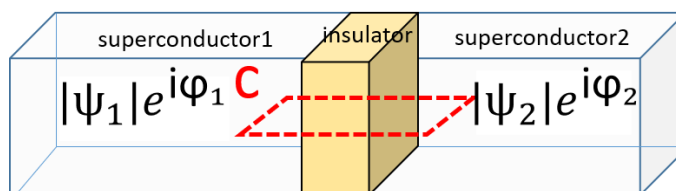


Figure 2.8: Scheme of a Josephson junction.

where C is any path across the junction. The supercurrent Eq. 2.72 can be described as a function of the gauge invariant phase difference

$$\delta \equiv \phi_2 - \phi_1 - \frac{2\pi}{\Phi_0} \int_C \mathbf{A} \cdot d\mathbf{l} \quad (2.74)$$

that is bounded by 2π so can be written as a Fourier Sine series. The series converges for almost all the junctions quickly, and the supercurrent in a Josephson barrier often simplifies to

$$I_s = I_0 \sin \delta \quad (2.75)$$

known as *first Josephson equation*. The density of supercurrent j_s is replaced by the superconducting current I_s and $I_0 = \frac{en_p \hbar}{m}$.

As the superconducting wave function is $\Psi \propto \exp(iEt/\hbar)$, the *second Josephson equation* can easily be obtained from the time derivative of Eq. 2.74.

$$\dot{\delta} = \dot{\phi}_2 - \dot{\phi}_1 - \frac{2\pi}{\Phi_0} \frac{d}{dt} \left(\int_C \mathbf{A} \cdot d\mathbf{l} \right) = \frac{E_2 - E_1}{\hbar} - \frac{2eU_{21}^{ind}}{\hbar} \quad (2.76)$$

$$\frac{d\delta}{dt} = \frac{2e}{\hbar} U = \frac{2\pi}{\Phi_0} U \quad (2.77)$$

where U_{21}^{ind} is the induced voltage by the magnetic field, and U is the voltage across the junction. The Josephson coupling energy, $E_j = \frac{I_0 \Phi_0}{2\pi}$ is obtained by direct integration of the product $U \cdot I_s$

$$E(\delta) = \int_0^\delta I_0 \sin \delta' \frac{\Phi_0}{2\pi} d\delta' = E_J (1 - \cos \delta) \quad (2.78)$$

If noise is neglected, Josephson junctions operation can be separated into two regions. In the zero-voltage state or static region, the time-averaged phase difference is constant and hence the time-averaged dc voltage $\langle U \rangle = V$ is zero. In this scenario the bias current, I_b , establishes the phase difference that makes the current in Eq. 2.75 match with I_b . When the bias current increases above the critical current $I_c = I_0$, the I-V junction curve goes into a dynamic region. Voltage is not zero and the supercurrent oscillates with the Josephson frequency given by $f = 2eV/h = U/\Phi_0 = 483.6 \text{ GHz/mV}$ in the microwave range. Above the critical current, the Josephson junction acts as a voltage-frequency converter. It can therefore be used as a voltage standard, since $\Phi_0 = 2.07 \cdot 10^{-15} \text{ Wb}$ is known with accuracy.

2.9.6 RCSJ model

For $V \neq 0$, in the dynamic region, there are other contributions to the current in a Josephson junction: the quasiparticle current I_{qp} generated in the insulator by the voltage V , and a displacement current I_d due to the field that affects the electrical carriers. I_{qp} in a s-i-s barrier is approximately 0 below $2\Delta e$ and ohmic above the energy barrier. Although the microscopic description of both currents requires a more complex analysis, in almost all the SQUIDS, I_{qp} and I_d can be approximated to an Ohmic shunt resistor and a capacitor connected in parallel, respectively. The approximation is known by the “resistively and capacitively- shunted junction model” or RCSJ-model. The equivalent circuit is shown in Fig. 2.9 (a), where effects of thermal and $1/f$ noises are illustrated by I_N . The equation of motion, Eq. 2.75 is now modified to

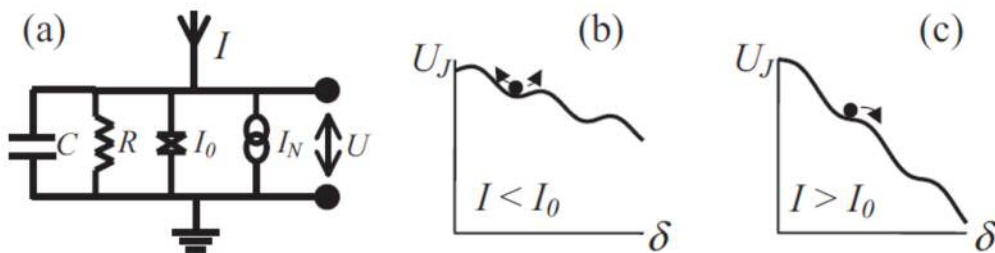


Figure 2.9: (a) RCSJ equivalent circuit. (b) The tilted washboard potential U_J as a function of the phase difference, δ in a bias current below and (c) above the critical current. Taken from ref. [69].

$$I = I_0 \sin \delta + \frac{U}{R} + C\dot{U} + I_N(t) \quad (2.79)$$

Introducing the second Josephson equation 2.77 and ignoring the noise current

$$I = I_0 \sin \delta + \frac{\Phi_0}{2\pi} \frac{\dot{\delta}}{R} + \frac{\Phi_0}{2\pi} C \ddot{\delta} \quad (2.80)$$

If the Josephson coupling energy E_j is used and the current is normalised to $i = I/I_0$

$$\frac{\Phi_0}{2\pi I_0} C \ddot{\delta} + \frac{\Phi_0}{2\pi I_0} \frac{\dot{\delta}}{R} = (i - \sin \delta) = -\frac{1}{E_j} \frac{\partial U_j}{\partial t} = -\frac{\partial [w - F\delta]}{\partial \delta} \quad (2.81)$$

Static and dynamic properties of the phase difference, δ were explained by Anderson [70] as a mechanical model of a point-like particle of mass $m = \frac{\Phi_0 C}{2\pi I_0}$ and friction $\eta = \frac{\Phi_0}{2\pi I_0 R}$ in the so-called tilted washboard potential $U_J = E_j (1 - \cos \delta - i \cdot \delta)$ with a potential w that is tilted by an external driving force F that corresponds with the normalised current i . The tilted potential U_j helps to understand the I-V characteristic of the Josephson junction. For $i < 1$, δ is confined in a potential well as it is outlined in Fig. 2.9 (b). $\langle \dot{\delta} \rangle = 0$ and the time averaged voltage is zero, according to Eq. 2.77. For the dynamic case, $i > 1$, the local potential minima disappears and the phase difference changes with the time. Hence, the dc voltage is not zero and increases with the bias current. When the bias current decreases the equivalent particle is trapped in a different potential well. The hysteretic behaviour, shown in Fig. 2.10(b), is a consequence of the inertia or the capacitive term. The dynamic equation in the RCSJ model can be depicted as a function of the Stewart-McCumber parameter β_c , the Josephson frequency, $\omega_c \equiv 2\pi I_0 R / \Phi_0$, at the characteristic voltage $V_c = I_0 R$ and the normalised potential $u_j \equiv U_j / E_j$

$$\beta_c \frac{\ddot{\delta}}{\omega_c^2} + \frac{\dot{\delta}}{\omega_c} = (i - \sin \delta) = -\frac{\partial u_j}{\partial t} \quad (2.82)$$

$$\beta_c \equiv \frac{\omega_c}{\omega_{RC}} = \frac{2\pi}{\Phi_0} I_0 R^2 C \quad (2.83)$$

being $\omega_{RC} = 1/RC$ the resonance frequency of a RC circuit. I-V curves can be analytically calculated at the limiting cases of β_c .

In the overdamped limit ($\beta_c \ll 1$), the capacitive term becomes negligible and the second order Eq. 2.82 converts to a first order one,

$$\frac{\dot{\delta}}{\omega_c} = i - \sin \delta \quad (2.84)$$

$$I - I_0 \sin \delta = \frac{\Phi_0}{2\pi} \frac{\dot{\delta}}{R} = \frac{V}{R} \quad (2.85)$$

reducing the model to the RSJ model.

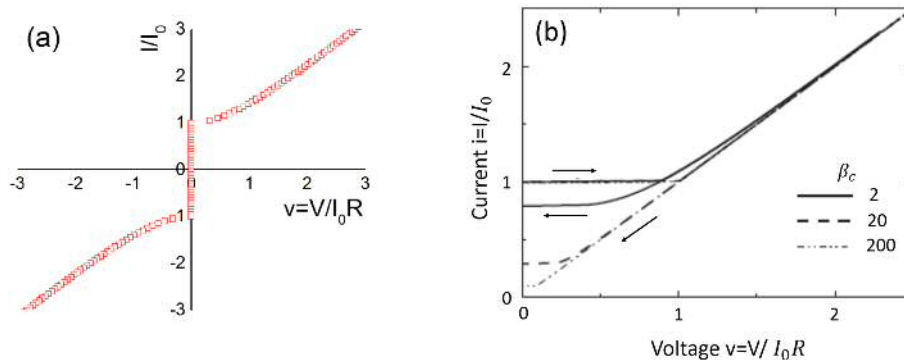


Figure 2.10: (a) Josephson junction with a non-hysteretic I-V characteristic curve, ($\beta_c \ll 1$) and (b) hysteretic I-V curve as a function of β_c .

In this scenario, when current decreases from above I_0 , the phase difference is trapped in a potential minima at $I = I_0$ and $\dot{\delta} = 0$ for $I < I_0$, removing the hysteretic behaviour. The following solutions for the time-averaged voltage can be deduced from Eq. 2.85

$$V = 0 \quad I < I_0 \quad (2.86)$$

$$V = R\sqrt{(I^2 - I_0^2)} \quad I > I_0 \quad (2.87)$$

The I-V characteristic curve for $\beta_c \ll 1$ is plotted in Fig. 2.10(a). It is relevant to mention that the voltage above the critical current oscillates with a high frequency $\omega = \omega_c\sqrt{i^2 - 1}$.

On the other hand, in the underdamped limit, $\beta_c \gg 1$, $\omega_{RC} \gg \omega_c$ the SQUID behaves like a RC circuit. The average voltage is linear when the current is decreased from above I_0 to zero. In contrast, the voltage remains zero when the current is increased from zero to the critical current producing a high hysteretic I-V curve as is shown in Fig. 2.10(b) from Clarke et al. SQUID handbook [69].

2.9.7 dc SQUID

Superconducting Quantum Interferometer Device (SQUID) combines the two quanta phenomena previously introduced. Josephson tunnelling and flux quantisation produce the most sensitive magnetic flux sensors. Other SQUID applications can be highlighted like two quantum level systems or quantum bits used in superconducting quantum computers [71, 72] or SQUID-based thermometers [73].

SQUIDs consist of a superconducting loop with one or two symmetric Josephson junction, connected in parallel. The former configuration is known as an ac-SQUID and the later as a dc-SQUID. The physics involved in both are in general the same and minor corrections in the dc-SQUID may easily lead to the equations that explain the ac-SQUID operation. The current in the superconducting loop is modulated by the magnetic flux enclosed and the SQUID current can be understood as the interference of the wave functions in the two loop paths. The static and dynamic performance of Josephson junctions are well-explained by the RCSJ model. Junctions are resistively shunted to avoid hysteretic behaviour in such a way that the dc-SQUID can be depicted by an equivalent circuit shown in Fig. 2.11 (b).

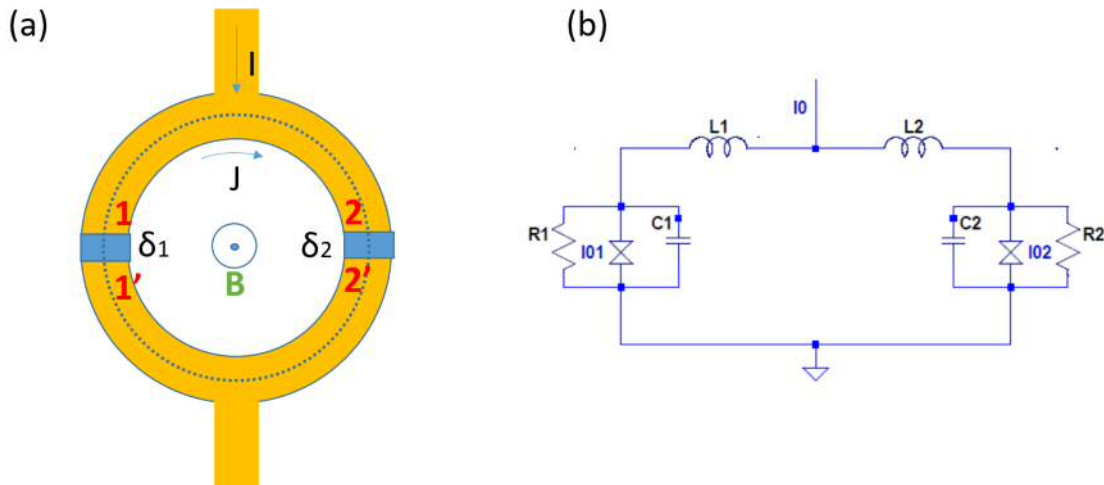


Figure 2.11: (a) dc-SQUID scheme. (b) Equivalent circuit of a dc-SQUID in the RCSJ model.

As a flux-to-voltage transducer, the SQUID operation is given by the I-V and

the $V\text{-}\Phi$ characteristic responses. To obtain them, the difference phase $\delta_2 - \delta_1$ in the SQUID junctions and the current equations are needed. Let's consider the integral of the superconducting phase over a closed path, e.g the dashed line in Fig. 2.11 (a). To guarantee the wavefunction is a single value, the integral must be an integer multiple of 2π . It can be calculated by splitting the path in 4 branches $(\phi_1 - \phi_2) + (\phi_2 - \phi_{2'}) + (\phi_{2'} - \phi_{1'}) + (\phi_{1'} - \phi_1) = 2\pi n$. First and third term is given by Eq. 2.73

$$\phi_2 - \phi_1 = +\frac{m}{en_p\hbar} \int_1^2 \mathbf{J} \cdot d\mathbf{l} + \frac{2\pi}{\Phi_0} \int_1^2 \mathbf{A} \cdot d\mathbf{l} \quad (2.88)$$

$$\phi_{1'} - \phi_{2'} = +\frac{m}{en_p\hbar} \int_{2'}^{1'} \mathbf{J} \cdot d\mathbf{l} + \frac{2\pi}{\Phi_0} \int_{2'}^{1'} \mathbf{A} \cdot d\mathbf{l} \quad (2.89)$$

and the second and the fourth by Eq. 2.74

$$\phi_i - \phi_{i'} = -\delta_i + \frac{2\pi}{\Phi_0} \int_{i'}^i \mathbf{A} \cdot d\mathbf{l} \quad (2.90)$$

With the resulting quantisation

$$2\pi n = \delta_2 - \delta_1 - \frac{2\pi}{\Phi_0} \oint \mathbf{A} \cdot d\mathbf{l} + \frac{m}{en_p\hbar} \left(\int_2^1 \mathbf{J} \cdot d\mathbf{l} + \int_{1'}^{2'} \mathbf{J} \cdot d\mathbf{l} \right) \quad (2.91)$$

The magnetic vector potential integral is equal to the total flux through the SQUID loop due to the Stokes integral theorem. It includes the applied flux $\Phi_a = \mathbf{B} \cdot \mathbf{A}$ plus the induced flux $L_s J$ by the circulating current \mathbf{J} , being L_s the SQUID loop geometric inductance. Although the current is zero deep in the superconductor, a superficial circulating current exists and it is the responsible for the field that cancels the magnetic field inside the superconductor. The supercurrent integral terms is non-zero close to the junction barriers. Besides, if the thickness of the superconducting loop is smaller or comparable to λ_L the term is non-zero in the whole loop. This contribution is normally described by a kinetic inductance, L_k , that has been exploited in different fields such as magnetometry or submillimeter-wave detection [74, 75].

The difference phase in the dc-SQUID is then modulated by the total flux

$$\delta_2 - \delta_1 = 2\pi n + \frac{2\pi}{\Phi_0}(\Phi_a + LJ) \equiv 2\pi(\phi_a + \frac{1}{2}\beta_L j) \quad (2.92)$$

with $L = L_s + L_k$ the sum of the geometric and the kinetic inductance and $\beta_L = \frac{2LI_0}{\Phi_0}$ the screening parameter. J and Φ are normalised to I_0 and Φ_0 respectively.

The current through the Josephson junctions in the RCSJ model together with the Kirchhoff's current law of the bias current $I = I_1 + I_2$ in the two SQUID arms complete the equations to understand the SQUID operation. Eq. 2.82 gives the two second order equations of the current (i is replaced by j to avoid confusion between the bias (i) and the Josephson current (j)) and assuming symmetric SQUID arms, $I_1 = I_2 = I$.

$$\frac{i}{2} \pm j = \sin \delta_i + \frac{\dot{\delta}}{\omega_c} + \beta_c \frac{\ddot{\delta}_i}{\omega_c^2} \quad (2.93)$$

Currents are normalised to $I_0 = (I_{0,1} + I_{0,2})/2$ and equivalent resistance $R = 2R_1R_2/(R_1 + R_2)$ and capacitance $C = (C_1 + C_2)/2$ are used to define β_c . Index i refers to the two junctions. The characteristic frequency ω_c , β_c and the screening parameter β_L are normally used to control the SQUID behaviour.

Current 2.93 and phase difference 2.92 equations are completed by the second Josephson relation, Eq. 2.77, to describe the SQUID operation. In the following analysis radiofrequency oscillations are neglected. Only the time-averaged voltage will be considered.

The junctions are the only dissipative elements in the SQUID. In the strongly overdamped region, $\beta_c \ll 1$, for a given external flux Φ , the I-V curve is not hysteric. When the bias current is increased from zero to above the critical current and then back to zero the curve is similar to the I-V curve of the Josephson junction shown in Fig. 2.10(a). Above the critical current $I > 2I_0$, voltages oscillates as a function of the applied flux with a Φ_0 period. Maxima are reached at flux $\Phi = (n + 1/2)\phi_0$ and

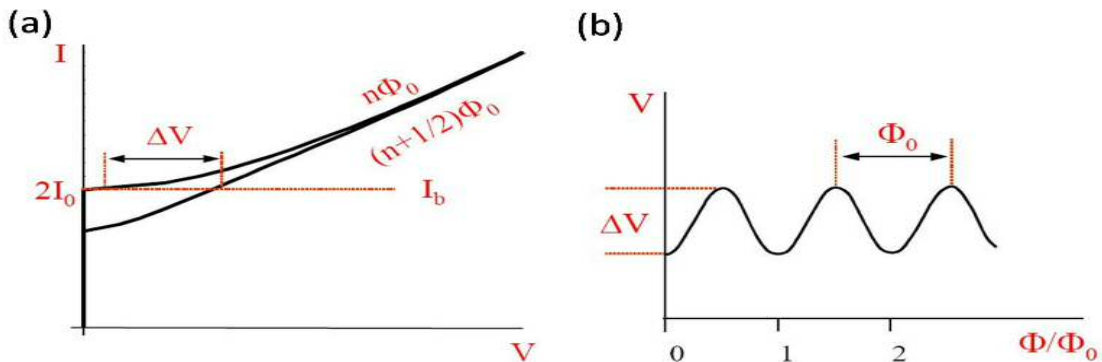


Figure 2.12: (a) dc-SQUID I-V characteristic curve for different magnetic flux. (b) The periodic V-flux curve.

minima at $n\Phi_0$ as shown Fig. 2.12. Optimisation of the voltage-to-flux transducer is achieved at a bias current I where $|(\frac{\partial V}{\partial \Phi})|_I = V_\Phi$, i.e. the flux-to-voltage transfer coefficient is maximum. At that point, the output voltage is maximised $\delta V = V_\Phi \delta \Phi$ for small flux changes. Current motion Eq. 2.93, can be analysed in the same way that the single Josephson junction one. The static region takes place for bias current lower than the critical current I_c . In this scenario the phase differences δ_i are trapped in the potential minima U_i and they are not time dependant $\dot{\delta}_i = \ddot{\delta}_i = 0$. For the general case of very low SQUID inductance L , $\beta_L \ll 1$, the phase difference (Eq. 2.92) does not depend on the circulating current and the critical current can be calculated by summing both motion Eqs. 2.93

$$i = \sin \delta_1 + \sin (\delta_1 + 2\pi\phi) \quad (2.94)$$

Using the following trigonometric identity

$$2 \sin \varepsilon \cdot \cos \eta = \sin (\varepsilon + \eta) + \sin (\varepsilon - \eta) \quad \begin{cases} \varepsilon = \delta_1 + \pi\phi \\ \eta = \pi\phi \end{cases} \quad (2.95)$$

the current, in absolute values, is

$$I = 2I_0 \sin \varepsilon \cdot \cos (\pi\Phi/\Phi_0) \quad (2.96)$$

in such a way that the bias current, $I_b = I$ will give the phase difference ε . The

maximum current in the static region determines the critical bias current needed to have a non-zero voltage read out:

$$I_c = 2I_0 \left| \cos \left(\pi \frac{\Phi}{\Phi_0} \right) \right| \quad (2.97)$$

hence, the critical current I_c oscillates from $2I_0$ at $\Phi = n\phi_0$ to 0 at $\Phi = (n + 1/2)\phi_0$, being n an integer. Although noise fluctuations are not discussed in this section, it is fair to say, that $I_c \neq 0$ in real dc-SQUIDs due to noise effects. That makes, the outline in Fig. 2.12 (a) more realistic. Finally, in cases where the SQUID inductance is not negligible, the critical current is affected by β_L . The critical current decreases with the screening parameter according to $I_c \propto 1/\beta_L$.

In the dynamic region, when the bias current is higher than the critical current, the voltage is non-zero and the phase difference changes with the time. For negligible β_L , $\dot{\delta}_1 = \dot{\delta}_2$ and $\ddot{\delta}_1 = \ddot{\delta}_2$, hence the Eq. 2.93 in the dynamic region can be solved

$$i = \sin \delta_1 + \sin (\delta_1 + 2\pi\phi) + 2\frac{\dot{\delta}_1}{\omega_c} + 2\beta_c \frac{\dot{\delta}_1}{\omega_c} \quad (2.98)$$

Using the trigonometric identity 2.95 and substituting β_c and ω_c we obtain

$$I = 2I_0 \cos \left(\frac{\pi\Phi}{\Phi_0} \right) \sin \varepsilon + \frac{\Phi_0}{2\pi} \frac{2\dot{\varepsilon}}{R} + \frac{\Phi_0}{2\pi} 2C\dot{\varepsilon} \quad (2.99)$$

identical to the RCSJ equation for a single junction Eq. 2.80 with $R = R/2$, $C = 2C$ and critical current Eq. 2.97. Hence, the voltage in Fig. 2.12 (a) will be

$$V = 0 \quad I < I_c \quad (2.100)$$

$$V = \frac{R}{2} \sqrt{(I^2 - I_c^2)} \quad I > I_c \quad (2.101)$$

Most SQUID applications require a linear response. To avoid changes in the transfer coefficient V_Φ , an electronic feedback circuit so-called Flux-Locked-Loop (FLL) is used to induce a negative flux $-\partial\Phi$ that cancels out the detected flux by the SQUID. In this constant-flux configuration the SQUID remains in a fixed

operation point V_{Φ} with an specific gain. The readout of the feedback voltage will be linearly dependent on the input flux and changes or "jumps" in the operation point due to noise will be removed or strongly damped. Although noise effects are not considered in the SQUID equations, thermal and 1/f noise affect the SQUIDS behaviour in a relevant way. The goal of this work is not to analyse noise effects in the SQUID operation but a brief introduction of noise sources in SQUIDS and the FFL circuit will be given in the magnetometer Sec. 4.2.

References

- [1] J. Mydosh, *Spin Glasses: An Experimental Introduction* (Taylor & Francis, 1993)
- [2] L. Balents, *Spin liquids in frustrated magnets*, Nature 464 (7286), p. 199 (2010)
- [3] R. F. Wang, C. Nisoli, R. S. Freitas, J. Li, W. McConville, B. J. Cooley, M. S. Lund, N. Samarth, C. Leighton, V. H. Crespi and P. Schiffer, *Artificial 'spin ice' in a geometrically frustrated lattice of nanoscale ferromagnetic islands*, Nature 439 (7074), p. 303 (2006)
- [4] A. P. Ramirez, *Strongly Geometrically Frustrated Magnets*, Annu. Rev. Mater. Sci. 24 (1), p. 453 (1994)
- [5] C. Lacroix, P. Mendels and F. Mila, *Introduction to Frustrated Magnetism: Materials, Experiments, Theory* (Springer Berlin, 2013)
- [6] J. S. Gardner, M. J. P. Gingras and J. E. Greedan, *Magnetic pyrochlore oxides*, Rev. Mod. Phys. 82, p. 53 (2010)
- [7] C. Castelnovo, R. Moessner and S. L. Sondhi, *Magnetic monopoles in spin ice*, Nature 451 (7174), p. 42 (2008)
- [8] L. Pauling, *The Structure and Entropy of Ice and of Other Crystals with Some Randomness of Atomic Arrangement*, J. Am. Chem. Soc. 57 (12), p. 2680 (1935)

- [9] S. T. Bramwell, M. J. Harris, B. C. den Hertog, M. J. P. Gingras, J. S. Gardner, D. F. McMorrow, A. R. Wildes, A. L. Cornelius, J. D. M. Champion, R. G. Melko and T. Fennell, *Spin Correlations in $\text{Ho}_2\text{Ti}_2\text{O}_7$: A Dipolar Spin Ice System*, Phys. Rev. Lett. 87, p. 047205 (2001)
- [10] B. C. Hertog and M. J. P. Gingras, *Dipolar Interactions and Origin of Spin Ice in Ising Pyrochlore Magnets*, Phys. Rev. Lett. 84, p. 3430 (2000)
- [11] M. J. Harris, S. T. Bramwell, D. F. McMorrow, T. Zeiske and K. W. Godfrey, *Geometrical Frustration in the Ferromagnetic Pyrochlore $\text{Ho}_2\text{Ti}_2\text{O}_7$* , Phys. Rev. Lett. 79, p. 2554 (1997)
- [12] M. Harris, S. Bramwell, T. Zeiske, D. McMorrow and P. King, *Magnetic structures of highly frustrated pyrochlores*, J. Magn. Magn. Mater. 177, p. 757 (1998)
- [13] A. Hallas, J. Paddison, H. Silverstein, A. Goodwin, J. Stewart, A. Wildes, J. Cheng, J. Zhou, J. Goodenough, E. Choi *et al.*, *Statics and dynamics of the highly correlated spin ice $\text{Ho}_2\text{Ge}_2\text{O}_7$* , Phys. Rev. B 86 (13), p. 134431 (2012)
- [14] H. Zhou, S. Bramwell, J. Cheng, C. Wiebe, G. Li, L. Balicas, J. Bloxsom, H. Silverstein, J. Zhou, J. Goodenough *et al.*, *High pressure route to generate magnetic monopole dimers in spin ice*, Nat. Commun. 2, p. 478 (2011)
- [15] H. Zhou, J. Cheng, A. Hallas, C. Wiebe, G. Li, L. Balicas, J. Zhou, J. Goodenough, J. S. Gardner and E. Choi, *Chemical pressure effects on pyrochlore spin ice*, Phys. Rev. Lett. 108 (20), p. 207206 (2012)
- [16] H. D. Zhou, C. R. Wiebe, J. A. Janik, L. Balicas, Y. J. Yo, Y. Qiu, J. R. D. Copley and J. S. Gardner, *Dynamic Spin Ice: $\text{Pr}_2\text{Sn}_2\text{O}_7$* , Phys. Rev. Lett. 101 (22), p. 227204 (2008)
- [17] J. Lago, I. Živković, B. Malkin, J. R. Fernandez, P. Ghigna, P. D. de Réotier, A. Yaouanc and T. Rojo, *CdEr_2Se_4 : a new erbium spin ice system in a spinel structure*, Phys. Rev. Lett. 104 (24), p. 247203 (2010)

- [18] L. R. Yaraskavitch, H. M. Revell, S. Meng, K. A. Ross, H. M. L. Noad, H. A. Dabkowska, B. D. Gaulin and J. B. Kycia, *Spin dynamics in the frozen state of the dipolar spin ice material Dy₂Ti₂O₇*, Phys. Rev. B 85, p. 020410 (2012)
- [19] L. Landau, *The theory of a Fermi liquid*, Sov. Phys. JETP 3, p. 920 (1957)
- [20] J. Custers, P. Gegenwart, H. Wilhelm, K. Neumaier, Y. Tokiwa, O. Trovarelli, C. Geibel, F. Steglich, C. Pepin and P. Coleman, *The break-up of heavy electrons at a quantum critical point*, Nature 424 (6948), p. 524 (2003)
- [21] C. J. Pethick, D. Pines, K. F. Quader, K. S. Bedell and G. E. Brown, *One-Component Fermi-Liquid Theory and the Properties of UPt₃*, Phys. Rev. Lett. 57, p. 1955 (1986)
- [22] C. Proust, E. Boaknin, R. W. Hill, L. Taillefer and A. P. Mackenzie, *Heat Transport in a Strongly Overdoped Cuprate: Fermi Liquid and a Pure d-Wave BCS Superconductor*, Phys. Rev. Lett. 89, p. 147003 (2002)
- [23] K. Andres, J. E. Graebner and H. R. Ott, *4f*, Phys. Rev. Lett. 35, p. 1779 (1975)
- [24] P. Misra, *Heavy-fermion systems*, vol. 2 (Elsevier, 2007)
- [25] A. C. Hewson, *The Kondo Problem to Heavy Fermions* (Cambridge University Press, Cambridge, 1993)
- [26] G. Stewart, *Non-Fermi-liquid behavior in d- and f-electron metals*, Rev. Mod. Phys. 73 (4), p. 797 (2001)
- [27] J. Kondo, *Resistance Minimum in Dilute Magnetic Alloys*, Prog. Theor. Phys. 32 (1), p. 37 (1964)
- [28] K. G. Wilson, *The renormalization group: Critical phenomena and the Kondo problem*, Rev. Mod. Phys. 47, p. 773 (1975)
- [29] K. Yosida, *Bound State Due to the s – d Exchange Interaction*, Phys. Rev. 147, p. 223 (1966)

- [30] M. A. Ruderman and C. Kittel, *Indirect Exchange Coupling of Nuclear Magnetic Moments by Conduction Electrons*, Phys. Rev. 96, p. 99 (1954)
- [31] S. Sykora and K. W. Becker, *Heavy fermion properties of the Kondo Lattice model*, Sci. Rep. 3, p. 2691 (2013)
- [32] S. Doniach, *The Kondo lattice and weak antiferromagnetism*, Physica B+C, 91, p. 231 (1977)
- [33] G. Knopp, A. Loidl, K. Knorr, L. Pawlak, M. Duczmal, R. Caspary, U. Gottwick, H. Spille, F. Steglich and A. P. Murani, *Magnetic order in a Kondo lattice: A neutron scattering study of $CeCu_2Ge_2$* , Z. Phys. B Condens. Matt. 77 (1), p. 95 (1989)
- [34] F. de Boer, J. Klaasse, P. Veenhuizen, A. Böhm, C. Bredl, U. Gottwick, H. Mayer, L. Pawlak, U. Rauchschwalbe, H. Spille and F. Steglich, *$CeCu_2Ge_2$: Magnetic order in a Kondo lattice*, J. Magn. Magn. Mater. 63, p. 91 (1987)
- [35] H. v. Löhneysen, A. Rosch, M. Vojta and P. Wölfle, *Fermi-liquid instabilities at magnetic quantum phase transitions*, Rev. Mod. Phys. 79 (3), p. 1015 (2007)
- [36] N. Grewe and F. Steglich, *Heavy fermions*, Handbook on the Physics and Chemistry of Rare Earths 14, p. 343 (1991)
- [37] F. Steglich, J. Aarts, C. D. Bredl, W. Lieke, D. Meschede, W. Franz and H. Schäfer, *Superconductivity in the Presence of Strong Pauli Paramagnetism: $CeCu_2Si_2$* , Phys. Rev. Lett. 43, p. 1892 (1979)
- [38] Y.-f. Yang, Z. Fisk, H.-O. Lee, J. D. Thompson and D. Pines, *Scaling the Kondo lattice*, Nature 454 (7204), p. 611 (2008)
- [39] W. A. Fertig, D. C. Johnston, L. E. DeLong, R. W. McCallum, M. B. Maple and B. T. Matthias, *Destruction of Superconductivity at the Onset of Long-Range Magnetic Order in the Compound $ErRh_4B_4$* , Phys. Rev. Lett. 38, p. 987 (1977)

- [40] R. Caspary, P. Hellmann, M. Keller, G. Sparn, C. Wassilew, R. Köhler, C. Geibel, C. Schank, F. Steglich and N. Phillips, *Unusual ground-state properties of UPd_2Al_3 : Implications for the coexistence of heavy-fermion superconductivity and local-moment antiferromagnetism*, Phys. Rev. Lett. 71 (13), p. 2146 (1993)
- [41] N. Sato, N. Aso, K. Miyake, R. Shiina, P. Thalmeier, G. Varelogiannis, C. Geibel, F. Steglich, P. Fulde and T. Komatsubara, *Strong coupling between local moments and superconducting 'heavy' electrons in UPd_2Al_3* , Nature 410 (6826), p. 340 (2001)
- [42] F. Steglich, P. Gegenwart, R. Helfrich, C. Langhammer, P. Hellmann, L. Donnevert, C. Geibel, M. Lang, G. Sparn, W. Assmus *et al.*, *Are heavy-fermion metals Fermi liquids?*, Z. Phys. B Condens. Matter 103 (2), p. 235 (1997)
- [43] Y. Liu, D. Xie, X. Wang, K. Zhu and R. Yang, *Field-induced magnetic instability and quantum criticality in the antiferromagnet $CeCu_2Ge_2$* , Sci. Rep. 6, p. 18699 (2016)
- [44] D. Jaccard, K. Behnia and J. Sierro, *Pressure induced heavy fermion superconductivity of $CeCu_2Ge_2$* , Phys. Lett. A 163 (5), p. 475 (1992)
- [45] T. Park and J. D. Thompson, *Magnetism and superconductivity in strongly correlated $CeRhIn_5$* , New J. Phys. 11 (5), p. 055062 (2009)
- [46] N. J. Curro, T. Caldwell, E. D. Bauer, L. A. Morales, M. J. Graf, Y. Bang, A. V. Balatsky, J. D. Thompson and J. L. Sarrao, *Unconventional superconductivity in $PuCoGa_5$* , Nature 434 (7033), p. 622 (2005)
- [47] N. D. Mathur, F. M. Grosche, S. R. Julian, I. R. Walker, D. M. Freye, R. K. W. Haselwimmer and G. G. Lonzarich, *Magnetically mediated superconductivity in heavy fermion compounds*, Nature 394 (6688), p. 39 (1998)
- [48] D. Marel, H. J. A. Molegraaf, J. Zaanen, Z. Nussinov, F. Carbone, A. Damascelli, H. Eisaki, M. Greven, P. H. Kes and M. Li, *Quantum critical behaviour in a high- T_c superconductor*, Nature 425 (6955), p. 271 (2003)

- [49] S. Sachdev, *Quantum Phase Transitions* (Cambridge University Press, UK, 2011)
- [50] T. Moriya, *Spin Fluctuations in Itinerant Electron Magnetism*, Springer Series in Solid State Sciences (Springer-Verlag, 1985)
- [51] C. Pfleiderer, G. J. McMullan, S. R. Julian and G. G. Lonzarich, *Magnetic quantum phase transition in MnSi under hydrostatic pressure*, Phys. Rev. B 55, p. 8330 (1997)
- [52] D. Belitz, T. R. Kirkpatrick and T. Vojta, *First Order Transitions and Multicritical Points in Weak Itinerant Ferromagnets*, Phys. Rev. Lett. 82, p. 4707 (1999)
- [53] M. Uhlarz, C. Pfleiderer and S. M. Hayden, *Quantum Phase Transitions in the Itinerant Ferromagnet ZrZn₂*, Phys. Rev. Lett. 93, p. 256404 (2004)
- [54] A. V. Chubukov, C. Pépin and J. Rech, *Instability of the Quantum-Critical Point of Itinerant Ferromagnets*, Phys. Rev. Lett. 92 (14), p. 147003 (2004)
- [55] D. Moroni-Klementowicz, M. Brando, C. Albrecht, W. Duncan, F. M. Grosche, D. Grüner and G. Kreiner, *Magnetism in Nb_{1-y}Fe_{2+y}: Composition and magnetic field dependence*, Phys. Rev. B 79 (22), p. 224410 (2009)
- [56] Y. Wang, Y. Feng, J.-G. Cheng, W. Wu, J. L. Luo and T. F. Rosenbaum, *Spiral magnetic order and pressure-induced superconductivity in transition metal compounds*, Nat. Commun. 7, p. 13037 (2016)
- [57] E. Fawcett, *Spin-density-wave antiferromagnetism in chromium*, Rev. Mod. Phys. 60 (1), p. 209 (1988)
- [58] E. Fawcett, H. L. Alberts, V. Y. Galkin, D. R. Noakes and J. V. Yakhmi, *Spin-density-wave antiferromagnetism in chromium alloys*, Rev. Mod. Phys. 66, p. 25 (1994)
- [59] T. E. Mason, G. Aeppli and H. A. Mook, *Magnetic dynamics of superconducting La_{1.86}Sr_{0.14}CuO₄*, Phys. Rev. Lett. 68, p. 1414 (1992)

- [60] T. Takahashi, H. Kawamura, T. Ohyama, Y. Maniwa, K. Murata and G. Saito, *Pressure Dependence of SDW Properties in the Organic Conductor, (TMTSF)₂PF₆*, J. Phys. Soc. Jpn. 58 (2), p. 703 (1989)
- [61] L. Keldysh and Y. V. Kopayev, *Possible instability of semimetallic state toward Coulomb interaction*, Phys. Solid State 6 (9), p. 2219 (1965)
- [62] H. Onnes, *Further experiments with liquid helium*, Commun. Phys. Lab. Univ. Leiden 119b,120b,122b,124c (1911)
- [63] M. R. Norman, *The challenge of unconventional superconductivity*, Science 332 (6026), p. 1960 (2011)
- [64] F. London and H. London, *The Electromagnetic Equations of the Supraconductor*, Z. für Phys 96 (866), p. 359 (1935)
- [65] V. Ginzburg and L. Landau, *On the theory of superconductivity*, Zh. Eksp. Teor.Fiz 20, p. 1064 (1950)
- [66] J. Bardeen, L. N. Cooper and J. R. Schrieffer, *Theory of Superconductivity*, Phys. Rev. 108, p. 1175 (1957)
- [67] C. Reynolds, B. Serin, W. Wright and L. Nesbitt, *Superconductivity of Isotopes of Mercury*, Phys. Rev. 78, p. 487 (1950)
- [68] M. Tinkham, *Introduction to superconductivity* (Courier Corporation, 1996)
- [69] J. Clarke and A. Braginski, *The SQUID Handbook: Fundamentals and Technology of SQUIDS and SQUID Systems* (Wiley, 2006)
- [70] P. Anderson, *Special Effects in Superconductivity*, in E. Caianiello (ed.), *Lectures on the Many-body Problems* (Academic Press, 1964), p. 113
- [71] M. H. Devoret, A. Wallraff and J. M. Martinis, *Superconducting qubits: A short review*, arXiv preprint cond-mat/0411174 (2004)
- [72] J. Clarke and F. K. Wilhelm, *Superconducting quantum bits*, Nature 453 (7198), p. 1031 (2008)

- [73] D. White, R. Galleano, A. Actis, H. Brixy, M. De Groot, J. Dubbeldam, A. Reesink, F. Edler, H. Sakurai, R. Shepard *et al.*, *The status of Johnson noise thermometry*, Metrologia 33 (4), p. 325 (1996)
- [74] J. Luomahaara, V. Vesterinen and J. Grönberg, L. Hassel, *Kinetic inductance magnetometer*, Nat. Commun. 5, p. 4872 (2014)
- [75] A. V. Timofeev, V. Vesterinen, P. Helistö, L. Grönberg, J. Hassel and A. Luukanen, *Submillimeter-wave kinetic inductance bolometers on free-standing nanomembranes*, Supercond. Sci. Technol. 27 (2), p. 025002 (2014)

“It seems possible that polarized positive and negative muons will become a powerful tool for exploring magnetic fields in nuclei, atoms, and interatomic regions.”

L.R. Garwin, 1957

3

Muon-spin relaxation and rotation

μ SR is a collection of methods that uses the muon spin to look at structural and dynamical processes in the bulk of a material on the atomic scale. The acronym stands for Muon Spin Relaxation, Rotation, Resonance and draws the attention to the analogy with nuclear magnetic resonance (NMR) and electron spin resonance (ESR). Unlike those resonance techniques, no magnetic field is necessary since the precessing muon can be followed directly due to their polarised nature. Muons are short-lived particles that violate the principle of invariance under space reflection (parity) by the weak interaction responsible for the muon and pion decay. As a result, fully spin-polarised muons can be created, accelerated and implanted into a sample. Once inside a material, they interact with the local fields at the muon sites as a sensitive local magnetic probe. Implantation of spin-polarised muons and the subsequent measurements of the time evolution of the muon spin polarisation provides a method to examine the distribution and fluctuations of the internal fields.

The chapter is organised to cover the relevant information to understand and carry out a μ SR experiment. Muon and its properties are introduced in Sec 3.1. Then, experimental aspects of the technique such as muon production, implantation, decay and detection are explored in Sec. 3.2. A summary of the technique capabilities and μ SR facilities is outlined in Sec. 3.3 followed by an overview of the relaxation functions which describe the effects of common magnetic structures in the muon-spin relaxation, paying attention to those used in this thesis, Sec. 3.4. Superconductivity is one of the most fruitful areas of muon research. μ SR applied to superconductors is finally introduced in Sec. 3.5.

Reference books and full reviews with technical aspects and μ SR applications in condensed matter can be found in Refs. [1–5].

3.1 Muon properties

Positive (μ^+) and negative (μ^-) muons are charged leptons with spin 1/2 carrying one elementary electric charge belonging to the same family as electrons. They have similar properties to electrons (positrons), except that the rest mass is about 207 times that of an electron and 9 times less than that of a proton. Although both can be used to perform μ SR, their behaviour in matter are different. μ^- behaves as a “heavy electron” and are easily captured by nuclei. In this process a significant amount of spin polarisation is lost and radiation is produced reducing the measured mean lifetime. These circumstances make μ^+ the preferred choice for most condensed matter applications (herinafter μ SR will refer to positive muons). Therefore, for μ SR community, the positively charged particle is consider like a “light proton”, although the proton is a hadron unlike the muon. By the standard of other unstable elementary particles, the muon is comparatively long-lived with a lifetime of $\tau = 2.2 \mu s$. The muon magnetic moment is about three times that of the proton, making it very sensitive to extremely small magnetic fields. Consequently muons are a very useful probe to study weak magnetism. Once the sample is im-

planted into the sample, the muon-spin precesses around a local magnetic field, \mathbf{B} with the Larmor precession frequency $\omega_\mu = \gamma_\mu \mathbf{B}$ given by the muon gyromagnetic ratio $\gamma_\mu = 851.6 \text{Mrad.s}^{-1} \text{T}^{-1}$ or 13.5 KHz/G. Muons in insulators use to capture an electron in a hydrogen-like atom known as muonium (Mu). Muon properties are summarised in Table 3.1.

Table 3.1: Main muon properties.

PROPERTY	VALUE	REMARKS
	$\mu^+ \mu^-$	
MASS	$m_\mu = 207m_e = 1/9m_p$	“heavy electron” or “light proton”
CHARGE	-e // +e	
SPIN	$S = \frac{1}{2}$	
MAGNETIC MOMENT	$\mu_\mu = 3.18\mu_p$	$\mu_\mu = g_\mu \frac{e\hbar}{2m_\mu} S$
GYROMAGNETIC RATIO	$\gamma_\mu = 851.6 \text{Mrad.s}^{-1} \text{T}^{-1}$	$\gamma_\mu = g_\mu \frac{e}{2m_\mu}$ $g_\mu = 2.001165$
LIFETIME	$\tau_\mu = 2.197\mu\text{s}$	
MOMENTUM	$P_\mu = 29.79 \text{MeV}/c$	
KINETIC ENERGY	$E_\mu = 4.12 \text{MeV}$	
BOUND STATE	$\mu^+ e^-$	muonium, H-isotop

3.2 μSR : experimental aspects

Experimentally, Garwin, Lederman and Weinrich [6] established the roots of a μSR experiment when they proved that the long held principle of parity conservation was violated in the weak decay of pions and muons. The violation of parity in weak interactions is responsible of the fully spin-polarised muons produced from pion decay.

3.2.1 Muon production

Muons are naturally generated in the upper atmosphere, being the dominant constituent of cosmic rays, but research in condensed matter physics requires particle accelerators to produce controllable and low energy muons thermalised in the

samples being studied. Low-energy muons are available in the required intensities only from ordinary two-body pion decay into a muon and a muon neutrino, ν_μ , according to

$$\pi^+ \longrightarrow \mu^+ + \nu_\mu \quad (3.1)$$

$$\pi^- \longrightarrow \mu^- + \nu_\mu \quad (3.2)$$

High-energy proton beams ($>500\text{MeV}$) produced in synchrotrons or cyclotrons provide a sufficient number of pions by colliding them with the nuclei of a target. Proton collisions with either protons p , and nucleons n , in the target's atomic nuclei give rise to positive π^+ or negative π^- pions via

$$p + p \longrightarrow \pi^+ + p + n \quad (3.3)$$

$$p + n \longrightarrow \pi^+ + p + n \quad (3.4)$$

Targets such as carbon on beryllium are used in order to maximize the pion production. The mean lifetime of charged pions are about 26 ns before decaying into a muon and muon neutrino, Fig. 3.1.

Most positive muon (μ^+) beams generated in μSR facilities are produced from pions decaying at rest in the surface of the production target, reason to call them *surface muons*. Muons are emitted from pions isotropically with momentum $p_\mu = 29.8\text{MeV}/c$ and kinetic energy $E_\mu = 4.2\text{ MeV}$ (in the π^+ rest frame). Unfortunately, this mode is not available for negative muons μ^- since a negative pion stopped in the production target almost always undergoes nuclear capture (depending on the atomic number Z) from low-lying orbitals of pionic atoms before it has a chance to decay. This problem is overcome by allowing the pions to decay in flight within a long superconducting solenoid. Muons that are emitted opposite to the direction of the pion momentum are called *backward muons*, which can be selectively extracted by a bending magnet. Backward muon beams are more energetic, their momentum distribution broader (approximately 50-100 MeV/c) and their phase

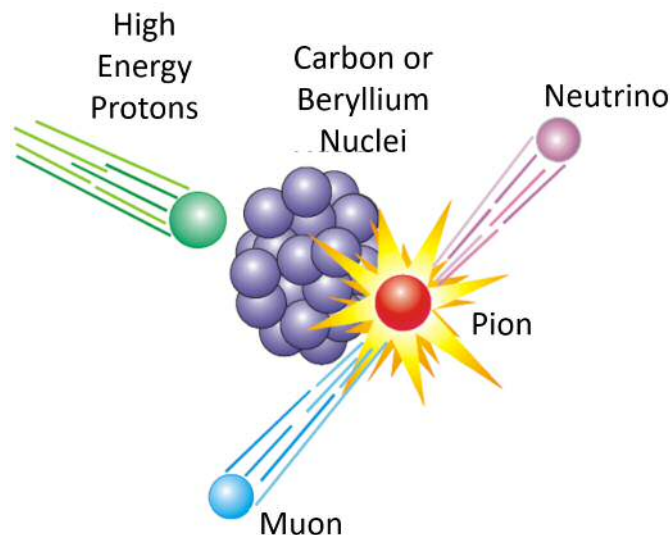


Figure 3.1: Scheme of muon production.

space much larger than surface muon beams. This gives rise to muons that penetrate deeper into material, very useful to study gases or liquids and in high-pressure experiments as muons can traverse vessels or pressure cells before coming to rest in samples. However, the lower stopping density and luminosity together with the loss of polarisation make them less desirable for standard experiments.

3.2.2 Polarized muons

If the pion decay is considered at rest in the laboratory frame, the momentum conservation of the two-body decay, Eq. 3.1, leads to a neutrino and muon with equal and opposite momentum. As pions are spinless particles, the muon and neutrino spin must have also opposite directions. The violation of parity invariance of weak interactions [7] makes neutrinos left-handed particles. i.e the helicity λ or the projection of the particle spin along its direction of motion or linear momentum \mathbf{p} is negative

$$\lambda = \mathbf{s} \cdot \frac{\mathbf{p}}{|\mathbf{p}|} < 0 \quad (3.5)$$

The conservation of linear and angular momenta and the helicity of neutrino ($\lambda = 1$) dictates that the muon beam is 100% polarised with the muon spin S_μ antiparallel to its linear momentum P_μ (See Fig. 3.2).

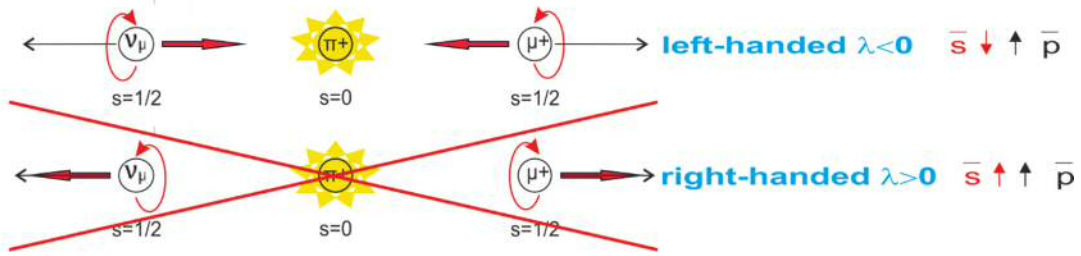


Figure 3.2: Parity violation of pion π^+ decay at rest frame into a muon μ^+ and a muonic neutrino ν_μ .

3.2.3 Muon implantation, thermalisation and localization

100% polarized muons are implanted into the sample with an implantation range for 4.12 MeV of 0.1 to 1mm, depending on material density, although μ^- with energies ranging from $\sim 4\text{MeV}$ to $\sim 100\text{MeV}$ can be produced. Muon implantation and thermalisation occurs rapidly in $10^{-10} - 10^{-9}\text{s}$, before they finally localise in interstitial crystallographic sites with an insignificant loss of polarisation. The kinetic energy of muons are reduced to a few tens of keV by inelastic scattering through atomic excitations and ionisations involving only Coulombic interactions. At lower energies, muons undergo collective excitations and charge exchange processes by capturing and losing electrons forming muonium atoms and reducing the muon energy to a few hundred of eV. If the μ^+e^- muonium bound state is ultimately formed, a last stage of thermalisation through collisions between Mu and atoms in the sample takes place until Mu is dissociated into a thermal μ^+ and a free e^- , in most cases. Systems studied in this thesis are metals, in which the bare muon is actually the stable state. Possible radiation damage by the energetic incoming muon is limited by the relatively few implanted muons ($\approx 10^8$) and the threshold energy required to form vacancies which is only accessible at the initial stages of the muon path and far enough from the final muon sites (about $1\ \mu\text{m}$) [4].

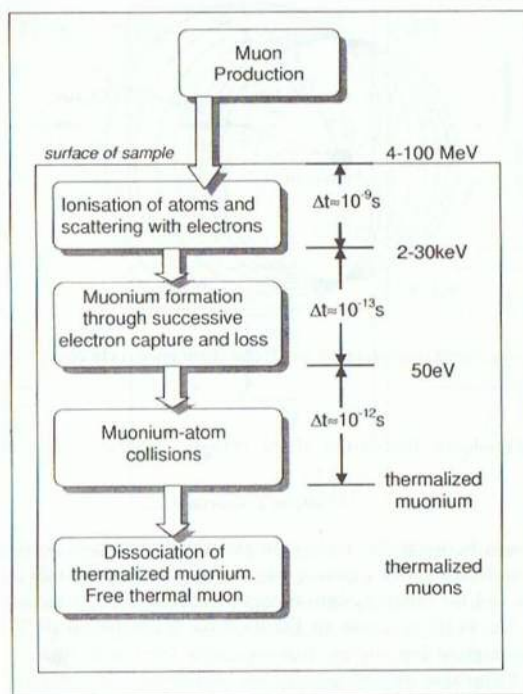


Figure 3.3: Schematic representation of the processes of implantation and thermalisation of a muon within a sample. Dissociation of thermal muonium does not always occur in the final stage. Taken from Ref. [1].

3.2.4 Muon decay and its anisotropy

The muon decays into a positron e^+ and two neutrinos,

$$\mu^+ \longrightarrow e^+ + \nu_e + \nu_\mu \quad (3.6)$$

Again, the negative helicity of neutrinos and the momentum conservation establish the emitted positron momentum. In this case, the three body process adds an extra degree of freedom and the emerging positron, which is the detectable particle, is now not parallel to the muon spin direction. Instead, positrons are emitted according to a probability function

$$W(\theta) = 1 + a \cos(\theta) \quad (3.7)$$

where θ is the angle between the muon spin and the direction of the emitted positron. The asymmetry factor a increases monotonically with the positron energy until a maximum $a = 1$ at $E = 52.83$ MeV. The probability function is plotted for the most energetically emitted positrons in Fig. 3.4. The theoretical value $a = \frac{1}{3}$ is obtained by integrating over all possible energies.

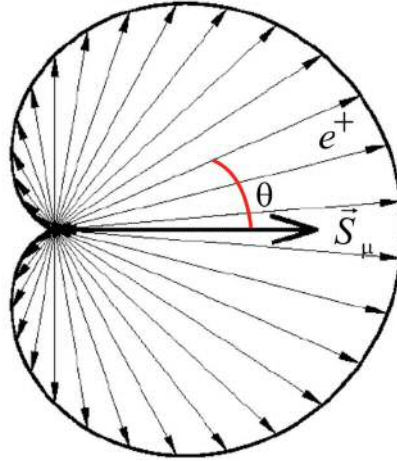


Figure 3.4: Angular distribution of emitted positrons with respect to the initial muon-spin direction (horizontal arrow) for a fixed energy. Positrons are preferentially emitted along the muon spin.

In real experiments, initial asymmetry a_0 is an empirical parameter that varies from one spectrometer to another with the limiting case of the theoretical value. There are several reasons for missing positrons. Only few of them have not energy enough to escape from the sample or are absorbed by the cryostat walls, but also the solid angle subtended by the detector bank does not cover all the area and some positrons are just missed. Electronics can also produce missing positrons. Detectors have limitations on the speed with which they can respond and there is a deadtime after each event during which further decays are missed. a_0 takes a value between 0.2 and 0.27 depending on the spectrometer used.

3.2.5 Experiment geometry

μ SR depends on the fact that positrons are emitted preferentially along the muon spin \mathbf{S}_μ direction at the moment of decay. The muon polarisation and its

time evolution are defined as the statistical average over the muon ensemble of the normalised muon spin

$$\mathbf{P}(t) = \frac{\langle \mathbf{S}_\mu(t) \rangle}{\mathbf{S}_\mu(0)} \quad (3.8)$$

which can be investigated by scintillation detectors located around the sample that count the outgoing positrons from a bunch of muons deposited at the same conditions. The density of positrons per solid angle Ω subtended by the detector at a given time is proportional to the probability function of the emitting positrons.

$$\frac{dN_{e^+}(\theta)}{d\Omega} \propto (1 + a_d \mathbf{P}(t) \cdot \mathbf{n}) \quad (3.9)$$

$$(3.10)$$

where \mathbf{n} is the normal vector of the positron detector and a_d is the intrinsic asymmetry of the detector integrated over all the positron energies.

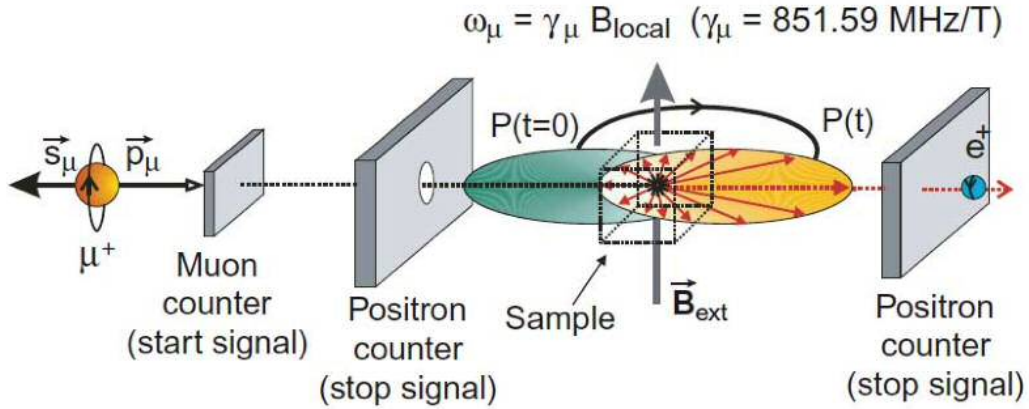


Figure 3.5: Sketch of a μ SR experiment in a continuous muon source taken from Muon Training Course notes.

The time evolution of the muon spin polarisation $\mathbf{P}(t)$ can be monitored by choosing an adequate experimental geometry as positron counts are proportional to the projection of the polarisation along the detector normal vector $P(t)$. In

the standard configuration one combines the time spectra of detectors grouped on opposite sides of the sample such as forward (F) and backward (B) with respect to the initial muon polarization as shown Fig. 3.5 for a continuous muon source. Thus, the positron intensity as a function of time after implantation is

$$N_{F,B}(t) = B_{F,B} + N_0 \epsilon_{F,B} [1 \pm a_{F,B} P(t)] \exp\left(\frac{-t}{\tau_\mu}\right) \quad (3.11)$$

The extraction of μ SR asymmetry detector a_i from the time histogrammed decay positron spectra $N_i(t)$ requires knowledge of the raw positron N_0 , background fraction B_i and efficiency of the detector ϵ_i . Therefore, the experimental quantity of interest is the positron asymmetry

$$A(t) = \frac{[N_B(t) - B_B] - \alpha[N_F(t) - B_F]}{[N_B(t) - B_B] + \alpha[N_F(t) - B_F]} \simeq a_0 P(t) \quad (3.12)$$

where $\alpha = \epsilon_F/\epsilon_B$ and a_0 the initial asymmetry. The background can be experimentally determined at $t < 0$ for continuous muon sources, whereas B_i is almost negligible for pulsed muon sources. Approximation in Eq. 3.12 is obtained by considering $a_F = a_B = a_0$. α is experimentally obtained by fitting transverse field data normally measured in a field of 2-4 mT. This experiment is called TF20 in this thesis.

The experimentalist can control some parameters in a μ SR experiments such as the orientation of the detectors or the applied magnetic field, but even the initial muon spin polarisation can also be modified in some spectrometers. According to that, there are two μ SR experimental geometries widely used with regard to the relative orientation of the external magnetic field \mathbf{B}_{ext} and the initial muon spin polarisation $\mathbf{P}(0)$. In a transverse field muon spin rotation (TF- μ SR) experiment, an external magnetic field is applied perpendicular to the muon polarisation, whereas in LF- μ SR geometry, field is applied along $\mathbf{P}(0)$. Zero-field experiments or ZF- μ SR is a special case of the LF configuration with no applied field. When large transverse fields are required, for instance to investigate superconducting phases, some spectrometers, including detectors and the powerful magnet, are rotated 90° to apply

large fields as it was done in Chapter 6 to investigate superconductivity in CeRhIn₅, Fig. 6.4.

3.2.6 Data acquisition and statistical uncertainties

Positron counts in a μ SR experiment is given by the number of muon decay events observed in a short period of time or “bin”. On the assumptions that the number of events is proportional to the bin size; the counting rate is constant; two events does not take place at the same time; and the number of events at different bins are independent, the experiment obeys Poissonian statistics. If uncertainties in the measurement arise from random fluctuations, the standard deviation scales with the square root of the measurement or number of counts \sqrt{N}

$$\sigma_i \propto \frac{1}{\sqrt{N-1}} \approx \frac{1}{\sqrt{N}} \quad (3.13)$$

The event rate in a muon spectrometer is some tens of millions per hour. For CeRhIn₅ experiment, in MuSR spectrometer, the rate was limited to ~ 45 MeV/h because of the transverse field geometry only can count up to 64 MeV/h without distorted the data. For the NbFe₂ the rate was ~ 20 MeV/h. Positron events can be grouped together in fixed or variable long “bins”. The usual length of a raw bin is 16 ns in ISIS pulsed muon source. However, significantly smaller bins are used in continuous muon sources (1 ns in Dolly). The uncertainties can be decreased by averaging several bins together. Therefore, the uncertainties in a muon experiment will be a function of the binning length and the time span of the experiment. μ SR data present in this thesis were taken approximately over a time span of one hour and averaged with a variable bunching factor. Transverse field and zero field measurements taken above the transition temperature to calibrate the experiment and investigate the muon sites in the paramagnetic phase did not require such amount of events.

A TF20 experiment is outlined in Fig. 3.6 where backward and forward counts and the resulting asymmetry in a paramagnetic phase are shown. As the number of

counts decay exponentially, uncertainties increase in the same way with time.

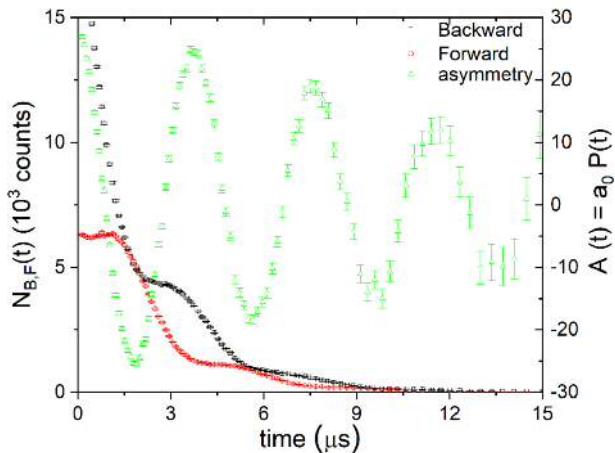


Figure 3.6: Backward (black squares), forward (red circles) and resulting asymmetry (green triangles) in a TF20 experiment. 16 ns raw bin is averaged with a bunching factor of 8

Data analysis were carried out by using Musrfit, the free platform-independent framework for μ SR data analysis developed at The Paul Scherrer Insititute (PSI) [8] and WIMDA, the muon data analysis program developed at Rutherford Appleton Laboratory (RAL) [9]. They use the χ^2 minimization method which is based on the statistics of the χ^2 function as defined:

$$\chi^2 = \sum_i^n \left[\frac{N_i(t_i) - f_i(t_i; \mathbf{a})}{\sigma_i} \right]^2 \equiv \mathbf{r}^T \mathbf{W} \mathbf{r} \quad (3.14)$$

where $N_i(t_i)$ are the number of counts per bin, and $f_i(t_i; \mathbf{a})$, the predicted value of the model. \mathbf{a} is the vector formed by the m fitting parameters and n the total number of bins. Matrix notation is also given with \mathbf{W} the diagonal weighting matrix $W_{ii} = 1/\sigma_{ii}^2$ and \mathbf{r} the $n \times 1$ residual matrix. The goodness of fit is determined by estimating the probability that the χ^2 minimum would the same if the experiment is repeated, which means that residuals falls within the standard deviations, σ_i . Therefore, the normalised χ^2/DOF with $DOF = n - m$ the number of degrees of freedom will approach to one in a good fit. Minimization requires to solve M partial

derivatives of χ^2 that in matrix notation is given by

$$\frac{\partial}{\partial \mathbf{a}} \chi^2 = -2\mathbf{r}^T \mathbf{W} \mathbf{J} \quad (3.15)$$

where the $n \times m$ Jacobian matrix \mathbf{J} represents the local sensitivity of the predicted model to variation in the fitting parameters. For nonlinear functions f_i minimization must proceed iteratively. The error measure for the parameters is given by the diagonal of the covariance matrix:

$$\sigma_{\mathbf{a}} = \sqrt{\text{diag}([\mathbf{J}^T \mathbf{W} \mathbf{J}]^{-1})} \quad (3.16)$$

Minuit is the minimization method used at PSI.

Propagation error was used to determine uncertainties where mathematical operation were involved like the experimental asymmetry or results of Chapter 4.

3.3 μ SR capabilities and muon sources

Comparing with other techniques μ SR has some unique capabilities:

- μ SR experiments have rapidly developed to provide a technique available in a large variety of environments. The use of dilution refrigerators, magnets and pressure cells makes possible to map out the μ SR signal in a compound as a function of the temperature down to a few tens of mK, pressures up to ~ 2.5 GPa and large fields of ~ 8 T in a reasonable amount of time (around 1 hour per experiment).
- μ SR is extremely sensitive to small internal fields that cannot be detected by similar techniques such as neutron scattering.
- It has no constraint in regard with the material to study as muons can be implanted into any material and is not limited to specific target nuclei.
- In terms of magnetic dynamics, μ SR can measure magnetic fluctuations in the range of 10^5 - 10^{12} Hz partially covering the time window between direct techniques such as AC-susceptibility and neutron scattering.

- μ SR is also able to recognize coexisting phases whose volume fraction will be proportional to the amplitude of distinguishable μ SR signals

On the other hand, there are some limitations in μ SR:

- It requires large and uniform samples with areas of a few square millimetres and material density larger than 150 mg/cm^2 to stop conventional surface muons. The development of low energy muons (LEM) reduces the thickness constraint and opens the technique to exciting physics that takes place in thin films, multilayers or interfaces by tuning the muon energy.
- Muon responds to the magnetic environment at the muon sites and the precise stopping sites are not always well-known.
- In contrast to techniques such as neutron scattering, μ SR has no k-space resolution so there is loss of momentum information.
- μ SR is an indirect probe, since magnetic moments are not directly measured and the lineshape of the muon depolarisation is not always an unambiguous response of a unique magnetic configuration. For instance, when magnetic fluctuations are strong the μ SR lineshape is fitted to exponential functions that are sometimes not straightforward interpreted.

In general, μ SR gives information that is complementary to that provided by other well-recognised probes of matter such as neutron scattering, NMR or AC-susceptibility. To use more than one provides clear advantages to study complex compounds, among the reasons, the different frequency bandwidth of the magnetic techniques outlined in Fig. 4.1.

μ SR is a technique that requires proton beam accelerators and nowadays there are only a few muon facilities. The muon beams currently available for μ SR are distinguished by the time structure of the proton sources.

The advantages of continuous source lie on its high time resolution of ~ 100 ps that allows to detect fields larger than 10 T. Although the measurement rate is limited to avoid detecting second positrons in the observation window. In contrast, pulsed beams require a time width of the muon pulse (~ 80 ns) shorter than the muon lifetime and a pulse repetition much larger (50 Hz). Thus, the time resolution is limited by the pulse width and internal fields larger than ~ 0.06 T are not detectable. Pulsed sources have a negligible background of outgoing positrons compared with continuous sources extending the μ SR signal up to $10 \tau_\mu$. It provides a better sensitivity to the form of the muon relaxation function being suitable to study weak magnetism. Resonance or pump/probes investigations can be also carried out by using RF fields or light pulses synchronised with muon pulses. On the other side, continuous sources are more convenient for high resolution studies, such as fast relaxation phenomena or to study flux vortices and high critical fields in superconductors.

The Paul Scherrer Institute (PSI) in Switzerland and the Tri-University Meson Facility (TRIUMF) in Canada are both continuous muon sources, whilst the Japanese Institute of Physical and Chemical Research (RIKEN) and the Rutherford Appleton Laboratory (RAL) in the United Kingdom are both sources of pulsed muon beams.

3.4 Relaxation functions

Once we know how to obtain the time evolution of muon spin polarisation from the positron asymmetry, how it sensitively depends on the spatial distribution of fields and magnetic fluctuations of the muon magnetic environment is necessary to obtain information of the magnetic structure. A short summary of the most common muon spin relaxation function $P(t)$ and those which are relevant for this thesis is given below under certain assumptions: there is no muon diffusion, i.e. each muon remains stationary after stopping at an interstitial site; muonium atoms are not formed; and a unique muon site is considered. If there are multiple muon sites in a unit cell or muon sites are magnetically inequivalent, local magnetic field at muon

sites produced by long-range ordered state with a unique internal field may result in multiple magnitudes of such field. In the standard configuration where F and B backward are used, the scalar $P(t)$ is considered the projection of $\mathbf{P}(t)$ on $\hat{\mathbf{z}}$ direction.

Effects of any external or local field $\mathbf{B}(t)$ in $\mathbf{P}(t)$ are governed by the Larmor equation:

$$\frac{d\mathbf{P}(t)}{dt} = \gamma_{\mu}\mathbf{P}(t) \times \mathbf{B}(t) \quad (3.17)$$

From this equation, we can see that the $\mathbf{P}(t)$ is a constant of motion, $|\mathbf{P}(t)| = |\mathbf{P}(0)|$.

If we consider the initial polarization along the z axis $|\mathbf{P}(0)| = P_Z(0)$ the time evolution will be given by

$$\mathbf{P}(t) = P_Z(0)[\cos\theta\hat{\mathbf{u}} + \sin\theta\cos\omega_{\mu}t\hat{\mathbf{v}} + A\hat{\mathbf{w}}] \quad (3.18)$$

The basis of the coordinate system and scheme of the polarisation time evolution are shown in Fig. 3.7. As $\hat{\mathbf{w}}$ is perpendicular to z axis, thus the projection of $\mathbf{P}(t)$ on $\hat{\mathbf{z}}$ is:

$$P(t) = P_Z(0)[\cos^2\theta + \sin^2\theta\cos\omega_{\mu}t] \quad (3.19)$$

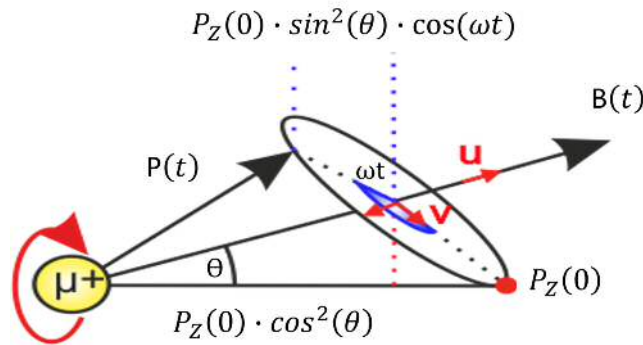


Figure 3.7: Muon spin polarization rotating around a magnetic field of arbitrary orientation.

where $\omega_\mu = \gamma_\mu |\mathbf{B}|$ is the Larmor frequency and

$$\cos^2 \theta = \frac{B_z^2}{\mathbf{B}^2}, \quad \sin^2 \theta = \frac{B_x^2 + B_y^2}{\mathbf{B}^2} \quad (3.20)$$

3.4.1 Zero-field μ SR

For greater clarity, cases that are studied below are organised as a function of the internal field distribution.

Case a):

Magnetic ordered phases in single-crystalline samples. All muons are exposed to the same field \mathbf{B}_0 :

aI): $\mathbf{B}_0 \perp \mathbf{P}(0)$:

$$P(t) = \cos \omega_\mu t \quad (3.21)$$

aII): $\mathbf{B}_0 \parallel \mathbf{P}(0)$,

$$P(t) = 1 \quad (3.22)$$

Case b):

Random orientated distribution of internal fields given by a $\rho(\mathbf{B})$:

$$P(t) = \int \rho(\mathbf{B}) \left[\frac{B_z^2}{\mathbf{B}^2} + \frac{B_x^2 + B_y^2}{\mathbf{B}^2} \cos(\gamma_\mu |\mathbf{B}| t) \right] d^3 \mathbf{B} \quad (3.23)$$

where $\int \rho(\mathbf{B}) d^3 \mathbf{B} = 1$

bI): Magnetic ordered phases in polycrystalline samples. Muons are submitted to the same field \mathbf{B}_0 with a random orientation, so there is no preferred orientation:

$$\rho(\mathbf{B}) = \frac{\delta(B - B_0)}{4\pi B_0^2}$$

to maintain a normalized field distribution:

$$P(t) = \frac{1}{4\pi B_0^2} \int \int_0^{2\pi} \int_0^\pi \delta(B - B_0) \left[\cos^2 \theta + \sin^2 \theta \cos(\gamma_\mu |\mathbf{B}|t) \right] \sin \theta |B|^2 dB d\phi d\theta \quad (3.24)$$

For $|\mathbf{B}_0| = B_0$, delta function properties lead to

$$P(t) = \frac{1}{3} + \frac{2}{3} \cos(\gamma_\mu B_0 t) \quad (3.25)$$

bII): Paramagnetic phases or some frozen states in cooperative paramagnets or spin glasses. In paramagnetic phases, electrons fluctuate faster than the μ SR time resolution and only the nuclear fields, which are randomly orientated, contribute to the muon depolarisation. The field distribution at the muon site can then be well approximated by a Gaussian distribution

$$\rho(\mathbf{B}) = \left(\frac{\gamma_\mu}{\sqrt{2\pi}\Delta} \right)^3 \exp\left[\frac{-(\gamma_\mu B_x)^2}{2\Delta^2} \right] \exp\left[\frac{-(\gamma_\mu B_y)^2}{2\Delta^2} \right] \exp\left[\frac{-(\gamma_\mu B_z)^2}{2\Delta^2} \right] \quad (3.26)$$

with a standard deviation Δ that results in a muon spin relaxation function in spherical coordinates

$$P(t) = \left(\frac{\gamma_\mu}{\sqrt{2\pi}\Delta} \right)^3 \int \int_0^{2\pi} \int_0^\pi \exp\left[\frac{-\gamma_\mu |\mathbf{B}|^2}{2\Delta^2} \right] \left[\cos^2 \theta + \sin^2 \theta \cos(\gamma_\mu |\mathbf{B}|t) \right] \sin \theta |\mathbf{B}|^2 d|\mathbf{B}| d\phi d\theta \quad (3.27)$$

Using Gaussian integral properties¹ and integration by parts with $dv(x) = xe^{-ax^2}$ the so-called Gaussian Kubo-Toyabe (GKT) function is obtained

$$P_G(\Delta_G, t) = \frac{1}{3} + \frac{2}{3} (1 - \Delta_G^2 t^2) \exp\left(-\frac{\Delta_G^2 t^2}{2} \right) \quad (3.28)$$

The subscript G is added to emphasise the Gaussian nature of the field distribution. Δ_G is sometimes known as the average local field because in an isotropic crystal

¹ $\int e^{-ax^2} \cos(kx) dx = \sqrt{\frac{\pi}{a}} e^{-\frac{k^2}{4a}}$ $\int e^{-ax^2} \sin(kx) dx = 0$ $\int e^{-ax^2} x^{2n} dx = \frac{1}{4a} \sqrt{\frac{\pi}{a}}$

$|\mathbf{B}| = \sqrt{2}\Delta_G$. Δ_G/γ_μ produced from nuclear fields are approximately a few gauss. The Gaussian distribution works also well in phases with several magnetic sources that give rise to random local fields. For instance, magnetic phases dominated by short-range interactions as occurs in concentrated spin glasses.

bIII): Dilute spin glasses. In contrast with densely packed spin glasses, when magnetic atoms in spin glasses are diluted, the distribution of fields at muon site has a Lorentzian shape rather than Gaussian and muons depolarise according to the Lorentzian Kubo-Toyabe (LKT) function

$$P_L(t) = \frac{1}{3} + \frac{2}{3}[1 - (\lambda t)]\exp[-(\lambda t)] \quad (3.29)$$

A generalisation, so-called Kubo's golden formula [10]

$$P(t) = \frac{1}{3} + \frac{2}{3} \frac{d}{dt} [tG(t)] \quad (3.30)$$

with $G(t) = \exp[-(\lambda t)^\alpha/\alpha]$, describes intermediate spin glass systems with a medium range of magnetic atoms concentration. The limiting cases of Gaussian $\alpha = 2$ and Lorentzian internal field distributions $\alpha = 1$ can be obtained.

Case c):

Incommensurate magnetic structures:

Spin density waves are spatial amplitude modulation of spin density whose period of modulation is not proportional to the lattice period. It will result in a field at the muon site which varies sinusoidally with the unit cell. The resulting field distribution

$$\rho(|\mathbf{B}|) \propto \left[1 - \left(\frac{|\mathbf{B}|}{B_{max}} \right)^2 \right]^{-1/2} \quad (3.31)$$

gives rise to a relaxation function with an oscillating behaviour dominated by a Bessel function j_0

$$P_B(t) = \frac{1}{3} + \frac{2}{3}j_0(\gamma_\mu B_{max}t) \quad (3.32)$$

Both Kubo-Toyabe and Bessel functions are characterised by a 1/3 tail corresponding to the muon-spin polarisation parallel to the initial polarisation and a 2/3 term of the perpendicular components that rapidly depolarised. Differences lies on the oscillating behaviour produced by the Bessel function, whereas KT functions are characterised by a dip before the 1/3 term dominates the relaxation (the dip is less pronounced in LKT).

3.4.2 Longitudinal-field μ SR

Application of a longitudinal field parallel to the initial polarisation $\mathbf{B} = B_{ext}\hat{\mathbf{z}}$ helps to analyse the static or dynamic nature of the internal fields. External field tends to align the local fields along the z axis recovering the initial polarisation. This phenomena called “decoupling” can be investigated in a Gaussian distribution of internal fields modifying Eq. 3.26 to

$$\rho(\mathbf{B}) = \frac{\gamma_\mu^3}{2\pi^{3/2}\Delta^3} \exp\left[\frac{-\gamma_\mu^2[\mathbf{B} - B_{ext}\hat{\mathbf{z}}]^2}{2\Delta^2}\right] \quad (3.33)$$

The LF relaxation function becomes the so-called longitudinal-field Gaussian Kubo-Toyabe (LFKT) function

$$P_G^{LF}(\omega_L, \Delta, t) = 1 - \frac{2\Delta^2}{\omega_L^2} \left[1 - \left(-\frac{1}{2}\Delta^2 t^2\right) \cos(\omega_L t)\right] + \frac{2\Delta^4}{\omega_L^3} \int_0^t \sin(\omega_L \tau) \exp\left(-\frac{1}{2}\Delta^2 \tau^2\right) d\tau \quad (3.34)$$

with $\omega_L = \gamma_\mu B_{ext}$. The applied field repolarises the asymmetry until muons no longer relax for $\omega_L \gg \Delta$ so the total field is parallel to the initial muon spin direction. The width Δ can be estimated from the maximum field where slight wiggles can still be observed, $\frac{\gamma_\mu B_{ext}^{max}}{\Delta} \sim 5 - 10$. In the other limit, the relaxation function becomes a GKT function at $\omega_L = 0$.

3.4.3 Transverse-field μ SR

The transverse field relaxation function was already introduced for an ideal case in Eq. 3.21, but in real samples the cosine relaxation may experience a slight shift in its frequency and undergoes a progressive depolarisation. This is a consequence of the internal fields contribution to the total field at muon sites. For a Gaussian internal field distribution Δ/γ_μ or local fields B_i much lower than the applied field B_0 , the relaxation function may be approximated to a precession signal enveloped by a quadratic relaxation function governed by the magnitude of the internal fields

$$P(t) = \exp\left(-\frac{\sigma^2 t^2}{2}\right) \cos(\gamma_\mu B_T t) \quad (3.35)$$

where σ takes into account the spread of internal fields $\sigma^2 = \gamma_\mu^2 \langle \Delta B^2 \rangle$. The precession will be given by B_T , the vector sum of the internal and external fields in the applied field direction. If the magnitude of the applied field is similar to the internal fields, more complex asymmetry will be generated. A wider shifts in the frequency precession or more than one oscillating term as a result of inequivalent muon sites might be observed.

3.4.4 Magnetic fluctuations

Static fields are not the only source of the muon ensemble relaxation. Internal field dynamics, resulting either from the muon hopping from site to site or from fluctuations of the internal fields can be accounted for within the strong collision approximation (SCA) [1]. It is assumed that the local field follows a stationary Gaussian-Markovian process and its direction changes at a time t according to a hopping probability $\rho(t) \propto \exp(-\nu t)$. The field after such a ‘‘collision’’ is chosen randomly from the internal field distribution $\rho(\mathbf{B})$ and is not correlated to the field before the collision. Hence, the fraction that has no experienced a field change at time t is $P^{(0)}(t) = P(t) \exp(-\nu t)$ being $P(t)$ the static relaxation function and

muons that have already undergone a change at time t' will remain stationary with a probability $\exp[-\nu(t-t')]$. The contribution to the total polarisation from all muons having had one field jump is then

$$P^{(1)}(t) = \nu \int_0^t P(t') \exp(-\nu t') P(t-t') \exp[-\nu(t-t')] dt' \quad (3.36)$$

As a recursive process, the higher order terms after n collisions can be derived as

$$P^{(n)}(t) = \nu \int_0^t P(t') \exp(-\nu t') P^{(n-1)}(t-t') dt' \quad (3.37)$$

the total muon relaxation function will be given as the sum over all n

$$P_{DKT}(t) = \sum_0^{\infty} P^{(n)}(t) = P^{(0)}(t) + \nu \int_0^t P_{DKT}(t-t') P^{(0)}(t') dt' \quad (3.38)$$

known as the dynamic Kubo-Toyabe function [11].

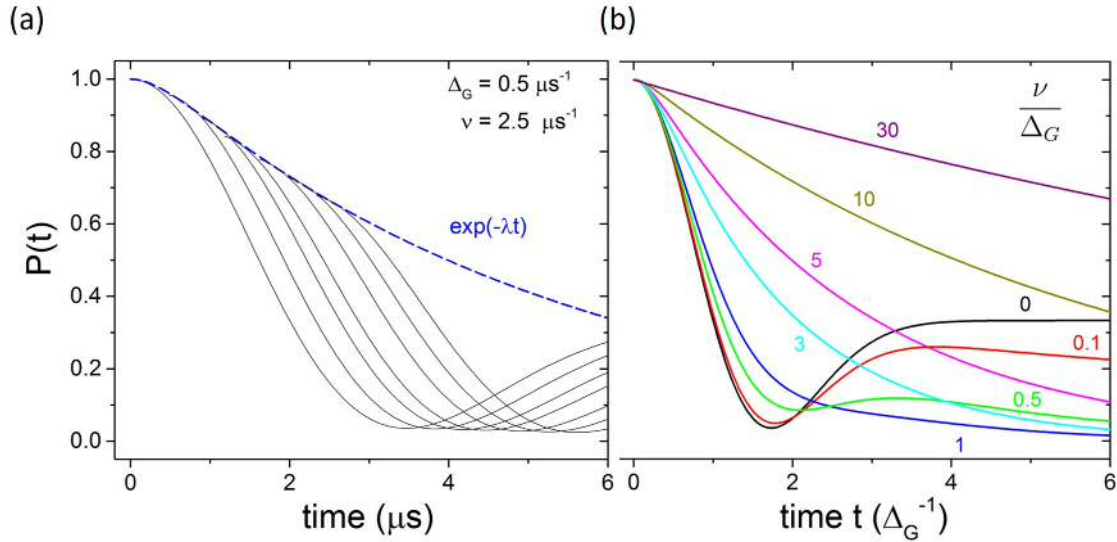


Figure 3.8: (a) Superposition of GKT functions delayed by the fluctuation rate ν for which the relaxation envelope is well described by an exponential decay. (b) Polarisation function for different ratios between the fluctuation rate and internal field of a GKT polarisation function.

The main consequence of the field dynamics is that the more collisions (larger ν) are the slower the depolarisation becomes. For a Gaussian distribution of field, the GKT relaxation function $P(t) = P_G(\Delta_G, t)$ changes into an exponential shape $\exp(-\lambda t)$ within the fast fluctuation (motional narrowing) limit determined by $R = \nu/\Delta_G = 5$. Eq. 3.38 can be seen as a superposition of GKT functions delayed by the fluctuation rate ν for which the relaxation envelope is well described by an exponential decay above the motional narrowing limit as shown Fig. 3.8. Figure also depicts $P_{DKT}(t)$ for different ratios R . For $R \gg 1$, $\lambda = 2\Delta_G^2/\nu$.

The so-called Abragam formula describes the polarisation function in the intermediate fluctuation limit $R > 1$

$$P_G(\Delta_G, \nu, t) = \exp\left(-\frac{2\Delta_G^2}{\nu}[\exp(-\nu t) - 1 + \nu t]\right) \quad (3.39)$$

For very slow fluctuations $R \ll 1$, only the 1/3 Kubo-Toyabe tail is depolarised

$$P_G(\Delta_G, \nu, t) = \frac{1}{3} \exp(-2/3\nu t) + \frac{2}{3}(1 - \Delta_G^2 t^2) \exp\left(-\frac{\Delta_G^2 t^2}{2}\right) \quad (3.40)$$

When a longitudinal field is applied ($\omega_L = \gamma_\mu B_{ext}$), in the fast fluctuation limit, λ gives information of both fluctuations and internal fields.

$$\lambda = \frac{2\Delta_G^2\nu}{\nu^2 + \omega_L^2} \quad (3.41)$$

known as the Redfield formula.

3.5 μ SR in superconductors

μ SR has been very successful investigating superconductivity. In Sec. 2.9.1, London equations were introduced as a macroscopic description of the superconducting ground state. From the assumption that the system condenses into a ground state of zero canonical momentum, the Meissner effect is deduced from the second London equation Eq. 2.64. A constant magnetic field applied parallel to the boundary (x axis) of a superconductor within free space will decay exponentially across

the superconductor (z axis) according to

$$B_x(z) = B_0 \exp\left(-\frac{z}{\lambda_L(T)}\right) \quad (3.42)$$

The μ SR experiment in the transverse-field geometry will be affected by the field distribution in the superconductor. The above field configuration involves $B_T = B_x(z)$ in Eq. 3.35. The magnetic field will decay as we move forward into the sample. Muons stopped outside the superconductor or at temperatures above the critical temperature ($T > T_c$) will precess with the frequency $\omega = \gamma_\mu \cdot B_0$, but at $T < T_c$, the more into the superconductors the muons stop, the lower the field and the precession frequency will be. Fig. 3.9 shows an scheme of the field decay and the μ SR asymmetry for muons stopped in three different positions along the decreasing field. The precession frequency decreases and the damping increases as further inside the superconductor muons stop because the field distribution spreads out asymmetrically to lower fields.

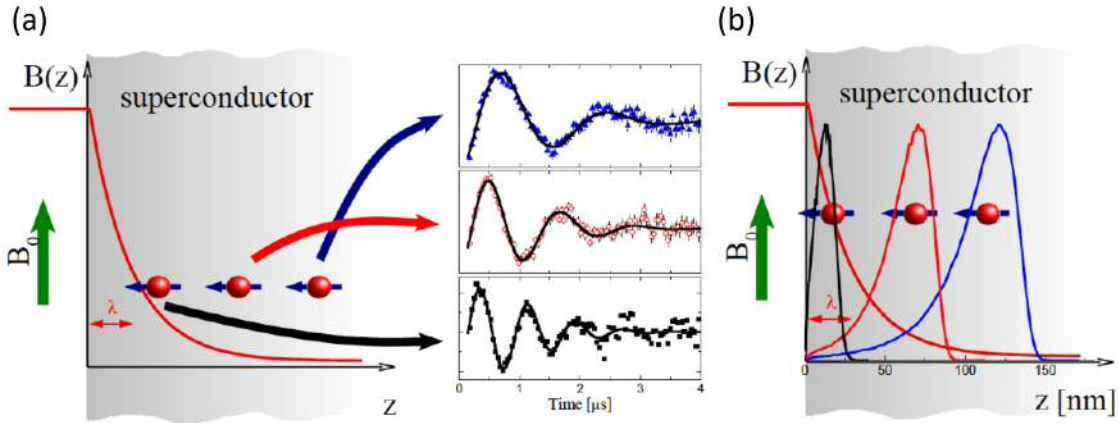


Figure 3.9: (a) Magnetic field suppression within a superconductor and the resulting μ SR depolarisation for three muon stopping sites. (b) Field distribution for the three muon sites. Data taken from [12] and scheme from [13].

As it is explained in Sec. 3.2.3 muon facilities produce the so-called surface muons with a fixed energy of $E = 4.2$ MeV. They are generally used for bulk condensed matter studies due to the implantation depth of a few hundreds of microme-

ters, so the technique is also called bulk- μ SR. In superconductors, the implantation depth is much larger than the London penetration depth. Although the muon's stopping profile can be tuned by metal degraders that decrease the muon energy, surface studies with bulk- μ SR are difficult. Nowadays, only the Low-energy muon beam (LEM) at PSI provides a tunable energy (0.5-30 keV) μ^+ source capable to implant muons in the λ_L range. The muon asymmetry can be then analysed as a function of the muon energy and the implantation depth as

$$A(t) = \int n(E, z) \cos [\gamma_\mu B(z)t + \phi] dz \quad (3.43)$$

where $n(E, z)$ is the number of muons with energy E at the position z . However, bulk- μ SR is still useful to investigate superconductivity. In type II superconductors the penetration depth is sufficiently greater than the coherence length $\lambda_L > \xi/\sqrt{2}$ and a flux lattice emerges when an external field is applied below T_c . The vortices with non-zero magnetic field cohabit with the rest that remains superconducting. Each vortex of the flux lattice contains one flux quantum and the density of vortices per unit area ($\rho \equiv B/\Phi_0$) is equal to the inverse of the unit area formed by the vortex lattice, $\rho = \frac{1}{A} = \frac{2}{\sqrt{3}a^2}$ for the usual triangular vortex lattice. The distance between vortices, a , is then

$$a = \left(\frac{2\Phi_0}{\sqrt{3}B} \right)^{1/2} \quad (3.44)$$

The vortex lattice depends on the applied field and it is normally incommensurate with the crystallographic lattice. However, muons will be sensitive to the local field distribution produced by the vortex lattice. The muon asymmetry will experience a damping in the precession amplitude as a result of the spread of the field distribution at the muon sites. The precession in the relaxation function $P(t)$ will be damped by a Gaussian function proportional to the magnetic field variation $\langle \Delta B^2 \rangle$

$$A(t) = a_0 P(t) = A_0 \exp \left(- \frac{\sigma^2 t^2}{2} \right) \cos (\gamma_\mu B(z)t + \phi) \quad (3.45)$$

that will increase inversely proportional to the penetration depth as can be seen in

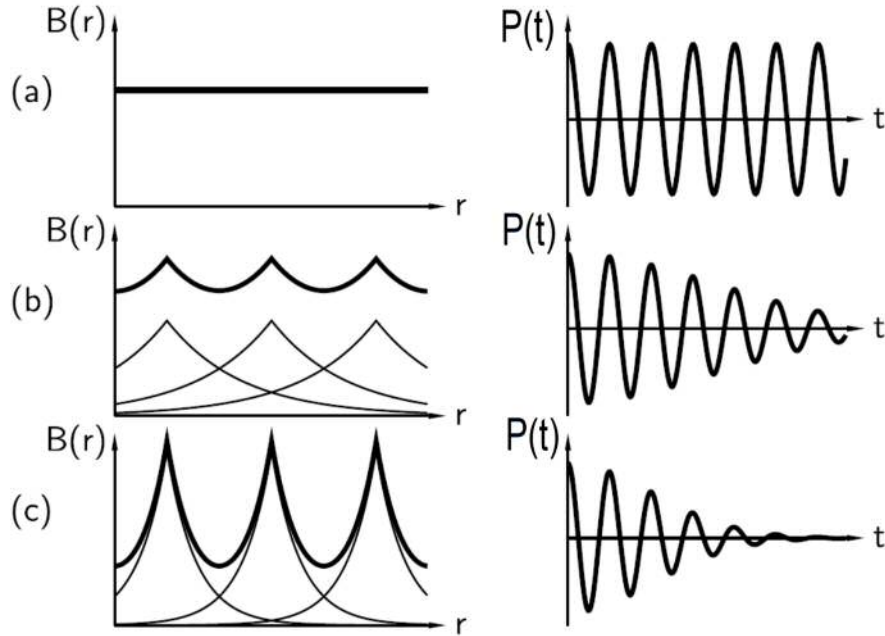


Figure 3.10: Field distribution inside a superconductor with magnetic vortices and the corresponding TF- μ SR function for three cases: (a) the normal state, (b) the superconducting state, (c) as (b) with a shorter penetration depth taken from [4].

Fig. 3.10. It shows the field distribution in the normal state (a) and in the superconducting state for two different penetration depths, (b) and (c).

The relaxation rate $\sigma^2 = \gamma_\mu^2 \langle \Delta B^2 \rangle$ is related with the penetration depth by the well-known relation [1, 14]:

$$\sigma^2 / \gamma_\mu^2 = \langle \Delta B^2 \rangle = 0.00371 \Phi_0^2 / \lambda_L^4 \quad (3.46)$$

so the larger the penetration depth is, the smaller the field varies. λ_L is, in turn, related with the superconducting carrier density, n_p by Eq. 2.61.

$$\sigma \propto \frac{1}{\lambda_L} \propto n_p$$

Information of the internal vortex lattice can be obtained from the distribution of muon precession fields, $p(B)$, obtained from the Fourier transform of the time de-

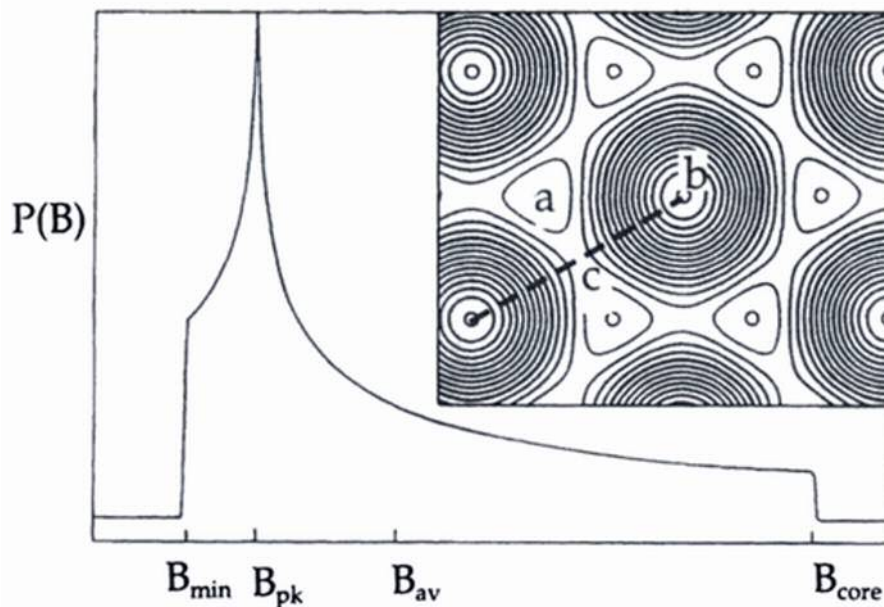


Figure 3.11: Field distribution lineshape, $p(B)$, produced by an ideal vortex line lattice taken from [1] with general features explained in text.

cay TF- μ SR. Fig. 3.11 shows an ideal vortex line lattice at temperatures and fields not near the critical values where the vortex lattice and the field distribution are deformed. Although the vortex line shape depends on the characteristic parameters, several features are generic. The asymmetric field distribution is characterised by a minimum field if the vortex distance is lower than the penetration depth, overlapping the flux lines (c point in figure). The maximum field corresponds to the vortex cores (b point). The long tail is due to the region around the vortices. Areas with slow spatial field variation around c give rise to a field peak, B_{pk} lower than the average field. Summarising, bulk- μ SR is able to detect superconducting transition and measure the penetration depth and superconducting carrier density by using the transfer-field configuration and the field distribution of muon precession fields. If the transition takes place from a ferromagnetic or antiferromagnetic phase, ZF- μ SR may also be affected by modifying the muon field distribution.

References

- [1] S. Lee, S. Kilcoyne and R. Cywinski (eds.), *Muon Science. Muons in Physics, Chemistry and Materials* (Scottish Universities Summer School in Physics and Institute of Physics Publishing, Bristol and Philadelphia, 1998)
- [2] A. Schenck, *Muon Spin Rotation: Principles and Applications in Solid State Physics* (Adam Hilger, Bristol, 1986)
- [3] A. Yaouanc and P. Dalmas de Réotier, *Muon Spin Rotation, Relaxation and Resonance: Applications to Condensed Matter* (Oxford University Press, Oxford, 2011)
- [4] S. J. Blundell, *Spin-polarized muons in condensed matter physics*, Contemp. Phys. 40 (3), p. 175 (1999)
- [5] P. D. de Réotier and A. Yaouanc, *Muon spin rotation and relaxation in magnetic materials*, J. Phys. Condens. Matter 9 (43), p. 9113 (1997)
- [6] R. L. Garwin, L. M. Lederman and M. Weinrich, *Observations of the Failure of Conservation of Parity and Charge Conjugation in Meson Decays: the Magnetic Moment of the Free Muon*, Phys. Rev. 105, p. 1415 (1957)
- [7] T. D. Lee and C. N. Yang, *Question of Parity Conservation in Weak Interactions*, Phys. Rev. 104, p. 254 (1956)
- [8] A. Suter and B. Wojek, *Musrfit: A Free Platform-Independent Framework for μ SR Data Analysis*, Physics Procedia 30, p. 69 (2012), 12th International Conference on Muon Spin Rotation, Relaxation and Resonance (μ SR2011)
- [9] F. Pratt, *WIMDA: a muon data analysis program for the Windows PC*, Physica B: Condensed Matter 289-290, p. 710 (2000)
- [10] T. Yamazaki, *Ryogo Kubo and μ SR*, Hyperfine interactions 104 (1), p. 3 (1997)
- [11] R. et al. Hayano, *Zero-and low-field spin relaxation studied by positive muons*, Phys. Rev. B 20 (3) (1979)

- [12] R. F. Kiefl, M. D. Hossain, B. M. Wojek, S. R. Dunsiger, G. D. Morris, T. Prokscha, Z. Salman, J. Baglo, D. A. Bonn, R. Liang, W. N. Hardy, A. Suter and E. Morenzoni, *Direct measurement of the London penetration depth in $YBa_2Cu_3O_{6.92}$ using low-energy μSR* , Phys. Rev. B 81, p. 180502 (2010)
- [13] S. J. Blundell, *Using muons to study superconductors*, Tech. rep., ISIS Muon Training School 2014 (2014)
- [14] E. H. Brandt, *Flux distribution and penetration depth measured by muon spin rotation in high- T_c superconductors*, Phys. Rev. B 37, p. 2349 (1988)

“To measure is to know.”

Lord Kelvin

4

Low temperature DC and AC magnetometer in a dry dilution refrigerator

4.1 Introduction

Magnetic fluctuations play an important role in the magnetic ground state of several systems that have revealed exotic behaviour. For instance, magnetic frustration takes place in materials where the local magnetic moments cannot simultaneously satisfy all the pairwise exchange interactions, so a unique ground state cannot be found. It gives rise to a large landscape of energetically equivalent states with a macroscopic degeneracy, separated by low energy barriers which can be crossed by thermal or quantum processes. Under certain conditions, these frustrated systems can lead to the formation of a frozen ground state, such as spin ice or stay

in a fluid-like states of matter, highly correlated, where the magnetic moments still fluctuate strongly down to zero Kelvin, called spin liquids [1]. Pyrochlore spin ice are an example of geometrically frustrated magnets that under specific conditions have revealed magnetic excitations that behave like magnetic monopoles, [2–4].

These magnetic fluctuations may be investigated with different techniques at different time scales. At low frequencies, AC susceptibility can measure the magnetic dynamics from a few Hz to tens of KHz and at high frequencies neutron scattering is able to detect magnetic fluctuations from 10^9 to 10^{13} Hz. These phenomena have also been successfully investigated with indirect techniques such as μ SR or NMR in the existing time window of the direct probes. The frequency dependence of the fluctuations in spin liquids or spin ice make it relevant to cover the time window between the bulk susceptibility and the local μ SR probe to compare the muons response with a direct technique. Fig. 4.1 outlines the frequency resolution of different techniques used to investigate magnetic fluctuations and the time window. Although experimental setups have achieved susceptibility measurements from hundred of kHz to several hours, there is not commercial equipment that can measure beyond tens of kHz and below 2 K. The development of a versatile AC and DC magnetometer able to work at milliKelvin temperatures and MHz resolution is presented in this work. There are a few features that make the magnetometer fabrication challenging such as, the complexity of working in the milliKelvin region and to be able to measure a wide range of magnetic moments. In fact, there are only few other examples around the world that meet these requirements [5–7] but, until now, no one has built a system in a dry and continuous dilution refrigerator or expanded the frequency response to MHz at low temperature as far as the author knows. However, resonant methods are able to measure the real part of the magnetic susceptibility at frequencies ranging from kHz to GHz. A self-oscillating tunnel-diode resonator (TDR) consists of a LC-tank circuit maintained at resonance by supplying power with a tunnel diode biased in the negative differential resistance region. The self-resonant circuit is very sensitive to small changes of its LC values and variation in magnetic susceptibility creates a measurable shift in the resonance

frequency [8–11]. To avoid refrigerators that require an expensive Helium bath to thermalise and be able to contrast the magnetic dynamics detected by μ SR at MHz in those interesting systems strongly motivates this project.

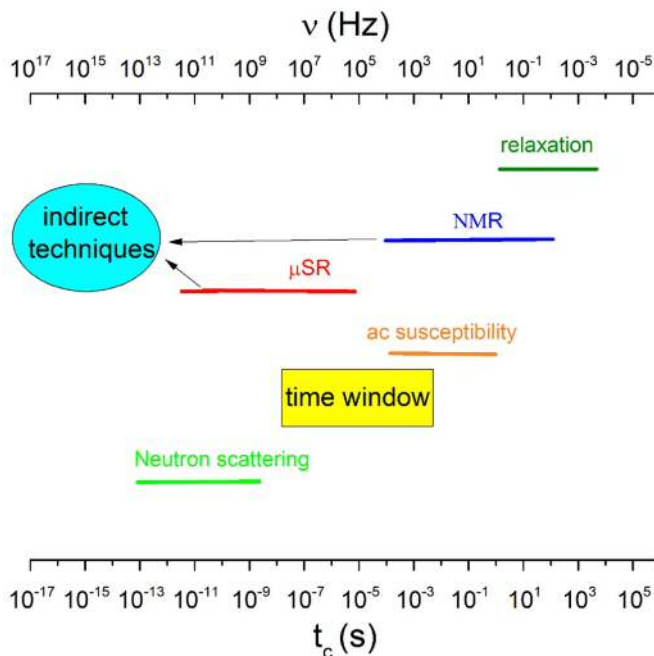


Figure 4.1: Frequency and time response of the most common techniques used to investigate magnetic fluctuations.

This chapter will introduce all the considerations that are crucial to build a low temperature magnetometer. As an experimental work, decisions are sometimes based on the available or affordable resources and different approaches to solve issues are almost always possible. Different approaches and the decision making to face the numerous challenges may be useful to potential readers. To make this chapter as understandable as possible without losing information, it was organised in the following order.

The first section 4.2 looks at the magnetometer principles of operation. Regarding to the magnetic flux detection, dc-SQUIDs and inductive methods will be compared. A reliable magnetometer needs to detect the flux, to transfer it to the

SQUID and to reduce the input flux to be measurable by a dc-SQUID. Gradiometers and flux transformers (FT) implement those tasks. Therefore, their operation and fabrication need to be explained to understand the magnetometer capabilities. The main sources of poor SQUID performance were detected and discussed. The SQUID readout linearisation and the two-stage integrated SQUID amplifier used to optimise the sensor performance is explained together with an introduction to cryogenic techniques in the appendices A

Experiments carried out in the dry fridge last no less than a week including the cooling and the warming time. In contrast, experiments in a Helium Dewar can be run in a few hours with a significant time saving. The second section 4.3 includes the fabrication of a set of different gradiometers and FT to investigate the challenges involved in building a magnetometer for a dilution fridge. To optimize the project time, a probe was designed to test the SQUID basics in the Helium Dewar. The section includes a FFT noise analysis of the background signal to identify the sources of a poor performance such as mechanical and/or electrical interference. These prototypes will provide enough information to build the final design in the dilution fridge.

The final design section 4.4 is organised in such a way that all the relevant parts of the design are discussed. Magnetometry requires moving parts. The solution to move the sample in and out of the detector coils is introduced. The design needs to deal with the mechanical noise from the movement and to avoid thermal load from the outside. The detection and the excitation coils are then described together with the methodology to transfer the magnetic flux to the SQUID and reduce it via flux transformers. Unexpected issues related with the instability of the SQUID response emerge linked to three factors: insufficient shielding; electrical noise introduced by the wires and heaters; and background signals. It requires a discussion about the materials used to insulate the magnetometer parts, to thermalise the setup or to feed the thermometers and heaters. Special attention will be paid to the magnetometer shielding. The magnetometer performance and its thermalisation is monitored and controlled by heaters and thermometers as explained later.

Then, a discussion about the sample holder, unexpected issues, base temperature approaching and implemented solutions are given. The measurements require automation. A self-consistent Labview project was designed to, among its task: take AC and DC measurements; move the sample; monitor the fridge, magnetometer and sample temperature; scan the field or temperature; or control the heaters.

Magnetometer calibration was carried out at section 4.5 by using a resistive coil that behaves as a magnetic dipole. For the final calibration a frustrated magnet, $\text{Dy}_2\text{Ti}_2\text{O}_7$ was used. Calibration will give the range of magnetic moments that may be measured with the magnetometer.

The spin ice was consciously chosen to investigate the low temperature performance. At milliKelvin temperatures, thermalisation becomes challenging and $\text{Dy}_2\text{Ti}_2\text{O}_7$ exhibits a freezing temperature highly dependant on the frequency. These properties will provide a very precise method to study the sample thermalisation in section 4.6 by comparing the freezing temperature as a function of the frequency with the literature.

An inductive magnetometer built as an alternative to the dc-SQUID is introduced in section 4.7. It includes the collaboration with ACREO company to build a novel inductive high frequency AC susceptometer. The collaboration intends to combine their expertise in high frequency inductive coils with our experience in low temperature physics. As a result, a prototype were fabricated with promising response at MHz frequencies at room and liquid Helium temperatures. The magnetometer is being prepared to be attached to the dilution fridge or to a commercial Physical Properties Measurement System (PPMS).

As a learning process this project has not only produced a working magnetometer at very low temperatures, it has provided new challenges that were not considered initially. In the conclusion section 4.8, main achievements and future improvements are highlighted.

4.2 Magnetometer

4.2.1 Magnetic flux detection method

There are different techniques to measure AC susceptibility and magnetic moment, such as inductive, SQUID and torque methods. In terms of simplicity, ease to implement and price, inductive coils are the best choice, but a few troubles emerge when low temperature or high sensitivity as heat dissipative coils are required instead of superconducting ones. Although the purpose of the dc-SQUID and inductive magnetometer is the same, to measure magnetic susceptibility, the physical principles are not. A summary of the principles and limitations of both techniques for this work is presented below.

Inductive methods are based on Faraday's law of induction. The induced electromotive force in any closed circuit is equal to the negative of the time rate of change of the magnetic flux enclosed by the circuit

$$\varepsilon = -\frac{d\Phi}{dt} \quad (4.1)$$

being ε the electromotive force or voltage induced in the closed circuit and Φ the flux enclosed. dc-SQUID combines the flux quantization and Josephson tunneling physical phenomena to convert flux to voltage. In this case, a magnetic flux induces a permanent current in a superconducting loop whilst, a *temporal change in the magnetic flux* is needed to induce a current in a dissipative conductor. Therefore, an inductive method can measure alternating magnetic fields or to move the sample in and out of the detecting coils to measure total magnetization by changing the effective area. Vibrating Sample Magnetometer (VSM), used with an inductive or SQUID detector is a standard technique to measure absolute moments: the sample is moved at a specific frequency changing the total flux. The induced voltage is integrated by a lock-in to work out the magnetisation.

The expected features of the magnetometer hinders the use of a VSM method for AC susceptibility, since a fast movement of the sample may ruin the thermali-

sation in a dry dilution refrigerator below few Kelvins as it is demonstrated in Sec. 4.4.1. But, what are the capabilities of an AC inductive magnetometer? There are two factors that define its performance: the sensitivity and the frequency bandwidth. An estimation of these parameters is presented using the dimensions of the high frequency inductive magnetometer designed and fabricated as an alternative to the SQUID magnetometer. An inductive magnetometer normally is configured as a Hartshorn bridge that consists of an excitation or primary coil and a detection or secondary coil. For simplicity only the detection circuit used is shown in Fig. 4.2. The excitation circuit supplies the AC field that will magnetise the sample to be studied. The voltage, which is measured, induced in the detection coil is simplified to an AC voltage source in the equivalent circuit. The detection coils behave as an RLC circuit. The wires contribute to the circuit with a dominant capacitance of around 200 pF per meter. The pick-up coils are fed by the AC source and the signal is detected by a lock-in amplifier that adds its own input capacitance and resistor. The circuit on the right includes a resistance network that avoids resonances as it will be explained in Sec. 4.7.

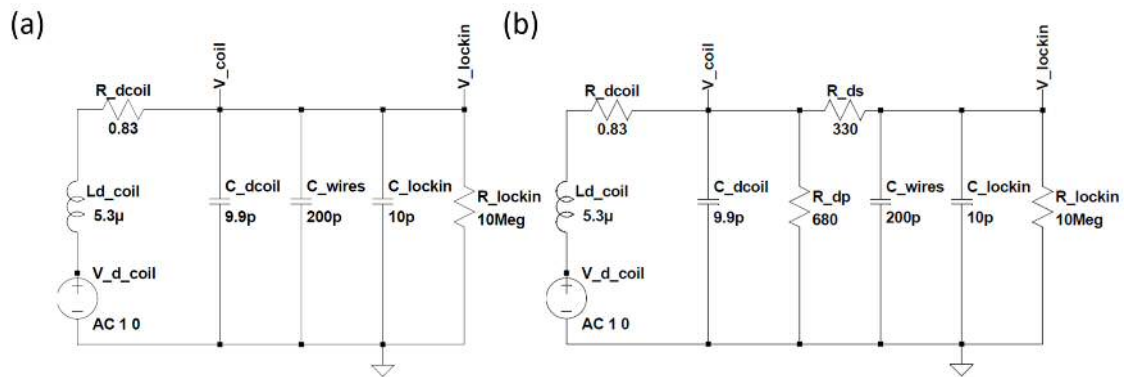


Figure 4.2: (a) Equivalent circuit used for the High Frequency Inductive Magnetometer without and with (b) the resistance network that removes the circuit self-resonance.

The secondary coils consist of two Copper solenoids of N turns wound in opposite directions so-called first-order gradiometer. More details about gradiometers are given in Sec. 4.2.2 but, as a first approximation, it can be said that only the

sample contribution is measured in Eq. 4.1 as,

$$\varepsilon = N \left(\frac{d\Phi_2}{dt} - \frac{d\Phi_1}{dt} \right) = \mu_0 2\pi\nu N\alpha\mu \quad (4.2)$$

for solenoid 1 and 2, μ_0 the vacuum permeability, $2\pi\nu$ the angular frequency and $[\mu] = Am^2$ or 10^3 emu the sample magnetic moment. α is a geometric factor, $1/\alpha \simeq V/A \approx 5mm$ with V and A the volume and the area of the sample respectively. 5mm is chosen as the length of a standard sample. From Eq. 4.2, the number of turns, N, and the frequency linearly increase the voltage but the cutoff frequency of the RLC filter decreases with the number of turns. Fig. 4.3 (a) shows the induced voltage of the magnetic moments in the interval of interest ($m = 10^{-2} - 10^{-7}emu$) for N=15 as a function of the frequency. Black and red lines are the RLC circuit transmission with and without the resistance network, using $1\mu V$ as a reference signal. $1\mu V$ is chosen as a detectable threshold, below which lock-in amplifier signal to noise ratio hinders the measurements. As a reference, although it is not comparable, dc-SQUID noise at 50 KHz, $V^N \simeq 1.1mV$. The RLC circuit has a cutoff frequency of

$$f = \frac{1}{2\pi\sqrt{LC}} \approx 4.7MHz \quad (4.3)$$

for N=15.

It is important to mention that the self-inductance of the coils is $L \propto N^2$ and the self-capacitance is proportional to its length and, hence the number of turns, although its contribution is residual compared with the wires capacitance, 200 pF/meter. Double the number of turns will improve the induced voltage but will halve the cutoff frequency. The final frequency response is the induced voltage weighted by the transmission coefficient and it is shown in Fig. 4.3 (b). Limiting factors are highlighted by red lines. Lock-in limit is estimated to $1\mu V$ based on experience, heat load limit value of 3.5 mW is based on the power dissipation of the inductive coils. $R = 0.83\Omega$ inductive coils resistance will produce a power dissipation, $P = V^2/R = 15\mu W$, equal to the DR cooling power at 20 mK, hampering to cool the refrigerator down to the base temperature. Fig. 4.4 outlines the High

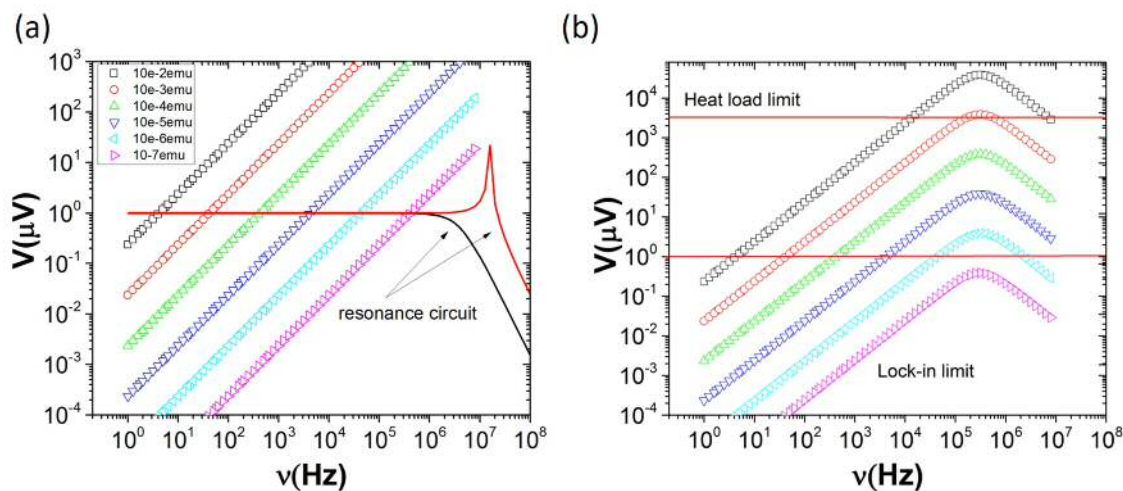


Figure 4.3: (a) Induced voltage in a first-order gradiometer for different magnetic moments and the frequency response of the circuit with and without the network resistance. (b) Circuit effects in the induced voltage. Red lines define the limiting factors. More details in text.

Frequency Inductive Magnetometer sensitivity and bandwidth with the above assumptions. A detailed review about inductive coils and electronics to improve the bandwidth can be found here [12]. Unfortunately, from the experimental point of view, to exceed MHz resolution is complex and, at the present, there is no commercial equipment that can work beyond a few hundreds of kHz at low temperatures as far as the author knows. At room temperature there is a commercial equipment from RISE Acreo able to reach a 10 MHz resolution with an acceptable sensitivity [13, 14]. Some groups were able to design mutual inductance bridge with frequency resolution close to MHz [15, 16]. These works described the difficulties to reach MHz resolution. Modifications in the standard design or the analysis method are required to expand the frequency response. Summarising, to measure dynamic magnetic properties above MHz with inductive methods is challenging and not reported at ultra-low temperatures.

On the other hand, dc-SQUIDS are the most sensitive flux-to-voltage transducers, able to detect fractions of a quantum flux, $\Phi_0 = 2 \cdot 10^{-15}$ Wb. Normally, SQUIDS are micrometric superconducting loops and, when they are used as a magnetometer,

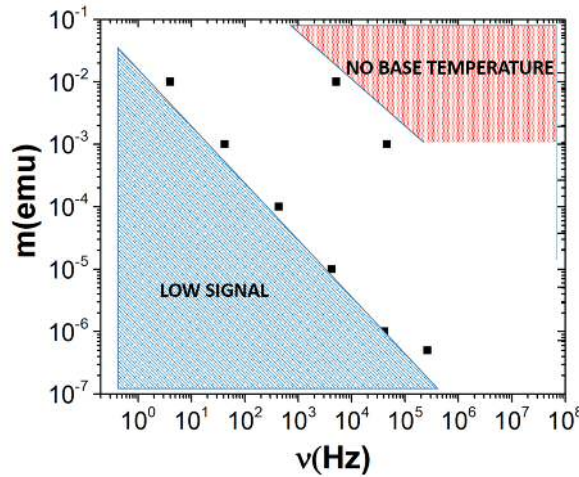


Figure 4.4: Estimations of the detectable magnetic moments of the High Frequency Inductive Magnetometer.

a superconducting circuit and flux transformers are needed to collect the magnetic flux of the sample. The flux induced by the sample in the pickup coils is transferred and reduced before reaching the SQUID. A flux-transfer function characterises the ratio between the input and the output flux that is directly related to the circuit and the SQUID inductances. For pickup coils of 10 mm diameter and no losses in the flux transfer, magnetic moments of 10^{-13} emu or magnetic fields of tens of pT might be achievable by a SQUID magnetometer. In practice, the transfer function reduces the flux by a few orders of magnitudes, but it is still more sensitive than any other magnetometer by far and smaller moments than 10^{-7} emu are easily measured.

In terms of the frequency response, the physical limit of the SQUID bandwidth is the Josephson frequency, $f_J \equiv V/\Phi_0 \simeq V \cdot 483.6 \text{ MHz}/\mu\text{V}$. SQUIDs are used for a broad range of applications at frequencies up to gigahertz. As amplifiers, high-gain, low-noise SQUID amplifiers have been used up to hundreds of MHz [17] in an open-loop operation mode. Unfortunately, SQUID response is not linear and an electronic circuit, known as flux-locked feedback loop (FLL), linearises the SQUID readout. Above MHz, FLL electronics stop working due to the cable length, and hence, the non-linear open-loop mode is required with a restriction in the dynamic range. The SQUID output voltage is normally around 40-100 μV and signal amplification is re-

quired. In a standard procedure, the signal can be modulated by a reference signal of hundreds of kHz. Then, the readout is amplified, filtered and demodulated by a lock-in amplifier [17]. In this case, a low temperature amplifier consists of an array of series SQUIDs was chosen due to the interest in large frequencies response. The SQUIDs amplify the readout before transferring it to the room-temperature amplifier resulting in an output of hundreds of millivolts as shown Fig. 4.5 with no need of modulation. The low temperature amplifier improves the SQUID performance as the upper frequency limit and the maximum magnetic moment detectable is restricted by the propagation delays of the FLL cryocables that connects the SQUID to the outside. Cables act as a low pass filter, so the larger the pre-amplifications, the higher magnetic moment and frequency will be reachable. The frequency and flux upper limits are determined by the Slew Rate in $M\Phi_0/s$ and the bandwidth. The Star Cyroelectronics SQUID amplifier used in this work has a theoretical slew rate and a maximum bandwidth of the feedback electronics for small signals ($0.2\Phi_0$) of about $1 M\Phi_0/s$ and 1.3 MHz, respectively. These parameters are highly affected by the preamplifier circuit and the length of the SQUID cables. A detailed explanation of the SQUID electronics is given in appendix A.2. At present, only a few works have reached a bandwidth larger than 1 MHz [18–20] reducing the pickup coils to micrometers. Summarising, the main problems arising from the use of a dc-SQUID magnetometer are:

- Very small voltage across the SQUID: $V_{pp} \approx 40 - 100\mu V$.
- Transfer coefficient $V_\Phi = dV/d\Phi$ depends on SQUID working point.
- Very small linear flux range $\Phi \ll \Phi_0$.

The SQUID electronics main tasks are:

- To amplify the small SQUID voltage without adding noise.
- To linearise the voltage-to-flux response to provide a large dynamic range.

4.2.2 Flux transformer and gradiometers

To build a SQUID magnetometer, a superconducting input circuit known as a gradiometer or/and a flux transformer is required to measure the sample magnetic

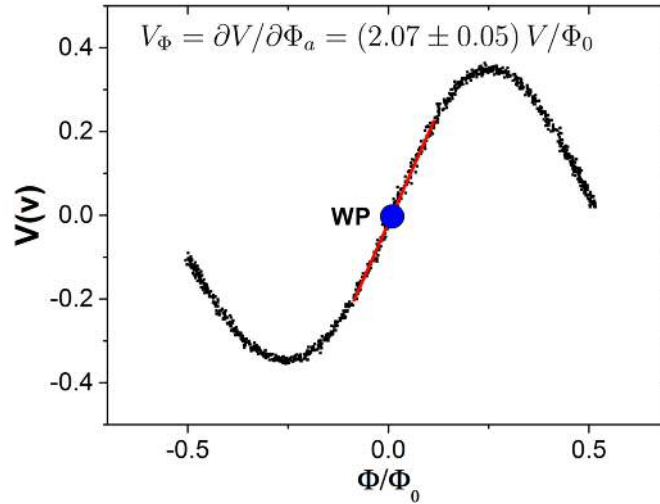


Figure 4.5: Input SQUID voltage-to-flux response with the final gradiometer attached. Transfer coefficient, V_{Φ} , obtained from the maximum slope (red line) at the working point (WP-blue circle) and locked by the FLL.

moment and transfer it to the SQUID.

The magnetic field or their spatial change is collected by a magnetometer (single loop) or a gradiometer (several loops spatially separated), respectively. Two loops separated axially by a distance z and connected in series opposition form a first-order gradiometer and two first-order gradiometers with opposite polarity give rise to a second-order gradiometer. They are vector devices that measure the magnetic field component perpendicular to the pickup loop plane. The use of gradiometers instead of magnetometers are highly recommended as the first way to shield the SQUID from the environment. The magnetic field from a magnetic dipole decays with distance r as $1/r^3$, the first derivative as $1/r^4$, and the second derivative as a $1/r^5$. As any source of magnetic noise can approximate to a magnetic dipole for r larger than the gradiometer loops distance, uniform magnetic fields ideally induces no net flux in a first-order gradiometer. If a second-order gradiometer is used, only the second derivative of the noise sources, that decays faster, is detected. In practice, to achieve a balance lower than 0.1% required complex and high-precision fabrication [21].

To measure the sample magnetic susceptibility, two methods may be used: either the sample is placed in one of the loops of the gradiometer and a magnetic field is applied, or the sample is moved from outside to one of the loop unbalancing the gradiometer. The former avoids issues associated with the sample movement, as a heat load from the motor, but absolute values cannot be measured and hysteretic samples will give different response depending on their magnetic record. At very low temperatures, this method is recommendable as the movement might ruin the sample thermalisation. On the other hand, the later gives an accurate value of the absolute magnetic moment. More details of the measurement protocol is given in the Sec. 4.4.8.

The magnetic flux per unit of magnetic moment induced in a superconducting circuit is outlined in Fig. 4.6 for a first- (green) and second- (red) order axial gradiometer. The flux is calculated by the reciprocity principle [22] that relates the flux

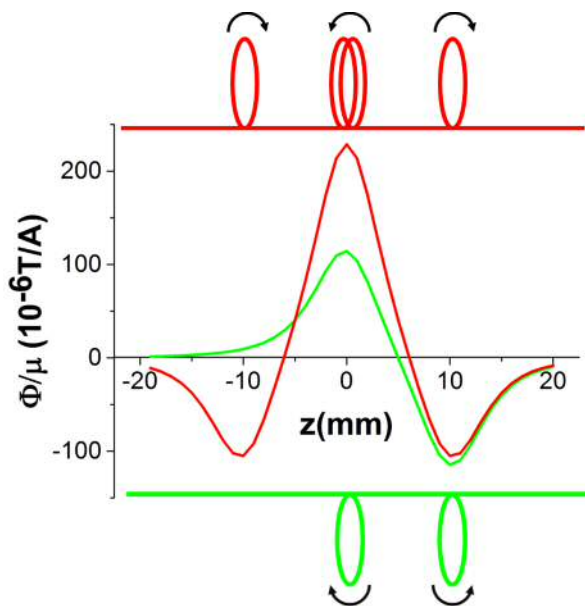


Figure 4.6: Flux per magnetic moment induced in a first-order (bottom-green) and a second-order (upper-red) gradiometer with loop radius $a=5\text{mm}$, according to the reciprocity principle (Eqs. 4.6 and 4.7).

Φ induced in a coil by a magnetic dipole, μ , with the magnetic field, \mathbf{B} , produced by a certain current, I , in the same coil:

$$\mathbf{B} \cdot \boldsymbol{\mu} = \Phi I \quad (4.4)$$

The resulting induced flux by the dipole moving along the coil axis, \hat{z} , in a coil of radius a at z_0 :

$$\frac{\Phi_{coil}}{\mu} = g(a, z - z_0) = \frac{\mu_0}{2} \frac{a^2}{[a^2 + (z - z_0)^2]^{3/2}} \quad (4.5)$$

The total flux for a first- and second-order gradiometer per unit of magnetic moment is then:

$$\frac{\Phi_{1st}}{\mu} = g(a, z) - g(a, z - d) = G^1(a, z) \quad (4.6)$$

$$\frac{\Phi_{2nd}}{\mu} = -g(a, z + d) + 2g(a, z) - g(a, z - d) = G^2(a, z) \quad (4.7)$$

The magnetic flux in the superconducting pickup coil induces a permanent current I_s in the superconducting circuit related by the flux quantisation

$$\Phi_{in} + \sum_{\forall i} L_i I_s = \Phi_{in} + L_T I_s = 0 \quad (4.8)$$

with L_i any inductance in the superconducting circuit. The flux is coupled to the output coil by its mutual inductance, M_i :

$$\Phi_{out} = M_i I_s \quad (4.9)$$

Combining Eqs. 4.8 and 4.9, the flux-transfer function of the SQUID or any intermediate flux transformer, f_i , is given by

$$\Phi_{in} = \frac{L_T}{M_i} \Phi_{out} = f_i \Phi_{out} \quad (4.10)$$

where f_i will be always higher than one as mutual inductance is lower than the self-inductance.

In this case, the inductance of a single-turn loop of diameter d in meters made

from wires of diameter w is given by Terman [23]:

$$L_{pc} = \frac{\mu_0 \cdot d}{2} (\ln 8d/w - 1.75) \text{ Henries} \quad (4.11)$$

From the same source, the mutual inductance between two single-turn loops is $M = N/2\sqrt{d \cdot D}$ with D , the diameter of the other loop, and N , a parameter highly dependant of the distance. Another source of inductance are the twisted pair leads used to transfer the flux with an inductance per unit of length around $L_{tp} \approx 5nH/cm$. Fig. 4.7 shows a scheme of a SQUID magnetometer, where the reciprocity principle is depicted by the function $G^n(a, z = 0)$ in Eq. 4.7, f_i are the flux transformers and/or the SQUID flux-transfer function and V_Φ the SQUID transfer coefficient.

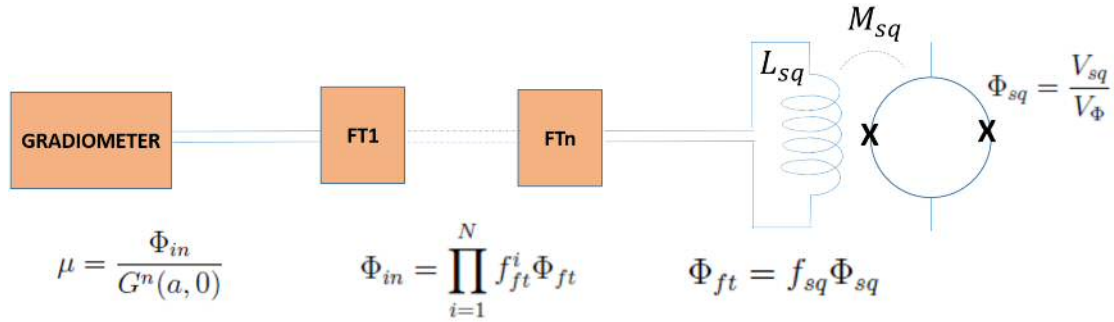


Figure 4.7: Scheme of the SQUID magnetometer. Flux is induced in the gradiometer and transferred through a set of flux transformers. Flux is coupled to the SQUID by an internal coil with a self, L_{sq} , and mutual inductance, M_{sq} . Transfer functions are explained in text.

Any magnetometer will be characterised by the dimensionless total flux-transfer function Γ or the magnetic moment-to-voltage coefficient $[S] = \frac{Am^2}{V}$ or $10^3 \frac{emu}{V}$

$$\Phi_{in} = \prod_{i=1}^N f_i \cdot \Phi_{sq} = \Gamma \cdot \Phi_{sq} \quad (4.12)$$

$$V_{sq} = \frac{G^n(a, z_0) V_\Phi}{\Gamma \cdot \Phi_0} \cdot \mu = \frac{1}{S} \cdot \mu \quad (4.13)$$

$\Gamma \propto f_{sq} > \frac{L_{sq}}{M_{sq}} = \frac{651nH}{10.3nH} \simeq 65$ is the lower threshold for the Two-Stage SQUID.

4.2.3 Sources of poor SQUID magnetometer performance

The SQUID response is very sensitive to all kind of interference that may hamper the performance and the sensitivity. The gradiometer, the flux transformer and the shielding can be highlighted as the most critical bits in the design. Flux jumps or drift signal may be observed in the SQUID output as a sign of poor performance. Flux jumps take place when the FLL temporarily loses the lock and is recovered at a different quantum level. A low signal-to-noise ratio or a bad shielding from external interference facilitate these output voltage jumps. At low frequency or even at the static performance, jumps are normally caused by trapped fluxons inside the SQUID or the flux transformer and gradiometer circuit. Critical current fluctuations in the Josephson junctions can also be the source of these jumps smaller than one quantum flux. The causes of the output voltage drift may be different. Thermo-electric effects in the SQUID electronics or a poor cryogenic temperature stability are possible sources of drift. External interference, such as the Earth's magnetic field, power-lines or any kind of electronic devices, the mechanical noise from the cryocooler or any moving part are easily detected by the SQUID. Signal-to-noise ratio is dramatically affected by these issue and may easily hinder the measurement of the magnetic moment.

Among the solutions for these issues, the superconducting circuits may be reset by thermal cycling to above T_c and back to remove trapped flux. It makes necessary to install heaters in all the superconducting circuits used to measure or transfer the flux from the sample space to the SQUID. The integrator in the electronics can also be reset if electronics are unable to feedback the SQUID. Gradiometers will remove the static fields and will reduce the effects of those external fields who temporally change at the sample space. If the compensation coils are not well balanced, in other words if the pickup coils are not built symmetric or if their effective area are not the same, a noise signal will be coupled to the SQUID.

Adequate shielding is another solution crucial to achieve a good magnetometer performance. In this work two magnetic shieldings were used. Firstly, the whole setup: SQUID, flux transformers, gradiometers and wires require a superconducting shielding. The SQUID is shielded by a Niobium cylindrical can and layers of malleable Lead were used to shield the rest of the equipment. In type-II superconductor, such as Niobium, the magnetic flux may cross through the magnetic vortices that are formed under an applied field. Experiments have demonstrated that the SQUID performance improves when it is wrapped in Lead (type I). High permeability material are used as a second magnetic shielding, Mu-metal, Metglas sheets and CuNi tubes were tested at low temperature as candidates. More details of shielding materials and properties are given in Sec. 4.4.4.

As the setup uses moving parts, both motor and drive amplifiers generate electromagnetic noise that must be damped by locating them as far as possible away from the SQUID sensor. To use cable with braided shields and ground all the wiring via a low resistive path to the main ground will improve the rf shielding. The fridge cans are also a natural shield. They were wrapped in Metglas to isolate the fridge from external magnetic fields.

4.3 First Prototypes

To analyse the magnetic shielding; the signal filtering; and the SQUID performance, no few tests are required and the cooling/warming time of a dry dilution refrigerator is unsuitable in the time scale of this project. In order to speed up these experiments, the probe sketched in Fig. 4.8 was built for quick tests in a Helium dewar.

The design consists of a long and thin-walled hollow tube with a retained ring to fit into a Helium dewar inlet and a KF-25 vacuum flange on the top to attach the SQUID room-temperature electronics and pump the probe out. The tube includes a thin rod to clamp the SQUID case at the bottom with flow retained rings that

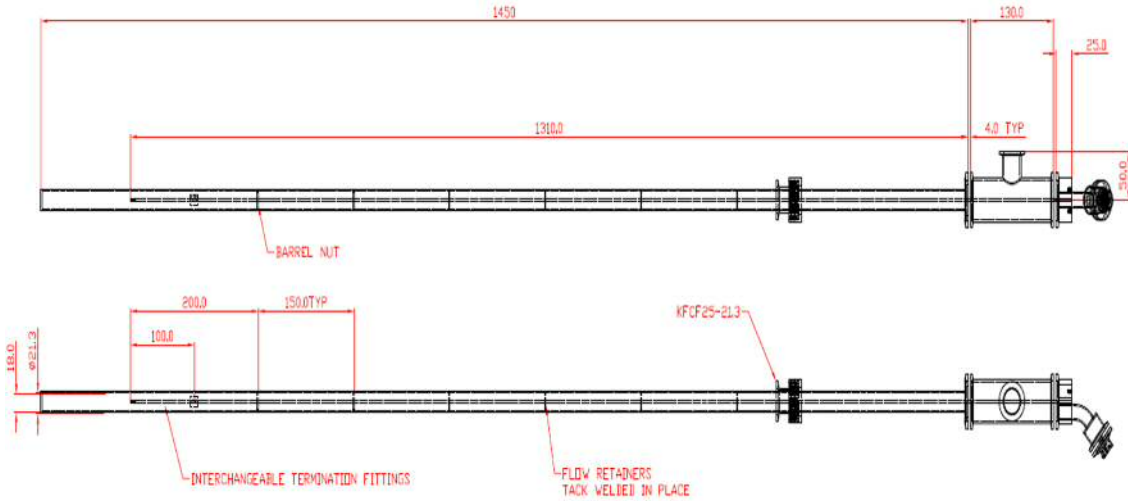


Figure 4.8: Design of the probe used to test the first prototypes. It includes an internal rod to fit the SQUID at the bottom and a KF-25 flange to fit the probe to the Helium dewar.

helps to thermalise the SQUID cables. This setup allows to cool down the SQUID and any FT connected to it to 4 K in a matter of minutes.

Different magnetometers and/or configurations were built to test the SQUID performance. The study intends to obtain information about: gradiometer shape effects, performances of different order gradiometers, how to optimise the FTs fabrication, how to connect superconducting circuits, distance effects in the coupling via the mutual inductance and the shielding required for a good SQUID performance. A resistive Copper coil was used as a sample coil (SC). It will behave as a magnetic dipole when a current is applied $\mu=IAN$ to test the gradiometers. A is the effective coil area and N the number of turns. Findings of this investigation are summarised for five gradiometers made of NbTi wires of 125 μm diameter schemed in Fig. 4.9. A $\phi=2.5\pm 0.5$ mm diameter SC with N turns will induce an input flux Φ_{in} in the gradiometers formed by single loops of diameter $A=7\pm 0.1$ mm that will be directly or indirectly coupled to the SQUID as shown the scheme in Fig. 4.7. *1st planar* and *1st cylindrical* are first-order gradiometer with planar and cylindrical geometry directly connected to the SQUID (purple line). For the other designs, a cylindrical second-order gradiometer were indirectly coupled by using a FT. The

current in the gradiometer flows through an extra loop inductively coupled to another single loop ($a=2.5\pm 0.5$ mm). This loop is part of a second circuit (brown line) screwed to the input SQUID coil (L_{sq}). 2^{nd} FT1 and 2^{nd} FT3 are formed via concentric loops, but the gradiometer circuit is closed in a different way. CC1 closes the circuit by stripping and twisting the wires, a superconducting foil improves the contact. CC2 screws the wires into a Lead pad in a similar way that the SQUID Niobium pads. 2^{nd} FT2 tests the effect of the distance in the mutual inductance by separating the coils $d=5$ mm. Twisted pairs (TP) lengths are needed for the flux-transfer function, f_i , calculation.

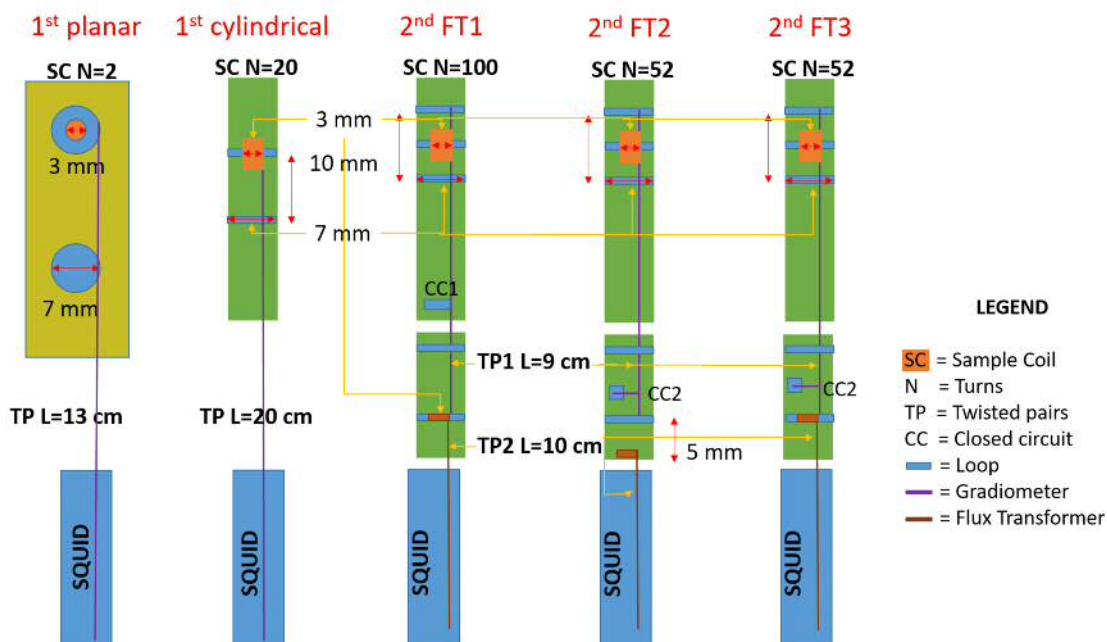


Figure 4.9: Scheme of 5 gradiometers tested in the Helium dewar. Description in text.

Table 4.1 includes the given name for later discussion, the gradiometer order, shape, the mutual inductance, M and the flux-transfer function, f_i calculated according to Eq. 4.10. f_i column in the table has two values for gradiometers with a FT, the first one is for the FT itself and the second characterises the circuit connected to the SQUID. The final design detailed in Sec. 4.4 and built to operate in the Dry Dilution Fridge is included. For gradiometers with FT, errors are calculated for

$a=2.5 \pm 0.5$ mm. M is also highly dependent of the FT distance d that is the main source of uncertainty in the final design transfer functions.

Table 4.1: List of the gradiometers tested in the Helium Dewar and their main features. It includes the mutual inductance and the FT flux-transfer functions, f_i .

Name	Order	Shape	FT	M	f_i
1st planar	1	planar	No	-	75 ± 2
1st cylindrical	1	cylindrical	No	-	82 ± 2
2nd FT1	2	cylindrical	1	1.4 ± 0.9	$200 \pm 80 / 71 \pm 2$
2nd FT2	2	cylindrical	1	0.14 ± 0.08	$1600 \pm 900 / 70 \pm 2$
2nd FT3	2	cylindrical	1	1.4 ± 0.9	$200 \pm 80 / 71 \pm 2$
Final Design	2	cylindrical	2	8 ± 2	$32 \pm 8 / 11 \pm 2 / 74 \pm 1$

4.3.1 Gradiometers response and discussion

Saturated SQUID output voltage, random flux jumps or lack of repeatability revealed the need to introduce a double magnetic shielding for all the superconducting circuits and the SQUID. They will consist of an inner superconducting case: Lead foil for the flux transformers and gradiometers; Niobium shield for the SQUID; and Pb/Sn tubing made from rosin-core solder for the superconducting twisted pairs. A second shield with a high permeability material was used for the whole setup. Mu-metal and the more malleable Metglas foils meet the needs as high-permeability shielding.

Firstly, the frequency response of four gradiometers and the bare SQUID were measured via an oscilloscope (Fig. 4.10). The output flux is calculated by V_Φ obtained from Fig. 4.5. The frequency response is linearly constrained by the slew rate. The flat response at low frequencies is explained in the following way. The sample coil used to calibrate is fed by a function generator whose maximum output voltage is 5 V, below few kHz the slew rate does not limit the SQUID readout up to 5V. To confirm the slew rate constraint at low frequencies, *1st cylindrical* gradiometer may produce higher magnetic fluxes with less applied current to the sample coil as it is made of more turns, N , and the transfer function, Γ is relatively low. Good

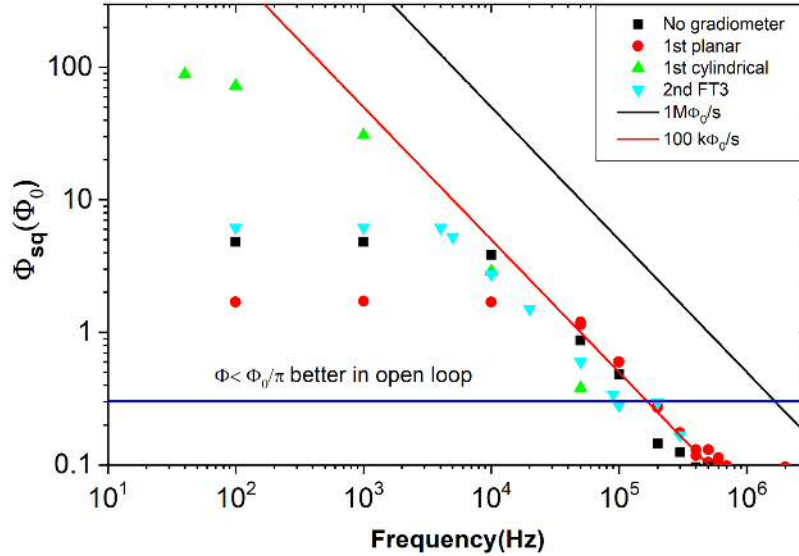


Figure 4.10: Frequency response of the bare SQUID and some of the gradiometers tested. A Copper coil is used to produce an input magnetic flux, according to Eq. 4.4. The voltage-to-flux coefficient relates the readout voltage to the SQUID flux, Φ_{sq} .

linearity is observed up to $\Phi_{sq} = 50\Phi_0$ but the slope changes above that value. That is explained by the SQUID electronics. Maximum SQUID readout is $10 \text{ V} \simeq 5\Phi_0$, to measure higher fluxes the FLL circuit needs to be modified to medium or low sensitivity configuration to reduce V_{Φ}^{high} 10 or 100 times respectively. The low sensitive configuration seems to have a $V_{\Phi}^{low} < 100 \cdot V_{\Phi}^{high}$. A different calibration will be needed for the low sensitivity configuration in case it was used.

At high frequency, the slew rate is the cause of the signal drop. All the gradiometers have a similar response to the the bare SQUID (black squares). It means that the superconducting wires attached to the input SQUID do not add any extra constraint to the frequency response. The slew rate is determined from the maximum peak-to-peak applied flux at which the SQUID FLL is able to remain lock. The flux rate can be evaluated as $SR=2\nu\Phi_{max}$ when a triangular signal with frequency ν is applied [21]. The expected slew rate of $1M\Phi_0/s$ and a more realistic $100 K\Phi_0/s$ that fits the data at high frequencies is included. For $\nu > 10^5 Hz$, only

signals lower than the open loop threshold were able to be locked. Signals above MHz were measured in the flux-locked mode but the slew rate limits the dynamic range below $\Phi < \Phi_0/\pi$. Hence, the open loop operation is recommendable at high frequencies since it was found to be more stable.

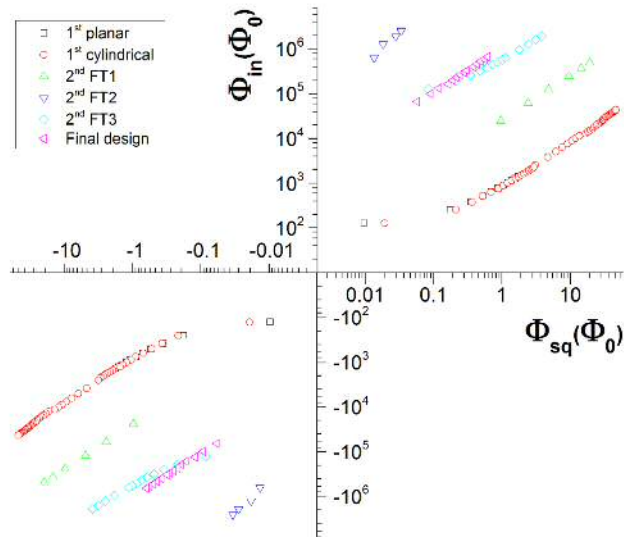


Figure 4.11: DC linear response of the gradiometers. Φ_{sq} higher than $5 \Phi_0$ are obtained changing the SQUID sensitivity via the FLL circuit. Linearity changes for output fluxes lower than $0.1 \Phi_0$ and higher than $5\Phi_0$.

To analyse the gradiometer quality, the flux-transfer function can be measured from Fig. 4.11. The input flux is calculated from the SC magnetic moment by using Eq. 4.7. The tests shed some light into the main problems related to the gradiometers and the flux transformers. Good linearity is obtained in all of them in the intermediate range but they fail at output fluxes below $0.1 \Phi_0$. The slope also changes for fluxes higher than $5 \Phi_0$ where FLL resistance is changed to reduce the sensitivity and measure larger signals. The former is a clear evidence of a faulty shielding that produces small SQUID jumps, mainly observed at low signals. The later is probably related with the electronics in the FLL. Both issues might be by-

passed with an appropriate measurement protocol. To use a large linear travel motor would allow to move the sample in and out of the gradiometer, or from the positive to the negative coil several times removing the spurious signals linked to the SQUID jumps. A calibration for each FLL range might sort out the different linear response.

Table 4.2: Measured and calculated transfer functions, moment to flux coefficients (according to Eqs: 4.12 and 4.13) and low and high frequency dynamic ranges for the tested gradiometers. Errors in the measured and calculated transfer functions explained in text.

Gradiometer Flux transformer	Γ_m	Γ_c	Γ_m/Γ_c	$S \cdot V_\Phi$ (emu/ Φ_0)	Low freq. res.(emu)	High freq res.(emu)
1st Planar	740±10	75±2	9.9±1.3	4.4·10 ⁻⁶	10 ⁻³ – 10 ⁻⁹	10 ⁻⁶ – 10 ⁻⁹
1st cylindrical	650±250	82±2	8±3	3.37·10 ⁻⁶	10 ⁻³ – 10 ⁻⁹	10 ⁻⁶ – 10 ⁻⁹
2nd FT1	15±6 · 10 ³	14±6 · 10 ³	1.1±0.5	104·10 ⁻⁶	10 ⁻² – 10 ⁻⁸	10 ⁻⁵ – 10 ⁻⁸
2nd FT2	48±15 · 10 ⁶	120±70 · 10 ³	400±200	0.25	10 ² – 10 ⁻⁴	10 ⁻¹ – 10 ⁻⁴
2nd FT3	48±18 · 10 ³	14±6 · 10 ³	3.5±2	1.97·10 ⁻³	1 – 10 ⁻⁶	10 ⁻³ – 10 ⁻⁶
Final Design	581·10 ³	26±10 · 10 ³	22±10	3.47·10 ⁻³	1 – 10 ⁻⁵	10 ⁻³ – 10 ⁻⁵

The flux-transfer function measured before can be compared with the expected values Γ_c calculated by using table 4.1 values and Eq. 4.12. The table 4.2 summarises the measured and calculated loss, the ratio and the moment-to-flux coefficient $S \cdot V_\Phi$ from Eq. 4.13 for the tested setups. The last two columns estimate the setup resolution for low and high frequency. The low frequency resolution column is the bandwidth where FLL can be used for three different sensitivities that allow to measure up to 500 Φ_0 . The high frequency resolution column includes the range of frequencies in which the slew rate constrains the resolution below the open loop threshold. According to Fig. 4.10 frequencies above tens of kHz are considered high frequencies and open loop operation is recommendable. The lowest resolution is determined by the SQUID noise.

The table reveals an unexpected mismatch between the measured and cal-

culated flux transfer function clearly observed in the ratio $r = \Gamma_m/\Gamma_c$ for all the gradiometers but the *2nd FT1*. r gives an idea of the accuracy of the design as a relation between the measured and the expected voltage for a given error. The error sources are analysed for Γ_c and Γ_m separately. As it was discussed earlier, errors in the FT output diameter causes major changes in M and f_i and therefore, errors in transfer function Γ_c . In setups with FT, errors are almost the half of the measured value. On the other hand, errors in Γ_m are mainly from the sample coils. They have several layers of turns to remain in the point-like magnetic dipole approximation and the error in the effective diameter $\phi = 2.5 \pm 0.5$ is propagated to Γ_m .

Notwithstanding the errors, several conclusions can be obtained. Firstly, mutual inductance is very sensitive to the coils ratio A/a and the distance between them d . Secondly, $r \gg 1$ are observed even in the planar gradiometer where FT are not used and the SC dimensions are more precise. That could be explained by a loss of superconducting current when it is connected to the SQUID. Contact potentials are formed when two different metals are connected (NbTi wires-Nb pad). They can be removed by using AC signals but, AC currents gave similar flux transfer functions. Wire oxidation might be the cause of the resistive joint. The mismatch is negligible for the FT1 where a different joint (CC1) is used to close the circuit. In the other setups, the gradiometer circuits are closed by using a second superconducting material (Lead) that increases the contact area (CC2). FT2 gradiometer is included to visualise the high dependence of the mutual inductance with the distance, d , increasing the errors and the ratio. These experiments provided the know-how to design and built gradiometers. In fact, the low and high resolution of the *2nd FT3* gradiometer matches with the expected features for the final design. Transfer function and ratio r with error bars are plotted in Fig. 4.12 for a better visualisation.

The design of the primary coil or the solenoid that would supply the external magnetic field was tested in the *1st cylindrical* gradiometer. To the setup, previously calibrated with a sample coil, a 25 mm long and 57 turns superconducting solenoid

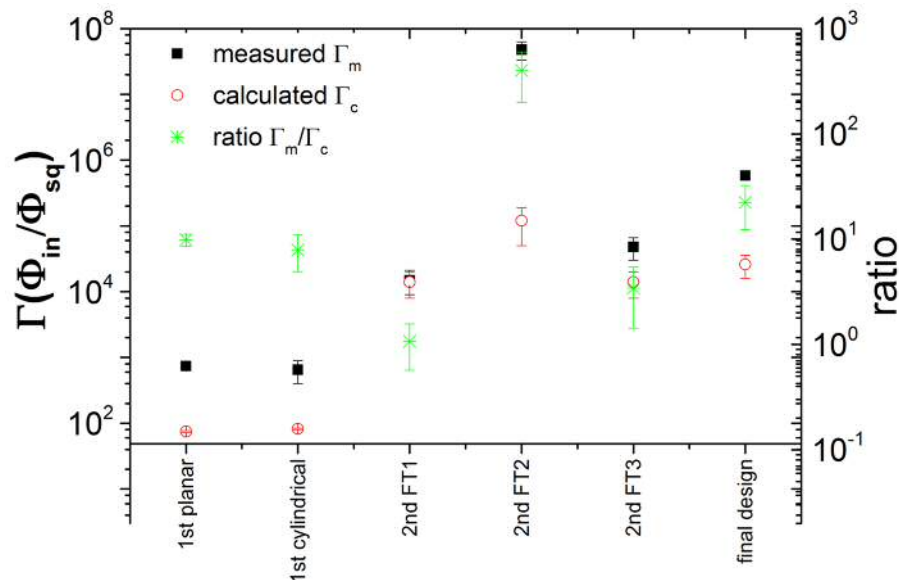


Figure 4.12: Measured (black filled square) and calculated flux loss (empty red circles) for the tested gradiometers. Green stars are the ratio between both values. Calculation method and propagation of the systematic errors are explained in text.

was added to generate a field of 71 G/A. As a testing sample, 9 mg of the fluoride pyrochlore, CsMgCrF_6 was used. In Fig. 4.13 the paramagnetic fluoride behaviour at 4K is observed but, when the sample is removed, a background signal stronger than the sample one remains. This effect is not expected from the diamagnetic coils holder. It might come from a bad alignment of the solenoid and the pickup coils although the asymmetry of the twisted pairs with respect the solenoid might be another cause of the unbalanced coils. For the final design, a solenoid with a larger ratio between the pickup coils and the solenoid length was built and special attention was paid to the twisted pairs quality. Besides, if a differential measurement protocol is used (signal is measured in different coils) background from unbalanced coils will be removed.

Finally, heater resistors were tested to estimate the required heat to warm the superconducting wires above the critical temperature. Heaters are imperative in any superconducting circuits directly or indirectly attached to the SQUID. Trapped flux may easily saturate the SQUID and a quick system to remove it is necessary. The

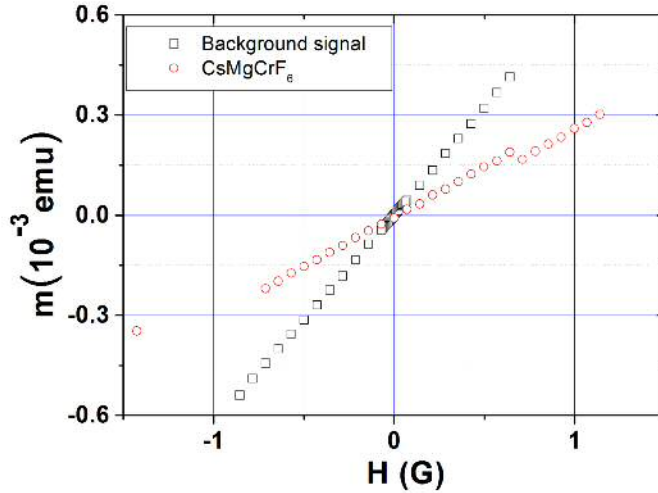


Figure 4.13: Effects of a bad balanced primary coil. CsMgCrF_6 paramagnetic response using a 25 mm long solenoid onto the 1st cylindrical gradiometer and a background signal when the sample is removed.

best way is to warm up the system to the normal state, thus the trapped current will vanish in the resistive wires. As warming up the whole magnetometer takes a long time, a heater that warms up a small amount of the superconducting wires will be enough to deal with the trapped flux.

To test the heater performance, a 60Ω resistor was placed on the top of the twisted wires attached to the SQUID. A triangular test signal of around $1 \Phi_0$ was coupled to the SQUID and different currents were applied to the resistor. Fig. 4.14 shows the current required to remove the flux coupled to the SQUID by warming the superconducting wires. The legend explains the temporal sequence of the events. Before applying the current to the resistor, $t < t_0$, the FLL reproduces the triangular signal. A few seconds after the the current is applied, Δt , the signal is partially decoupled for 50 and 100 mA but only for the higher current is completely decoupled after a longer time (red and green plots). The SQUID response is restored when the current is switched off in both cases (blue and cyan plots). Although, these results are clear evidence of the possibility of controlling the superconducting state of the circuits in a short period of time, it reveals the need to improve the

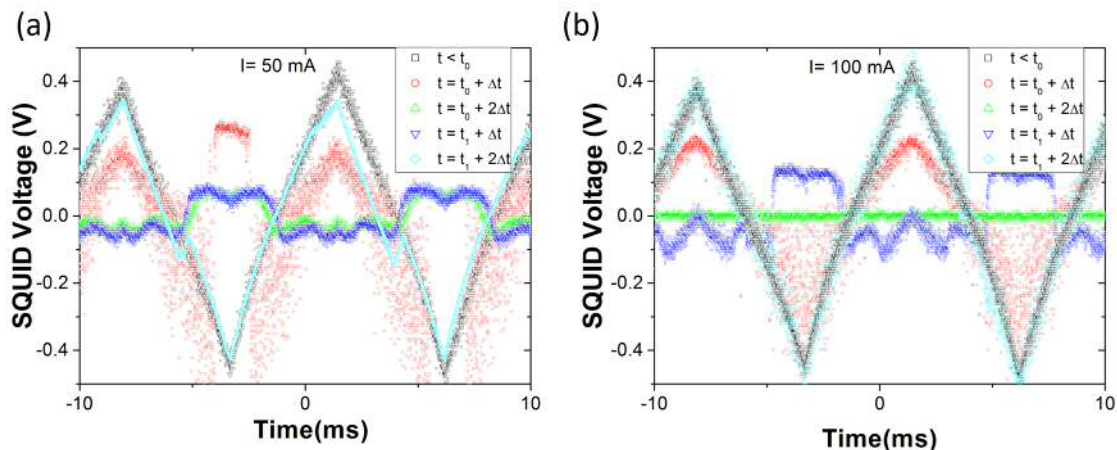


Figure 4.14: Test of a 60Ω heater resistor located over the superconducting twisted pairs with 50 mA (a) and 100 mA (b) applied current. t_0 and t_1 are the time when the heater is turned on and switched off, respectively. Δt is a few seconds lapse.

heat transfer between the heater and the wires. The 100 mA required to heat the wires up corresponds to a Joule heating of 600 mW that would ruin the refrigerator thermalisation if the setup is not thermally isolated or a different configuration that requires less current is implemented.

4.3.2 Noise measurements

Fourier analysis will provide information of the magnetometer threshold but also pinpoint failures in the design. In Fig. 4.15 (a) the amplitude spectral density of the magnetic noise floor is plotted for *1st planar*, *1st cylindrical* and the *final design* gradiometers. Spectrum is obtained from the noise amplitude spectrum $V_n(V)$, the effective noise bandwidth (BW) and the pickup coil effective area A_{eff} .

$$B_{rms}^n = \frac{V_n(V)}{\sqrt{2}\sqrt{BW}} \cdot \frac{\Gamma\Phi_0}{V_\Phi A_{eff}} \quad (4.14)$$

The later result 4.20 of the transfer function Γ is used here for the final design setup. It is seen that the noise floor increases with the length and the complexity of the setup. For the final design setup, a noise floor of $B^n \sim 50pT/\sqrt{Hz}$ was measured at large frequencies ($\nu > 10kHz$). A threshold of magnetic signals that might

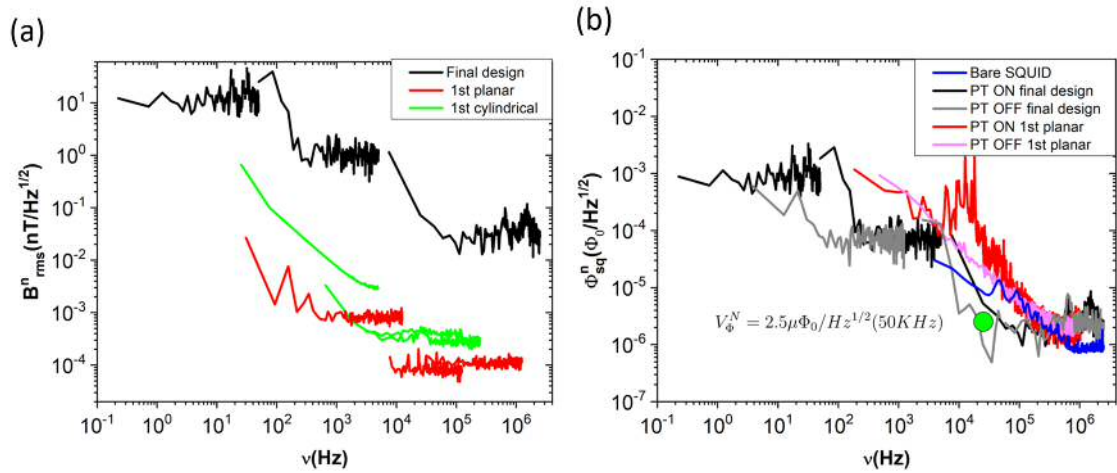


Figure 4.15: (a) Magnetic noise floor spectral density for two testing gradiometers (green and red) and the final design. (b) Effects of the Pulse Tube in the SQUID noise floor in the planar gradiometer (red-magenta) and the final design (black-grey). Bare SQUID noise is included (blue) with the reference noise given by the SQUID manufacturer highlighted by a green circle.

be measurable at those frequencies may be estimated as $B^{thres} \simeq B^n \cdot \sqrt{\Delta\nu}$. For the frequency resolution of that particular spectrum, $\Delta\nu = 2.5kHz$, fields $B^{thres} > 3nT$ might be detectable as it is sketched in Fig. 4.16. Similar thresholds were obtained for the the other range of frequencies.

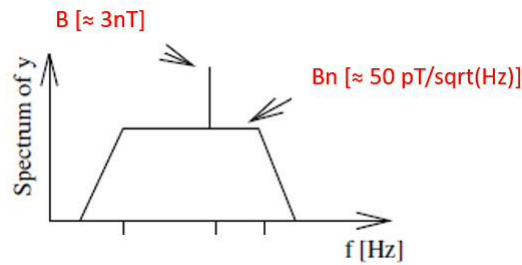


Figure 4.16: Sketch of a magnetic field spectrum consisting of a measurable signal in the order of nT in a noise spectrum of $pT\sqrt{Hz}$.

On the other hand, the spectral density in the SQUID magnetic flux was also investigated. Note that this spectrum is the frequency analysis of the noise floor in the pick coils attenuated by the transfer function. Fig. 4.15 (b) shows the mechani-

cal noise effects of the Pulse Tube in the gradiometers. The planar gradiometer was tested in a Dry Dilution Fridge with (red) and without (magenta) the PT. A clear effect in the range of tens of kHz is observed. Although the PT thermal cycle works at low frequencies, mechanical resonance produced by the gas expansion might explain the results. In the final design special attention was paid to the magnetometer anchorage and shielding. As a result, FFT with (black) and without (grey) the PT turned on do not show any relevant variation. The minimum flux detectable in the SQUID is estimated in the same way than before, $\Phi_{sq}^{thres} \sim 1m\Phi_0$. Therefore, the linear range of the SQUID ($\Phi_{sq} < \Phi_0/\pi=318 \text{ m}\Phi_0$) will give a dynamic range of at least two order of magnitude.

4.4 Final Design

The SQUID-based magnetometer for operation down to milliKelvin Temperatures was designed and built to work in a Bluefors BF-LD400 Dilution Refrigerator. The removable magnetometer consists of a SQUID flux-to-voltage transducer, a detection coils holder, superconducting magnet to apply field to the sample, a superconducting circuitry to detect and transfer the magnetic flux, a FT box, a sample holder, a moving system to introduce and extract the sample from the detection coils, that includes a stainless Steel shaft and an insulating rod, and a set of tools to monitor, control, shield and thermalise the magnetometer. It includes, among other things, thermometers, heaters and specific materials to thermalise and shield the setup. See Fig. 4.17.

4.4.1 Motion

Two different options were considered to move the sample through the gradiometer. In Piatek's work [7], an Attocube piezomotor that produces a sufficiently small amount of heat and has small dimensions gave a performance summarised in Fig. 4.18. Although the piezomotor velocity may be controlled by the frequency, the generated heat increases proportionally with the speed and more than 1 mW is

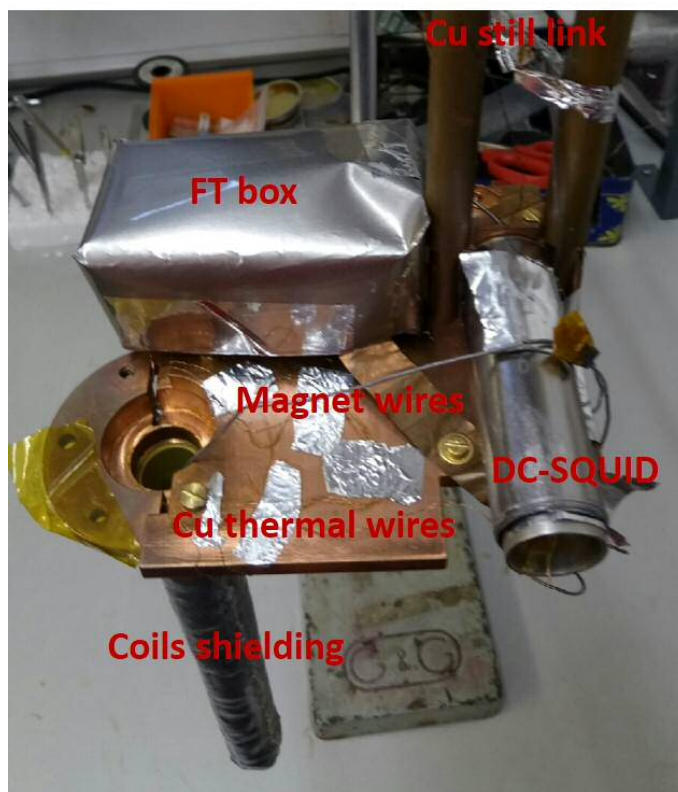


Figure 4.17: Picture of the magnetometer. It includes the Cu rods to thermalise it to the still plate, the dc-SQUID, the FT box and the coils shielded by the Lead can. Coils are thermalised by Cu thermal wires and the magnet wires shielded by Pb/Sn solder.

transferred to the refrigerator at a velocity of $66 \mu\text{ms}^{-1}$. Both the heat load and the speed are unsuitable for this work. The heat load is too high for the refrigerator cooling power ($450 \mu\text{W}$ at 100 mK) and the speed is too slow to move a few millimetres sample in at least 30 mm long gradiometer. Besides these piezomotors are constraint to micrometric movements and the travel range is less than 12 mm.

Instead, an external stepper motor attached to the top of the fridge was the chosen option. Linear movement is measured in 0.254 mm increments on the rotary barrel scale, although a stepper control board was made to control the number of steps, speed and direction by a computer via a USB connection. The long length travel of 50 mm is enough to move the sample in and out of the pickup coils and the speed may be tuned from tens of micrometers to millimetres per second. A Variohm

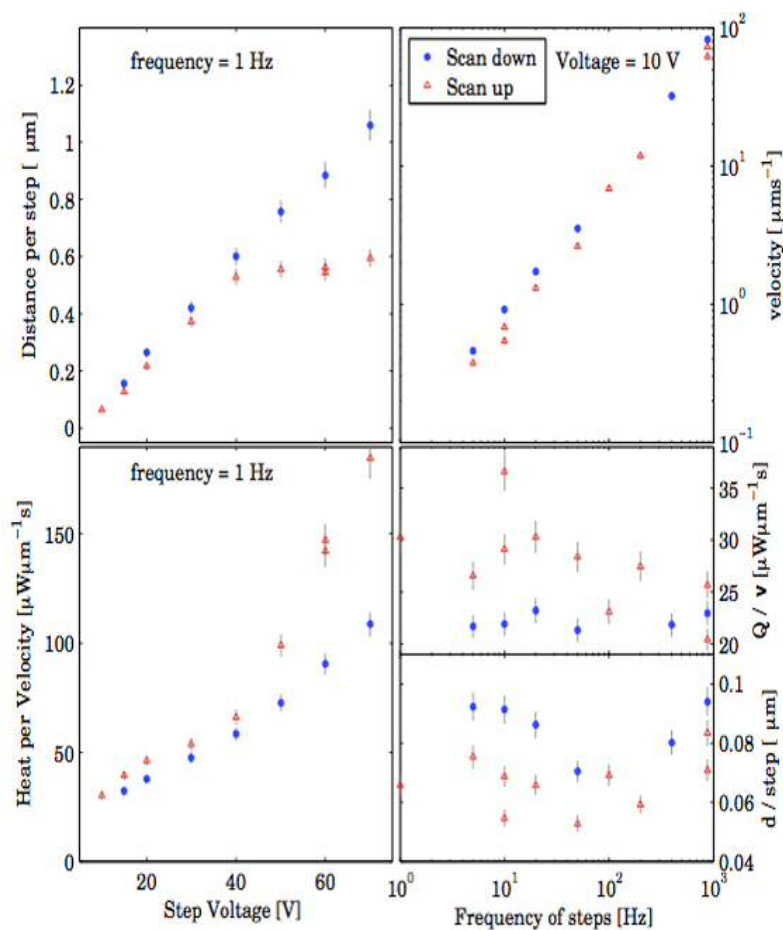


Figure 4.18: Attocube piezomotor performance in a dilution refrigerator taken from [7]. Distance per step, velocity and heat generated for several frequencies and voltages of the saw-tooth profile. The heat generated is measured for a $1\mu\text{ms}^{-1}$ velocity.

IPL linear sensor clamped to the stepper motor will assure the exact position of the motor. The movement is transferred to the fridge vacuum by means of a mechanical feedthrough. A stainless Steel hollow tube attached to the linear shaft transfers the motion to the sample holder clamped at the bottom end as it is depicted in Fig. 4.19 (a).

The shaft needs to be thermalised in every stage of the fridge to avoid a huge heat load from outside. According to Eq. 4.15 the heat flow in Watts, Q , transferred from the warm to the cold part is proportional to the conductivity of

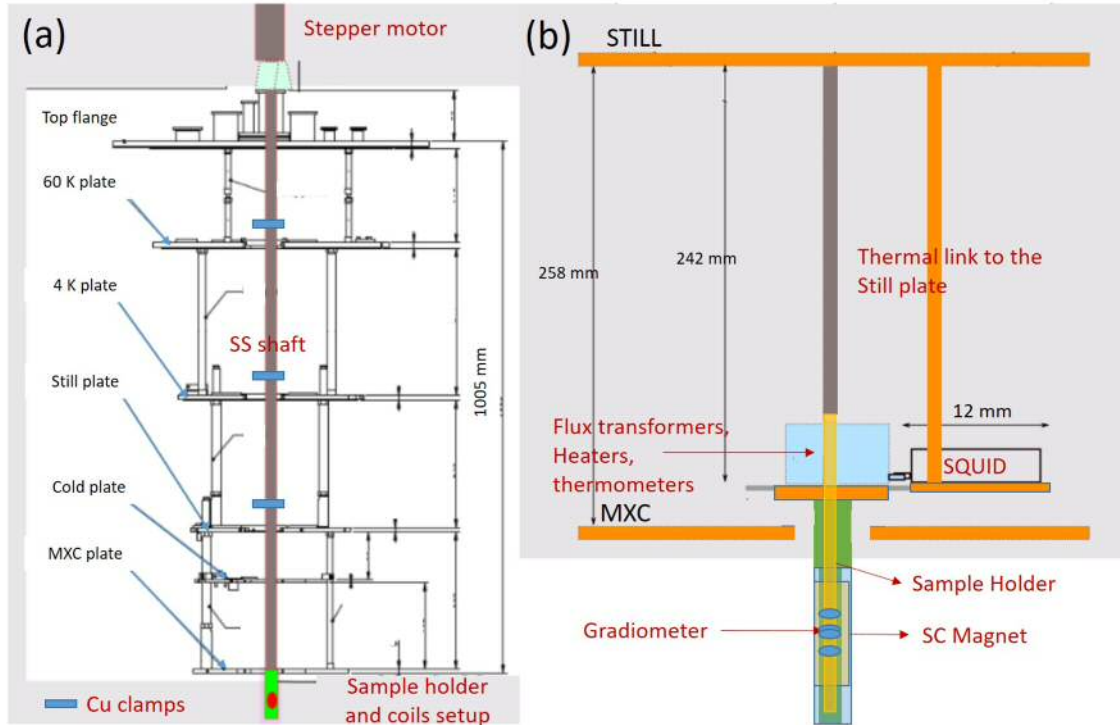


Figure 4.19: (a) Scheme of the dilution fridge with the stepper motor, the stainless Steel shaft is linked to the coils setup at the bottom. Copper clamps are used to thermalise the shaft. (b) Scheme of the magnetometer, thermally linked to the Still Plate. It includes the SQUID, a box with the flux transformers, heaters and thermometers and the coils setup.

the material, k , the cross-sectional area, A , and the temperature gradient, ΔT and inversely proportional to the length, L .

$$Q = k \cdot A \cdot \frac{\Delta T}{L} \quad (4.15)$$

In order to minimise the heat flow, a metal with low thermal conductivity, stainless Steel, but enough to assure the thermalisation was chosen. The area was reduced using a very thin tube (0.25 mm wall thickness), but rigid enough to hold the sample holder. The 12.7 mm outer diameter tube does the job without introducing excessive tilt in the sample movement. Three other measures were taken to reduce the heat flow. Copper clamps were threaded to the Steel shaft, as shown Fig. 4.26, and attached to every fridge plate with Copper braid and thus the temperature gradient

slashed. Multi-layer insulation is commonly used to reduce heat-loss by thermal radiation in cryogenics vessels and dilution fridge. Its malleable nature make it suitable to fill the gap between the shaft and the Copper vacuum flange designed for each fridge plate. The thin sheets behave as a perfect thermal radiation insulator without hindering the motion. The friction heat is low enough not to affect the measurements. A small amount of Steel wool was placed inside the shaft at the height of the plates to avoid radiation along it.

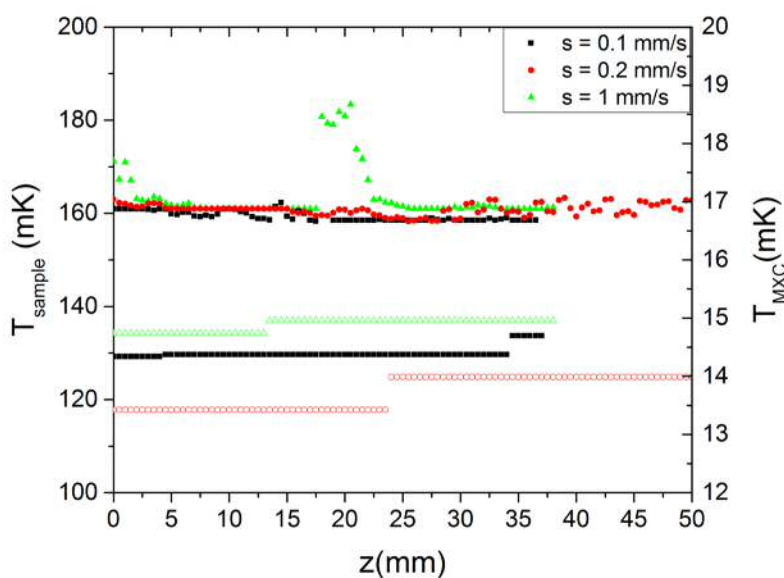


Figure 4.20: Sample movement effects on the sample (full dots) and MXC temperature (empty dots) for three different velocities.

The movement effects on the sample (full dots) and in the MXC temperature (empty dots) were tested for velocities from 0.1 to 1 mm/s as shown Fig. 4.20. Although the sample was not able to thermalise to the mK base temperature of the MXC, the movement does not affect the 160 mK base temperature of the sample.

4.4.2 Detection and excitation coils

As a pickup coil a second-order gradiometer was built to detect the magnetic moment of the sample. The gradiometer was mounted in a hollow cylinder with a

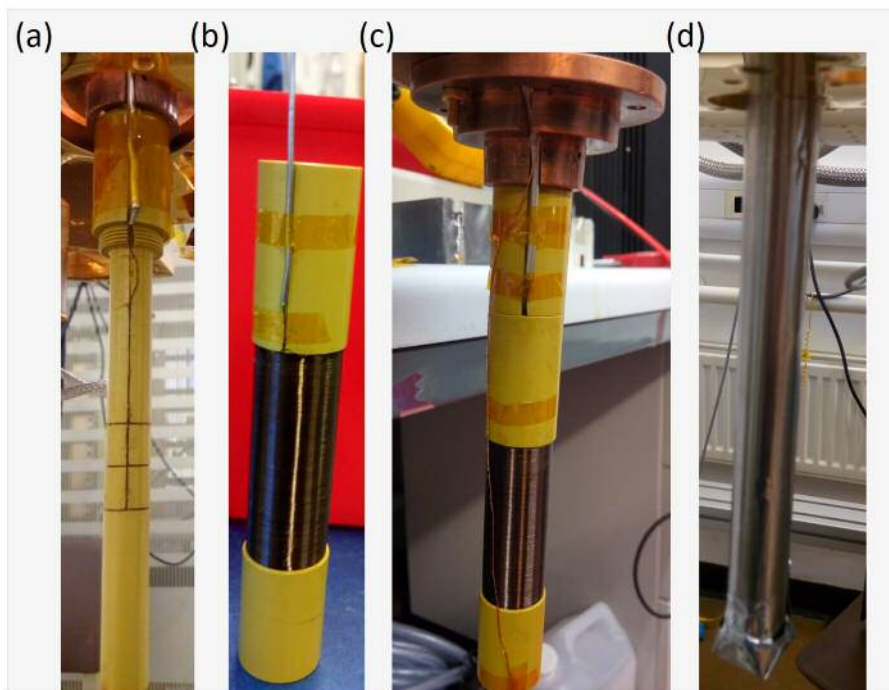


Figure 4.21: From left to right, pictures of the second-order gradiometer (a), the solenoid magnet (b), the primary and secondary coil mounted together and attached to the Cu clamp (c), and the setup with the two magnetic shields (d).

groove to fit the NbTi wires. The coil holder is made of a polyamide-imide known as Torlon. The 150 mm-long and 10 mm-diameter tube is threaded to a round Cu clamp, thermally anchored to the SQUID plate. It includes another thread to place the solenoid magnet. The single loops are spaced out by 10 mm.

A NbTi solenoid magnet was made to apply the magnetic field to the sample. A 50 mm-long and 20 mm-diameter superconducting solenoid provides a 152 G/A homogeneous field. The insulating nature of the magnet and pickup coil holders is counteracted by bare and Oxygen free Cu wires all across them to provide a thermal contact with the well-thermalised SQUID plate. A Lead cylinder and a Mu-metal can, previously annealed to improve its shielding properties, shield the coils from external magnetic fields. The coil holders are long enough to minimise the electromagnetic interference from the upper part that can not be shielded since the sample holder needs freedom to move into the pickup coils. The superconducting

twisted pairs that transfer the signal to the flux transformers box are doubled-shielded by the Pb/Sn solder and a high permeability CuNi tube. The pickup coils, the magnet and the shielding is shown in Fig. 4.21.

4.4.3 dc-SQUID and flux transformers

The Niobium dc-SQUID is thermalised to the still plate as shown Fig. 4.19 (b) to assure a reliable and stable operation. The quasi-static still temperature will avoid drifts in the SQUID working point. The SQUID is clamped to a 5 mm thick Copper plate close to the MXC plate from which two solids Copper rods connect the setup to the still plate. The linking plate includes two long slots that allows some freedom of movement in the final position to control the magnetometer-sample holder alignment.

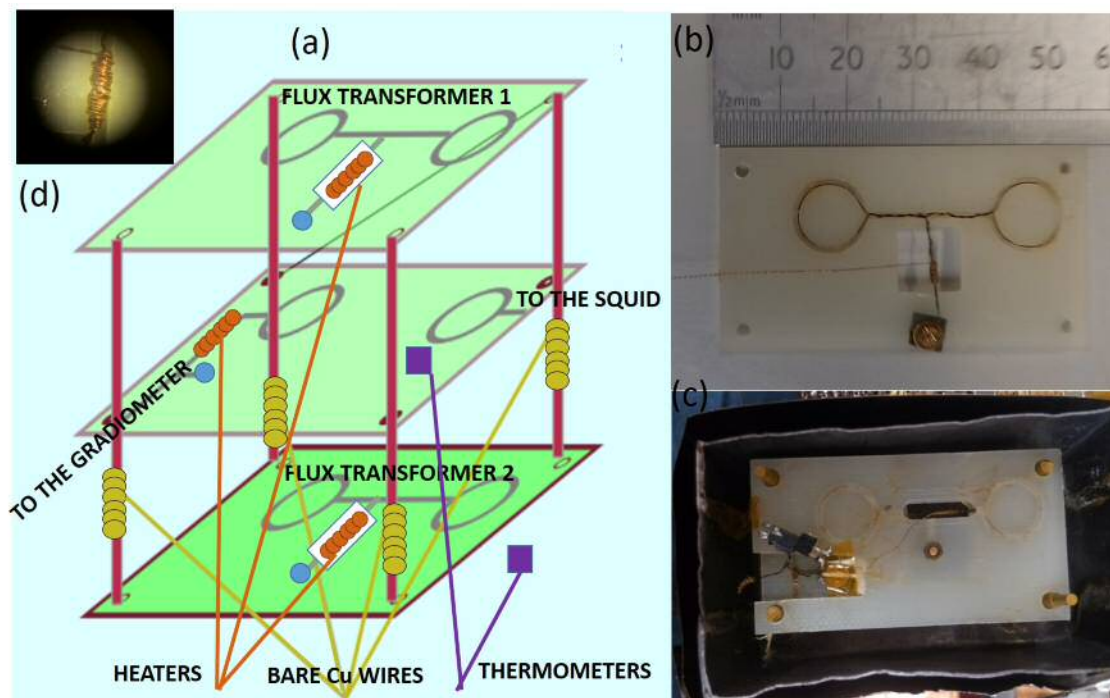


Figure 4.22: (a) Scheme of the flux transformers (FT), including the heaters, the thermometers and the thermalisation wires. (b) Picture of a FT with the heater. (c) Picture of the FT inside the shielding box. (d) A zoomed image of the heater. Details in text.

A NbTi input circuit connects the SQUID to the flux transformer box, whose

scheme is shown in Fig. 4.22 (a). It shows a system of one or two removable flux transformers. Flux transformers consist of two NbTi single loops coupled to the SQUID input circuit and the gradiometer, respectively, via a mutual inductance ($M_j^{i,o}$ for the j FT and the input, i , or the output o loop). The circuit is closed as it described in Sec. 4.3.1 for the FT2/FT3 cylindrical gradiometers. The bare superconducting wires are wrapped on a Brass screw and threaded onto a superconducting Lead pad. The idea behind this configuration is to have a close ($d=1$ mm) and a far ($d=5$ mm) FT with high and low mutual inductance depending on the magnetic moment to measure. Each FT includes a coil heater described in Sec. 4.4.5. For high magnetic moments, the close FT can be removed or disabled by heating it up above the critical temperature. Dimensions of the FT and details of the heater is shown in Fig. 4.22 (b),(d). The FT lies on a G-10 glass epoxy sheets and are fixed by means of four pillars made of Torlon. Heaters are suspended to avoid heating up the whole box. The insulating glass epoxy is thermalised via bare Copper wires wrapped in the pillars and attached to the external plate. The system is located in a double box made of magnetic shields, Lead and Mu-metal , Fig. 4.22 (c), that rests on the Copper plate. The system includes two diodes thermometers in the SQUID plate and in the FT-G10 sheet to investigate the setup thermalisation.

4.4.4 Materials and shielding

To fabricate a cryogenic device special attention must be paid to the selected materials. Table 4.3 summarises the thermal conductivity at 1 K, the electrical resistivity and the volume magnetic susceptibility at 4 K of the materials considered to build the magnetometer.

In terms of insulators the fiberglass G-10, the polyamide-imide Torlon and PTFE were the chosen compounds. As they have similar thermal conductivity and negligible resistivity and susceptibility, they are suitable to isolate parts of the setup. Torlon were used to make the coil holders and the flux transformer pillars since it is easy to machine and its low thermal expansion. G-10 sheets hold the FT and PTFE

Table 4.3: Thermal conductivity at 1 K, resistivity and volume susceptibility of some insulators and metals used in the setup at 4 K. *Depends on purity¹ or grade².* Data taken from [24, 25].

COMPOUND	K_{1K} [$W/(m \cdot K)$]	ρ_{4K} ($\mu\Omega \cdot cm$)	χ_{4K}^V
G-10CR	0.01	–	–
Torlon	$3 \cdot 6 \cdot 10^{-3}$	–	–
PTFE	$2 \cdot 3 \cdot 10^{-3}$	–	–
Sapphire	2-4	–	–
Pure Cu ¹	100-1000	~ 0.04	$-9 \cdot 10^{-6}$
Brass	0.5-0.8	2.88	$-6 \cdot 10^{-5}$
Phosphor Bronze	0.08-0.2	110	$-3.3 \cdot 10^{-5}$
Manganin	0.08-0.1	42.9	$1.3 \cdot 10^{-2}$
Stainless Steel ²	0.04-0.08	50-70	$1 \cdot 2 \cdot 10^{-2}$
Constantan	$< 2 \cdot 10^{-3}$	49.9	4.3

tape is suitable to isolate the sample or to separate the sample from the pickup coil holder.

For wiring, Phosphor Bronze (PhBr), Constantan and Manganin, Cu-Ni and Cu-Mn alloy respectively, are highly suited since they are metals with a relatively low thermal conductivity and a resistivity weakly dependent on the temperature. These properties allow to feed thermometers and heaters without a large thermal load from outside that may ruin the refrigerator thermalisation. The Bluefors fridge includes 35 AWG PhBr wiring down to the 4K plate. Manganin wires were used to connect the thermometers and to make the heaters.

As was mentioned earlier, the magnetic shielding was carried out by double shielding. Superconducting magnetic shield presents zero electrical resistivity below the critical temperature and expels external magnetic fields due to the Meissner effect. Superconducting properties of compounds used for shielding are summarised in Table 4.4.

For the second shielding two compounds with a high permeability were used. Mu-metal is a Nickel-Iron alloy with composition $\approx 75\%$ Nickel, $\approx 15\%$ Iron, plus

Table 4.4: Critical temperature and field of superconductors used in this work.

COMPOUND	$T_c(K)$	$B_c(T)$
NbTi	10	13
Pb/Sn(40/60)	8.5	0.3
Pb	7.3	0.08
Nb	9.5	0.2
Al	1.1	0.01

Copper and Molybdenum that requires annealing to enhance its properties. On the other hand, Metglas are thin and flexible magnetic shielding sheets made of high permeability FINEMET of Hitachi Metals that does not need annealing. Maximum permeability and magnetic flux density at 10 Oe are given in Table 4.5.

Table 4.5: Magnetic flux density at 10 Oe and maximum permeability of the high-permeability materials used.

MATERIAL	$B_{10}(T)$	μ_{max}
Mu-metal	≥ 0.75	≥ 400000
Metglas	1.23	70000

Initially, the field attenuation along the axis of a superconducting and a highly permeable tube with diameter a are similar:

$$B_{axial} \propto \exp\left(-3.832\frac{z}{a}\right) \quad (4.16)$$

According to that, an external magnetic field would be attenuated in a superconducting can of diameter $a = 20$ mm as a function of the ratio z/a as shown Fig. 4.23. The input flux is calculated for a pickup coil area of πr^2 , $r = 5$ mm, and $B_0 = 0.5$ G. The first pickup coil is located around 85 mm apart of the shielding can edge that corresponds to $z/a \sim 4$. The blue line flags the flux-transfer function Γ , i.e, the input flux required to obtain one quantum flux in the SQUID detector. Therefore, the contribution of the Earth's magnetic field to the SQUID signal is lower than $1 \mu\Phi_0$.

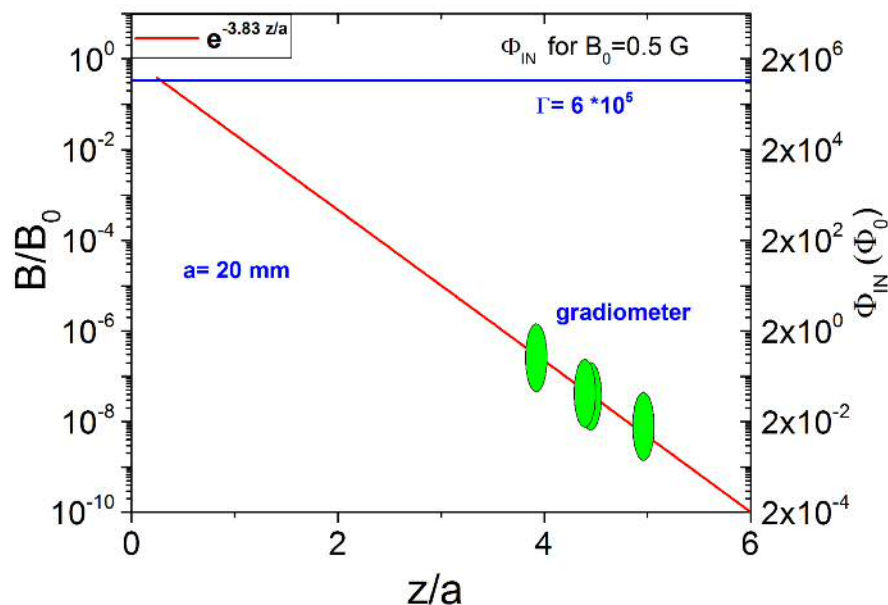


Figure 4.23: Calculation of the axial component of an external field B_0 inside a cylinder shield of diameter a and distance z from the edge. Input flux is calculated for $B_0 = 0.5 \text{ G}$ and pickup coil with 5 mm radius. The blue line is the flux-transfer function. In green, the approximated gradiometer position at $z \simeq 85 \text{ mm}$.

4.4.5 Heaters

To control the setup temperature and remove trapped flux, the solid state resistor, previously tested, was replaced by heating coils made of a high resistance Manganin as shown Fig. 4.22 (d). 100 turns solenoid and $R \approx 20 \Omega$ resistance of $80 \mu\text{m}$ diameter wires were wound onto the superconducting wires. To avoid coupling a magnetic field to the FT, two coils in opposite direction counteract the produced magnetic field. Heater performance is tested in Fig. 4.24 by applying current to the pickup coil and the flux transformer heaters several times. Simultaneously, FT box and SQUID plate temperatures are monitored to detect any heat caused by the heaters. Purple and blue lines indicate the time in which 1 and 2 mA currents are applied respectively. The SQUID output slightly drops from $0.1 \Phi_0$ when 1 mA is

applied to the FT, but 2 mA is required to reduce the output to zero (green triangles). At that time, the superconducting wires are locally heated to the normal state and all the flux is dissipated by the resistive bit of wires. The signal is instantly restored to the initial value when current source is switched off. In a similar way, 2 mA was applied to the pickup coils heater (red circles) dropping the SQUID readout from 0.35 to $-0.07 \Phi_0$ and restoring the signal when current is switched off. Current removes the flux in the pickup coils but, as flux remains in the FT that is connected to the SQUID, the signal detected is not zero. The bottom graph shows how the power, $P=I^2R$, is low enough not to heat the SQUID plate or the FT box as it occurs when higher current is applied. Summarising, Manganin coil heaters were made to remove the superconducting current or trapped flux in all the gradiometer circuits by applying a power of $P \approx 80 \mu\text{W}$ with a negligible impact in the magnetometer temperature. Heaters prevent to warm the whole magnetometer above the superconducting transition with a significant time saving.

4.4.6 Thermalisation at 4K

The setup thermalisation at 4K is measured by three thermometers. One in the SQUID plate, another inside the FT box and an extra one at the bottom of the pickup coil holder. The diode thermometers are able to measure the temperature down to 1.8 K and help to test the different methods to thermalise the setup at the PT base temperature. Thermometers and heaters were thermalised and filtered with a 220 nF capacitor to avoid thermal loads and electromagnetic coupling. Fig. 4.25 (a) shows the required time to reach the PT base temperature. The excessive time to thermalise the gradiometer was decreased by adding high-purity and Oxygen free Copper wires to the magnet and pickup coil holders, clearly observed in Fig. 4.25 (b) where the still and MXC temperature are added. Although the gradiometer or pickup coil thermometer still cools slower as it is placed further away from the SQUID, the whole setup and the fridge reach the PT base temperature simultaneously.

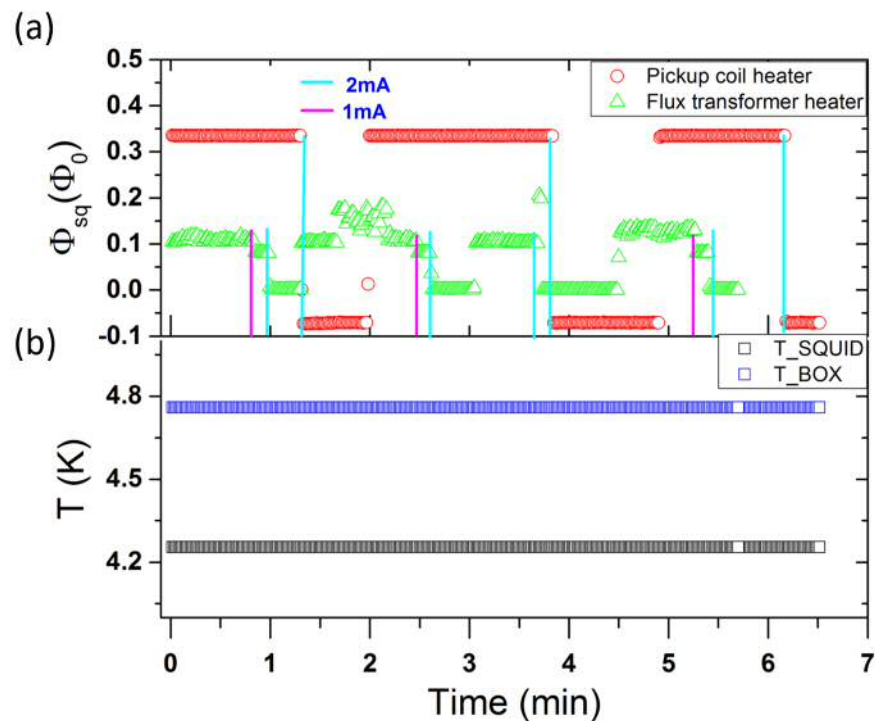


Figure 4.24: (a) SQUID response as a function of time when 2 mA (blue vertical line) and 1 mA (purple vertical line) currents are applied to the coil heaters located in the pickup and the flux transformer circuit. (b) No thermal effects on the SQUID and the FT BOX temperature when the current is applied.

4.4.7 Sample holder: thermalisation, issues and improvements

A sample holder is attached to the SS shaft to move the sample in and out the pickup coil holder. The design must fulfil the following requirements:

- Long enough to avoid the SS shaft touching the 1 K setup when the bottom position is reached.
- Narrow enough not to touch the 1 K pickup coil holder.
- Good thermal links to the MXC plate.
- Room for the RuO₂ thermometer.

For this purpose, a 5 mm wide and 240 mm long Copper strip attached to the SS tube was designed. The sample holder includes the RuO₂ thermometer on

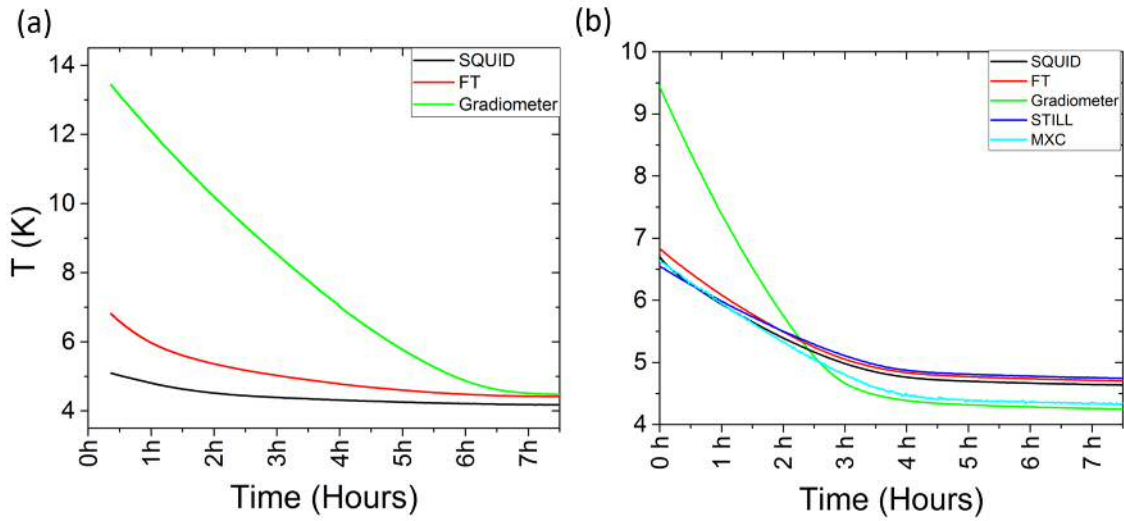


Figure 4.25: (a) Thermalisation to 4 K of the SQUID plate, the flux transformers and the coils holder. (b) Thermalisation after adding high-purity Copper wires to the setup. The Bluefors plates temperatures are added.

the upper part at a sufficient distance from the sample to avoid magnetic effects. The thermalisation was initially addressed by connecting Copper braids from the head of the holder to the MXC plate and the isolation from the coils by gluing a Teflon separator at the bottom of the coil holder. The thermometer and the sample was glued with Ge-varnish. Details of the sample holder can be seen in Fig. 4.26.

First designs revealed issues related with poor shielding. In Fig. 4.27 (a) the position scan of a sample coil throughout the motor range displays an unexpected behaviour. The spacial response of a second-order gradiometer (see Fig. 4.6) experienced a voltage drift. Besides, sample coil currents larger than 10 mA (3 Oe) heated the magnetometer up. Issues related with electromagnetic coupling to the SQUID when the field is applied to the magnet were also found. Fig. 4.27 (b) shows how the initial values of the spatial scan depends on the applied field. The fact that the failures disappear by resetting the SQUID (warming it to the normal state for few seconds), is an evidence that the coupling only affects the SQUID and was easily removed by wrapping the SQUID case with extra layers of Metglas shielding.

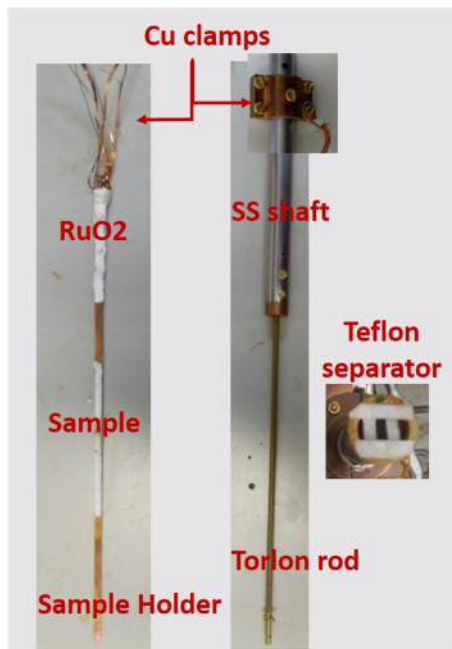


Figure 4.26: (Left) Copper sample holder. It includes the RuO₂ thermometer, the sample and Copper stripes that link it to the MXC. (Right) Stainless Steel shaft to transfer the movement from outside and Torlon rod connected to the sample holder. Details of the Teflon separators at the bottom of the coil holder is included.

Background issues were also observed. An unexpected magnetic behaviour of the stainless Steel shaft is revealed when the sample holder is moved into the pickup coils without any sample. Evidences of magnetic impurities were detected by measuring the magnetization in a PPMS magnetometer. The background was dramatically reduced by shortening the SS tube by around 17 cm and the insertion of a non-magnetic PhBr rod or an insulating Torlon. Finally, the background became almost negligible when the shielding was improved by wrapping the end of the SS shaft and the SQUID with Metglas. Background progress with the different setup is displayed in Fig. 4.28 (a).

The use of different materials to link the SS shaft to the sample holder and to thermalise the sample with the MXC had effects in the base temperature reached. In the setup with the PhBr rod, Copper braid was used to thermal link the sample holder with the MXC. In the one with a Torlon rod, high purity and Oxygen

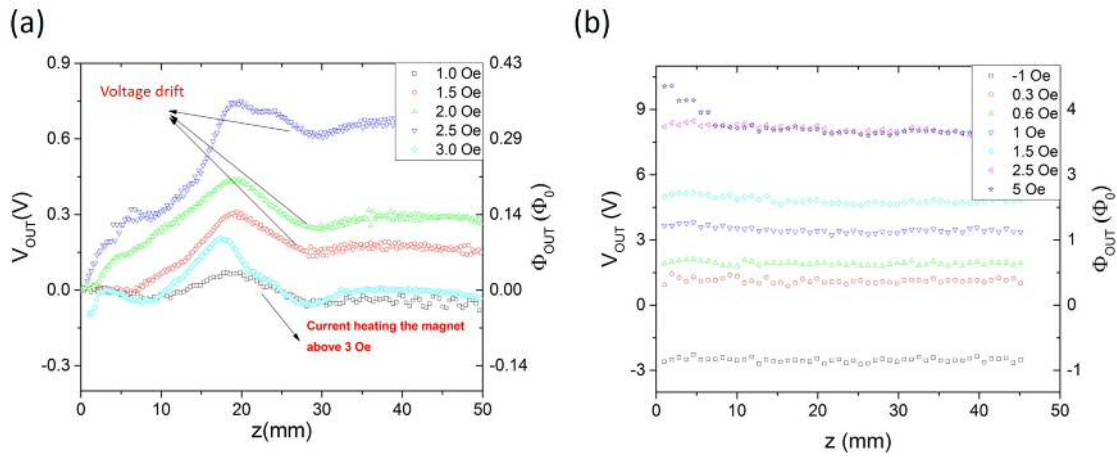


Figure 4.27: Position scan of the sample coil for different fields showing evidences of a faulty shielding. (a) Voltage drift in the SQUID readout. (b) Electromagnetic coupling to the SQUID when field is turned on.

free Copper substituted the Copper braid. Finally, the number of Copper strips were increased and the Teflon used to isolate the sample holder removed because it adds a heat load of around $10\text{-}20 \mu\text{W}$ to the system (in the same order than the cooling power at base temperature). The efforts to thermalise the sample to the MXC are summarised for these three different setups in Fig. 4.28 (b). Both the sample and the MXC base temperature decreased with the updates. MXC temperature between 13 and 26 mK are close to the 8 mK base temperature of the pristine fridge. Unfortunately, the achieved sample temperature is still far away of the MXC temperature. Besides, by removing the Teflon separator and adding extra Copper affects the sample-to-coils alignment as the strips bend the sample holder. Fig. 4.29 shows how the temperature dramatically increased when the position is scanned due to a touch between the sample and the pickup coils holders from 200 to 700 mK.

The following measurements were carried out by using the teflon separator. Future improvements to decrease the base temperature must focus in the sample-to-coils alignment or in a new design with more space between them.

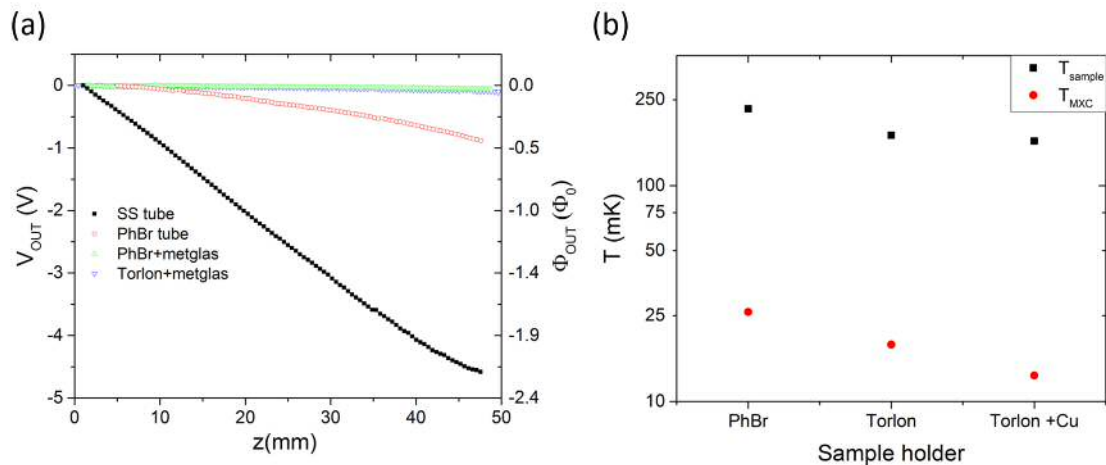


Figure 4.28: (a) Position scan for different setups. Background effects depending on the way to link the SS tube to the sample holder. (b) Sample and MXC base temperature reached by the PhBr and the Torlon rod setup. To the final design, high purity Cu strips were added to improve the sample thermalisation. More details in text.

4.4.8 Automotion

The automotion of the measurement system is achieved by a PC. The PC runs a home-written software, which provides a Labview project with several Graphical User Interfaces (GUI). It contains all the required functionality: setup management, monitoring, measurement and automated sequence execution. The controlled instruments include:

- STAR Cryoelectronics SA632 dc-SQUID and the PFL-102 Programmable Feedback Loop;
- stepper motor drive and the Variohm IPL linear sensor;
- SR830 and SR844 high frequency Lock-in amplifier for AC susceptibility measurements;
- 34460 Agilent digital multimeter for DC measurements;
- Keithley 220 current source to control the heaters;
- 336 Lakeshore Temperature Controller for controlling the diode thermometers;

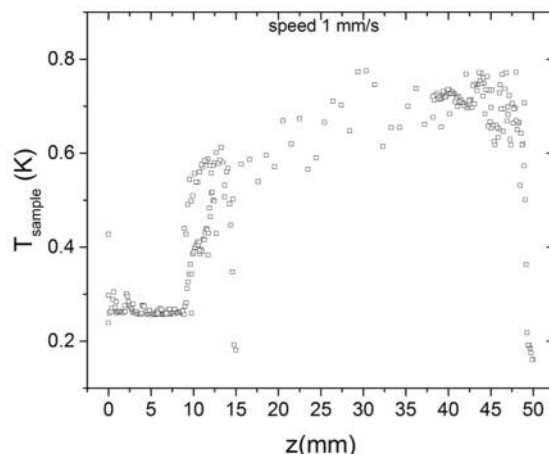


Figure 4.29: Sample temperature when the position is scanned without a teflon separator. A touch between the sample holder and the coils dramatically increased the sample base temperature.

- Picowatt AVS 47 resistance bridge for the RuO₂ sample thermometer,
- Internet connection to monitor the Bluefors thermometers;

The project is organised in an Acquisition, a Configuration, Control and Data folders. The first two includes subfolders for DC and AC magnetometry, Thermometry and Resistivity with the “VIs” to carry out these tasks and the subVIs and drivers required for the acquisition, respectively. The common Labview Controls are in the Control folder and the Temperature Logfiles and Data per run are in the Data folder. The code is built following the good coding practices to assure the “dataflow” execution, the readability and the modularity to ease the comprehension and the upgrade of the project by future users. E.g. state machines provide an easy-to-read code that allows to add new functions such as data analysis or scripts to scan temperature and field.

A set of VIs provides freedom to carry out different experiments: DC magnetometry allows to center/calibrate/locate the sample, to measure by DC extraction or by holding the sample in the coils; AC magnetometry gives the option to measure in the extraction or the static mode. In the extraction mode, the sample is moved to the three different coils and the reading done, subtracting the readings

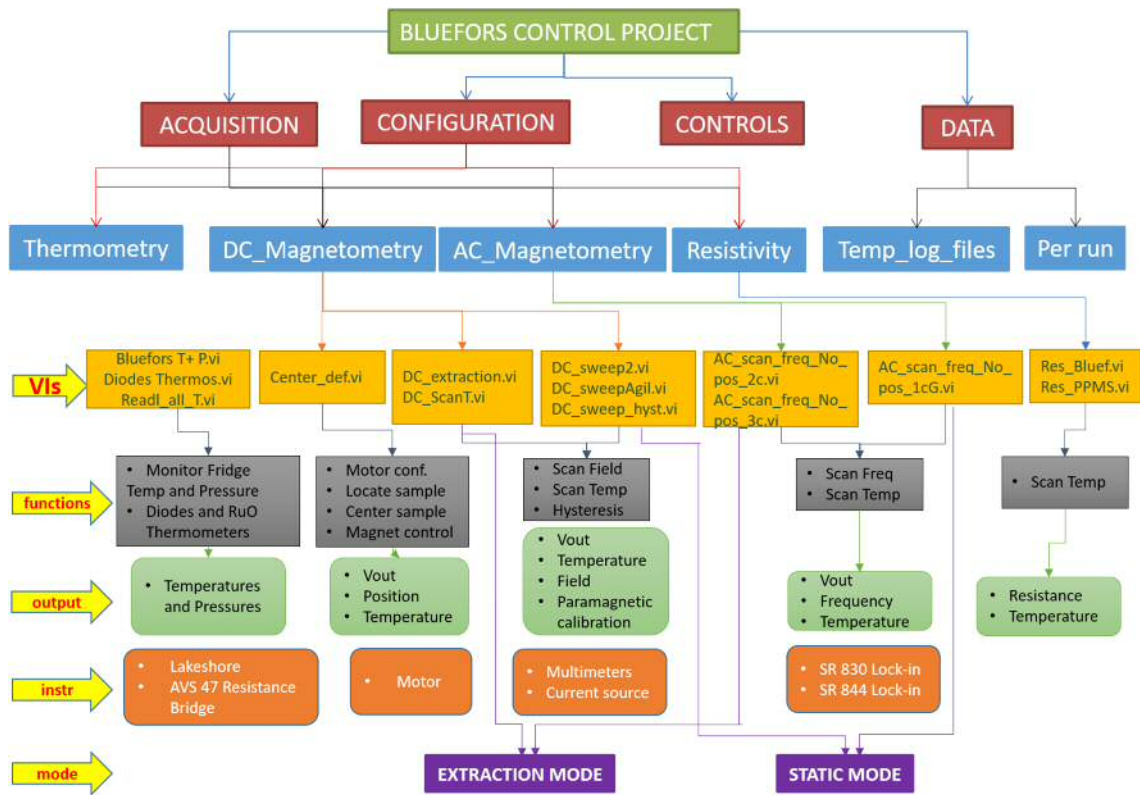


Figure 4.30: Flowchart of the scalable Labview projects to carry out measurements in the Bluefors fridge.

the sensitivity is increased and spurious signals from SQUID jumps or voltage drifts minimised. In the static mode, the sample is fixed in the main pickup coil and the frequency or the temperature scan. This method is less accurate as it is affected by the SQUID jumps but recommendable for ultra-low temperatures or sample with hysteresis behaviour as the sample movement below 100 mK will affect the sample temperature. The flowchart in Fig. 4.30 depicts the project organisation, including the folders, the VIs with their functions and output parameters and the instrument that they control. Two specific screenshots of a DC and AC GUI of the Labview project is shown in Fig. 4.31.

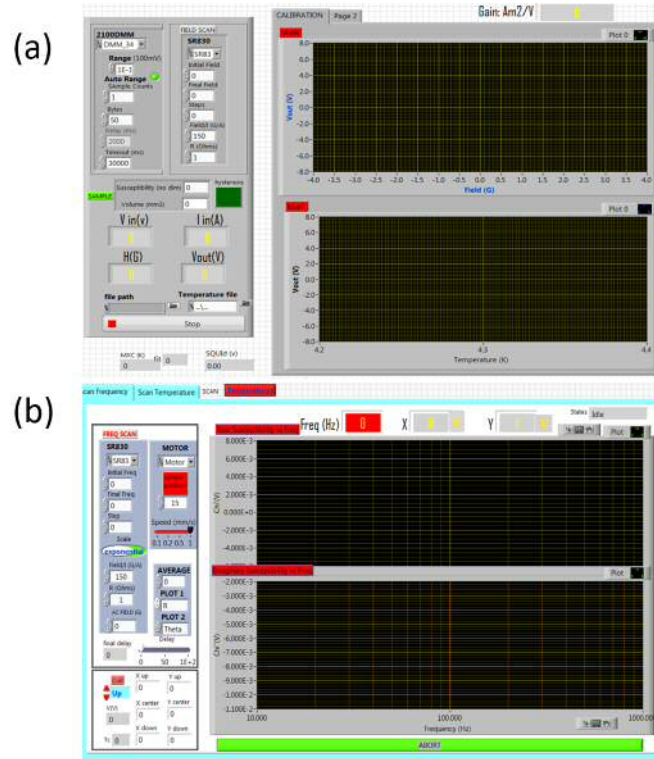


Figure 4.31: Screenshot of a DC (a), and AC (b) data acquisition GUI. DC protocol includes field and temperature scan option and gain calibration. AC protocol includes frequency and temperature scan in the extraction mode.

4.5 DC Calibration

Two different methods were used to calibrate the magnetometer. A Copper solenoid that simulates a sample and a real sample that requires an external field to be magnetised. A 8 mm long and 1.5 mm radius solenoid with $N=200$ turns generates a field of $H/I= 312 \text{ Oe/A}$. However, the picture of a localised magnetic dipole $\mu = NIA$, for A the solenoid cross-section and I the applied current is more appropriate. The quality of the second-order gradiometer is tested by scanning the dipole position. Fig. 4.32 shows the position scan at 4 K for different magnetic moments. The signal, centred at $z = 25 \text{ mm}$, is fitted to the expected second-order gradiometer response given by Eq. 4.13

$$V_{sq}(z) = \frac{G^2(5, z) \cdot V_{\Phi}}{\Gamma \cdot \Phi_0} \cdot \mu = \frac{\mu}{S} \quad (4.17)$$

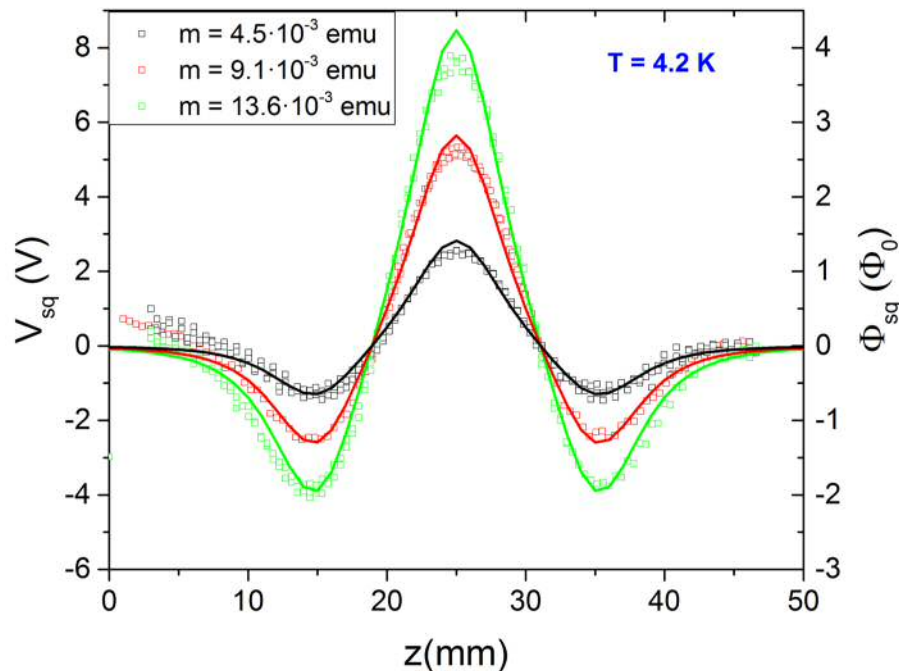


Figure 4.32: Sample coil position scan for different current-magnetic moment at 4K. Fits to the expected second-order gradiometer are included.

The experimental results are fairly reproduced by the fit, but it slightly fails at the tails. A small offset was also added to compensate the observed background. To avoid these calibration issues and to increase the magnetometer sensitivity, the *extraction mode* was used. The measurement protocol consists of measuring the output voltage in the center coil and then in the upper or the lower coil. The voltage subtraction will also remove the effects of trapped fluxes as it is a relative measurement. If the background is not negligible $G^2(5, 15) \neq G^2(5, 35)$, both values may be averaged. Then, Eq. 4.13 is amended to:

$$S = \frac{2}{2V_{sq}(z_0) - V_{sq}(z_0 + d) - V_{sq}(z_0 - d)} \cdot \mu = \frac{\mu}{\bar{V}_{sq}} \quad (4.18)$$

given a moment-to-voltage coefficient $S = (1.1 \pm 0.4) \cdot 10^{-3}$ emu/V and $\Gamma = (380 \pm 140) \cdot 10^3$. The large uncertainty is produced by the propagation of the systematic error in the measurement of the effective radius of the sample coil. The geometry of the coil makes difficult to obtain an accurate measurements of the effective radius $r \simeq 1.5 \pm 0.25$ mm.

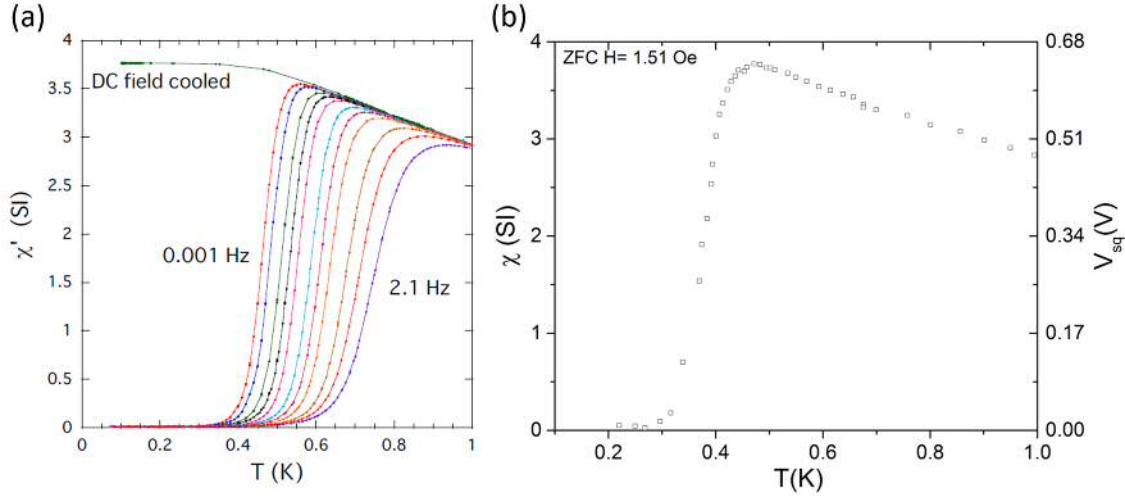


Figure 4.33: (a) Temperature dependence of the DC field cooled and low frequency susceptibility in $\text{Dy}_2\text{Ti}_2\text{O}_7$ taken from the supplementary information of Paulen et al. work [3]. (b) Magnetometer calibration. SQUID voltage in the same sample is measured by cooling in zero field.

As it is discussed in Sec 4.3.1, the sample coil is an useful tool to study the magnetometer performance as a first approximation, but it is not accurate enough. A $\text{Dy}_2\text{Ti}_2\text{O}_7$ ellipsoid used in Paulen et al. work [3] is an ideal sample to calibrate the magnetometer sensitivity and detect thermalisation issues. The highly frustrated pyrochlore freezes to the ground state below 400 mK and its transition temperature depends dramatically on the frequency. The temperature dependence of the susceptibility from Paulsen et al. work and the measured voltage in the magnetometer agrees as it is shown in Fig. 4.33. V_{sq} in the graph is measured following the Eq. 4.18 protocol. To obtain the relation between magnetic moment and the SQUID voltage (S), the maximum voltage \bar{V}_{sq}^{max} is compared with the maximum

susceptibility χ^{max} . Hence, the magnetic moment can be calculated

$$\mu^{max} = \chi^{max} \cdot H \cdot V \quad (4.19)$$

for a volume, $V = (2.4 \pm 0.2) \cdot 10^{-9} m^3$ and an applied field of $H = 1.51$ Oe. It gives a magnetic moment-to-voltage coefficient

$$S = (1.7 \pm 0.1) \cdot 10^{-3} \text{emu/V} \quad (4.20)$$

and a flux transfer function $\Gamma = (580 \pm 30) \cdot 10^3$. Propagation of the volume uncertainty dominates the final error.

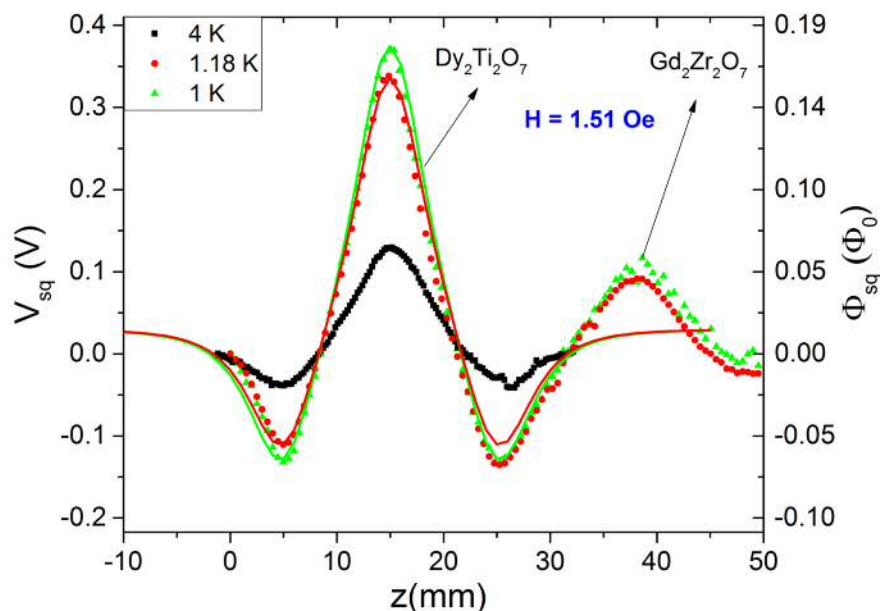


Figure 4.34: $\text{Dy}_2\text{Ti}_2\text{O}_7$ and $\text{Gd}_2\text{Zr}_2\text{O}_7$ position scan at different temperatures. Fits to the expected second-order gradiometer are included.

A new calibration of the gradiometer is carried out by scanning the position. In this case, the sample holder includes the $\text{Dy}_2\text{Ti}_2\text{O}_7$ ellipsoid and a $\text{Gd}_2\text{Zr}_2\text{O}_7$ powder sample, another frustrated pyrochlore oxide. Fig. 4.34 shows the position scans at different temperatures for an applied field of $H = 1.51$ Oe. Samples are located at $z = 15$ mm and at $z = 37$ mm, respectively. The different between the voltage at the upper and the lower coil justifies again the measurement protocol

that will be used in further measurements.

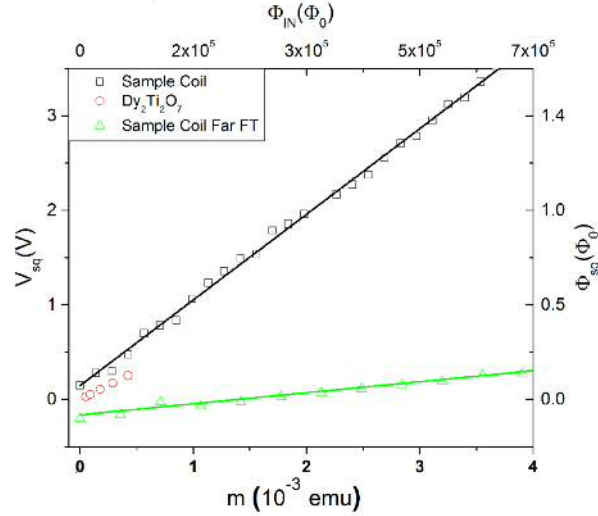


Figure 4.35: Magnetometer calibration using a sample coil and the spin-ice $Dy_2Ti_2O_7$ as described in text.

A third calibration was made with the same sample coil by separating 5 mm the FT. The calculated mutual inductance changes from 8 ± 2 nH to 2.2 ± 0.3 nH and Γ_c and Γ_m obviously increase, although the ratio remains in the same order. It brings under the spotlight how sensitive the flux coupling is to the FT location. Regions, where high frequency measurements are feasible ($\Phi_{sq} < \Phi_0$), will be easily reach by modifying the FT position.

Table 4.6: Moment to voltage coefficients, measured and calculated losses and ratios for the calibration sample and the sample coil with the FT in two different positions.

	S (emu/V)	Γ_m	Γ_c	Γ_m/Γ_c
SC	$(1.1 \pm 0.4) \cdot 10^{-3}$	$(380 \pm 140) \cdot 10^3$	$26 \cdot 10^3$	15
$Dy_2Ti_2O_7$	$(1.7 \pm 0.1) \cdot 10^{-3}$	$(580 \pm 30) \cdot 10^3$	$26 \cdot 10^3$	22
SC far FT	$(8 \pm 3) \cdot 10^{-3}$	$(2.9 \pm 0.9) \cdot 10^6$	$220 \cdot 10^3$	13

Calibrations are compared in Fig. 4.35 at 4 K and the main parameters summarised in Table 6.3. Discrepancy between the sample coil and the spin ice pa-

rameters with the same setup falls in the limit of the systematic errors. However, more precise measurements of the effective radius and the pyrochlore volume will clarify if the mismatch is due to systematic errors or there are other causes. For instances, an induced current in the pickup coils from the magnet might contribute to modify S in the real sample but not in the sample coil. The flux loss ratio Γ_m/Γ_c is consistent with the Sec. 4.3.1 results and supports the assumption of current loss in the superconducting junctions.

Corrections due to demagnetizing fields are now taken into account. The ellipsoid shape of the sample gives a demagnetization factor $N_d \approx 0.09$ that results in a demagnetizing field $H_d = N_d M$ for $M = \mu/V$. Hence, Eq. 4.19 should be written as a function of the internal field H_i

$$H_i = H_a - N_d M = \frac{H_a}{1 + N_d \chi_{true}} = H_a (1 - N_d \chi_{meas}) \quad (4.21)$$

defining the true and the measured susceptibility as $\chi_{true} = M/H_i$ and $\chi_{meas} = M/H_a$. In this particular case, the susceptibility data used as a reference in Fig. 4.33 were taken in the same sample with no corrections for demagnetisation effects (as it is specified in the supplementary information). Therefore, the measured susceptibility must be also replaced by the true susceptibility

$$\chi_{true} = \frac{\chi_{meas}}{1 - N_d \chi_{meas}} \quad (4.22)$$

Then it is easy to deduce that

$$\chi_{true} \cdot H_i = \chi_{meas} \cdot H_a \quad (4.23)$$

and no corrections are needed.

4.6 AC Calibration

The high frequency dependence of the AC susceptibility freezing temperature of the frustrated spin ices make them very suitable to investigate the magnetometer

thermalisation. Previous AC susceptibility studies on $\text{Dy}_2\text{Ti}_2\text{O}_7$ can be found in polycrystalline [26–28] and single-crystalline [29–31] samples given a good idea of the expected behaviour.

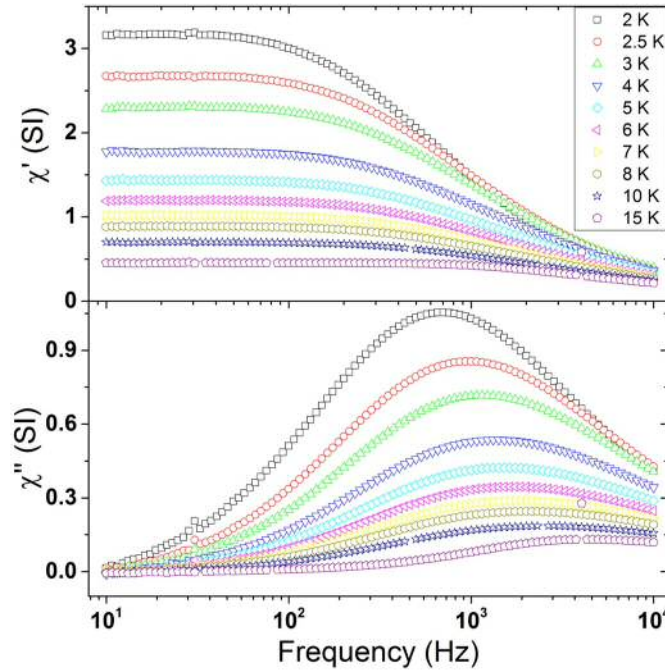


Figure 4.36: Frequency scan of χ' and χ'' of the spin-ice $\text{Dy}_2\text{Ti}_2\text{O}_7$ from 2 K (black squares) to 15 K (purple pentagons).

The AC susceptibility of the $\text{Dy}_2\text{Ti}_2\text{O}_7$ was measured as a function of the frequency, firstly, by a commercial Physical Properties Measurement Systems (Quantum Design PPMS) down to 2 K as shown Fig. 4.36. The real susceptibility increases when the temperature decreases and the transition evolves from tens of Hz to a few kHz from 2 K to 15 K.

Measurements at lower temperatures were carried out in the magnetometer by the extraction method. Fig. 4.37 summarises a set of measurements taken place with the GUI depicted in Fig. 4.31 for different temperatures. Sample thermalisation is investigated by comparing χ'' peaks with the expected values obtained by extrapolating the results from Paulsen et al. [3], that used the same sample, and the Yaraskavitch et al. work [31] (vertical lines). At temperatures of 0.75, 0.85 and

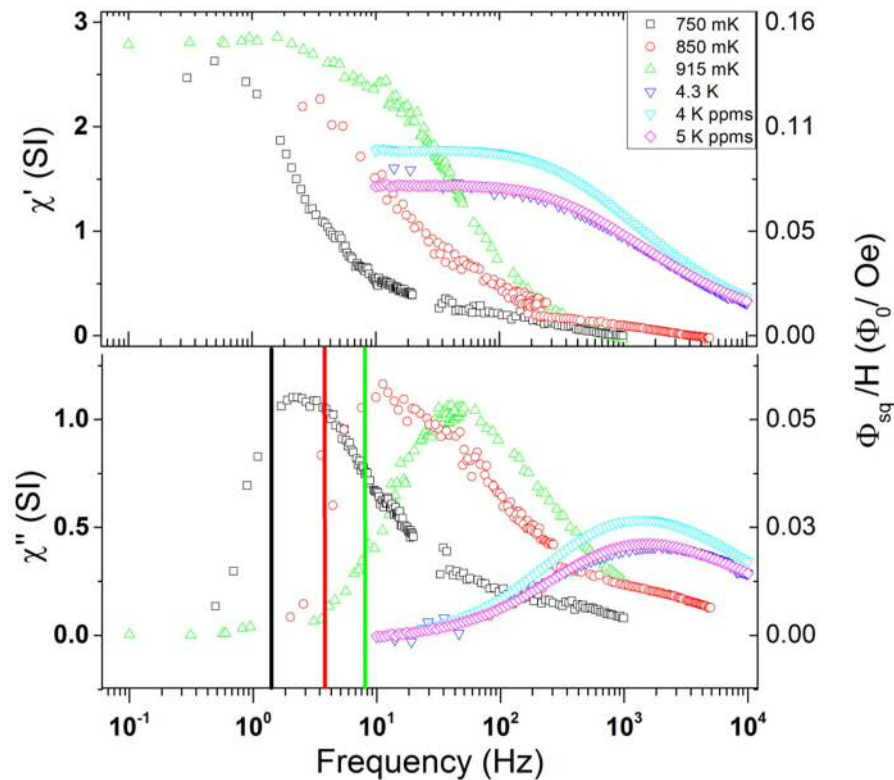


Figure 4.37: Frequency scan of χ' and χ'' of the spin-ice $\text{Dy}_2\text{Ti}_2\text{O}_7$ taken in the Bluefors magnetometer below 1K. Peak extrapolation from reference [3] at the studied temperatures are depicted by vertical lines. High temperature (4.3 K) plot is compared with 4 and 5 K PPMS results.

0.91 K, the transition is expected at $\nu \simeq 1.3, 3.7$ and 8 Hz. However χ'' peaks are observed at 2.2, 11 and 40 Hz, which corresponds to 0.8, 0.94 and 1 K. In this range of temperatures the mismatch between the expected and the measured temperatures increases from 50 mK at 750 mK to 90 mK at 1K. At higher temperatures data are compared with the 4 and 5 K PPMS results, frequency scan of AC susceptibility at $T = 4.3$ K behaves similar to the data obtained at 5 K in the PPMS. In this case, the temperature is measured with the diode thermometer located at the bottom of the coil holder. The large distance between the sample and the thermometer and the low temperature dependence of the transition above 2 K might explain the different values. Regarding χ' , the saturated susceptibility increases when temperature decreases, which is not observed below 1 K. At these frequencies (some Hz) the magnetometer has shown difficulties to have reliable measurements.

These plots are part of an investigation about the measurement methodology and magnetometer performance. Data precision is not ideal and outlier points are common, furthermore, at very low frequencies, there is room for accuracy improvement and the measured transition temperatures disagree with the literature. It sheds light upon the parameters that needs to be controlled in AC susceptometry and how to improve the Lock-in technique used to take data. Some relevant aspects are:

- To measure the susceptibility using the three coils (Up, Down and Center) improves the sensitivity of the gradiometer from $\Phi_{in}/\mu = 229$ to $334 \mu Wb/Am^2$ (Eq. 4.7) and minimises the effects of the background and SQUID jumps.
- Moving parts demands a time delay (that depends on the Lock-in time constant, t_c) before taking data to stabilise the Lock-in readout.
- To average the Lock-in readouts will help to the experimental precision.

The three coils method and a large delay time and averaging will improve the accuracy and the precision of the measurements but also will extend the time span and will give more room for failures, such as temperature drifts or SQUID jumps. The suitable trade-off between those parameters were settled for future measurements.

Another possibility is to scan the temperature at a specific frequency. This method eases the Lock-in performance as t_c , the time delay and averaging may be fixed for the whole run. Fig. 4.38 shows the DC susceptibility and the real and imaginary susceptibility for 1 Hz and 3.1 Hz. Imaginary peaks are fitted to a Gaussian to obtain the transition temperature at 735 and 810 mK. The transition are expected at 750 and 825 mK, which means a mismatch of 15 mK. If frequency and temperature scan methods are compared, the relative error $\Delta T/T \in (6 - 9)\%$ obtained in the former method is reduced to $\Delta T/T \simeq 2\%$ when the temperature is scanned. These results could suggest that scanning the frequencies might heat the system. This is supported by the fact that the higher the temperature, the higher

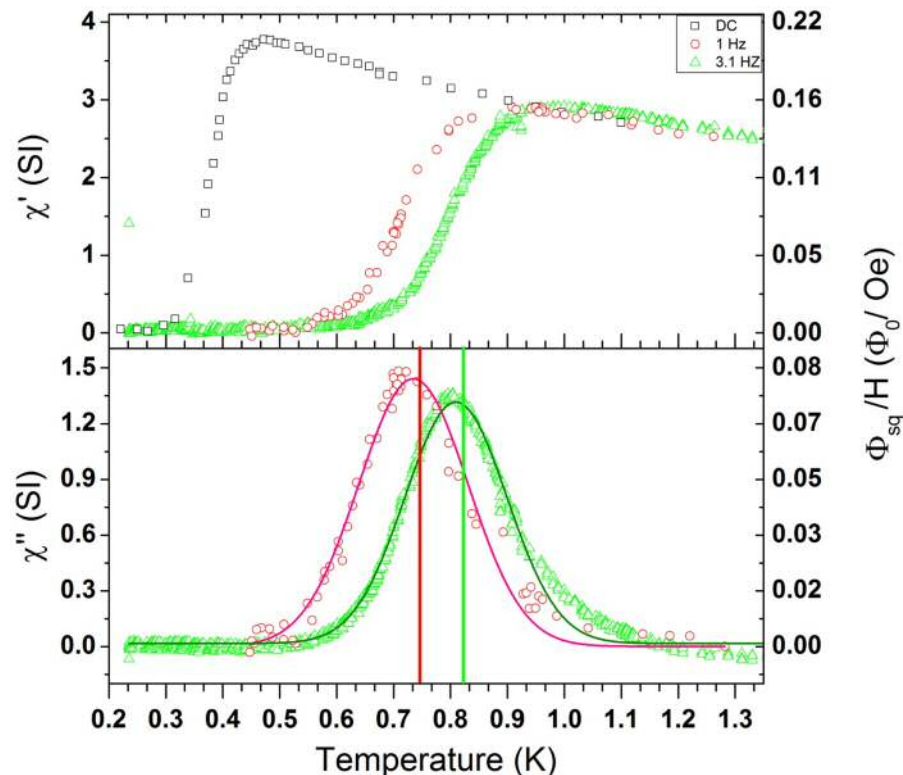


Figure 4.38: Temperature scan of χ' and χ'' of the spin-ice $Dy_2Ti_2O_7$ at 1 Hz (red circles) and 3.1 Hz (green triangles) and the DC susceptibility (black squares). Vertical lines are the expected transitions $\delta T \simeq 15$ mK.

the error is as the frequency scan needs to be spanned to higher frequencies and the heating effects must increase with the frequency.

The measured χ'' peak of the transition is plotted as a function of the temperature in Fig. 4.39 for the PPMS and the Bluefors Magnetometer measurements and compared with the Paulsen et al. work [3] and the Yaraskavitch et al. work [31]. The mismatch between the expected and the measured value is more evident above 900 mK from the frequency scan data. Although it seems to be explained by heating effects, the noisy behaviour of the RuO_2 thermometer shown in Fig. 4.40 and the small temperature dependence of its resistance above 800 mK encourage to calibrate a new thermometer with a better performance and larger temperature range.

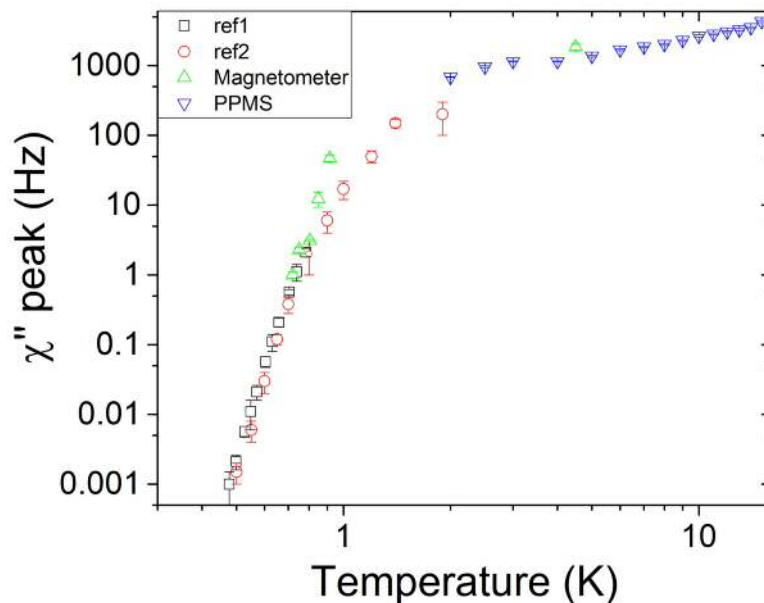


Figure 4.39: Temperature dependence of χ'' peak in $Dy_2Ti_2O_7$ from references 1 [3] and 2 [31] and the PPMS and the magnetometer measurements. Gaussian fits give the errors in the magnetometer data.

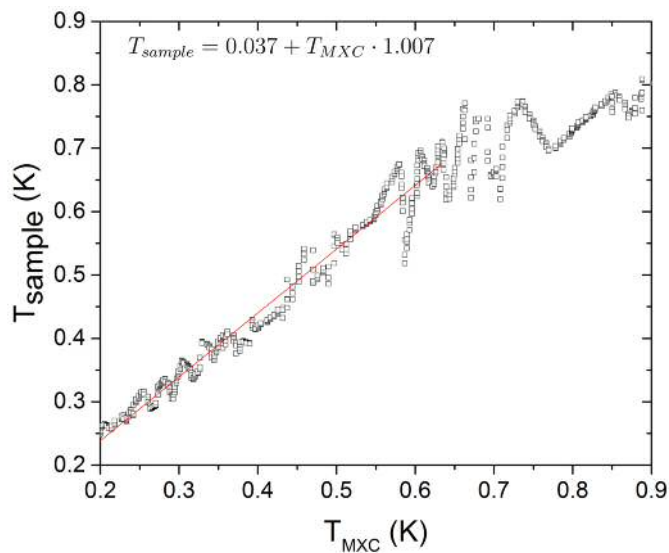


Figure 4.40: RuO_2 sample thermometer vs MXC thermometer.

Both the frequency and temperature scan plots include the output readout in fluxons per Oersted, clearly below the SQUID threshold of the open-loop operation ($\Phi_{sq} < \Phi/\pi$). It would make the high frequency measurement (\sim MHz) affordable.

4.7 Inductive magnetometer

In parallel to the dc-SQUID magnetometer, inductive techniques were investigated. The study of the advantages and limitations of the inductive magnetometer and the review of the existing literature confirmed the difficulties to expand the frequency response to MHz (see Sec. 4.2.1). To obtain a detectable induced electromotive force by using a Lock-in technique, a considerable number of turns in the detection coils are required and hence the inductance of the circuit increases. As a result the RLC circuit normally presents a cut-off frequency lower than MHz if the pickup coils are not reduced to micrometers. The RISE Acreo equipment is the only commercial magnetometer able to measure beyond 1 MHz at room temperature. This investigation was materialised in a fruitful collaboration with Acreo to adapt their susceptometer to low temperatures.

The high frequency inductive susceptometer depicted in Fig. 4.41, consists of a first-order inductive gradiometer connected to a resistance network at room temperature to avoid the circuit resonance. The primary coil is made of superconducting wires to avoid heat load at low temperatures. The high frequency response is achieved by an unconventional method to wind the coil. The zigzag shape reduces the mutual inductance to such an extent that MHz susceptibility is achievable. To be able to connect the inductive magnetometer to the Bluefors setup, the coils were built in a Torlon holder with similar dimensions that the dc-SQUID magnetometer.

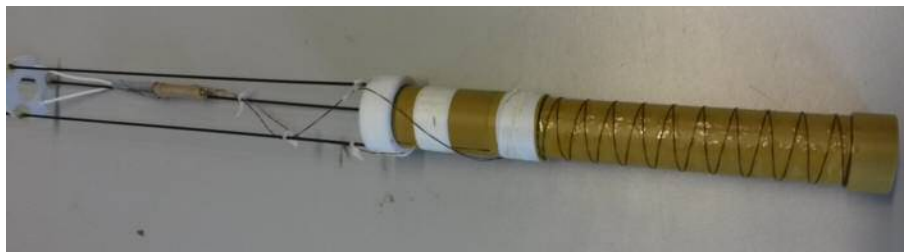


Figure 4.41: High frequency inductive magnetometer.

The setup was successfully tested at 1 MHz at room temperature using the stepper motor. The $\text{Ho}_2\text{Ti}_2\text{O}_7$ spin ice sample was centred with a good noise-to-

ratio response up to 2 MHz. The setup includes a SR844 high frequency lock-in to feed the primary coil and measure the susceptibility. The resistance network was located in a Faraday cage to avoid electromagnetic interferences. For low temperature measurements, the setup was modified to attach it to the PPMS. Fibre Carbon rods were added to hold and located the coils at the bottom of the PPMS. At low temperature, $\text{Ho}_2\text{Ti}_2\text{O}_7$ susceptibility has been measured before in polycrystalline [32–34] and single-crystalline [35, 36] samples with a freezing temperature higher than 1 K above 1 kHz. Promising results were also obtained at low temperatures. Frequency scan of χ' and χ'' were measured from tens of kHz to 1 MHz at $T=11.5$ K and $T=12.5$ K with a maximum susceptibility χ' around 60 and 70 kHz, respectively. Room temperature and low temperature measurements taken by Edward Riordan are shown in Fig. 4.42.

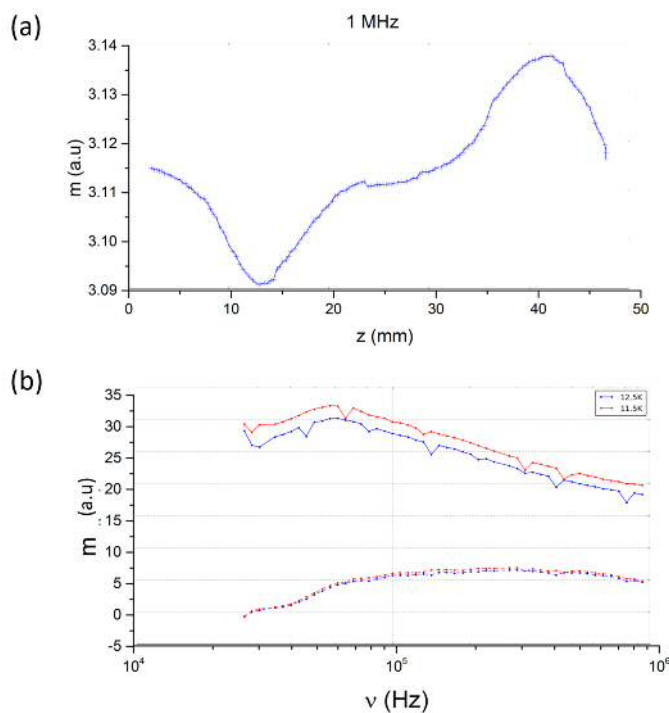


Figure 4.42: (a) Position scan of $\text{Ho}_2\text{Ti}_2\text{O}_7$ susceptibility at 1 MHz at room temperature. (b) χ' and χ'' high frequency scan taken by Edward Riordan at 11.5 and 12.5 K.

4.8 Conclusions and future work

In conclusion, the first low temperature magnetometer in a dry dilution refrigerator has been designed and built to investigate the correlated disorder role on the dynamics properties of frustrated magnets. The dc-SQUID magnetometer has demonstrated the capability to extend the temperature range of commercial magnetometer down to a hundred milliKelvins. Furthermore, the control of the magnetic flux from the sample to the SQUID via flux transformers provided a flexible path to easily reduce the flux in such a way that susceptibility up to MHz may be measurable in the open-loop mode. To work in the open-loop mode, the sample magnetic flux must be reduced to the linear range of the SQUID ($\Phi_{sq} < \Phi_0/\pi=318 \text{ m}\Phi_0$) with a good voltage-to-noise ratio. The frequency spectrum (Sec. 4.3.2) reveals a magnetic noise floor of $\sim 50pT/\sqrt{Hz}$ in the pickup coil and a SQUID flux noise floor of $\sim 2.5\mu\Phi_0/\sqrt{Hz}$. It corresponds to threshold values of $B^{thres} \sim 3nT$ and $\Phi_{sq}^{thres} \sim 1m\Phi_0$. Thresholds were found to be quasi-frequency independent. Therefore, the magnetometer has a dynamic range of at least two order of magnitude for the open-loop configuration. The magnetometer sensitivity is $S \cdot V_\Phi = (3.5 \pm 0.3) \cdot 10^{-3} \text{ emu}/\Phi_0$. As SQUID flux up to $500\Phi_0$ are measurable at low frequencies in the lock-loop mode the final dynamic range is $(1 - 10^{-5}) \text{ emu}$ for the lock-loop mode at frequencies lower than 1 kHz that will progressively decrease according to an effective slew rate of $100 \text{ k}\Phi_0/\text{s}$ and $(10^{-3} - 10^{-5}) \text{ emu}$ for the open-loop mode. Although the lock-loop mode can work in the later dynamic range up to MHz, it is recommendable to swap to the open-loop mode when the slew rate lower the FLL operation to the dynamic range of the open-loop mode. It takes place around 100 KHz.

Future works in the dc-SQUID must be faced to solve the sample thermalisation issue and carry out high frequency measurements. The temperature difference between the sample thermometer and the MXC points out a temperature gradient in the sample holder that increases at low temperature with a maximum value of $\simeq 150 \text{ mK}$ at the base temperature. The noisy behaviour and low precision above 800 mK of the thermometer used suggests the calibration of a new thermometer with a better performance and larger temperature range. Although a new thermome-

ter may improve the precision of the temperature measurements, the gradient will hinder to take accurate temperatures if the thermometer is not located near the sample. As the thermometer interferes with the magnetometer performance if it is placed inside the pickup coil volume a different solution is needed to avoid the temperature gradient. Therefore, the temperature gradient must be removed via a better thermalisation.

The use of more, purer and Oxygen free Copper strips to thermally link the top of the sample holder with the MXC and to remove the Teflon separator decreased the sample base temperature and hence the gradient as shown Fig. 4.28 (b) but not enough to minimise the gradient effects. Besides, the sample-coils alignment was affected by increasing the number of strips producing a thermal contact between them (Fig. 4.29) that ruined the thermalisation. The best solution to thermalise the sample would be to design a new sample holder thermally linked to the MXC from the top and the bottom. It would reduce the gradient and improve the sample-coils alignment. Unfortunately, it requires to build a wider coil holder because the 10 mm wide pickup coil holder does not provide enough gap with the sample holder.

Regarding the high frequency measurements, Eddy currents are observed above 1 kHz. The investigation of the measurement protocol has revealed to be very useful not only to remove spurious signals from interferences but also to avoid the Eddy currents effects. Fig. 4.43 highlights the Copper sample holder effects above 1 kHz when the susceptibility is measured in the the static mode (black dots) and the suppression of the Eddy currents when the center and the bottom coil signal are subtracted (grey dots). Furthermore, a very pure Sapphire rod was designed to substitute the Copper holder. The idea is to take advantage of its electrical insulating properties and its relatively high thermal conductivity to avoid the Eddy currents. The combination of the new and wider coil holder with a sample holder thermally linked to the MXC from both ends might provide a design with a good thermalisation, even below 100 mK and able to measure at MHz frequencies.

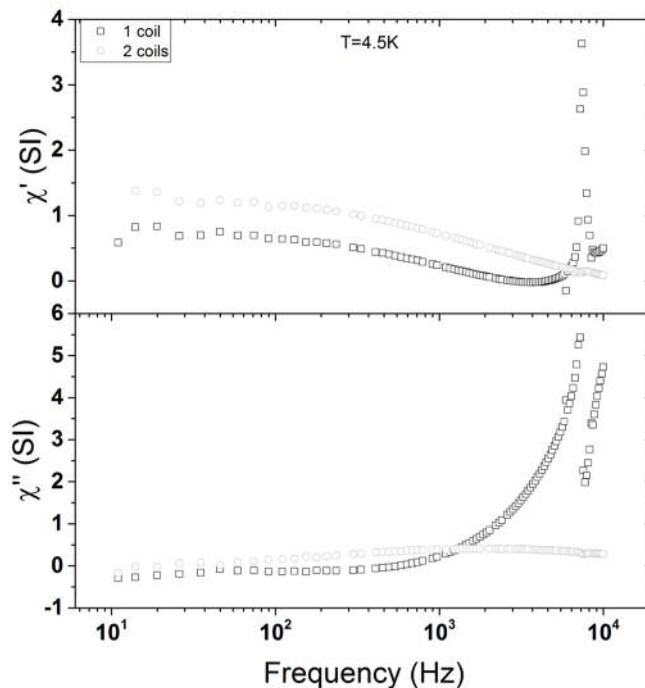


Figure 4.43: Frequency scan of χ' and χ'' $\text{Dy}_2\text{Ti}_2\text{O}_7$ using one or two coils. Eddy currents at high frequencies due to the diamagnetic sample holder are removed by using the extraction mode.

No further experiments were able to carry out during this project. The delay in the Dilution Fridge delivery (1.5 year after the project starting date) and a recent ^3He leak hampered the use of the Fridge.

References

- [1] L. Balents, *Spin liquids in frustrated magnets*, Nature 464 (7286), p. 199 (2010)
- [2] D. J. P. Morris, D. A. Tennant, S. A. Grigera, B. Klemke, C. Castelnovo, R. Moessner, C. Czternasty, M. Meissner, K. C. Rule, J.-U. Hoffmann, K. Kiefer, S. Gerischer, D. Slobinsky and R. S. Perry, *Dirac Strings and Magnetic Monopoles in the Spin Ice $\text{Dy}_2\text{Ti}_2\text{O}_7$* , Science 326 (5951), p. 411 (2009)
- [3] C. Paulsen, S. Giblin, E. Lhotel, D. Prabhakaran, G. Balakrishnan, K. Matsuhira and S. Bramwell, *Experimental signature of the attractive Coulomb force*

- between positive and negative magnetic monopoles in spin ice*, Nature Phys. (2016)
- [4] T. Fennell, P. P. Deen, A. R. Wildes, K. Schmalzl, D. Prabhakaran, A. T. Boothroyd, R. J. Aldus, D. F. McMorrow and S. T. Bramwell, *Magnetic Coulomb Phase in the Spin Ice $\text{Ho}_2\text{Ti}_2\text{O}_7$* , Science 326 (5951), p. 415 (2009)
- [5] C. Paulsen, *Introduction to Physical Techniques in Molecular Magnetism: Structural and Macroscopic Techniques—Yesa 1999* (2001)
- [6] A. Morello, W. Angenent, G. Frossati and L. De Jongh, *Automated and versatile SQUID magnetometer for the measurement of materials properties at millikelvin temperatures*, Rev. Sci. Instrum. 76 (2), p. 023902 (2005)
- [7] J. Piatek, *Ultra Low Temperature Susceptometer and Magnetometer: Study of the Spin Glass Series $\text{LiHo}_x\text{Er}_{1-x}\text{F}_4$* , Ph.D. thesis, Thèse École polytechnique fédérale de Lausanne EPFL (2012)
- [8] R. B. Clover and W. P. Wolf, *Magnetic Susceptibility Measurements with a Tunnel Diode Oscillator*, Rev. Sci. Instrum. 41 (5), p. 617 (1970)
- [9] F. Habbal, G. E. Watson and P. R. Elliston, *Simple cryostat for measuring rf susceptibility from 4.2 to 300 K*, Rev. Sci. Instrum. 46 (2), p. 192 (1975)
- [10] M. Vannette, A. Sefat, S. Jia, S. Law, G. Lapertot, S. Bud'ko, P. Canfield, J. Schmalian and R. Prozorov, *Precise measurements of radio-frequency magnetic susceptibility in ferromagnetic and antiferromagnetic materials*, J. Magn. Magn. Mater. 320 (3), p. 354 (2008)
- [11] L. Spinu, H. Srikanth, E. E. Carpenter and C. J. O'Connor, *Dynamic radio-frequency transverse susceptibility in magnetic nanoparticle systems*, J. Appl. Phys. 87 (9), p. 5490 (2000)
- [12] S. Tumanski, *Induction coil sensors—a review*, Meas. Sci. Technol. 18 (3), p. R31 (2007)

- [13] F. Ahrentorp, A. P. Astalan, C. Jonasson, J. Blomgren, B. Qi, O. T. Mefford, M. Yan, J. Courtois, J. Berret, J. Fresnais, O. Sandre, S. Dutz, R. Müller and C. Johansson, *Sensitive High Frequency AC Susceptometry in Magnetic Nanoparticle Applications*, AIP Conf. Proc. 1311 (1), p. 213 (2010)
- [14] A. P. Astalan, C. Jonasson, K. Petersson, J. Blomgren, D. Ilver, A. Krozer and C. Johansson, *Magnetic response of thermally blocked magnetic nanoparticles in a pulsed magnetic field*, J. Magn. Magn. Mater. 311 (1), p. 166 (2007)
- [15] L. van de Klundert, C. de Rooij, M. Caspari and L. van der Marel, *Induction methods used in low temperature physics*, Cryogenics 15 (10), p. 577 (1975)
- [16] J. Tafur, A. P. Herrera, C. Rinaldi and E. J. Juan, *Development and validation of a 10 KHz - 1 MHz magnetic susceptometer with constant excitation field*, J. Appl. Phys. 111 (7), p. 07E349 (2012)
- [17] J. Clarke, M. Mück, M.-O. André, J. Gail and C. Heiden, *The Microstrip DC Squid Amplifier* (Springer Netherlands, Dordrecht, 2001), p. 473
- [18] M. E. Huber, N. C. Koshnick, H. Bluhm, L. J. Archuleta, T. Azua, P. G. Björnsson, B. W. Gardner, S. T. Halloran, E. A. Lucero and K. A. Moler, *Gradiometric micro-SQUID susceptometer for scanning measurements of mesoscopic samples*, Rev. Sci. Instrum. 79 (5), p. 053704 (2008)
- [19] M. J. Martínez-Pérez, J. Sesé, F. Luis, D. Drung and T. Schurig, *Highly sensitive superconducting quantum interference device microsusceptometers operating at high frequencies and very low temperatures inside the mixing chamber of a dilution refrigerator*, Rev. Sci. Instrum. 81 (1), p. 016108 (2010)
- [20] S. T. P. Boyd, V. Kotsubo, R. Cantor, A. Theodorou and J. A. Hall, *Miniature Thin-Film SQUID Susceptometer for Magnetic Microcalorimetry and Thermometry*, IEEE Trans. Appl. Supercond. 19 (3), p. 697 (2009)
- [21] J. Clarke and A. Braginski, *The SQUID Handbook: Fundamentals and Technology of SQUIDs and SQUID Systems* (Wiley, 2006)

- [22] J. Mallinson, *Magnetometer Coils and Reciprocity*, J. Appl. Phys. 37 (6), p. 2514 (1966)
- [23] F. Terman, *Radio engineers' handbook* (New York: McGraw-Hill Book Co., 1943)
- [24] J. W. Ekin, *Experimental Techniques for Low-Temperature Measurements: Cryostat Design, Material Properties, and Superconductor Critical-Current Testing* (Oxford U. Press, New York, 2006)
- [25] <http://woodcraft.lowtemp.org/>
- [26] J. Snyder, J. S. Slusky, R. J. Cava and P. Schiffer, *How 'spin ice' freezes*, Nature 413, pp. 48–51 (2001)
- [27] J. Snyder, B. G. Ueland, J. S. Slusky, H. Karunadasa, R. J. Cava and P. Schiffer, *Low-temperature spin freezing in the $Dy_2Ti_2O_7$ spin ice*, Phys. Rev. B 69, p. 064414 (2004)
- [28] K. Matsuhira, C. Paulsen, E. Lhotel, C. Sekine, Z. Hiroi and S. Takagi, *Spin Dynamics at Very Low Temperature in Spin Ice $Dy_2Ti_2O_7$* , J. Phys. Soc. Jpn. 80 (12), p. 123711 (2011)
- [29] H. Fukazawa, R. G. Melko, R. Higashinaka, Y. Maeno and M. J. P. Gingras, *Magnetic anisotropy of the spin-ice compound $Dy_2Ti_2O_7$* , Phys. Rev. B 65, p. 054410 (2002)
- [30] J. Shi, Z. Tang, B. Zhu, P. Huang, D. Yin, C. Li, Y. Wang and H. Wen, *Dynamical magnetic properties of the spin ice crystal $Dy_2Ti_2O_7$* , J. Magn. Magn. Mater. 310 (2), p. 1322 (2007)
- [31] L. R. Yaraskavitch, H. M. Revell, S. Meng, K. A. Ross, H. M. L. Noad, H. A. Dabkowska, B. D. Gaulin and J. B. Kycia, *Spin dynamics in the frozen state of the dipolar spin ice material $Dy_2Ti_2O_7$* , Phys. Rev. B 85, p. 020410 (2012)

- [32] K. Matsuhira, Y. Hinatsu, K. Tenya and T. Sakakibara, *Low temperature magnetic properties of frustrated pyrochlore ferromagnets $\text{Ho}_2\text{Sn}_2\text{O}_7$ and $\text{Ho}_2\text{Ti}_2\text{O}_7$* , J. Phys. Condens. Matter. 12 (40), p. L649 (2000)
- [33] G. Ehlers, A. L. Cornelius, M. Orendác, M. Kajnaková, T. Fennell, S. T. Bramwell and J. S. Gardner, *Dynamical crossover in 'hot' spin ice*, J. Phys. Condens. Matter 15 (2), p. L9 (2003)
- [34] G. Ehlers, A. L. Cornelius, T. Fennell, M. Koza, S. T. Bramwell and J. S. Gardner, *Evidence for two distinct spin relaxation mechanisms in 'hot' spin ice $\text{Ho}_2\text{Ti}_2\text{O}_7$* , J. Phys. Condens. Matter 16 (11), p. S635 (2004)
- [35] A. L. Cornelius and J. S. Gardner, *Short-range magnetic interactions in the spin-ice compound $\text{Ho}_2\text{Ti}_2\text{O}_7$* , Phys. Rev. B 64, p. 060406 (2001)
- [36] J. a. Quilliam, L. R. Yaraskavitch, H. a. Dabkowska, B. D. Gaulin and J. B. Kycia, *Dynamics of the magnetic susceptibility deep in the Coulomb phase of the dipolar spin ice material $\text{Ho}_2\text{Ti}_2\text{O}_7$* , Phys. Rev. B 83 (9), p. 094424 (2011)

“ The insights into QPT promise to lead to an understanding of the phase transformations of many body strongly correlated systems, most notably of the mechanisms of high temperature superconductivity in cuprates, which is encoded in the physics of the critical region near QCP.”

M. Vasin et al., 2015 [1]

5

μ SR study of stoichiometric NbFe₂

5.1 Introduction

Detailed investigations of the phase diagram around quantum critical points (QCP) in correlated electron systems show rich behavior including unconventional superconductivity and magnetic order. QCPs have been widely studied in heavy fermion systems [2] and their role in cuprates [3] and iron pnictide high- T_c [4] superconductors is still debated. Novel magnetic phases can also emerge [5] from a QCP. The Nb_{1- y} Fe_{2+ y} intermetallic is a particularly interesting material in which to investigate QCP behavior since it displays a rich-magnetic phase diagram and quantum criticality in a d -band metal. The high temperature paramagnetic metal becomes a weakly ordered ferromagnet at relatively low temperatures in Nb-rich ($y < -0.02$) and Fe-rich ($y > 0.01$) compounds and the magnetic transition can be tuned to zero temperature at a doping of $y = -0.015$ [6]. The proposed magnetic phase diagram as a function of doping is shown in Fig. 5.1. Long-range antiferromagnetism (AFM)

or a spin density wave (SDW) have both been suggested to describe the magnetic ground state around criticality ($-0.02 < y < 0.01$) [6–13]. However ferrimagnetism in Fe-rich samples found by magnetic Compton scattering [14] and the failure to detect the magnetic order by neutron scattering [6, 9] suggests further experiments are required to clarify the nature of the ground state. In parallel with the writing of this thesis, a neutron scattering work was able to detect a long-wavelength spin density wave state caused by an intrinsic instability of the ferromagnetic QCP [15] consistent with the theoretically predicted scenario of a hidden ferromagnetic QCP masked by a continuous transition towards either incommensurate ordering or first-order transition into a commensurate state [16].

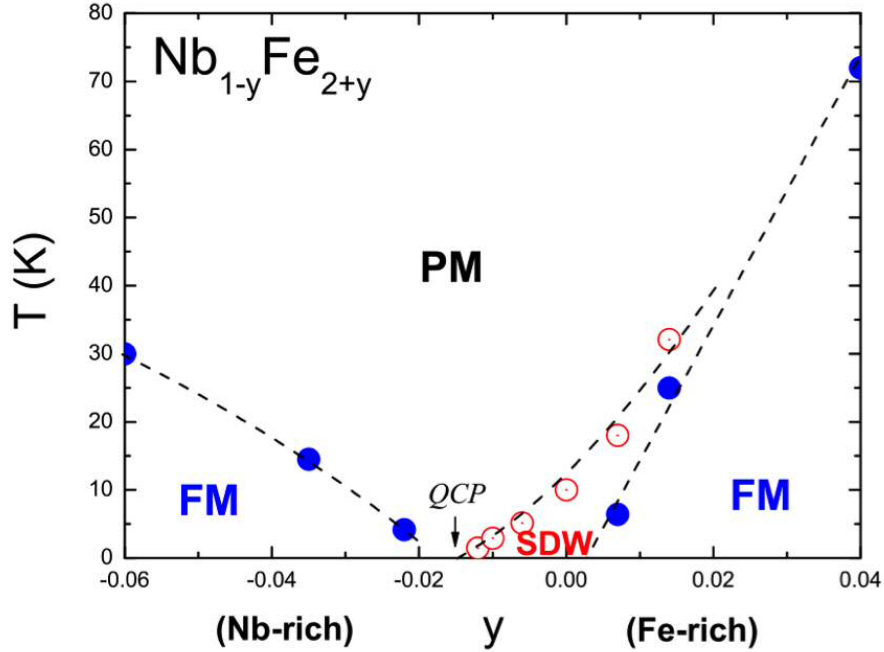


Figure 5.1: Magnetic phase diagram of $\text{Nb}_{1-y}\text{Fe}_{2+y}$ with the apparent ground states as a function of doping. Ref [6].

Early magnetic studies of stoichiometric NbFe_2 [17] suggested a Pauli paramagnet ground state, but NMR work and magnetic investigations resolved an AFM order [7, 18] with a transition temperature, $T_N \sim 10$ K. Subsequent work suggested that the ordering resulted in a SDW [19] structure that can be suppressed by applying field [20–22]. The AFM or SDW ground state is characterised by a high

magnetic susceptibility, non-Fermi liquid behaviour in e.g. the electrical resistivity and the absence of magnetic remanence. Recently, significant efforts have been made in order to further understand the nature of the apparently ambiguous magnetic ground state in NbFe_2 [6, 8–13, 15]. Furthermore, the possibility of competing and frustrated interactions can be postulated from the crystal structure since NbFe_2 crystallizes in the C14 hexagonal Laves phase with the magnetic Fe atoms (6h sites) forming two planar triangular kagomé lattices in a hexagonal lattice, stacked normal to the c-axis, and separated by linking Fe (2a sites) atoms and Nb atoms occupying interstitial sites, as shown Fig. 5.2, leading to numerous possible exchange pathways.

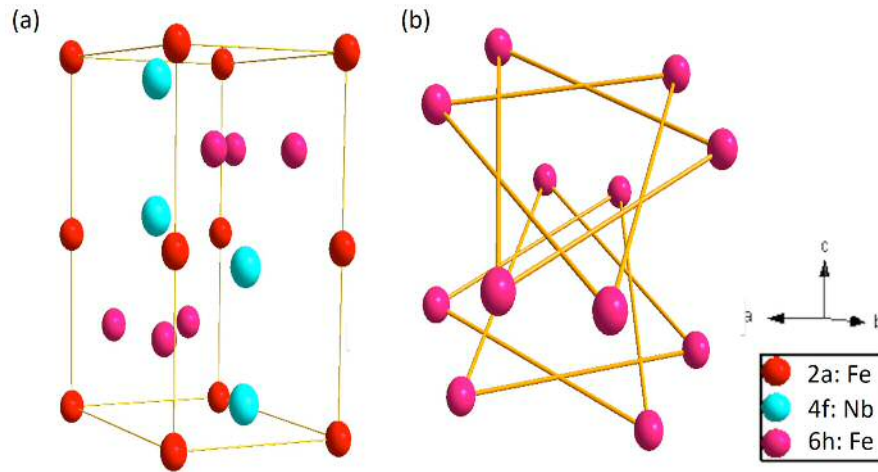


Figure 5.2: (a) NbFe_2 C14 Hexagonal Laves with the Fe atoms at the 6h sites (pink) separated by the 2a sites Fe atoms (red) and the Nb atoms at the interstitial sites. (b) Planar triangular kagomé lattices formed by the Fe atoms at the 6h sites.

Theoretical studies have arrived at contradictory conclusions. The lowest-energy magnetic ground state varies according to the approach chosen in Density Functional Theory calculations. Asano and co-workers [23] suggest that an AFM ground state, and a “weak” as well as a “strong” ferromagnetic state have very similar ground state energies using the local-spin-density approximation. The more recent study of Subedi [24] found magnetic ground states governed by competing interlayer interactions, one which supports FM between 6h and 2a Fe atoms and

another with no magnetic moment on 2a Fe sites and AFM order. The AFM interactions within the kagomé lattice were found to be weak, which is supported by experiments [6], leading to the conjecture that geometric frustration is not associated with the quantum criticality. A new ferrimagnetic arrangement was also discovered using the generalised gradient approximation [25].

The Stoner enhancement factor, $S = 1/(1 - JN(E_F))$, determined by experiment to be > 100 , [9, 11] is associated with an unusually large exchange interaction, J . In this scenario, any tiny increase in $N(E_F)$ by doping should drive the magnetic ground state towards a ferromagnetic instability. Accordingly, calculations using the Koringa-Kohn-Rostoker electronic-structure method to study how chemical disorder affects the magnetic properties [26] or using Moriya's theory of weak magnetism [27] suggest an unconventional band critical point (uBCP) as the most likely cause for a QCP, which is accessible by disorder due to alloying. Unlike the rigid-band approximation used in previous work, $N(E_F)$ increases in both the Fe and Nb rich alloys, thereby satisfying the Stoner criterion on both sides of the phase diagram.

Although an extensive amount of bulk magnetic, thermodynamic, transport and theoretical work has been performed, no definitive ground state has been identified. Direct evidence of a modulated SDW has recently been reported using muon spin relaxation (μ SR) [13]. Clear evidence of long range order in the doped samples was observed, the muon signal relaxed with an oscillatory behaviour which is a strong indication of static and ordered bulk magnetism as it is shown in Fig. 5.3. However, the nature of the relaxation in the stoichiometric material is not as clear as the signal relaxes without any oscillatory behaviour making interpretation difficult. For NbFe_2 , μ SR is, in principle, able to differentiate between commensurate (AFM) and incommensurate (SDW) magnetic order and weak ferromagnetism. Although correlation lengths are difficult to obtain directly from μ SR, a phenomenological way to study short-range spin correlations in frustrated and/or magnetically disordered systems and spin glasses in the slow fluctuations limit has been proposed [28–33].

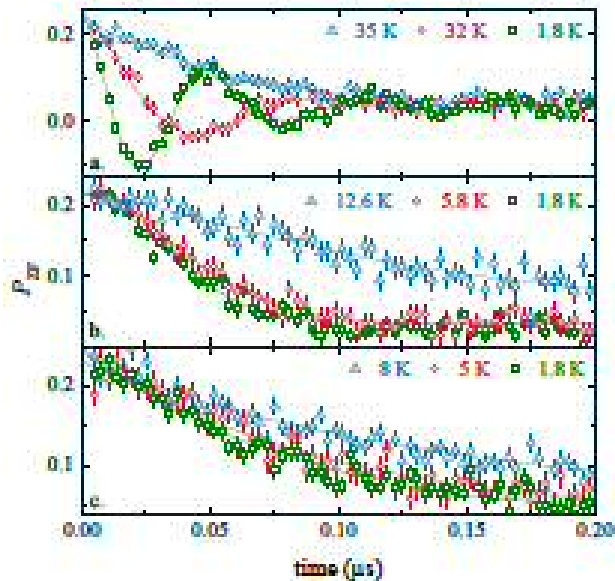


Figure 5.3: Zero-field μ SR asymmetry spectrum of $\text{Nb}_{1-y}\text{Fe}_{2+y}$ for $y = +0.016$ (FM) (a), 0.0 (b) and -0.004 (c) (SDW?) from [13]. Oscillations are only observed in the FM phase.

In this chapter, a detailed μ SR study of single crystalline stoichiometric NbFe_2 , supported by d.c. and a.c. bulk magnetisation measurements are presented in order to investigate the magnetic ground state. Single crystal was prepared by arc melting performed by Ross Stewart and the quality confirmed by neutron Laue diffraction along the c axis as shown Fig. 5.4.

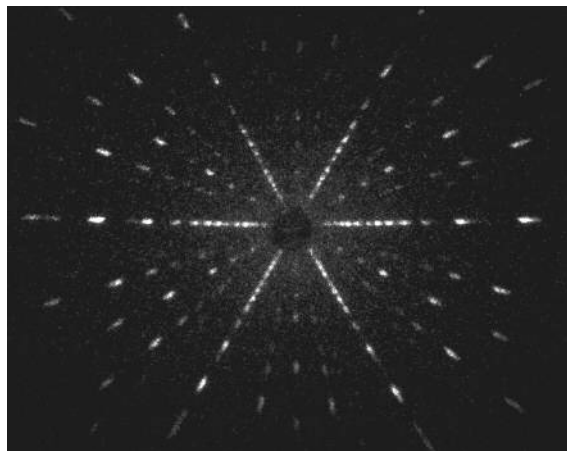


Figure 5.4: Neutron Laue diffraction along the c axis.

Using both zero field and longitudinal field μ SR measurements the observed magnetic order in this sample is revealed to be static and short range although a SDW with a helical and incommensurate amplitude modulation is also possible. The sensitivity of the ground state to stoichiometry is demonstrated. Comparison of the data to that already in the literature [13] suggests that muons are sensitive to the field distribution and fluctuations as the QCP is approached [34].

5.2 Bulk magnetization

Magnetic data were taken in commercial Physical Properties Measurement Systems (Quantum Design PPMS). All experimental data were taken with the magnetic field applied along the c -axis of the crystal. Initial magnetisation measurements as a function of temperature for both field-cooled and zero-field-cooled protocols (FC-ZFC) show an obvious magnetic transition in Fig. 5.5.

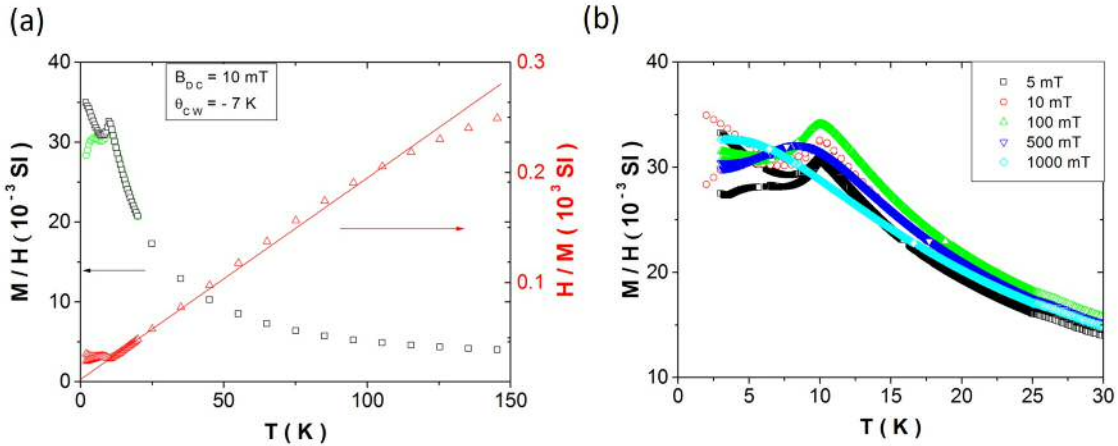


Figure 5.5: (a) Temperature dependence of the field-cooled (black squares), zero field-cooled (green circles) susceptibility and inverse susceptibility (red triangles) showing a peak at $T_N \sim 10$ K. The inverse susceptibility displays approximately linear Curie-Weiss like behaviour, commonly observed in weak itinerant magnets [35]. (b) ZFC-FC susceptibility as a function of the field. The transition disappears at $B = 1$ T.

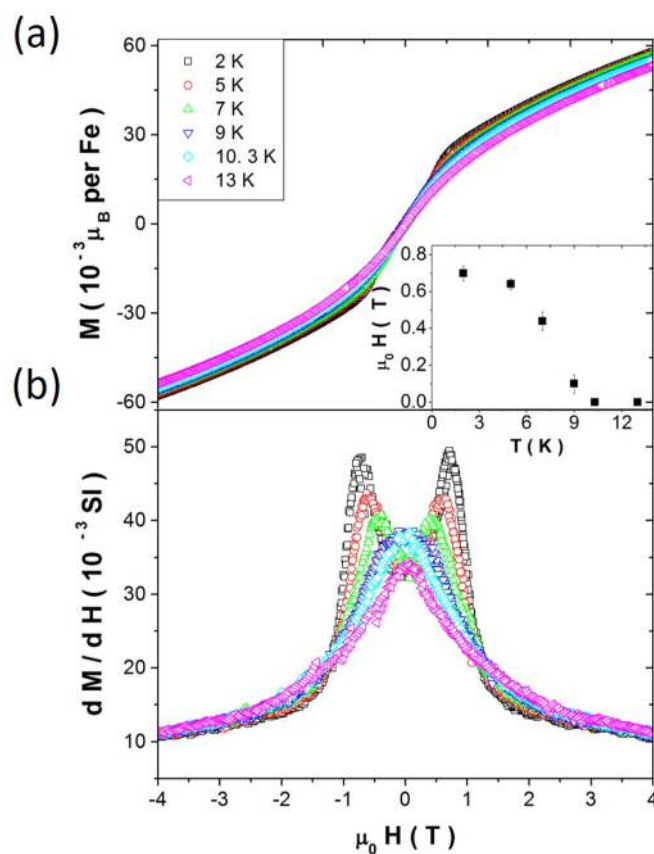


Figure 5.6: (a) Magnetic isotherms. (b) Susceptibility $\frac{dM}{dH}$ at different temperatures. Inset. Critical field as a function of the temperature. Error bars are given from data precision in the susceptibility.

Curie-Weiss (CW) like behaviour is observed down to the transition temperature, $T_N \simeq 10.3$ K, indicated by a peak along with a bifurcation of field-cooled and zero-field-cooled magnetization. This transition temperature is in good agreement with previously reported T_N values for stoichiometric samples of NbFe_2 . A second peak in the susceptibility is seen in the zero field cooled data around 5 K indicating the possible occurrence of a second magnetic transition. The magnetic interactions in the ordered phase were subjected to an applied field. The low temperature bifurcation is removed by fields higher than 100 mT and the temperature transition decreases for higher fields until it disappears at $B = 1$ T. Below T_N , a “S”-shaped magnetic field dependence exhibits a turning point at the critical field B_c necessary to suppress the observed order. The derivative $\frac{dM}{dH}$ displays a critical field or

maximum at $B_c \sim 0.7$ T at 2K (Fig. 5.6), which is interpreted as a metamagnetic transition field, and is somewhat higher than previously reported [6, 9, 18, 21]. The link between the critical field and the main transition is clearly observed in the temperature dependence that decreases to 0 when critical temperature is reached.

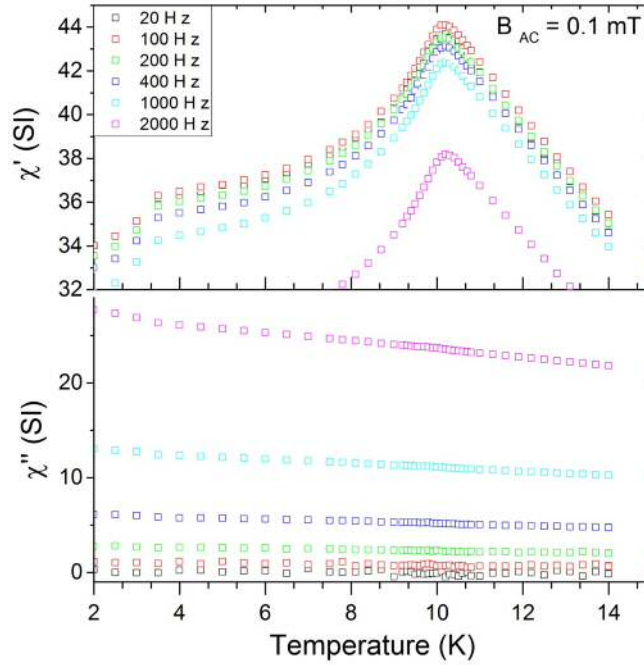


Figure 5.7: Temperature scan of χ' and χ'' for different frequencies. No frequency-dependent behaviour is observed. Data are distorted by eddy currents above 1000 Hz.

The magnetisation below 100 K may be described in the local magnetic moment context with a CW shape, an effective moment of $\mu_{eff}=2.06 \mu_B$ per Fe atom and $\theta_{CW} = -7$ K. However, NbFe₂ is an itinerant paramagnet and the reason for a CW shape is rather the temperature dependence of the spin-fluctuation amplitude [35]. In this scenario, the fact that the frustration parameter, $f = \frac{|\theta_{CW}|}{T_N}$ [36] is low may be not a reason to dismiss the geometrically frustrated kagomé lattice role in the magnetic ground state. However, there is no frequency shift of the transition temperature in the susceptibility peak expected in a spin-glass system as shown in Fig. 5.7. Above 1000 Hz the data are distorted by eddy currents induced in the metallic compound by the alternating field. No absorption is detected in the imag-

inary part $\chi''(\omega)$.

In the Stoner theory of itinerant ferromagnets, the enhanced Pauli susceptibility is $S = \frac{\chi}{\chi_p} \simeq 300$ with a Pauli susceptibility $\chi_p \simeq 10^{-4}$ estimated from band-structure DOS [37] that do not consider the Coulomb interactions. This analysis implies larger exchange interactions than in previous works [6, 22]. It can be concluded that, in this sample, the magnetic transition is closer to a ferromagnetic instability than in previous works.

5.3 Muon spin relaxation

The Dolly muon spectrometer at the continuous muon source at the Paul Scherrer Institute (PSI) in Villigen, Switzerland was used to study the magnetic ground state due to its high frequency resolution and hence its ability to probe higher internal magnetic fields (binning length= 1ns). The precise value of a_0 is dependent on the muon spectrometer. In the event that the muons find a stationary interstitial site in the sample (no hopping), then any relaxation in the observed $P(t)$ is a consequence of fluctuations around that muon site from nuclear or electronic spins. In the paramagnetic “motionally narrowed” regime, the muon relaxation in zero-field is dominated by nuclear spins which are static compared with the muon decay lifetime. As any magnetic transition is approached and electronic spin-fluctuations slow down, electronic moments will dominate the relaxation because of the larger associated magnetic fields at the muon site.

On application of a transverse field (TF20) in the paramagnetic phase above T_N , the muon polarization will oscillate around the applied field and the initial asymmetry, a_0 , and the α parameter for the specific experiment can be experimentally obtained. For this experiment $a_0 = 0.25$. Background contribution to the muon asymmetry due to the Silver sample holder was found to be almost constant with temperature with a value of $a_{Ag} \simeq 0.02$. Therefore the contribution from the sample, a_s , can be calculated from $A(t = 0) = a_s + a_{Ag} = 0.25$.

The sample was aligned with the muon polarisation along the c -axis. Firstly, zero field relaxation in the paramagnetic phase is discussed. Electron spins fluctuate faster than the muon time scale and the relaxation is dominated by weak and randomly oriented static nuclear moments. Local fields at the muon sites in each coordinate i , B_{loc}^i , are distributed according to an isotropic Gaussian field distribution, with a standard deviation (Δ_G) and muons relax with a lineshape given by the well known Gaussian Kubo-Toyabe function (GKT) introduced in Eq. 3.28

$$P_G(\Delta_G, t) = \frac{1}{3} + \frac{2}{3}(1 - \Delta_G^2 t^2) \exp\left(-\frac{\Delta_G^2 t^2}{2}\right) \quad (5.1)$$

In the paramagnetic phase, the analysis of the measured muon relaxation should include the possibility of numerous interstitial muon stopping sites so that the field distribution below the ordering temperature can be understood. An extensive study of the interstitial muon sites in the paramagnetic phase of NbFe₂ was performed in the work of Crook [22]. The muon relaxation was described by the distribution of the Nb and Fe ions around the implanted muons, which are distinguishable because of their different nuclear moments. Around the muon site the local environment can be described by the elements surrounding it, three possible (Nb-Fe) nearest neighbour coordinations of 4-0, 3-1 and 2-2 are possible. Simulations of the nuclear field distribution due to Gaussian distributed atomic moments for each of these site coordinations result in the following Δ_G values: 0.199, 0.39 and 0.48 μs^{-1} respectively. In the work of Crook, a single GKT relaxation with a field width of 0.284 μs^{-1} was associated with a single muon stopping site at the 4-0 position [22].

In this study, data can be fitted with more than one muon site in the paramagnetic regime as shown Fig. 5.8. To fit with more than one muon sites the silver background needs to be removed which disagrees the experimental data, therefore the one site model was chosen. It is important to note that the site allocation is more difficult to perform at PSI in this sample as the time scale only extends to 10 μs . The average nuclear field we found is $\Delta_G/\gamma_\mu = 0.29$ mT or $\Delta_G = 0.253$ μs^{-1} , where γ_μ is the muon gyromagnetic ratio. This is close to the value found in the

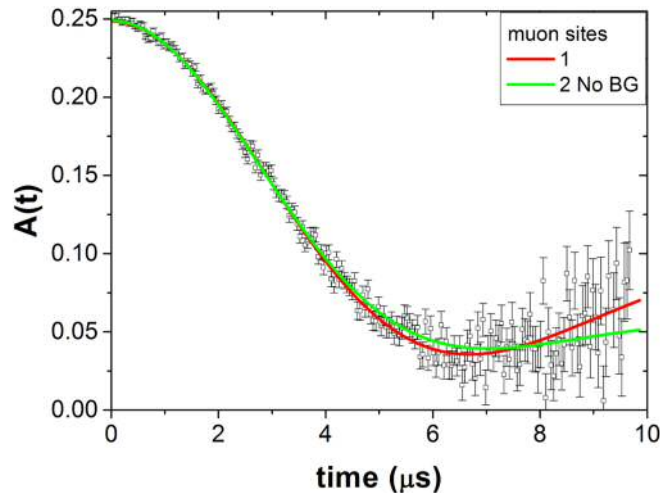


Figure 5.8: Zero field- μ SR run above T_N fitted with 1 muon site or 2 muon sites without any background contribution.

previous work. The difference between the measured and the calculated values can be explained and simulated [22] by site mixing (anti-site disorder) which would also have an effect on the local field distribution in the ordered regime.

The magnetic phase was analysed with zero field (ZF- μ SR) above and below T_N . The Gaussian relaxation from the nuclear contribution dominates above T_N but below the transition the relaxation is modified by the magnetic order with a fast muon depolarisation as shown Fig. 5.9 (a). Several scenarios can be distinguished by the nature of the relaxation below T_N . Specifically, if oscillations were observed this would signify long range order and a modulated SDW possible [38]. However, oscillations are not seen in $P(t)$, in agreement with recent work [13] where clear oscillations are only observed in the ferromagnetic phase of Fe-rich samples (see Fig 5.3). In the absence of oscillations, μ SR can distinguish two possible cases [39]. In the fast fluctuation or motional narrowing limit, an exponential decay characterises the muon depolarisation [40], and the relaxation rate contains information about both magnetic fluctuations and field-distribution widths (Eq. 3.41). In the other case, when fluctuations are slow, the magnetic field at the muon sites can be considered quasi-static. These scenarios can be distinguished by the application of a longitudinal field (along the direction of the muon polarization). μ SR spectra in

Fig. 5.9 display absence of oscillations and a relaxing tail at $\sim 1/3$ of the muon polarisation below 5 K in ZF- μ SR and muon repolarisation under longitudinal applied field in LF- μ SR. These features suggest a magnetic state with slow spin fluctuations of randomly orientated quasi-static fields and a relaxation lineshape reminiscent of a Kubo-Toyabe (KT) function (more details in Sec. 3.4). In the “static” approximation, the long time muon asymmetry is independent of time and equal to the $1/3$ term in Eq. 5.1. This is known as the “ $1/3$ tail” region. However, the presence of slow fluctuations can further depolarize the “ $1/3$ tail” region as it is observed in the high time spectra.

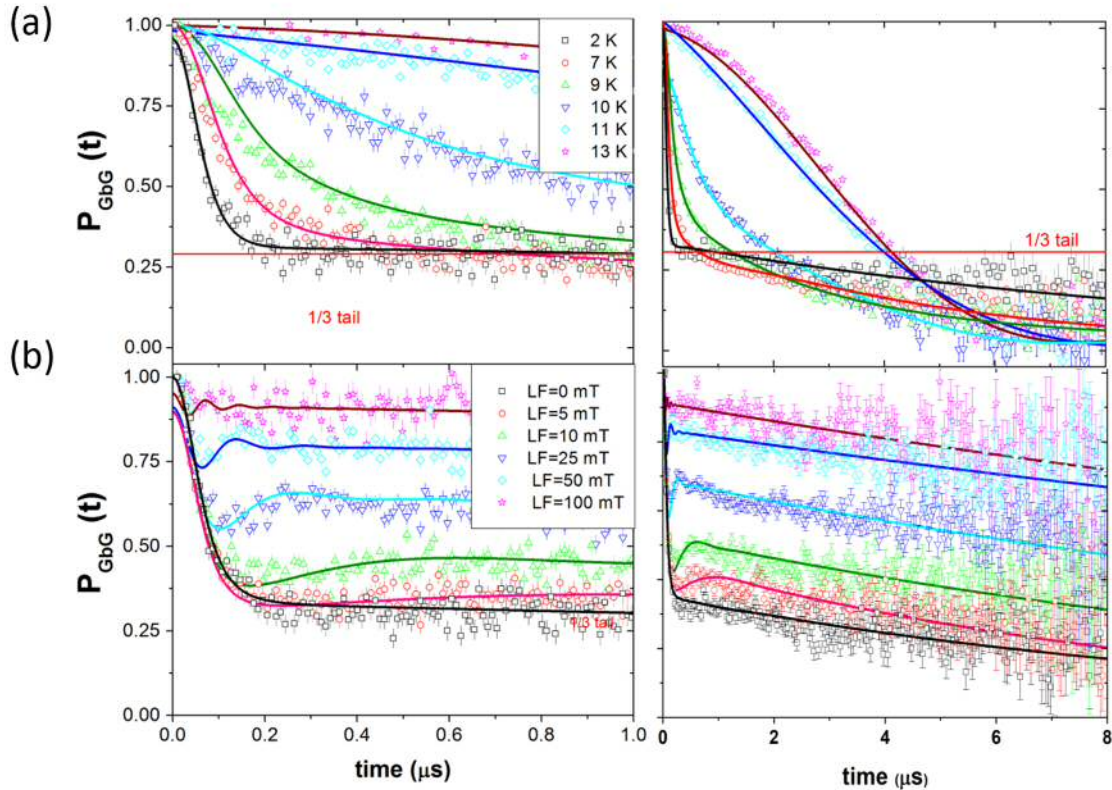


Figure 5.9: (a) Zero-field muon spectra above and below T_N fitted to a GbG form. The $1/3$ tail is emphasised by the red line. (b) Muon repolarisation in LF- μ SR confirms the quasi-static nature of the internal fields. High time spectra in right panel. Statistical errors are given by the number of events ≈ 15 MeV and the binning length 10 ns. For visualization binning factor of 80 and 40 was chosen for the high-time ZF-and LF- μ SR spectra.

KT functions in magnetically ordered single-crystalline samples are often used to fit the muon relaxation in disordered and/or frustrated magnetic phases with slow spin dynamics [41]. In such cases, relaxation is dominated by randomly-orientated magnetic fields at the muon sites. Densely packed magnetic moments use to generate a Gaussian field distribution at muon sites whilst systems with dilute magnetic impurities may produce a Lorentzian field distribution (Eq. 3.29) as takes place in canonical spin glasses [42]. Both cases present a distinctive dip in the muon asymmetry and a “1/3 tail”. Moreover, a limited number (3) of combined KT representing different possible muon sites or the Bessel functions (Eq. 3.32) that characterise a standard SDW were also considered. However, neither can fit the muon spectra in NbFe₂ ruling out these simple interpretations of the magnetic ground state.

The possibility of an unknown number of magnetically unequal muon sites that could all contribute to a non-trivial relaxation is taken into account with a phenomenological Gaussian-broadened GKT function (GbG) introduced by Noakes et. al. to explain several dense magnetic systems [28].

A ground state with strong fluctuations that relax exponentially or by a stretched exponential was also taken into account. Two components were required to fit the fast and the slow relaxation observed. Those possible models are compared in Fig. 5.10. Bessel relaxation, added as the model chosen in the previous muon work [13], clearly fails to fit as oscillations were not observed and standard KT relaxations always display the characteristic dip. In contrast, the monotonic lineshape was fairly well-fitted to the GbG model (and its discretisation in 17 GKT functions) and the extreme case of two Gaussian functions ($\beta = 2$). Residual analysis was carried out to compare both models with similar χ^2 (Eq. 3.14) up to 8 μs , although residuals are larger in the Gaussian model when the fast relaxation dominates ($t < 0.2 \mu\text{s}$). Despite the Gaussian one is a simpler model, different reasons support the GbG interpretation of random-orientated static fields. The “1/3 tail” observed in Fig. 5.9, evidence of the field randomness, is also witnessed by the 1:3 ratio of the two Gaussian ($35 \pm 3\%$) where relaxation rates of 3.4 and 0.25 μs^{-1} were obtained.

On the other hand, the goodness of GbG fit was confirmed by its success to explain the LF- μ SR that revealed the same internal field magnitude that the ZF analysis.

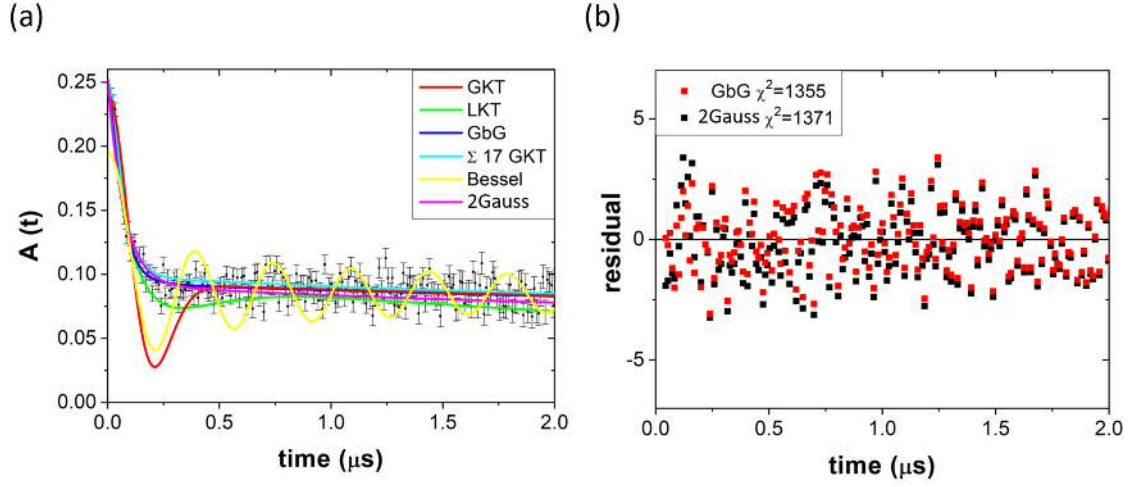


Figure 5.10: (a) Short time muon spectra at 2 K fitted to different models. The monotonic decay of the asymmetry was reasonable well-fitted to the GbG model described in text (and its discretisation in 17 GKT) and two gaussian functions with a weight ratio 1:3. (b) Residual analysis of both models. χ^2 for a fitting range up to 8 μ s.

In the GbG model, the single isotropic Gaussian field distribution $D_G(B_{loc}^i, \Delta_G)$, assumed in the GKT function of Eq. 5.1, is replaced by a distribution of Gaussian distributions D_{GBG} of width ρ centred on Δ_0 and with a standard deviation $R_b \Delta_0$. This lineshape was used to describe systems with static dense magnetic moments below a freezing temperature, but correlated only over a short range, with examples of its use being found in the pyrochlore $\text{Yb}_2\text{Ti}_2\text{O}_7$ [43] and the 5d hyperkagomé lattice $\text{Nd}_4\text{Ir}_3\text{O}_8$ [31]. Both geometrically frustrated lattices. The GbG field distribution is:

$$D_{GbG}(B_{loc}^i) = \int_{-\infty}^{\infty} D_G(B_{loc}^i, \Delta_G) \rho(\Delta_G, \Delta_0, R_b) d\Delta_G \quad (5.2)$$

where the Gaussian weight function is

$$\rho(\Delta_G, \Delta_0, R_b) = \frac{1}{\sqrt{2\pi}} \frac{1}{R_b \Delta_0} \exp\left[-\frac{(\Delta_G - \Delta_0)^2}{2(R_b \Delta_0)^2}\right] \quad (5.3)$$

The resultant muon depolarisation is the analytical solution of the integral Fourier transform of Eq. 5.2: Although the integral runs only over positive Δ_G values, it was extended to $-\infty$ to simplify to the following solution [39]:

$$P_{GbG}(\Delta_0, R_b, t) = \frac{1}{3} \exp\left(-\frac{2}{3}\nu t\right) + \frac{2}{3} \left(\frac{1}{1 + R_b^2 \Delta_0^2 t^2} \right)^{\frac{3}{2}} \left(1 - \frac{\Delta_0^2 t^2}{1 + R_b^2 \Delta_0^2 t^2} \right) \exp\left[-\frac{\Delta_0^2 t^2}{2(1 + R_b^2 \Delta_0^2 t^2)} \right] \quad (5.4)$$

In the slow fluctuation limit, the magnetic fluctuation rate ν depolarises the “1/3 tail” at long relaxation times. The muon depolarisation (Eq. 5.4) describes an effective local field $\Delta_{eff}^2 = \Delta_0^2 + R_b^2 \Delta_0^2$ and evolves from a Gaussian KT when $R_b = 0$ (displaying a distinctive dip in the data) towards a monotonic relaxation when $R_b \simeq 1$. Data in Fig. 5.10 (a) and 5.9 (a) were fitted to the GbG function using the Musrfit software [44] between 1.8 K and T_N with a maximum effective local field at 2 K ($\frac{\Delta_{eff}}{\gamma_\mu} = 0.014$ T) and $R_b \simeq 1$.

The mathematical approximation in Eq. 5.4 entails $\rho(\Delta_G) \neq 0$ for $\Delta_G < 0$ if $R_b \simeq 1$. As Δ_G is an absolute value the equation is redefined:

$$\rho(\Delta_G) \equiv \begin{cases} \rho(\Delta_G) + \rho(-\Delta_G) & \Delta_G > 0 \\ 0 & \Delta_G < 0 \end{cases} \quad (5.5)$$

its effect over the distribution of internal fields $\rho(\Delta_G)$ (Eq 5.3) as a function of Δ_G at 2 K and its temperature dependence are plotted in Fig. 5.11. The randomly orientated internal fields are evenly distributed from 0 to the fitted effective local field Δ_{eff} (shown by the arrow for $T=2$ K). Δ_{eff} as a function of the temperature is plotted in Fig. 5.12 (a) and fitted as an order parameter

$$\Delta_{eff} \propto (T_N - T)^\beta \quad (5.6)$$

with a critical exponent $\beta = 0.66 \pm 0.06$.

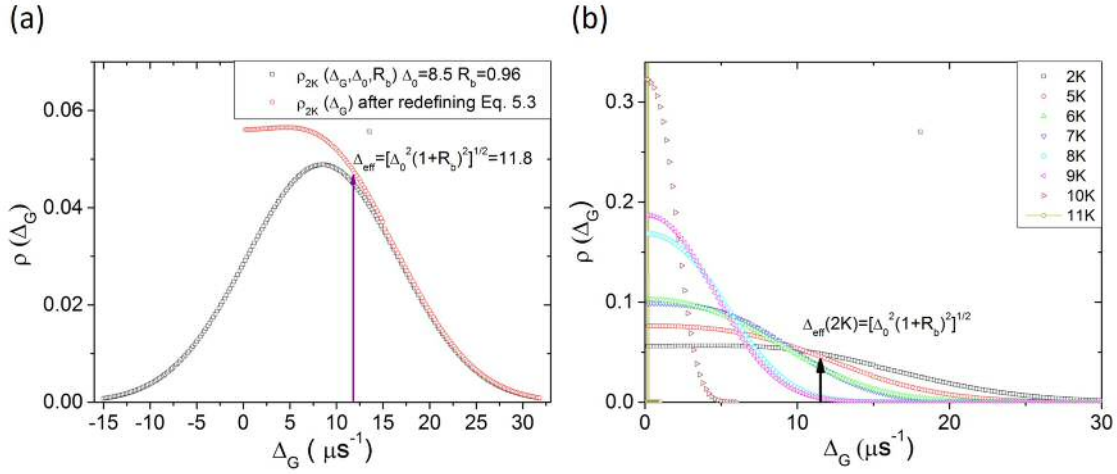


Figure 5.11: Gaussian weight function at 2 K and after redefining it by Eq. 5.5. (b) Distribution of the Gaussian weight function of internal fields as a function of temperature that spreads homogeneously from 0 to beyond Δ_{eff} .

The quasi-static nature of the internal fields was confirmed by longitudinal field LF- μ SR. In order to analyse and to test the distribution of fields described previously, the D_{GBG} function was discretised and the data fitted to a sum of single gaussian distributions, $D_G(\Delta_G)$, according to the weighting obtained from Fig. 5.11. ZF- μ SR were well-fitted to 17 gaussian distributions that were used to fit the longitudinal field data in Fig. 5.9 (b) by using the GKT under longitudinal field function introduced in Eq. 3.34.

The LF muon asymmetry spectra are repolarised when fields are applied, as expected from quasi-static internal fields. The effective local field at the muon sites can be estimated from the maximum field where slight wiggles can still be observed, $\frac{\gamma_\mu B_{ext}^{max}}{\Delta_{eff}} \sim 5 - 10$ (Sec. 3.4.2). $B_{ext}^{max} = 0.1$ T gives a $\frac{\Delta_{eff}}{\gamma_\mu} \sim 0.01 - 0.02$ T, in the same order of values obtained in ZF- μ SR measurement and hence, supporting the model. The scaling method from Rauch et al. [13] may be used to estimate the local magnetisation. The local magnetisation is calculated assuming it scales to the effective internal fields in the same way as the bulk magnetisation of the ferromagnetic doped samples scales to the muon oscillation frequency (Ω_B in that work). A local magnetisation of $M \approx 0.0075\mu_B/\text{Fe}$ is estimated.

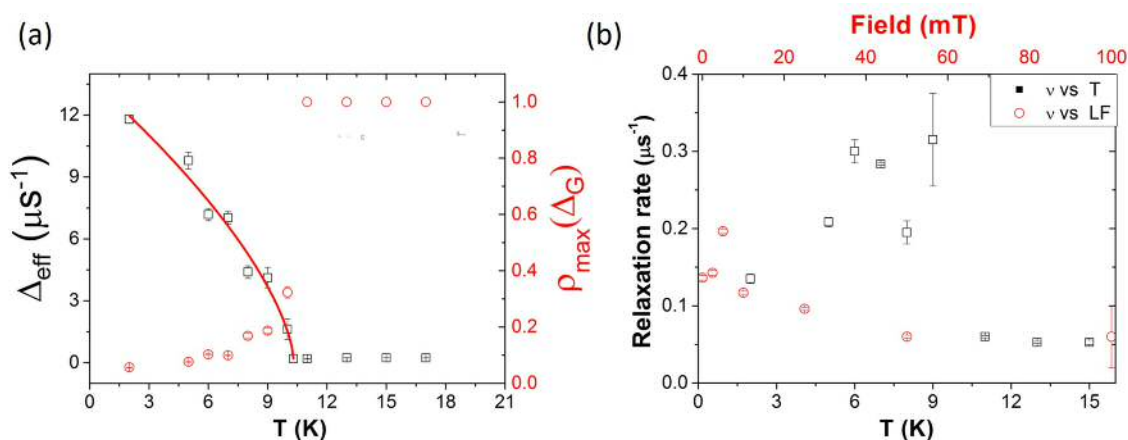


Figure 5.12: (a) Temperature dependence of the effective local fields and the maximum of the Gaussian weight function fitted to a critical exponent Eq. 5.6. (b) Fluctuations as a function of temperature (black squares) and field at 2 K (red circles) which remain below the slow fluctuation limit $\nu < \Delta_{eff}$. Values and errors are extracted from fitting data to Eq. 5.4.

The magnetic relaxation rate ν increases slightly when the temperature approaches T_N but remains in the slow fluctuation limit: $\nu < \Delta_{eff}$. When the longitudinal field is applied, the relaxation rate remains lower than $0.2\mu\text{s}^{-1}$ at 2K as can be seen in Fig. 5.12 (b). The nature of the magnetically ordered phase for this sample of NbFe_2 does not uniquely describe a simple spin density wave, as no oscillations are seen in the muon spectra in agreement with previous work [13]. In an incommensurate SDW phase, muons could depolarise according to a Bessel function, behaviour which could not describe the measured relaxation. However the quasi-static nature of random orientated internal fields were confirmed by the experiments.

In ZF- μSR , two relaxation processes are observed: a fast depolarisation due to the randomly-orientated static fields; and a slowly depolarising 1/3 region, corresponding to the internal fields parallel to the muon polarisation. In LF- μSR , muon decoupling is observed by applying fields as expected from quasi-static fields. The homogeneous distribution of internal fields Δ_{eff} is described by the GbG relaxation in the ZF data and by an equivalent sum of Gaussian relaxations for the LF

data. There is some evidence that this phenomenological behaviour might be induced by short-range spin correlations. However, simulations to determine the static field distribution to be expected from uncorrelated frozen states of non-dilute alloy spin glasses generated static-relaxation functions with a not significantly shallow minimum [28]. Some modifications lead to a range-correlated moment magnitude variation (RCMMV) microscopic model [29] that is able to generate shallow or monotonic static relaxation functions. It involves similar values of the magnitude of nearby magnetic moments that have uncorrelated orientations. The phenomenological R is the range of the correlations but no physical mechanism was suggested. A different approach related the short-range spin correlations in the quantum spin-liquid $\text{Yb}_2\text{Ti}_2\text{O}_7$ to describe the deviation of the Gaussian field distribution and the shallow KT [33]. In the present work, the value of R_b (R in the model) is always around 1 and a new physical mechanism is proposed for the phenomenological Gaussian-broadened GKT relaxation. In a helical SDW phase the moment orientation rotates from one unit cell to another and the muons will be affected by a broad distribution of fields but if the propagation vector is commensurate to the lattice randomness would not be expected at muon sites, therefore incommensurate and helical SDW might also explain the muon depolarisation. The subtle change of muon relaxation between our work and that of Rauch et. al [13], for at and just off stoichiometry as the QCP is approached suggests the importance of site mixing and that muon relaxation can be used to study the local magnetic environment in detail as the material is tuned towards the QCP. Importantly, the μSR data presented here and in previous work [13] suggest that application of longitudinal fields may reveal changes in the field distribution and fluctuation rates as the QCP is approached.

5.4 Conclusions

The magnetic ground state of nominally stoichiometric single crystalline NbFe_2 is investigated by bulk magnetisation and muon spin relaxation techniques. Magnetic order clearly emerges below the critical temperature $T_N=10.3$ K that is consistent with the Neel temperature reported at stoichiometry [6, 9, 11, 12]. However

this sample has a higher critical field, in the magnetically ordered phase.

A long range magnitude modulated SDW order cannot be confirmed by μ SR, but the system remain in the slow fluctuation regime of a magnetic state of randomly orientated quasi-static fields. The muon repolarisation under longitudinal field and the “1/3” region slowly depolarised is reminiscent of a Kubo-Toyabe function. The monotonic μ SR asymmetry was fitted with a phenomenological GbG Kubo-Toyabe function. The muon relaxation is due to randomly-orientated static fields with magnitudes homogeneously distributed from 0 to an effective field, Δ_{eff} , equivalent to $M \sim 0.0075\mu_B/\text{Fe}$ at 2K. Similar results by Rauch et al. [13] are explained as a magnitude modulated SDW with a large correlation length but the absence of oscillations and the distribution of the randomly-orientated quasi-static fields suggest a magnetic phase controlled by short-range correlations. However, an alternative mechanism is proposed. A SDW with a helical and incommensurate amplitude modulation as possible ground states. Recently, a new neutron scattering work demonstrated that SDW order emerges near the border of ferromagnetism [15] which would support the second interpretation of the μ SR experiment.

The sensitivity of μ SR to the distribution of local magnetic field in the vicinity of the QCP is clearly demonstrated, this suggests that further investigation of the muon relaxation as the QCP is approached will shed some light on the field distribution and fluctuations in $\text{Nb}_{1-y}\text{Fe}_{2+y}$.

References

- [1] M. Vasin, V. Ryzhov and V. M. Vinokur, *Quantum-to-classical crossover near quantum critical point*, Sci. Rep 5, p. 18600 (2015)
- [2] Q. Si and F. Steglich, *Heavy Fermions and Quantum Phase Transitions*, Science 329 (5996), p. 1161 (2010)
- [3] D. v. d. Marel, H. J. A. Molegraaf, J. Zaanen, F. Nussinov, Z. and Carbone,

- A. Damascelli, H. Eisaki, M. Greven, P. H. Kes and M. Li, *Quantum critical behaviour in a high- T_c superconductor*, Nature 425, p. 271 (2003)
- [4] G. Giovannetti, C. Ortix, M. Marsman, M. Capone, J. van den Brink and J. Lorenzana, *Proximity of iron pnictide superconductors to a quantum tricritical point*, Nat. Commun. 2, p. 398 (2011)
- [5] Y. Tokiwa, J. J. Ishikawa, S. Nakatsuji and P. Gegenwart, *Quantum criticality in a metallic spin liquid*, Nat. Mater. 13 (4), p. 356 (2014)
- [6] D. Moroni-Klementowicz, M. Brando, C. Albrecht, W. Duncan, F. M. Grosche, D. Grüner and G. Kreiner, *Magnetism in $Nb_{1-y}Fe_{2+y}$: Composition and magnetic field dependence*, Phys. Rev. B 79 (22), p. 224410 (2009)
- [7] Y. Yamada and A. Sakata, *Weak Antiferromagnetism in $NbFe_2$* , J. Phys. Soc. Jpn. 57 (1), p. 46 (1988)
- [8] D. Moroni-Klementowicz, R. Burrell, D. Fort and M. Grosche, *Quantum criticality in the frustrated Laves phase compound*, Physica B: Condens. Matter 359-361 (0), p. 80 (2005)
- [9] M. Brando, D. Moroni-Klementowicz, C. Albrecht and F. M. Grosche, *Quantum criticality in $NbFe_2$* , Physica B: Condens. Matter 378-380, p. 111 (2006)
- [10] R. Sato Turtelli, J. Sinnecker, R. Grössinger, a. Penton-Madrigal and E. Estevez-Rams, *Magnetic orderings and temperature dependence of the hysteresis loops of $Nb_{1-x}Fe_{2+x}$* , J. Magn. Magn. Mat. 316 (2), p. 492 (2007)
- [11] M. Brando, W. Duncan, D. Moroni-Klementowicz, C. Albrecht, D. Grüner, R. Ballou and F. M. Grosche, *Logarithmic Fermi-Liquid Breakdown in $NbFe_2$* , Phys. Rev. Lett. 101 (2), p. 026401 (2008)
- [12] S. Friedemann, M. Brando, W. Duncan, A. Neubauer, C. Pfleiderer and F. M. Grosche, *Ordinary and intrinsic anomalous Hall effects in $NbFe_2$* , Phys. Rev. B 87 (2), p. 024410 (2013)

- [13] D. Rauch, M. Kraken, F. J. Litterst, S. Süllo, H. Luetkens, M. Brando, T. Förster, J. Sichelschmidt, A. Neubauer, C. Pfleiderer, W. J. Duncan and F. M. Grosche, *Spectroscopic study of metallic magnetism in single-crystalline Nb_{1-y}Fe_{2+y}*, Phys. Rev. B 91, p. 174404 (2015)
- [14] T. D. Haynes, I. Maskery, M. W. Butchers, J. a. Duffy, J. W. Taylor, S. R. Giblin, C. Uffeld, J. Laverock, S. B. Dugdale, Y. Sakurai, M. Itou, C. Pfleiderer, M. Hirschberger, a. Neubauer, W. Duncan and F. M. Grosche, *Ferrimagnetism in Fe-rich NbFe₂*, Phys. Rev. B 85 (11), p. 115137 (2012)
- [15] P. G. Niklowitz, M. Hirschberger, M. Lucas, P. Cermak, A. Schneidewind, E. Faulhaber, J.-M. Mignot, W. J. Duncan, C. Neubauer, A. and Pfleiderer and F. M. Grosche, *Ultra-small moment incommensurate spin density wave order masking a ferromagnetic quantum critical point in NbFe₂*, arXiv:1704.08379 (2017)
- [16] A. V. Chubukov, C. Pépin and J. Rech, *Instability of the quantum-critical point of itinerant ferromagnets*, Phys. Rev. Lett. 92 (14), p. 147003 (2004)
- [17] M. Shiga and Y. Nakamura, *Magnetic Properties of Stoichiometric and Off-Stoichiometric NbFe₂*, J. Phys. Soc. Jpn. 56 (11), p. 4040 (1987)
- [18] M. Kurisu, Y. Andoh and Y. Yamada, *Magnetic properties of NbFe₂ single crystal*, Physica B: Condens. Matter 237-238, p. 493 (1997)
- [19] Y. Yamada, H. Nakamura, Y. Kitaoka, K. Asayama, K. Koga, A. Sakata and T. Murakami, *NMR Study of Weak Antiferromagnetism in NbFe₂*, J. Phys. Soc. Jpn. 59 (8), p. 2976 (1990)
- [20] R. Crook, M R. Cywinsky, *Spin Fluctuations and Magnetic Order in Nb_{1-x}Zr_xFe₂*, Hyperfine Interact. 85, p. 203 (1994)
- [21] M. R. Crook and R. Cywinski, *Magnetic transition in Nb_{1-y}Fe_{2+y}*, J. Magn. Mater. 144, p. 71 (1995)

- [22] M. Crook, *Spin Fluctuations and itinerant magnetism in the hexagonal Laves phase $NbFe_2$ and related compounds*, Ph.D. thesis, The University of Reading (1995)
- [23] S. Asano and S. Ishida, *Competition of magnetism in iron Laves phase compounds*, J. Phys. Condens. Matter 1 (44), p. 8501 (1989)
- [24] A. Subedi and D. J. Singh, *Band structure and itinerant magnetism in quantum critical $NbFe_2$* , Phys. Rev. B. 81 (2), p. 024422 (2010)
- [25] D. A. Tompsett, R. J. Needs, F. M. Grosche and G. G. Lonzarich, *Doping-driven magnetic instabilities and quantum criticality of $NbFe_2$* , Phys. Rev. B 82 (15), p. 155137 (2010)
- [26] A. Alam and D. D. Johnson, *Chemically Mediated Quantum Criticality in $NbFe_2$* , Phys. Rev. Lett. 107 (20), p. 206401 (2011)
- [27] B. P. Neal, E. R. Ylvisaker and W. E. Pickett, *Quantum criticality in $NbFe_2$ induced by zero carrier velocity*, Phys. Rev. B 84 (8), p. 085133 (2011)
- [28] D. R. Noakes and G. M. Kalvius, *Anomalous zero-field muon spin relaxation in highly disordered magnets*, Phys. Rev. B 56 (5), p. 2352 (1997)
- [29] D. R. Noakes, *A correlation length measured by zero-field muon spin relaxation in disordered magnets*, J. Phys. Condens. Matter 11, p. 158 (1999)
- [30] P. Dalmas de Réotier, V. Glazkov, C. Marin, A. Yaouanc, P. Gubbens, S. Sakarya, P. Bonville, A. Amato, C. Baines and P. King, *Studies of $R_2Ti_2O_7$ ($R=Gd$ and Yb); new results*, Physica B 374-375, p. 145 (2006)
- [31] R. Dally, T. Hogan, A. Amato, H. Luetkens, C. Baines, J. Rodriguez-Rivera, M. J. Graf and S. D. Wilson, *Short-Range Correlations in the Magnetic Ground State of $Na_4Ir_3O_8$* , Phys. Rev. Lett. 113, p. 247601 (2014)
- [32] D. E. MacLaughlin, P.-C. Ho, L. Shu, O. O. Bernal, S. Zhao, A. A. Dooraghi, T. Yanagisawa, M. B. Maple and R. H. Fukuda, *Muon spin rotation and relax-*

- ation in $Pr_{1-x}Nd_xOs_4Sb_{12}$: *Magnetic and superconducting ground states*, Phys. Rev. B 89 (14), p. 144419 (2014)
- [33] A. Yaouanc, A. Maisuradze and P. Dalmas De Réotier, *Influence of short-range spin correlations on the μ SR polarization functions in the slow dynamic limit: Application to the quantum spin-liquid system $Yb_2Ti_2O_7$* , Phys. Rev. B 87, p. 134405 (2013)
- [34] D. Margineda, J. Duffy, J. Taylor and S. Giblin, *μ SR study of stoichiometric $NbFe_2$* , Physica B: Condens. Matter 504, p. 121 (2017)
- [35] T. Moriya, *Spin Fluctuations in Itinerant Electron Magnetism*, Springer Series in Solid State Sciences (Springer-Verlag, 1985)
- [36] A. P. Ramirez, *Strongly Geometrically Frustrated Magnets*, Annu. Rev. Mater. Sci. 24 (1), p. 453 (1994)
- [37] J. Inoue and M. Shimizu, *Electronic structure and magnetic properties of off-stoichiometric $NbFe_2$* , J. Magn. Magn. Mater. 79 (2), p. 265 (1989)
- [38] S. Lee, S. Kilcoyne and R. Cywinski (eds.), *Muon Science. Muons in Physics, Chemistry and Materials* (Scottish Universities Summer School in Physics and Institute of Physics Publishing, Bristol and Philadelphia, 1998)
- [39] A. Yaouanc and P. Dalmas de Réotier, *Muon Spin Rotation, Relaxation and Resonance: Applications to Condensed Matter* (Oxford University Press, Oxford, 2011)
- [40] M. J. Graf, S. M. Disseler, C. Dhital, T. Hogan, M. Bojko, A. Amato, H. Luetkens, C. Baines, D. Margineda, S. R. Giblin, M. Jura and S. D. Wilson, *Magnetism and magnetic order in the pyrochlore iridates in the insulator-to-metal crossover region*, J. Phys. Conf. Ser. 551 (1), p. 012020 (2014)
- [41] D. Ryan, J. Van Lierop and J. Cadogan, *Zero-field muon spin relaxation studies of frustrated magnets: physics and analysis issues*, J. Phys. Condens. Matter 16 (40), p. S4619 (2004)

- [42] J. A. Mydosh, *Spin glasses: an experimental introduction* (Taylor and Francis, 1993)
- [43] J. A. Hodges, P. Bonville, A. Forget, A. Yaouanc, P. Dalmas De Réotier, G. André, R. M. K. K. Ritter, P. C. M. Gubbens, C. T. Kaiser, P. King and C. Baines, *First-Order Transition in the Spin Dynamics of Geometrically Frustrated $\text{Yb}_2\text{Ti}_2\text{O}_7$* , Phys. Rev. Lett. 88, p. 077204 (2002)
- [44] <http://lmu.web.psi.ch/musrfit/technical/index.html> (2016)

“...although more than 30 years have elapsed since the discovery of heavy-fermion superconductors, the actual symmetry of the Cooper pairs of any of them has not yet been unambiguously determined.”

M.R. Norman, 2011 [1]

6

Ground state of CeRhIn₅ at ambient pressure

6.1 Introduction

The discovery of pressure-induced superconductivity (SC) in the antiferromagnet (AFM) CeRhIn₅ [2] and at ambient pressure (P_{amb}) in CeCoIn₅ [3] and CeIrIn₅ [4] with $T_c = 0.4$ K and 2.3 K respectively gave rise to a new family of compounds (Ce-115) to investigate unconventional SC that interplays with localised AFM.

CeRhIn₅ is an example of the high sensitivity to the density of states of the Fermi volume in some heavy-fermions. The antiferromagnetic order at P_{amb} , with $T_N = 3.8$ K, is consistent with a small Fermi volume deduced from de Haas-van-Alphen (dHvA) results [5] associated with localised 4f-electrons but under hydrostatic pressures it becomes a superconductor. Under pressure the lattice parameter

is distorted until it corresponds to CeIrIn₅ [6] and a drastic change from small to large Fermi surface at $P_c = 2.35$ GPa [7] takes places in agreement with CeCoIn₅. The large Fermi surface with a quasi-two-dimensional character of the Ir and Co compounds are well explained by the 4f-itinerant band model where the heavy-fermions condense into the superconducting state. The 4 f-electron character in CeRhIn₅ is thus changed from localized to itinerant at P_c where the superconducting transition temperature becomes a maximum [7].

The limiting cases of localised and itinerant 4f-electrons are approached in CeRhIn₅ by applying moderate pressures. The transition is predicted by the Doniach's diagram for heavy fermions (see Sec. 2.6) where the Kondo exchange interaction competes with the RKKY interaction. However, the temperature-pressure (T-P) phase diagram in CeRhIn₅ has created interest due to a region where AFM and SC coexist common in some unconventional superconductors [8]. The nature of the superconducting phase in that region is still unclear. Filamentary SC is proposed based on the anisotropic resistivity transition [9] or the absence of SC evidence in some specific heat works [10, 11] at low or ambient pressures. They do not agree with the SC occurrence at P_{amb} [12] where bulk SC is claimed [13, 14]. In this work μ SR experiments down to 50 mK at P_{amb} , never been performed before, are carried out in order to add a new tool to investigate the nature of the magnetic ground state of CeRhIn₅. The local magnetic probe can differentiate coexisting phases in the same specimen. The μ SR signal is proportional to the muons stopped at the different phases and distinct signals are able to recognise and provide quantitative information of the coexisting and competing phases. Results are complemented by resistivity measurements down to 20 mK.

CeRIn₅ compounds with R=Rh, Co and In have the HoCoGa₅-type tetragonal structure (P4 /mmm) with alternating layers of CeIn₃ and RIn₂ (Fig. 6.1). At P_{amb} the RKKY interaction is dominant and there is some agreement about the magnetic structure among the used techniques including, nuclear quadrupole resonance (NQR) [15] and neutron scattering [16–19]. At T_N , the compound enters into

an incommensurate helical structure with the moments residing on the Ce ion and confined in the (a,b) plane that propagate in spiral along the c axis with a magnetic wave vector $\mathbf{q} = (0.5, 0.5, 0.297)$ [16]. Therefore, the nearest neighbour moments are aligned antiferromagnetically on the tetragonal basal plane and turn by about 107° per CeIn_3 layer. Minor discrepancies are found in μSR Schenck et al. work [20]. The relaxation is not understood without the occurrence of a small and undetectable, by neutron diffraction, Rh moment with magnitude $\mu = 0.09 \mu_B$ parallel to the c axis that might play a particular role in the helical structure. Neutron scattering results also determine the ordered magnetic moment $m_0 = 0.37 \mu_B/\text{Ce atom}$ [16, 17], although a substantially larger value were also found [18, 19]. The rather moderate enhanced Sommerfeld coefficient γ below T_N [10, 11] and the low $T_K \approx 0.15\text{K}$ [21] support the dHvA measurements confirming the localised nature of the 4f electrons that do not contribute to the Fermi Volume.

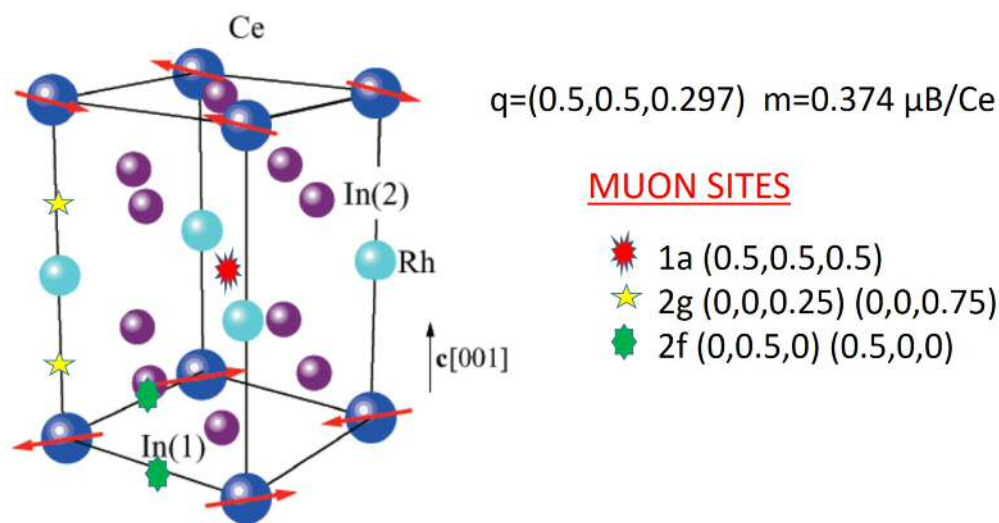


Figure 6.1: Schematic plot of the CeRhIn_5 tetragonal crystal structure. The interstitial muon sites suggested by [20] 1a (red), 2g (yellow) and 2f (green) are flagged in the unit cell. Ce magnetic moments (m) are confined in the ab plane aligned antiferromagnetically. They propagate in spiral along the c axis forming an incommensurate helical structure with propagation vector q [16].

To understand the goal of this work it is necessary to briefly discuss the CeRhIn₅ ground state as a function of pressure. Widely investigated with thermodynamic, magnetic, transport and local magnetic probes [10, 19, 22, 23], the ground state broadly corresponds to the T-P phase diagram suggested by Park et al. [11] from specific heat and resistivity measurements shown in Fig. 6.2. Inset includes Chen et al. ac-susceptibility measurements (black dots) where SC at P_{amb} were found [13]. Color dots correspond to previous works. General features and relevant discrepancies from other comprehensive studies like the Knebel et al. work [10] will be discussed. For instance different critical values from the later work will be in parenthesis. The few works that have reported SC at P_{amb} and the unsolved features that motivate this work are discussed afterwards.

By applying pressure, the transition from the localised AFM to the itinerant SC can be divided in three regions. At low pressure, $P < P_x = 0.9$ GPa, the ground state is purely antiferromagnetic with a subtle increase in T_N . The maximum T_N is reached at P_x where the onset of a SC transition in specific heat (susceptibility) and resistivity [19] were found. Above those pressures, T_N decreases monotonically until the magnetic transition abruptly disappears at a critical pressure $P_1 = 1.75$ (1.95) GPa suggesting a first-order like transition. Simultaneously, T_c increases until it meets T_N at P_1 . Above P_1 , the ground state is purely superconducting with a maximum $T_c = 2.2$ K at 2.05 GPa. AFM is not suppressed continuously to zero Kelvin by pressure but a smooth extrapolation of T_N (dotted line) suggests a QCP at P_2 near 2.3 GPa. Specific heat measurements at $P > P_1$ and under applied field, H , found hidden magnetism at $T < T_c(H)$ giving rise to a line (in the pressure-field phase diagram) of QCPs induced inside the superconducting state at pressures $P_1 < P < P_2$ [8]. The field required to induce magnetism meets the critical field at P_2 , a tetra-critical point as disordered phases emerges at fields larger than the critical value. The superconducting ground state is suppressed at pressures ≈ 8.5 GPa [22] and its nature is most likely an unconventional (d-wave) superconducting phase [10, 11, 24].

Although the low-pressure magnetic ordered phase and the high-pressure un-

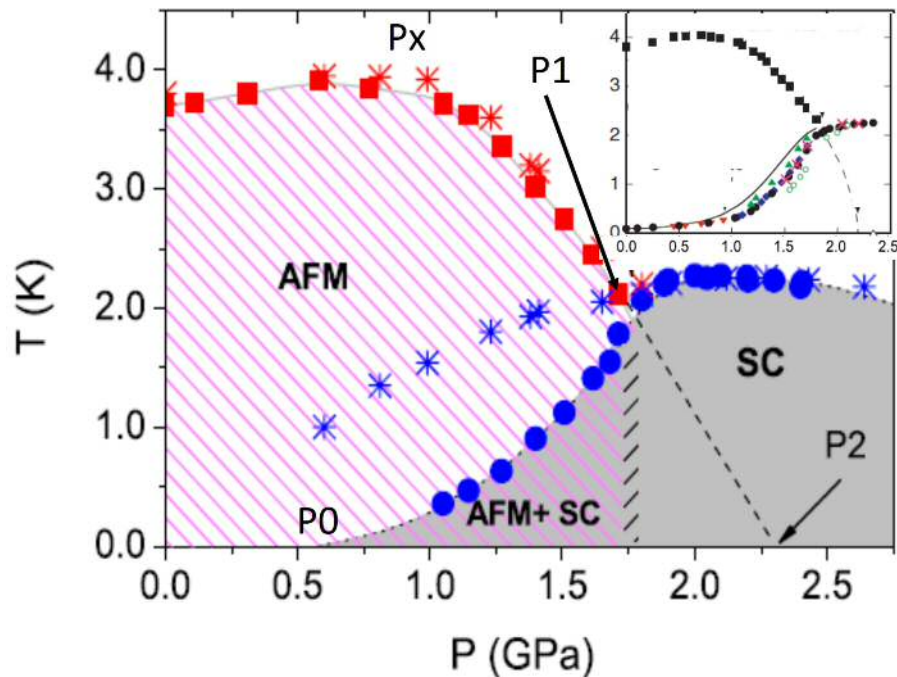


Figure 6.2: CeRhIn_5 T-P phase diagram at zero field determined by specific heat (filled symbols) and resistivity (crosses) from [11]. SC onset at $P_x \simeq 0.9$ GPa coincides with the maximum T_N . AFM phase vanishes at P1 although a field-induced QCP can be reached at P2. Inset. Different behaviour has been found at low pressures. The updated phase diagram proposed by [13] is shown in the inset figure. T_c from ac susceptibility (filled symbols) coincides with bulk SC from previous measurements (color symbols) under pressure, but a new SC transition was also reported at low and ambient pressure.

conventional SC seems to be well understood, the nature of the SC order parameter in the coexisting region is still under debate. Theoretical predictions are varied, from d-wave [25] to a gapless p-wave SC [26] with some experimental evidences of both d-wave [27] and p-wave [28]. This leads to the question that motivates this experiment. Do AFM and SC phases really coexist at ambient pressure? Are the same 4f electrons responsible of both magnetism and unconventional SC like Cu 3d electrons in high- T_c cuprates or like in some Fe-pnictide superconductors? [29] Arguments for separated phases without bulk SC are given by Knebel et al. [10] whose specific heat data do not present any anomaly below P1. The absence of anomalies would suggest a gapless superconductivity and a transition from a gapless p- to a gapped d-wave state is opposed to the P_c point nature [10]. They argue that the

appearance of SC in the AFM ordered state is not homogeneous as the resistivity and susceptibility transitions are not a bulk probe of SC. Instead of the coexistence, they claim that superconducting filaments can be created due to internal stress induced by dislocations or stacking faults or even a phase segregation. Other possible causes of inhomogeneity such as pressure gradients in the pressure cell are ruled out. The broad region of pressure where phases coexists is larger than the pressure differences expected inside the cells.

Access to lower temperatures allowed the observation of the SC transition in the specific heat and a better understanding of the coexisting phases. The entropy at T_N and T_c as a function of the pressure displays an entropy transfer from the AFM to the SC entropy that may be interpreted as a 4f electron participation in both phases [11]. These measurements suggest a magnetic origin in the unconventional SC that would be supported by the SC at P_{amb} , however they were unable to detect any hint in the specific heat above 70 mK which is consistent with the bulk T_c extrapolation, $P_0 (T_c=0) = 0.5$ GPa. In the phase diagram (Fig. 6.2), the SC transition in the resistivity measurements was found at different temperatures. Although the authors observed a slight decrease below 50 mK at P_{amb} , resistivity sharply drops at P_0 with a larger T_c than in specific heat data. It opposes the bulk nature of the SC and encourages one to think that filamentary SC is possible for instance by magneto-elastic coupling that induces SC at AFM domain walls before it becomes SC at lower temperatures. The onset of superconducting filaments is supported by anisotropic resistivity [9]. The discrepancy between the thermodynamic and resistive transition disappear at P_1 suggesting that SC does not arise from internal structural strains or defects. Instead, the emergence of a new incommensurate [30] or commensurate [31] magnetic structure at P_1 might induce the formation of lamellar SC that would explain the anisotropic resistivity and the different bulk and resistive transition.

The SC found at P_{amb} opens a new scenario in the controversial nature of the superconducting phase in the intermediate pressure region. The first evidence

of SC at P_{amb} was found in the ac magnetic susceptibility that drops to a perfect diamagnet at 90 mK, a transition that disappears after powdering the sample [12].

A more detailed study of the ac-susceptibility as a function of the pressure was carried out by Chen et. al. [13]. It provided more information about the low-pressure transition and the correlation between the unconventional SC and the AFM order. The real susceptibility-temperature curve for different pressures clearly drops to a diamagnetic signal below $T_c \simeq 90mK$ at P_{amb} , (Fig. 6.3 (a)).

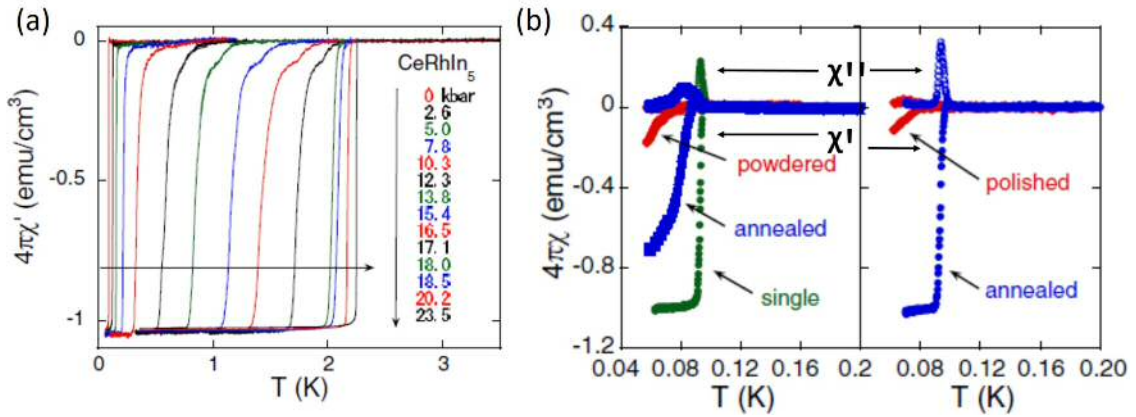


Figure 6.3: (a) $\chi'(T)$ for different pressures. (b) Powdering and polishing effects in χ at P_{amb} taken from [13].

T_c measurements taken on several samples roughly overlap with the specific heat transition found in Park et al. work. Although in the new T-P phase diagram (Fig. 6.2 inset) the T_c extrapolation line is overdamped and SC remains down to ambient pressure. Again, the decrease in T_N , above 1 GPa matches with the step rise of T_c .

In that work, evidences of the competition of SC and AFM at the Fermi surface were also given by fitting the critical temperatures to

$$T_c^n T_N^{1-n} = T_{c0} \quad (6.1)$$

where $n \equiv \gamma_0/\gamma_n$ denotes the ratio between the electronic Sommerfeld specific heat coefficient in the AFM and the PM phase and T_{c0} is a hypothetical SC transition

temperature in the absence of the AFM order. $n \simeq 0.13\%$ at P_{amb} indicates that only 13% of the Fermi surface states participate in the SC phase. The curve given by T_c^n in Eq. 6.1 has a good agreement with the experimental data and an extrapolation of n , $P_y = \lim_{n \rightarrow 1} P = 2.2$ GPa was used to estimate $T_{c0} = 2.2$ K. It is relevant that P_y is close to the field-induced QCP, P2 where T_c is maximum. It may infer that AFM order does not disappear at P1 and the SC screens out its signal. Again, the sensitivity to inhomogeneity is shown in the loss of superconductivity by powdering and polishing the sample that is recovered after annealing (Fig. 6.3 (b)). Although the diamagnetic signal is not conclusive to claim if the SC nature is filamentary or bulk, the sharp drop in $\chi'(T)$, the full shielding effect ($4\pi\chi'(T) \simeq -1$), the correlation between T_N and T_c and the similar (in contrast with other works) T_c from bulk (specific heat) and susceptibility measurements under pressure support the bulk character of the SC.

This interpretation is sustained by Paglione et al. work [14] where the observation of a phase transition in specific heat data (110 mK) occurs simultaneously with both a diamagnetic drop in magnetic susceptibility and a drop in electrical resistivity at P_{amb} . Unfortunately, the evidence of the bulk transition is obscured by a large contribution from a nuclear Schottky anomaly, which is removed by a fitting procedure, and the lowest temperature reached in the experiment (70-80 mK) was very close to the transition which motivates to find new proofs of SC at P_{amb} .

Summarising, it seems clear from the entropy [11] and the susceptibility [13] studies that the unconventional SC is correlated with the AFM order in such a way that the SC is enhanced when the long-range AFM decreases in the region where both coexists. The nature of the SC phases is still under debate. Although the pressure inhomogeneity can be ruled out as a reason of the apparent coexistence, the textured or bulk nature is not completely clear. Whereas, the anisotropic resistivity [9] and discrepancies in bulk and resistive T_c [11, 19, 32] may indicate laminar SC emerging from a new AFM phase [30, 31], the agreement in the specific heat and susceptibility T_c at low [13] and ambient pressure [14] together with the full

diamagnetism support the bulk SC.

6.2 Muon spin relaxation

Muon spin relaxation measurements were performed at ISIS Muon Facility using the general purpose spectrometer (MuSR) to investigate the CeRhIn_5 ground state. MuSR is a 64-detector μSR spectrometer with two circular arrays of detectors which can be rotated through 90° to enable both longitudinal and transverse measurements. The incommensurate and antiferromagnetic helical structure was analysed with zero-field (ZF- μSR) in the longitudinal configuration and the reported superconducting ground state was investigated by transverse-field (TF- μSR) according to Sec. 3.5. Fig. 6.4 depicts detectors with the field orientation (yellow arrow) regarding the muon beam (red arrow) and polarisation (\mathbf{S}_μ) for both configurations. The positron detectors are grouped in 8 clusters in which each one detectors have similar orientation with the sample.

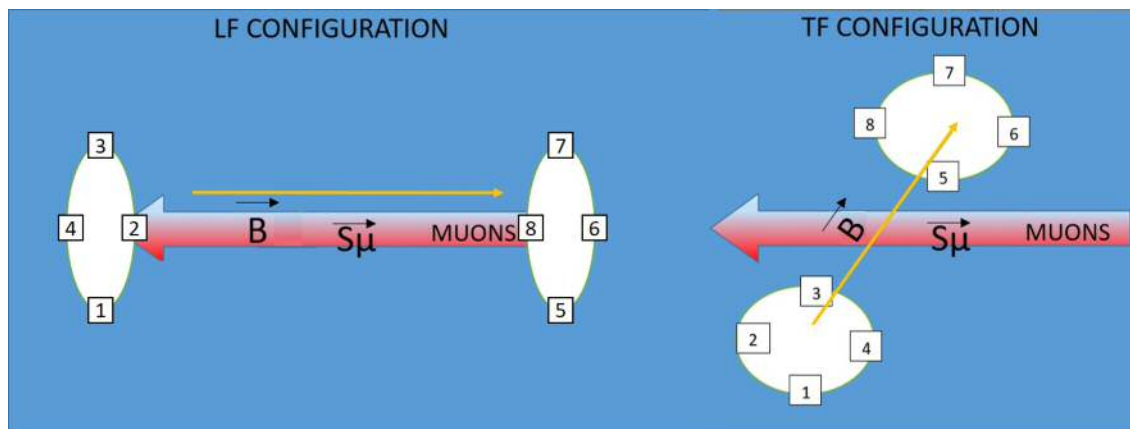


Figure 6.4: Scheme of LF- and TF- configurations of the MuSR spectrometer. 64 detectors are grouped in 8 detector clusters. The red and the yellow arrow specify the muon beam (antiparallel to the muon spin polarisation, \vec{S}_μ) and the field direction.

Three different experiments were run in the spectrometer to deal with different issues faced. The first one registered some problems to thermalise at the base temperature that were fixed in the second one. In the last one the sample area was

increased to decrease the background signal of the Silver sample holder previously detected. Samples were prepared using the self-flux method [4]. The mounted samples for the different experiments are shown in Fig. 6.5. As the sample and the muon depolarisation for the first two experiment were similar only results for the last two experiments, labelled (s1) and (s2), will be discussed. Samples were aligned by Chris Stock using neutron scattering and located with the c axis out of plane and parallel to the muon beam. In the transverse configuration, the field was applied along the b axis.



Figure 6.5: Samples mounted in a Silver holder.

6.2.1 Longitudinal field configuration

In the PM phase, above T_N , only randomly orientated static nuclear moments contribute to the muon depolarisation. The non-relaxing background contribution due to the fraction of muons that stop at the Silver sample holder, a_{bg} , is calculated by fitting the μ^+ -decay asymmetry to

$$A(t) = a_s P_G(\Delta_G, t) + a_{bg} \quad (6.2)$$

being $P_G(\Delta_G, t)$ the GKT function given by Eq. 3.28. $A(t)$ for s1 is plotted in Fig. 6.6. Three muon sites were predicted by Schenck et al. [20] but data are well-fitted to one average relaxation rate from all muon sites. The average local field is

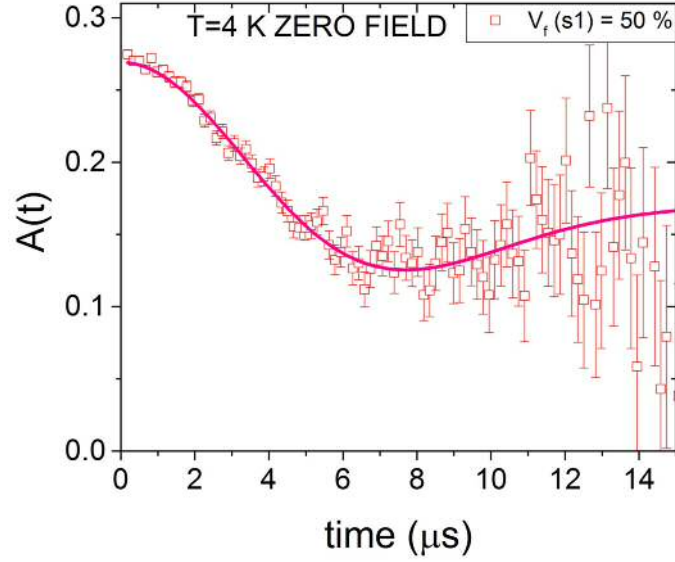


Figure 6.6: (a) ZF- μ SR at $T=4.2$ K (above T_N) for sample1. Silver background and then the volume fraction V_f is calculated from the GKT fits.

$\Delta_G = (0.23 \pm 0.01)\mu s^{-1}$ or $\Delta_G/\gamma_\mu \simeq 2.7$ G. Volume fraction or muons that stop at the sample ($V_f \simeq 50$ %) is given by $a_{bg} = 0.135$ and the initial asymmetry $A(t=0)=a_0 = a_s + a_{bg} = 0.27$. The initial asymmetry and α , that depends on the relative position of the sample with the detectors, are calculated by the application of a 20 Oe transverse field perpendicular to the muon beam (TF20) in the PM phase. The oscillating behaviour reflects the precession of the muons around the applied field and the μ^+ -decay asymmetry will respond to

$$A(t) = a_0 P(t) = a_0 \left[\sum_{i=1}^N f_i e^{-\frac{\sigma_i^2 t^2}{2}} \cos(\gamma_\mu B_i t + \phi_i) + f_{bg} e^{-\lambda t} \cos(\gamma_\mu B_0 t + \phi_0) + f_{no} \right] \quad (6.3)$$

where $\gamma_\mu = 2\pi \cdot 13.55$ kHz/G is the muon gyromagnetic ratio. The oscillating spin polarisation of muons in the sample are fitted by the first term, the second term takes into account those that stop in the sample holder. f_{no} is added to reflect muons that are not affected by the transverse field in the magnetically ordered phase below T_N .

Fig. 6.7 shows the TF20 polarisation above and below T_N for $s1$ and $s2$ in the frequency (fields) and time domain. $\alpha = 1.64$ and 1.72 are obtained for each sample respectively. In the PM phase, muon polarisation is precisely fitted to Eq. 6.3 with fields $B_{0,1} \simeq 20$ G and $f_{no} = 0$. It was assumed that muons in the sample oscillate jointly, $N=1$, with $f_1 = f_{bg} = 0.5$ as $V_f \simeq 50\%$. In this case, the relaxation rate σ takes into account the field spread produced by the In nuclear-dipole fields [20]. Muons in Silver barely depolarise $\lambda = 0.05 \mu s^{-1}$. The fact that muons stop in two different materials that are physically separated prevents an accurate fitting with only one term. As a result, an initial phase $\phi_0 \simeq 10$ and different values for B_0 and B_1 are detected.

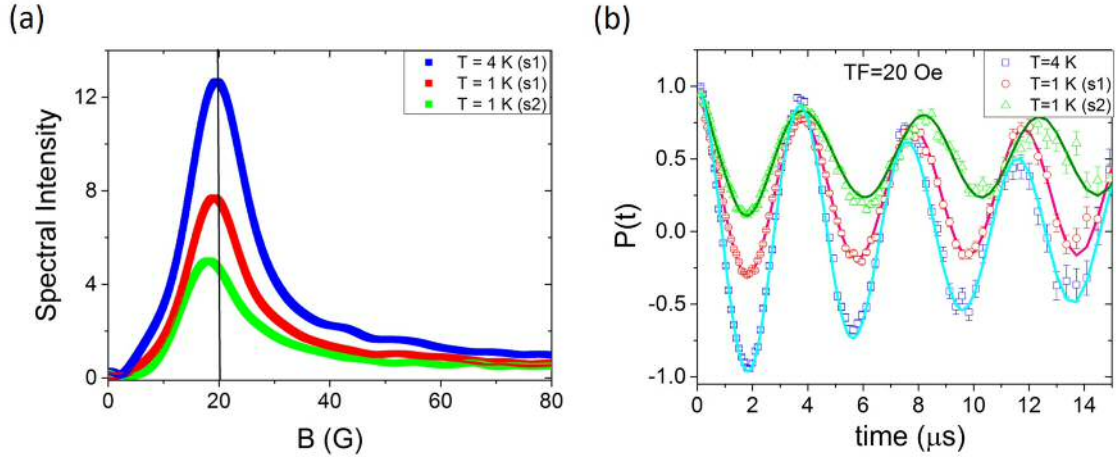


Figure 6.7: (a) Fourier transform of TF- μ SR by applying $H \simeq 20$ Oe for $s1$ above T_N and below for $s1$ and $s2$. $B_p^{s1}(4K) = 19.6$ G, $B_p^{s1}(1K) = 19.1$ G and $B_p^{s2}(1K) = 18.7$ G. (b) TF- μ SR in the time domain. The volume fraction V_f is estimated to be $V_f \simeq 90\%$ for $s2$ from fitting parameters. A variable binning parameter was used to reduce error bars at large times.

The magnetically ordered phase is firstly investigated by carrying out TF20 measurements below T_N . Qualitatively, some evidences of the magnetic phase are clearly observed in both time and frequency domain data. A significant proportion of the muons do not oscillate under the field, but also there is a shift to lower frequencies. There are also indications of more than one component or magnetically non-equivalent muon sites in the time domain, since the frequency shift is less

noticeable at early times. However, the FT is unable to solve a second peak but a widening is observed. Furthermore, a unique component N in Eq. 6.3 failed to achieve a reasonable good fit. The large baseline may be explained by fields along the c axis at the muon sites larger than the transverse field.

Quantitatively, the ratio of muons that oscillate below the transition are $\sim 71\%$ for $s1$ and $\sim 47\%$ for $s2$. It was assumed that muons stopped in the Silver holder are not affected by the sample magnetic moment. Therefore, fits to Eq. 6.3 were made by fixing the Silver parameters obtained in the paramagnetic phase: $B_0 = 19.6$ G from the FT data; and ϕ_0 and λ from the time domain data. For $s1$, $f_{bg} = 0.5$ from the volume fraction. For muons in the magnetic sample, the main value of the single broad peak in Fig. 6.7 (a) was used initially with a poor agreement, so two components $N=2$ were used as suggested before. $\sigma^2 = \gamma_\mu^2 \langle \Delta B^2 \rangle$ is now produced by the spread of fields at the muon sites resulting from the sum of the internal and the applied fields.

For $s2$ the frequency shift is more pronounced since the volume fraction is larger, but ZF- μ SR above T_N was not measured and the volume fraction has to be estimated by an alternative method. It can be obtained from the background f_{no} and $x \equiv \sum \frac{f_i}{V_f}$

$$1 = \frac{f_{no}}{V_f} + \sum \frac{f_i}{V_f} \quad (6.4)$$

$$V_f = \frac{f_{no}}{1 - \sum f_i/V_f} \quad (6.5)$$

If it is assumed that $x = 41\%$ obtained for $s1$ does not change from one sample to another $V_f \sim 90\%$ for $s2$. The constraint will give consistency to the fit. Fitting parameters for the oscillating components are summarised in Table 6.1.

This analysis is unable to give a full picture of the magnetic phase but different muon sites and depolarisation rates for each sample reveal a magnetic phase that

Table 6.1: Fitting parameters of the TF20 measurements above and below T_N for the muons stopped in the sample. Fitting errors in parentheses.

sample	B_1 (G)	ϕ_1	$\sigma_1(\mu\text{s}^{-1})$	f_1/V_f	B_2 (G)	ϕ_2	$\sigma_2(\mu\text{s}^{-1})$	f_2/V_f
s1 (4K)	20.2(1)	0	0.14	100%	–	–	–	0%
s1 (1K)	16.7(2)	-23(2)	0.141(2)	19%	21.6(1)	56(2)	0.14(1)	22%
s2 (1K)	16.8(1)	36(1)	0.02(1)	24%	21.6(3)	-20(5)	0.51(1)	17%

produces a less simple distribution of fields. Although this work does not seek to give a very detailed picture of the antiferromagnetic helical structure, the ZF- μ SR study of the ordered phase can be compared with the Schenck et al. muon work [20]. In that work, a TF experiment above T_N together with calculations of the dipolar interactions were used to work out the paramagnetic Knight shift and the muon sites depicted in the crystal lattice structure (Fig. 6.1).

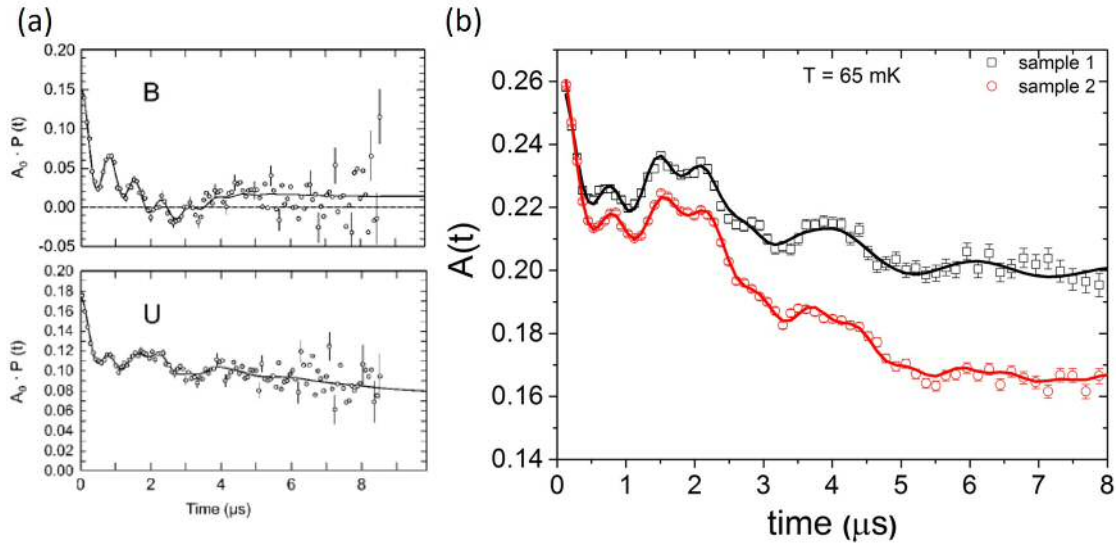


Figure 6.8: (a) ZF- μ SR at different orientations from ref. [20]. (b) ZF- μ SR for sample 1 (black squares) and sample 2 (red circles) with a non-relaxing signal equivalent to the U orientation in (a). Non-relaxing signal is due to internal fields at muon sites parallel to the detectors or muons stopped at the silver holder, which are reduced in sample 2. The raw bin size 16 ns is increased for visualisation by a variable bunching factor. Fits described in text.

The ZF- μ SR with the forward and backward detectors aligned to the c axis is depolarised by the effect of several internal fields down to a baseline that does not correspond to the volume fraction, Fig. 6.8 (b). The lower baseline for $s2$ is due to the larger volume fraction. The assumption of the large proportion of fields at the muon sites aligned to the c -axis is confirmed by the Schenck's work in the GPS spectrometer at PSI that gives the freedom to rotate the sample with respect the beam direction. Fig. 6.8 (a) shows the μ^+ -decay asymmetry with the muon beam aligned to the a -axis. B and U refers to the backward-forward or up-down detectors used to measure. According to the sample orientation U detectors are along the c -axis and equivalent to our measurements. In those detectors, the internal fields at the muon sites aligned to the c -axis that do not produce an oscillating signal in the detectors is $\sim 55\%$. Asymmetry at B detectors, aligned to the a -axis, depolarises completely because the initial muon polarisation is rotated by about 47° from parallel to the beam direction.

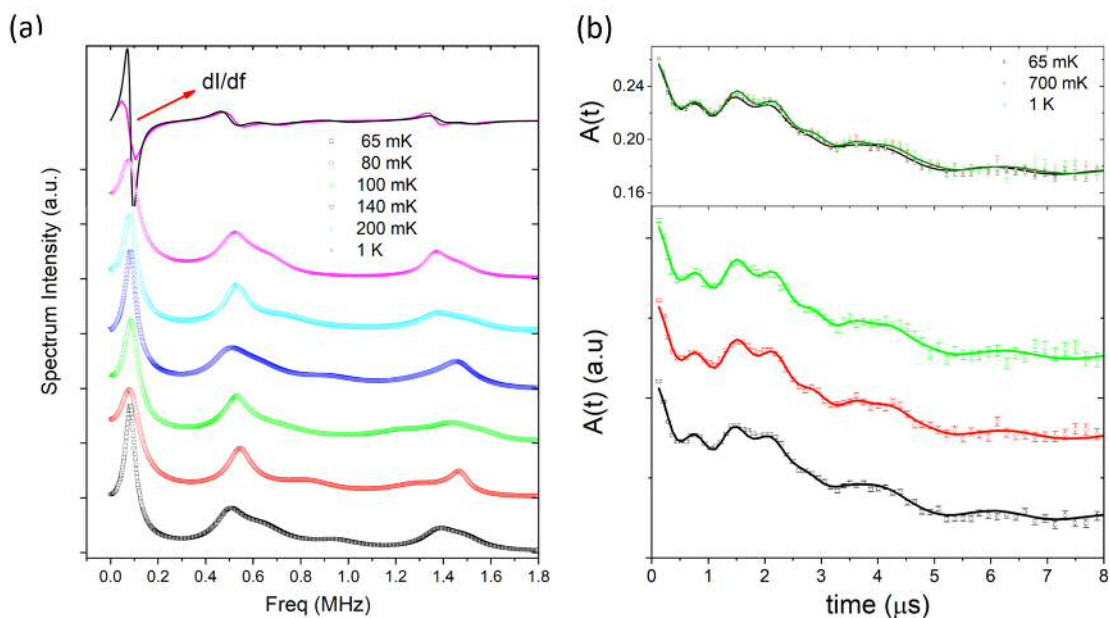


Figure 6.9: (a) Shifted Fourier transform (FT) of ZF- μ SR at different temperatures. (Top) FT derivative at 65 mK and 1 K. (b) ZF- μ SR at 0.065, 0.7 and 1 K. (Bottom) shifted curves. No relevant change in the frequency and time spectra from 1 K to the base temperature.

The frequency and time spectra of the μ SR asymmetry barely change below the expected superconducting transition $T_c \sim 90$ mK (see Fig. 6.9). At first sight, different frequencies are observed in the μ^+ -decay asymmetry but, sometimes, the μ SR lineshape is open to several interpretations as different fitting functions may satisfactorily resolve the muon asymmetry. In this case, the μ SR asymmetry was fitted to Eq. 6.3 and a Fourier analysis was initially done to figure out the depolarising participants and initial values ν_i , f_i and σ_i of the fitting parameters. $\nu_1 = 0.07 \pm 0.02$, $\nu_2 = 0.47 \pm 0.07$, $\nu_3 = 0.62 \pm 0.07$ and $\nu_4 = 1.38 \pm 0.04$ MHz are obtained from the derivative of the spectrum intensity at 65 mK. Due to the large number of fitting parameters in the model, the following fitting protocol was used. Using the Fourier results as starting point, f_i and σ_i were fixed and frequencies and phases were fitted. Later, the fractions and relaxation rates were fitted by keeping the other parameters constant.

The fitting parameters are summarised in Table 6.2 for *s1* and *s2* at $T = 65$ mK. The initial asymmetry a_0 and f_{bg} were fixed from the paramagnetic analysis. The normalised fractions f_i/V_f have a large contribution (25 – 27%) of the lowest internal field. The spread of internal fields ΔB_i are larger than those produced by the nuclear-dipole fields from the In nuclei ($\sim 2G$) [20] for signal 3 and 4. It may be explained by the incommensurate magnetic order with the crystal structure producing a broad range of internal fields at the muons sites. The ratio of muons that do oscillate $\sum f_i/V_f \in 45 - 48\%$ are in the same range that the values obtained from the TF20 measurements and the value estimated from the Schenck's work.

Both *s1* and *s2* have shown evidences of a large ratio of the magnetic fields at the muon sites ($f_{no}/V_f > 50\%$) out of the basal plane in the tetragonal structure that do not affect the initial polarisation of the muons. Similar ratios were obtained in TF20 and ZF- μ SR measurements because most of the internal fields not along the *c*-axis (B_1 in Table 6.2) are much lower than the transverse field in TF20 and those muons will oscillate around the applied field. The ratio is shorter in TF20 because muons that “feel” the internal field B_4 are barely affected by the transverse

Table 6.2: Fitting parameters of the ZF- μ SR from Eq. 6.3 for s1 at 65 mK. Same parameters were found for s2 with different f_i (last column). The silver contribution was fixed to $f_{bg}=a_0 \cdot (1 - V_f)$. Ratio of muons that contribute to the relaxation is $(1 - f_{no})/V_f \simeq 48\%$ and 45% for s1 and s2 respectively. Fitting errors in parentheses.

signal	ν_i (MHz)	B_i (G)	ϕ_i (deg)	σ_1 (μs^{-1})	ΔB_i (G)	f_i/V_f	$f_i/V_f _{s2}$
1	0.0392(1)	2.9(1)	11(4)	0.24(1)	2.8(1)	26.6%	25.7%
2	0.481(3)	35.5(3)	16(3)	0.18(2)	2.0(3)	5.6%	5%
3	0.60 (5)	44(3)	34(4)	1.2(1)	14(1)	11%	11%
4	1.45(1)	107(1)	-34(7)	0.42(4)	4.9(4)	4.5%	3%

field. Discrepancies in the ratio between the samples are probably due to V_f which was not accurately measured in s2.

Temperature dependence of the precession frequencies are plotted in Fig. 6.10 where effects in the precession frequencies below the reported transition are not observed. The phase transition was fitted to a power law, known as critical exponents [33], defined by

$$\nu_i(T) = \nu_i(0) \left[1 - \frac{T}{T_N} \right]^\beta \quad (6.6)$$

with the fitting parameters summarised in Table 6.3. Internal fields at muon sites vanish at the transition temperature $T_N \sim 3.7K$ with a low critical exponent, $\beta \in (0.1 - 0.17)$. Critical exponents have been widely used to study phase transitions on the hypothesis of universality. They seem to be surprisingly independent of the type of phase transitions, whether liquid-gas, ferromagnetic-paramagnetic, or any other [33]. In fact, for a continuous phase transitions, it is supposed that critical exponents depend only on the dimensionality of the system, d , and order parameter, D and the range of the interactions. The obtained critical exponent seems to respond to the 2-D Ising model, with $D=1$, $d=2$ and $\beta = \frac{1}{8}$ in agreement with an antiferromagnetic alignment of the Ce moments confined in the tetragonal basal plane.

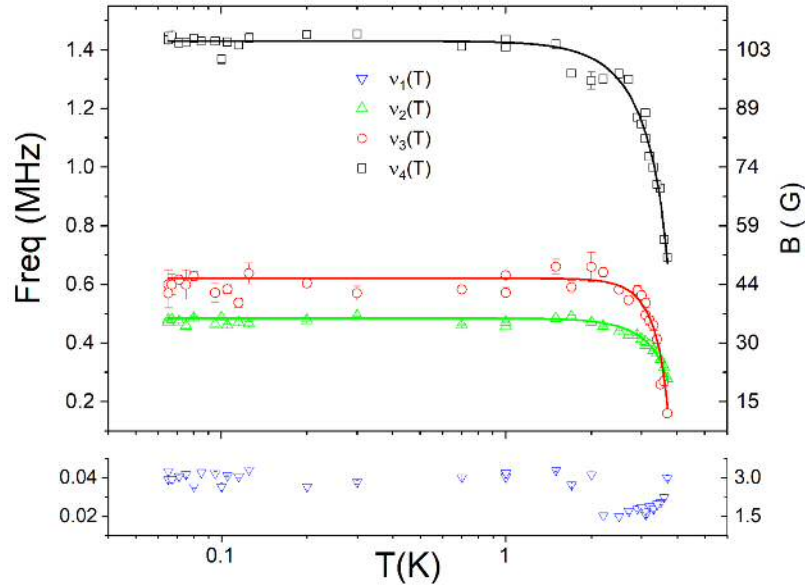


Figure 6.10: Temperature dependence of the four precession frequencies fitted to a critical exponent described in text (line). The lowest frequency remains unaltered in the paramagnetic phase suggesting that the AFM arrangement does cancel out the magnetic field at the muon sites.

Table 6.3: Fitting parameters of the temperature dependence of the frequencies. The lowest frequencies is not fitted. Fitting errors in parentheses.

$\nu_i(\mathbf{0})$ (MHz)	$B_i(0)$ (G)	T_N (K)	β
0.0392(1)	2.9(1)	–	–
0.5(1)	37(7)	3.6(2)	0.1(1)
0.64(5)	47(4)	3.70(2)	0.17(7)
1.46(6)	108(4)	3.62(9)	0.13(5)

The weight of each component, f_i/V_f , and the non oscillating signal, f_{no}/V_f , that does not take into account the fraction of muons stopped in the sample holder are plotted together with the relaxation rates σ_i as a function of the temperature in Fig. 6.11. Same protocol on fittings was used with the base temperature parameters as starting point and fixed initial phases ϕ_i . Except for component 3, whose contribution and large spread of internal fields drops to 0 from 1 K to the transition temperature, any distinguishable temperature variation was found. Standard errors

obtained by the χ^2 method on fitting parameters were found to be lower than the variations of the parameter with temperature or between the two samples s1 (empty dots) and s2 (full dots). Even, the same sample s1 showed slightly different values for two different experiments (1 K empty data points). These discrepancies might be due to a normalised χ^2 a few tenths larger than one, although not significant effects were observed in the μ SR lineshape (Fig. 6.9).

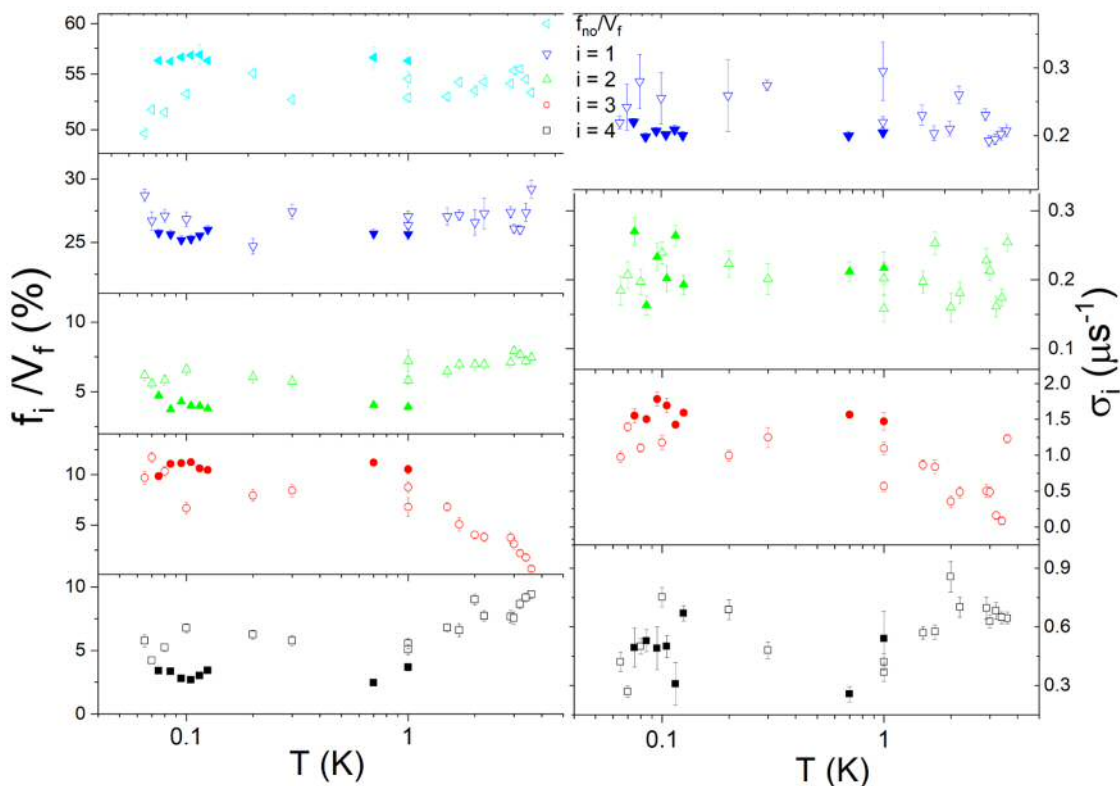


Figure 6.11: (a) Temperature dependence of the normalised fractions, f_i/V_f , and the non-oscillating signal, f_{no}/V_f , (b) and the relaxation rate, σ_i for s1 (empty dots) and s2 (full dots). Standard errors on parameters given by the χ^2 method.

The spectrometer features limited the scope of the magnetic ordered investigations, which was meticulously and comprehensively done in Schenck et al. work. If ZF- μ SR data are qualitatively compared, they both have a similar lineshape, although some discrepancies are found in ν_1 and ν_3 , probably caused by the different configuration of the spectrometer. In the previous work the initial muon polarisa-

tion $P(0)$ is rotated far away from the crystallographic axis modifying the muon asymmetry. The calculation of the internal fields at the muon sites generated by the AFM arrangement of the Ce^{3+} magnetic moments yields a magnetic field confined in the (a,b) plane [20] at the a site and zero field at f . In fact, a non-temperature dependent internal field ν_1 , unlike the previous work, and its low value (comparable with nuclear moments) will suggest that it corresponds with f site.

It is remarkable that the large magnetic fields along the c axis at the muon sites is contradictory to the dipolar fields produced by the helical magnetic structure. The disagreement was overcome by the assignment of a small and short-range induced moments to the Rh site along the c -axis in such a way that the effect of the induced moments in the In sites are negligible and would be undetected by ^{115}In Nuclear Quadrupole Resonance (NQR) [15, 31]. The short-range correlation and the small values of the moments will make them invisible to neutron diffraction [16].

The existence of four magnetically non-equivalent muon sites plus the large baseline seems to be consistent in both μSR works but requires a furtive induced moment on Rh sites to reconcile with the incommensurate helical magnetic ground state. However, another scenario might be investigated. Can the occurrence of a phase separation below the order parameter be compatible with the muon spectra? If a diamagnetic phase were the source of the baseline, it would be independent of the initial polarisation and the detector orientation in disagreement with Fig. 6.8 (a) were muons completely depolarised when B orientation is chosen. Another configuration that might explain the low field TF- and ZF- μSR , would be the helical structure coexisting with a phase that gives rise to magnetic fields along the c axis at the muon sites, large enough to not be decoupled by 20 Oe and elusive to other local magnetic probes.

Regarding the SC transition reported at 90 mK. The ZF- μSR measurements within the helical magnetic structure do not detect any change in the time and the frequency domain down to the base temperature for any of the two samples analysed.

If superconductivity takes place, the Meissner effect would repel the magnetic field from the superconducting regions affecting the field distribution at the muon sites. Although μ SR is a statistical probe with a limited sensitivity, the experiment was able to detect a low proportion of muons ($< 5\%$) oscillating at different frequencies $\nu_{2,4}$ thus, there is no signature of SC down to 50-60 mK in these samples at least in regions larger than few per cent of the total volume. It means that superconducting and antiferromagnetic coexistence is not observed at ambient pressure.

6.2.2 Transverse field configuration

As it is described in Sec. 3.5, TF- μ SR is the best configuration to investigate superconducting phases. The spectrometer was rotated 90° to the transverse configuration and the sample cooled down following the field-cooled protocol to investigate any potential superconducting vortex state. Temperature dependence was measured for three applied fields, $B = 75, 150$ and 400 G. To investigate the potential transition to a superconducting ground state, fields were chosen below and above the highest internal field at the muon sites ($B_4 \approx 108$ G). In order to see any variation in the magnetic phase, all fields are lower than the field (600 G) in which the reported bulk SC by a specific heat anomaly seems to vanish [14].

In the transverse configuration the asymmetric position of the detectors with regard the muon beam encourages to group the positron detectors differently. The positron counts $N_i(t)/e^{-t/\tau_\mu}$ of each detector cluster, i , are fitted to specific parameters such as the average counts $N_i(0)$ or the initial phase that differ from one to another detector cluster but also to common parameters from which the information is obtained.

$$\frac{N_i(t)}{N_i(0)e^{-t/\tau_\mu}} = \left[\sum_{i=1}^N f_i e^{-\frac{\sigma_i^2 t^2}{2}} \cos(\gamma_\mu B_i t + \phi_i) + f_{bg} e^{-\lambda t} \cos(\gamma_\mu B_0 t + \phi_0) \right] \quad (6.7)$$

Fig. 6.12 plots the normalised positron counts for a specific detector cluster in

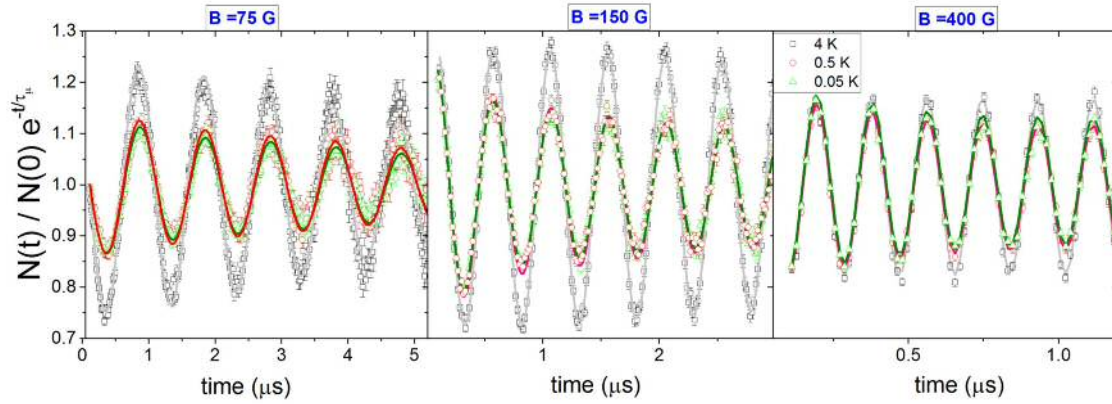


Figure 6.12: TF- μ SR asymmetry for a specific detector cluster in the PM phase ($T = 4\text{K}$), the AFM phase ($T = 0.5\text{ K}$) and at the base temperature ($T = 0.05\text{ K}$) for three applied fields. $N=2$ on fits to Eq. 6.7 is only observed for $B= 150\text{G}$. At the lowest field, depolarisation is too fast for the spectrometer resolution $\sigma_2^{75\text{G}} \rightarrow \infty$. For the highest field, not a second depolarisation is observed $f_2^{400\text{G}} = 0$.

the PM phase ($T = 4\text{K}$), in the AFM phase ($T = 0.5\text{ K}$) and at the base temperature ($T = 0.05\text{ K}$) for the chosen applied fields. The precession signals were analysed with two components for muons in the sample ($N=2$) in Eq. 6.7. Three scenarios are distinguished. For the lowest field ($B=75\text{ G}$), a loss of asymmetry is observed below the transition. The applied field is unable to partially or totally align the internal fields along the c axis. For $B=150\text{ G}$, two relaxation rates are observed. The initial polarisation in the PM phase is rapidly lost until certain level that depolarised slowly. For $B=400\text{ G}$, the only observable change below the transition is a slight increased in the depolarisation rate. The component which is strongly affected by the applied field will be analysed by f_2 . The depolarisation rate σ_i , proportional to the spread of internal fields is first analysed for the strongly field-dependent component. $\sigma_2(75\text{ G}) \rightarrow \infty$ tend to big values below the transition, as a sign of the loss of asymmetry. For $B= 400\text{ G}$, the component vanishes as no fast depolarisation is observed, $f_2(400\text{ G}) \simeq 0$. However, two different depolarisation rates are clearly observed at $B= 150\text{ G}$. Table 6.4 summarises the fitting parameters at the base temperature. Fields and $\lambda \sim 0.09\ \mu\text{s}^{-1}$ for the muons stopped on Silver are fixed from the fits at 4 K and f_{bg} is fixed from the volume fraction.

Table 6.4: Fitting parameters of the TF- μ SR experiments at T= 50 mK. Fitting errors in parentheses.

Field (G)	$V_f(1-f_{BG})$	B_{Ag} (G)	$\sigma_1(\mu s^{-1})$	B_1 (G)	$\sigma_2(\mu s^{-1})$	f_2/V_f
75	90%	68.9	0.12(1)	74.9	∞	53%
150	50%	148.8	0.54(1)	147.9	2.28(5)	64%
400	50%	400	0.16(1)	402.4	–	0%

These results can be analysed in the context of the zero-field and low transverse-field measurements. For $B = 75$ G, the TF- μ SR results are similar to the low-field spectra. Muons that do not oscillate $f_2/V_f \simeq 53\%$ are in the same order than before, but for fields $B = 150$ G, some of the fields along the c-axis are affected by the applied field. The fast depolarisation vanishes for $B = 400$ G where most of the longitudinal fields are aligned by the applied field.

To confirm the absence of transition, the relaxation rates that are related with the penetration depth and the superconducting carrier density in a superconducting phase are plotted as a function of the temperature for the applied fields, B_{app} , in Fig. 6.13 together with the normalised fraction f_i and fields B_i/B_{app} . Empty dots correspond to the first component ($f_1(400 \text{ G}) = 1$) and full dots to the second one. The relaxation rates are almost unaltered by the temperature. The fast relaxation rate for the second component at 150 G is also quasi-constant $\sigma_2 = 2.29 \pm 0.04 \mu s^{-1}$. It can then be confirmed that no signature of a superconducting transition were found down to 50-60 mK.

In the expected case of SC and AFM coexistence in a very small superconducting proportion (a 13% of the density of states are expected to contribute to the SC), the superconducting contribution might be screened by the AFM or not detected in the fits as they are done collectively for all the detectors. The Fourier transform (FT) of the time decay signal that gives the probability distribution of the internal flux density, $P(B)$, is a better tool to detect tiny effects. If a vortex line lattice emerges several distinctive features of the $P(B)$ lineshape should be observed.

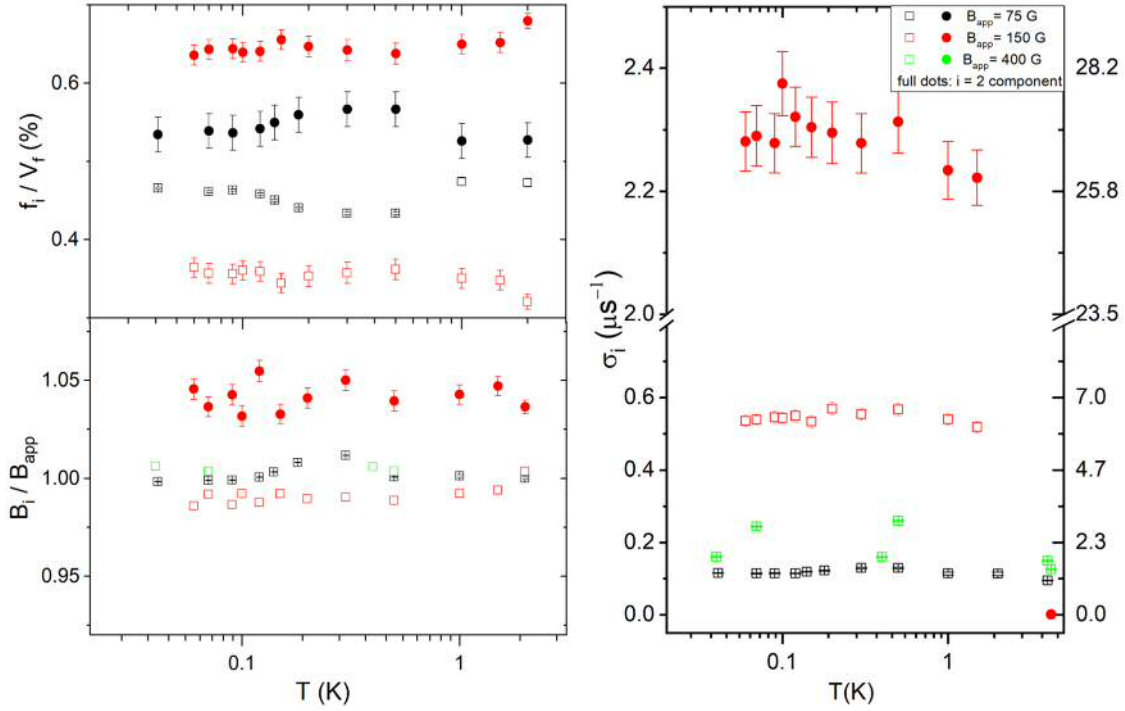


Figure 6.13: Temperature dependence of the Eq. 6.7 fitting parameters for three TF- μ SR experiments (black, red, green dots). Empty (full) dots correspond to $i = 1(2)$, respectively. f_2 (400 G) = 0 and σ_2 (75 G) = ∞ .

The symmetric field distribution around the applied field evolves to an asymmetric lineshape. A peak at a field lower than the average field is followed by a long tail of fields with a maximum which corresponds to the field in the vortex cores. Penetration depth can be also investigated. If it is lower than the vortex distance the field distribution will display a minimum. More details in Sec. 3.5. Temperature dependence of the field distribution for $B = 75$ and 150 G does not show in Fig. 6.14 any evidence of superconducting transition as the symmetric distribution remains unaltered from 1 K to the base temperature. However, the SC upper critical magnetic field H_c (69 mK) $\simeq 10$ Oe estimated by Chen et al [13] at P_{amb} is by far larger than the transverse field. The shift to lower fields in the field distribution for $B = 150$ G is explained by the effect of the internal fields of the AFM phase as it is also observed at 1 K.

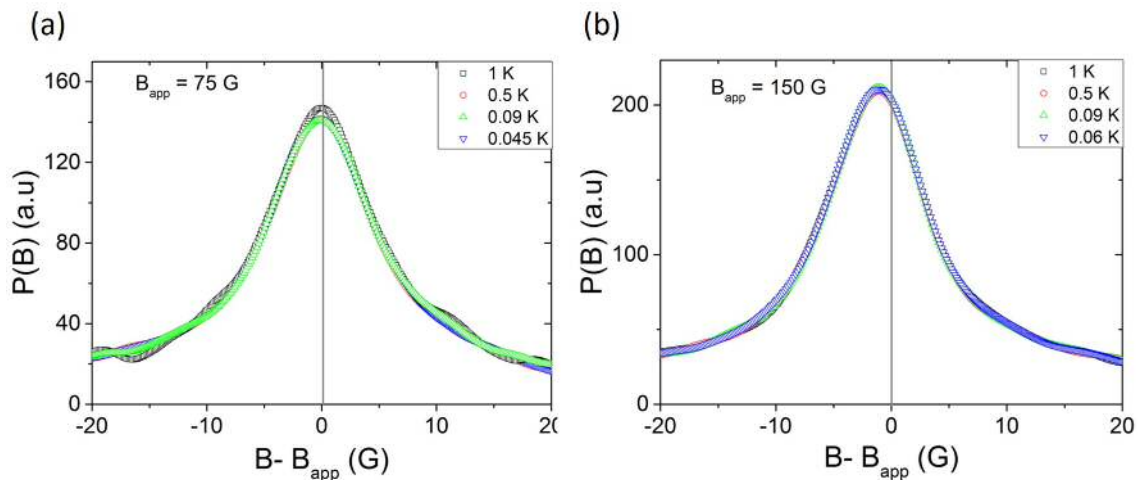


Figure 6.14: Probability distribution of the internal flux density at different temperatures for 75 (a) and 150 G (b) applied fields.

6.3 Resistivity

The ground state was also investigated by resistivity measurements since its value is expected to drop to zero if any partial or total transition takes place on the sample.

The model of "free" electrons predicts a conductivity linearly dependent on the mean free path of electrons, strongly affected by the electron-electron scattering. It has been seen that the simple model of interactions adiabatically activated given by the Fermi Liquid theory does not take into account the electron-phonon interactions. The T^2 -dependence of the resistivity when electron-electron is dominant turns to a resistance that varies linearly on T at high temperatures and transforms smoothly into a T^5 -dependence at low temperatures if thermal vibrations govern the electrons free path. In real metals, systems are not so simple and the entire crystal lattice also enters into the scattering process known as Umklapp phonon scattering that differs from one compound to another. At low temperature, when phonons are frozen out, defects gain relevance and give rise to a residual resistivity, ρ_{res} , which is temperature independent. Their contribution is usually described by the residual resistivity ratio [$RRR \equiv R_{RT}/R_{4K} = \rho_{RT}/\rho_{4K}$] that does not depend on the sample

shape. The assumption $\rho_{res} \simeq \rho_{4K}$ is usually made as the temperature variation is low below 4 K. In the heavy fermion family is also relevant the electronic scattering with magnetic impurities introduced in Sec. 2.6.1.

Although resistivity may seem a straightforward technique, several complications show up when metals or low resistivity compounds are measured. CeRhIn_5 is a metal with a low resistivity of several $\mu\text{m}\cdot\Omega$ so any resistance from the wires will be larger than the sample one. This inconvenience is normally overcome by using the four-lead arrangement or Kelvin method which avoids spurious voltmeter readings from the leads resistance. A sketch of the setup is shown in Fig. 6.15

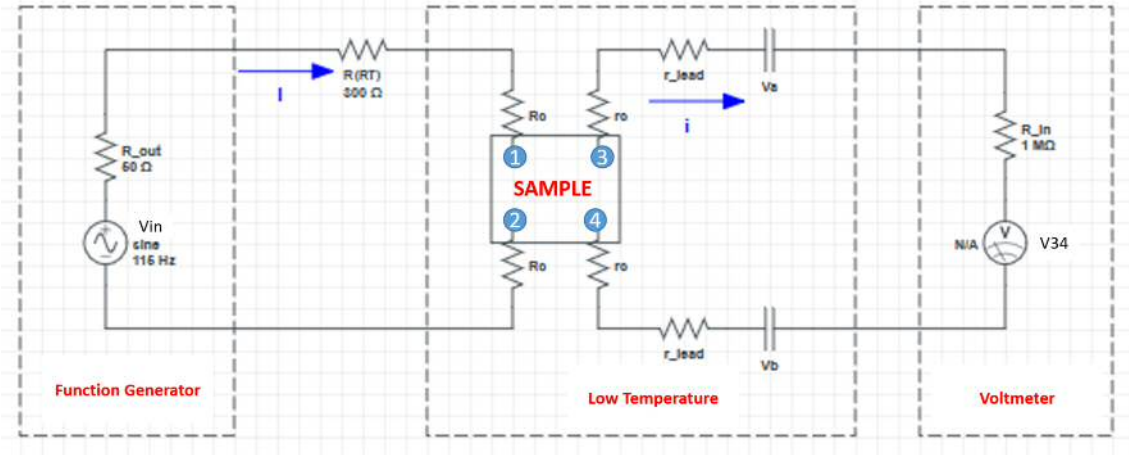


Figure 6.15: Four-lead arrangement for measuring transport properties.

In this case the voltage measured at the voltmeter, V_{34} , is

$$V_{34} = (I - i)R_{1234} - i(2r_0 + 2r_{lead} + R_{ln}) + V_a - V_b \quad (6.8)$$

where V_a and V_b are the contact potentials that are easily removed by reversing the source polarity or using an AC source, r_0 is the contact resistance and r_{lead} is the lead resistance. A large input voltmeter impedance $R_{ln} = 10M\Omega$ makes $i \ll I$ and then

$$V_{34} \cong I_{12}R_{1234} \quad (6.9)$$

being $V_{34} = V_4 - V_3$ and $I_{12} \equiv I \cong \frac{V_{in}}{R_{out} + R(RT)}$. $R(RT)$ is an external resistance at room temperature much larger than the contact resistance R_0 to assure a constant applied current. R_{out} is the function generator output resistance.

The van der Pauw method [34] provides a method to measure the resistivity, particularly useful for measurements of materials that are not easily fabricated into long, uniform and bar shapes: the type of configuration that is usually required for common transport measurements. Samples must satisfy the following conditions to use the technique:

- they must have a flat shape of uniform thickness.
- they must not have isolated holes.
- They must be homogeneous and isotropic.
- The ratio between the area of the contact should be much smaller than the sample area.

In fact, the resistivity error, $\Delta\rho$ due to contacts of size δ and sample size D is

$$\frac{\Delta\rho}{\rho} \approx \left(\frac{\delta}{D}\right)^2 \quad (6.10)$$

Furthermore, technique accuracy is improved if contacts are spaced apart around the edges of the sample.

Resistivity of an arbitrarily shaped flat sample and thickness t were found to be

$$\rho = \frac{\pi \cdot t}{\ln 2} \cdot \frac{R_{1234} + R_{1324}}{2} \cdot f\left(\frac{R_{1234}}{R_{1324}}\right) \quad (6.11)$$

where f takes into account the sample asymmetry. It becomes 1 for $R_{1234} = R_{1324}$ that takes place in samples with a line of symmetry if two contacts are placed in the line of symmetry and the other two symmetrically with respect to the line. In this case only one measurement is required to obtain the resistivity.

6.3.1 Sample preparation

A small bit of the sample used for the μ SR experiment was ground and polished to meet the requirements of the van der Pauw resistivity method. The sample was cut to a square shape without holes and the Struers' Labo System, a modular grinding and polishing system, provides grinding clothes that were used to reduce the thickness down to a uniform and flat $320\ \mu\text{m}$ thick sample with an almost symmetric surface. The smooth surface was obtained by polishing clothes. A scheme of the almost symmetric sample used is depicted in Fig. 6.16 including the sample dimensions and contact nomenclature.

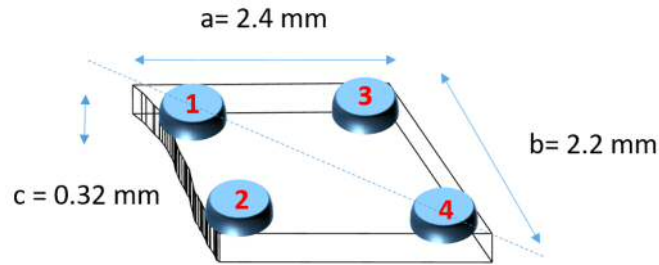


Figure 6.16: Scheme of the sample used in resistivity measurements with an axis of symmetry, dimensions and contact nomenclature.

Bright and thin samples present some difficulties to make contact for transport measurements. In metals, contacts with low surface resistance, r_0 in Eq. 6.8, are needed to avoid spurious contribution. Ekin's book [35] gives an extensive and practical discussion about contact choice as a function of their applications, mainly for superconducting samples. To investigate the contact resistance effects two kinds of contacts were made. First measurements were carried out by pressing Indium solder against the metal surface with the soldering iron at relatively low temperature. $70\ \mu\text{m}$ Gold wires connect the sample to the PPMS resistive sample puck. On the other hand, $35\ \mu\text{m}$ Aluminium wires were electrically connected by wire-bonding to the sample. For low temperature transport measurements in the Bluefors Dilution Refrigerator, a specific sample holder made of high-purity and Oxygen free Copper was designed to improve the sample thermalisation. For these measurements, superconducting Lead contacts ($T_c = 7.2\ \text{K}$) and Al wires ($T_c = 1.2\ \text{K}$) were used to

avoid heating the sample. Details of the resistivity puck, the sample and the sample holder for low temperature measurements are depicted in Fig. 6.17.

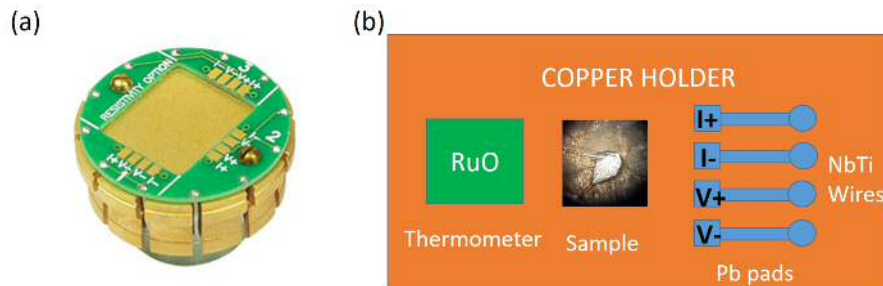


Figure 6.17: (a) Picture of the PPMS resistive sample puck. (b) Scheme of the setup for low temperature transport measurements in the dilution refrigerator. It includes a pure Cu holder to improve sample thermalisation, the RuO_2 thermometer and superconducting Pb pads and Al contact wires to avoid heating effects due to the applied current.

The sample was isolated from the holder by a thin piece of rizla paper. If contacts are compared, In solder provides a larger contact surface that should reduce the contact resistivity, although the large contact and sample size ratio will give an error of $\Delta\rho/\rho \sim 10\%$. Wire-bonding reduces the size error dramatically but they have less grip. Contact effects on the measurements will be discuss in the results section 6.3.3.

6.3.2 Experimental setup

The four-lead arrangement was prepared for transport measurements in the Resistivity option of the PPMS. Potential difference was measured by a SR830 Lock-in amplifier and its function generator used to inject a 117 Hz AC current. As the contact potential are polarity dependent their contribution will be removed by using an AC source. The potential difference measured in any two contacts $V_{k,l} = V_l - V_k$ in Eq. 6.8 will result in

$$V_{kl} = (I_{ij} - i)R_{ijkl} - i(2r_0 + 2r_{lead} + R_{ln}) \quad (6.12)$$

for any i, j, k, l contact. A load resistance at room temperature of $R(\text{RT})= 300 \Omega$, located in a Faraday cage to isolate from electromagnetic interferences, plus the 50Ω output resistance of the voltage source prevent changes in the input current, I_{ij} . The thermal dependence of lead resistance will be negligible compared with the load resistance. For the dilution refrigerator setup, the room temperature resistance is replaced by a $1 \text{ K}\Omega$ as the fridge leads resistance are larger. The large input Lock-in impedance $R_{in}= 10 \text{ M}\Omega$ make, in principle, the current in the detecting circuit, i zero or negligible, therefore

$$V_{kl} \cong I_{ij} R_{ijkl} \quad (6.13)$$

6.3.3 Results

The resistance was measured in two perpendicular directions of the sample surface (ab plane). According to the contacts nomenclature given in Fig. 6.16, the temperature dependence of the single-crystalline CeRhIn₅ resistance was measured by using Gold wires, $R_{1234} \equiv R_{\parallel}$ and with Aluminium wires in the perpendicular direction, $R_{1324} \equiv R_{\perp}$. Resistivity and resistance temperature dependence from RT to 2K are shown in Fig. 6.18 for R_{\parallel} (black and red lines) and R_{\perp} (green and blue lines). Similar results in both direction confirm the axial symmetry and van der Pauw resistivity will be simplified, for a sample thickness t , to $\rho = \frac{\pi \cdot t}{\ln 2} \cdot \frac{R_{\parallel} + R_{\perp}}{2}$ (cyan line) as $f \approx 1$. For simplicity we can define $\rho_{\parallel, \perp} \equiv \frac{\pi \cdot t}{\ln 2} R_{\parallel, \perp}$. An unusual peak appears at $T_1 \approx 38 \text{ K}$ that is not related with the kind of contact used as it occurs with both Al, R_{\parallel} , and Au wires, R_{\perp} . Three different temperature regimes are observed. An almost constant resistivity begins to decrease below 100 K until T_1 is reached. From the peak to the PPMS base temperature at 2 K, the behaviour is slightly unequal for the setups. Whereas the perpendicular resistivity (Al wires) remains in a quasi-stable value of $\rho_{\perp}^{4K} \simeq 31.5 \mu\Omega \cdot \text{cm}$, the parallel resistivity has a turning point at 13.5 K, below which the resistivity increase slightly until the base temperature. The magnetic nature of the transition is confirmed by applying a perpendicular field along the c axis, $B= 1 \text{ T}$. The resistivity under the field does not exhibit the peak, although the resistivity trend remains similar than the

non-field data. It would mean that the magnetic transition is intrinsic to the sample.

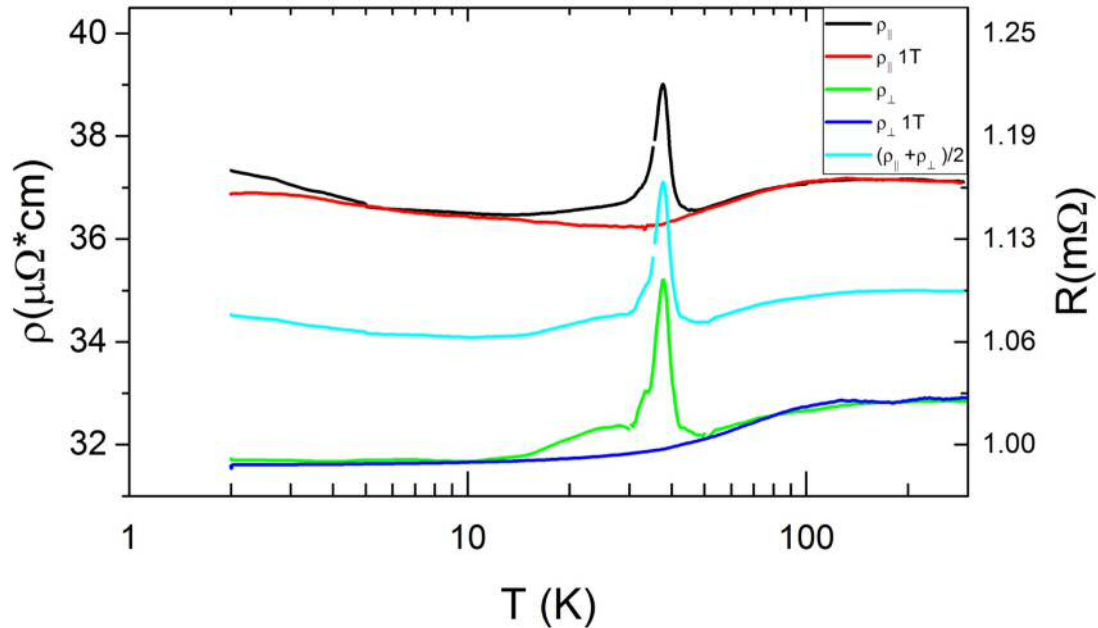


Figure 6.18: CeRhIn₅ resistivity and resistance temperature dependence in two perpendicular directions of the ab plane with and without an applied field $H = 1\text{T}$. ρ_{\parallel} (black and red lines) and ρ_{\perp} (green and blue lines) are defined as $\rho_{\parallel,\perp} \equiv \frac{\pi \cdot t}{ln2} R_{\parallel,\perp}$. Axial symmetry results in an average total resistivity ρ for a sample thickness = $320 \mu\text{m}$ (cyan line).

The uneven behaviour below 13.5 K suggests a contribution of the contact wires in the resistivity. The 10 M Ω input impedance avoids circulating current in the detecting circuit but if the contact wires resistance r_0 in Eq. 6.12 would be in the same order than the sample one, some current might circulate through the wires and come back to the sample. That might explain the different behaviour of the measurements with Gold and Aluminium contact wires. Fig. 6.19 plots the resistivity measured in-plane, ρ_a , and out-plane, ρ_c , from Moll et al. work [36] and the resistivity and the calculated resistance of 1 cm long Gold wires [37] and Aluminium wires for two residual resistivity [38]. There is a wide agreement in literature about the dramatic change of the CeRhIn₅ resistivity below 40 K that corresponds to the

resistivity peak in our measurements. Below that temperature, the wires resistance have a residual resistance around $1 \text{ m}\Omega$ that is approximately the sample resistance. It might justify the current through the wires and the uneven sample resistivity depending on the wires used.

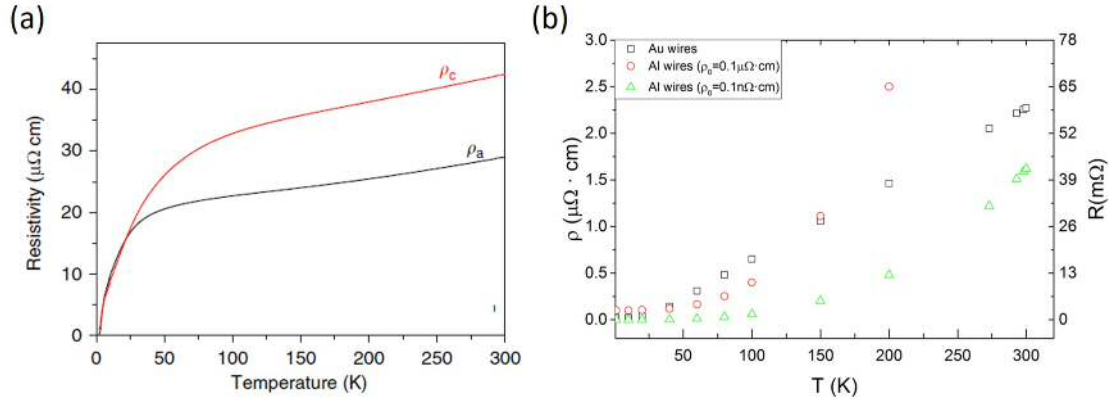


Figure 6.19: (a). Temperature dependence of in-plane (a) and out-plane (b) resistivity of CeRhIn_5 taken from [36]. (b) Resistivity and resistance of 1 cm and $70 \mu\text{m}$ Gold wires [37] and Aluminium wires with two residual resistivity, ρ_0 [38].

These results motivated the double Al contact wires used for the low temperature resistivity measurements. Double wiring was bonded to the sample and connected to a Lead pads for two reasons: both Lead and Aluminium are superconducting at the interesting temperature and any contribution should disappear below the Al superconducting transition at $T_c = 1.2 \text{ K}$ and the risk of wasting time due to broken wires by thermal expansion minimised. Fig. 6.20 shows the temperature dependence below 1.3 K for two applied current 1.6 mA (black line) and 3 mA (red line). An abrupt drop in the resistivity from $\sim 37 \mu\Omega \cdot \text{cm}$ due to the Al wires superconducting transition is observed for 3 mA data (inset figure). Below 1 K , a residual resistivity of 12.7 and $12.3 \mu\Omega \cdot \text{cm}$ for the applied currents do not exhibit any signature of a superconducting transition. CeRhIn_5 has a weak temperature dependence with a residual resistivity ratio [$\text{RRR} \equiv R_{RT}/R_{1K} = \rho_{RT}/\rho(1K) \approx 3$] much lower than the nominal values ~ 100 [22, 39]. Two possible explanations are found for the low RRR ratio. The discrepancies of the resistivity below 10 K suggest that the con-

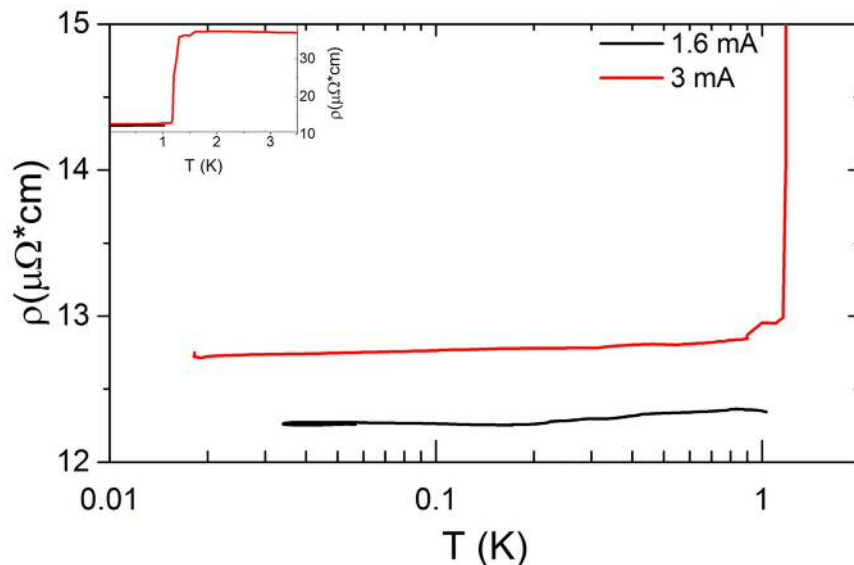


Figure 6.20: Low temperature in-plane ($\rho_{||}$) resistivity of CeRhIn_5 for two different currents. All wires superconducting transition is seen at 1.2 K (inset).

tact wires contribute to the low temperature resistivity hindering the measurement of the sample resistivity. The RRR ratio is normally a hint of the sample quality, defects or impurities in a low-quality sample will increase the residual resistivity but the sample was previously used in the neutron scattering experiment carried out by Stock et al. [17] and the CeRhIn_5 weak magnetism requires high quality samples for neutron experiments so causes should be different. The polishing and grinding work conducted on the sample might have modified the sample properties, in fact, powdered [12, 13] and polished [13] samples have reported lost of superconductivity as shown Fig 6.3.

6.4 Conclusions

The CeRhIn_5 ground state has been claimed to become superconducting at $T \sim 90$ mK at ambient pressure [12–14], although other work were unable to observe superconductivity above 70 mK [11]. The pure superconducting phase at high pressures and the incommensurate helical antiferromagnetism at ambient and low pressures is well understood but the nature of the coexisting phases is still under de-

bate. Either textured superconducting phase residing in the magnetic domain walls or in the nucleated domains of a new helical phase [9] or a bulk superconductivity very sensitive to sample inhomogeneities [13] have been suggested. The occurrence of a superconducting ground state at ambient pressure would indicate that other phenomena rather the pressure contributes to the superconducting state and would support the bulk superconductivity. The ground state have been investigated down to 50 mK by a local magnetic probe, μ SR and by resistivity measurements down to 20 mK. The μ SR success investigating superconductors is widely recognised. In this work, ZF- μ SR and TF- μ SR are a useful tool to study the magnetic ground state that become antiferromagnetic with an incommensurate and helical structure. The large proportion of internal fields along the c axis ($f_{no}/V_f > 55\%$) supports the assignment of induced and short-range magnetic moments in Rh atoms along the c axis [20], but also a phase separation scenario was considered. Neither the ZF- μ SR, the time-resolved TF-asymmetry or the field distribution at the muon sites exhibited any signature of superconductivity. The magnetic fields chosen for the TF- μ SR experiment were lower than 60 mT, field in which the claimed bulk superconductivity vanishes [40]. However, a low critical field of $H_c(T) = 10$ Oe at $T \simeq 69$ mK were estimated [13] that is lower than the lowest field used in the experiment (75 Oe). Even so, in the ZF- μ SR experiment superconductivity was not found confirming that there is no a coexistence of phases. The possibility of a low density of states participating in the SC transition (13%), estimated by Chen et al. [13], that may be screened out by the large asymmetry that does not depolarise must be ruled out as contributions of internal fields lower than 5% were easily detected.

Temperature dependence of the resistivity has been investigated in the basal plane (ab plane) of a single-crystalline CeRhIn₅ sample using the van der Pauw arrangement. Two kind of contacts, Gold and Aluminium wires, were tested to identify spurious voltage difference from the detecting circuit. An unusual magnetic transition, not observed before [36, 39], were found at $T_1 \sim 38K$, whose nature seems to be intrinsic to the sample as it was reported for both setups and it is vanished by applying field. Resistivity below 1 K remains constant with a residual

resistivity $\rho_{res} \simeq 12.5 \pm 0.3 \mu\Omega \cdot cm$. The slightly different behaviour below T_1 depending on the contact wire used, the large residual resistivity and the unexpected behaviour at higher temperatures encourage to carry out a more comprehensive study of the resistivity. The observation that superconducting resistive transitions under pressure are more prominent in high-quality samples but vanishes in lower quality specimens [9] would motivate the fabrication of high quality samples. The degradation of the superconductivity at ambient pressure by polishing or powdering the sample requires to restate the sample preparation as the sample was ground and polished to remove irregularities in the surface. A batch of samples should be fabricated with different geometries as a starting point for a systematic study of the impurities and contact effects. The superconducting transition at $T \sim 75mK$ would require a more exhaustive study of the sample thermalisation. Although a well-calibrated thermometer was located close to the sample, thermal heat on the sample due to the applied current has not been studied in details. Furthermore, the magnetometer developed in this project might be used to investigate the magnetic susceptibility as soon as the thermalisation issues were sorted out.

References

- [1] M. R. Norman, *The Challenge of Unconventional Superconductivity*, Science 332 (6026), p. 196 (2011)
- [2] H. Hegger, C. Petrovic, E. G. Moshopoulou, M. F. Hundley, J. L. Sarrao, Z. Fisk and J. D. Thompson, *Pressure-Induced Superconductivity in Quasi-2D CeRhIn₅*, Phys. Rev. Lett. 84, p. 4986 (2000)
- [3] C. Petrovic, P. Pagliuso, M. Hundley, R. Movshovich, J. Sarrao, J. Thompson, Z. Fisk and P. Monthoux, *Heavy-fermion superconductivity in CeCoIn₅ at 2.3 K*, J. Phys. Condens. Matt. 13 (17), p. L337 (2001)
- [4] C. Petrovic, R. Movshovich, M. Jaime, P. G. Pagliuso, M. F. Hundley, J. L. Sarrao, Z. Fisk and J. D. Thompson, *A new heavy-fermion superconductor CeIrIn₅ : A relative of the cuprates?*, EPL 53 (3), p. 354 (2001)

- [5] U. Alver, R. G. Goodrich, N. Harrison, D. W. Hall, E. C. Palm, T. P. Murphy, S. W. Tozer, P. G. Pagliuso, N. O. Moreno, J. L. Sarrao and Z. Fisk, *Localized f electrons in $Ce_xLa_{1-x}RhIn_5$: de Haas-van Alphen measurements*, Phys. Rev. B 64, p. 180402 (2001)
- [6] Y. Haga, Y. Inada, H. Harima, K. Oikawa, M. Murakawa, H. Nakawaki, Y. Tokiwa, D. Aoki, H. Shishido, S. Ikeda, N. Watanabe and Y. Ōnuki, *Quasi-two-dimensional Fermi surfaces of the heavy fermion superconductor $CeIrIn_5$* , Phys. Rev. B 63, p. 060503 (2001)
- [7] H. Shishido, R. Settai, H. Harima and Y. Ōnuki, *A drastic change of the Fermi surface at a critical pressure in $CeRhIn_5$: dHvA study under pressure*, J. Phys. Soc. Jpn. 74 (4), p. 1103 (2005)
- [8] T. Park, F. Ronning, H. Yuan, M. Salamon, R. Movshovich, J. Sarrao and J. Thompson, *Hidden magnetism and quantum criticality in the heavy fermion superconductor $CeRhIn_5$* , Nature 440 (7080), p. 65 (2006)
- [9] T. Park, H. Lee, I. Martin, X. Lu, V. A. Sidorov, K. Gofryk, F. Ronning, E. D. Bauer and J. D. Thompson, *Textured Superconducting Phase in the Heavy Fermion $CeRhIn_5$* , Phys. Rev. Lett. 108, p. 077003 (2012)
- [10] G. Knebel, M. Measson, B. Salce, D. Aoki, D. Braithwaite, J. Brison and J. Flouquet, *High-pressure phase diagrams of $CeRhIn_5$ and $CeCoIn_5$ studied by ac calorimetry*, J. Phys. Condens. Matt. 16 (49), p. 8905 (2004)
- [11] T. Park and J. D. Thompson, *Magnetism and superconductivity in strongly correlated $CeRhIn_5$* , New J. Phys. 11 (5), p. 055062 (2009)
- [12] V. S. Zapf, E. J. Freeman, E. D. Bauer, J. Petricka, C. Sirvent, N. A. Frederick, R. P. Dickey and M. B. Maple, *Coexistence of superconductivity and antiferromagnetism in $CeRh_{1-x}Co_xIn_5$* , Phys. Rev. B 65, p. 014506 (2001)
- [13] G. Chen, K. Matsubayashi, S. Ban, K. Deguchi and N. Sato, *Competitive coexistence of superconductivity with antiferromagnetism in $CeRhIn_5$* , Phys. Rev. Lett. 97 (1), p. 017005 (2006)

- [14] J. Paglione, P.-C. Ho, M. Maple, M. Tanatar, L. Taillefer, Y. Lee and C. Petrovic, *Ambient-pressure bulk superconductivity deep in the magnetic state of CeRhIn₅*, Phys. Rev. B 77 (10), p. 100505 (2008)
- [15] N. Curro, P. Hammel, P. Pagliuso, J. Sarrao, J. Thompson and Z. Fisk, *Evidence for spiral magnetic order in the heavy fermion material CeRhIn₅*, Phys. Rev. B 62 (10), p. R6100 (2000)
- [16] W. Bao, P. G. Pagliuso, J. L. Sarrao, J. D. Thompson, Z. Fisk, J. W. Lynn and R. W. Erwin, *Incommensurate magnetic structure of CeRhIn₅*, Phys. Rev. B 62, p. R14621 (2000)
- [17] C. Stock, J. Rodriguez-Rivera, K. Schmalzl, E. Rodriguez, A. Stunault and C. Petrovic, *Single to multiquasiparticle excitations in the itinerant helical magnet CeRhIn₅*, Phys. Rev. Lett. 114 (24), p. 247005 (2015)
- [18] A. D. Christianson, J. M. Lawrence, P. G. Pagliuso, N. O. Moreno, J. L. Sarrao, J. D. Thompson, P. S. Riseborough, S. Kern, E. A. Goremychkin and A. H. Lacerda, *Neutron scattering study of crystal fields in CeRhIn₅*, Phys. Rev. B 66, p. 193102 (2002)
- [19] A. Llobet, J. S. Gardner, E. G. Moshopoulou, J.-M. Mignot, M. Nicklas, W. Bao, N. O. Moreno, P. G. Pagliuso, I. N. Goncharenko, J. L. Sarrao and J. D. Thompson, *Magnetic structure of CeRhIn₅ as a function of pressure and temperature*, Phys. Rev. B 69, p. 024403 (2004)
- [20] A. Schenck, D. Andreica, F. N. Gygax, D. Aoki and Y. Ōnuki, *Evidence for ordered moments on the Rh sites in CeRhIn₅*, Phys. Rev. B 66 (14), p. 144404 (2002)
- [21] Y. Yang, Z. Fisk, H. Lee, J. D. Thompson and D. Pines, *Scaling the Kondo lattice*, Nature 454 (7204), p. 611 (2008)
- [22] T. Muramatsu, N. Tateiwa, T. C. Kobayashi, K. Shimizu, K. Amaya, D. Aoki, H. Shishido, Y. Haga and Y. Ōnuki, *Superconductivity of CeRhIn₅ under high pressure*, J. Phys. Soc. Jpn. 70 (11), p. 3362 (2001)

- [23] R. Heffner, T. Goko, D. Andreica, K. Ohishi, W. Higemoto, T. Ito, A. Amato, J. Spehling, H.-H. Klauss, E. Bauer *et al.*, μ SR study of $CeRhIn_5$ under applied pressure, in *J. Phys. Conf. Ser.* (2010), vol. 225, p. 012011
- [24] T. Mito, S. Kawasaki, G.-q. Zheng, Y. Kawasaki, K. Ishida, Y. Kitaoka, D. Aoki, Y. Haga and Y. Onuki, *Pressure-induced anomalous magnetism and unconventional superconductivity in $CeRhIn_5$: ^{115}In -NQR study under pressure*, Phys. Rev. B 63, p. 220507 (2001)
- [25] Y. Bang, M. J. Graf, A. V. Balatsky and J. D. Thompson, *Nuclear spin-lattice relaxation rate in the d-wave superconducting state with coexisting antiferromagnetism*, Phys. Rev. B 69, p. 014505 (2004)
- [26] Y. Fuseya, H. Kohno and K. Miyake, *Realization of Odd-Frequency p-Wave Spin-Singlet Superconductivity Coexisting with Antiferromagnetic Order near Quantum Critical Point*, J. Phys. Soc. Jpn. 72 (11), p. 2914 (2003)
- [27] T. Park, E. Bauer and J. Thompson, *Probing the nodal gap in the pressure-induced heavy fermion superconductor $CeRhIn_5$* , Phys. Rev. Lett. 101 (17), p. 177002 (2008)
- [28] S. Kawasaki, T. Mito, Y. Kawasaki, G.-q. Zheng, Y. Kitaoka, D. Aoki, Y. Haga and Y. Onuki, *Gapless Magnetic and Quasiparticle Excitations due to the Coexistence of Antiferromagnetism and Superconductivity in $CeRhIn_5$: A Study of ^{115}In NQR under Pressure*, Phys. Rev. Lett. 91, p. 137001 (2003)
- [29] A. D. Christianson, E. A. Goremychkin, R. Osborn, S. Rosenkranz, M. D. Lumsden, C. D. Malliakas, I. S. Todorov, H. Claus, D. Y. Chung, M. G. Kanatzidis, R. I. Bewley and T. Guidi, *Unconventional superconductivity in $Ba_{0.6}K_{0.4}Fe_2As_2$ from inelastic neutron scattering*, Nature 456 (7224), p. 930 (2008)
- [30] N. Aso, K. Ishii, H. Yoshizawa, T. Fujiwara, Y. Uwatoko, G.-F. Chen, N. K. Sato and K. Miyake, *Switching of magnetic ordering in $CeRhIn_5$ under hydrostatic pressure*, J. Phys. Soc. Jpn. 78 (7), p. 073703 (2009)

- [31] M. Yashima, H. Mukuda, Y. Kitaoka, H. Shishido, R. Settai and Y. Ōnuki, *Strong coupling between antiferromagnetic and superconducting order parameters of CeRhIn₅ studied by ¹¹⁵In nuclear quadrupole resonance spectroscopy*, Phys. Rev. B 79 (21), p. 214528 (2009)
- [32] G. Knebel, D. Aoki, D. Braithwaite, B. Salce and J. Flouquet, *Coexistence of antiferromagnetism and superconductivity in CeRhIn₅ under high pressure and magnetic field*, Phys. Rev. B 74 (2), p. 020501 (2006)
- [33] S. Blundell, *Magnetism in condensed matter* (AAPT, 2003)
- [34] L. J. van der Pauw, *A method of measuring specific resistivity and Hall effect of discs of arbitrary shape*, Philips Res. Repts. 13, p. 1 (1958)
- [35] J. W. Ekin, *Experimental Techniques for Low-Temperature Measurements: Cryostat Design, Material Properties, and Superconductor Critical-Current Testing* (Oxford U. Press, New York, 2006)
- [36] P. J. W. Moll, B. Zeng, L. Balicas, S. Galeski, F. F. Balakirev, E. D. Bauer and F. Ronning, *Field-induced density wave in the heavy-fermion compound CeRhIn₅*, Nature Commun. 6, p. 6663 (2015)
- [37] D. R. Lide *et al.*, *Handbook of chemistry and physics* (2004)
- [38] S. Senoussi and I. A. Campbell, *The low temperature electrical resistivity of aluminium*, J. Phys. F 3 (1), p. L19 (1973)
- [39] A. Christianson, A. Lacerda, M. Hundley, P. Pagliuso and J. Sarrao, *Magneto-transport of CeRhIn₅*, Phys. Rev. B 66 (5), p. 054410 (2002)
- [40] J. Paglione, M. Tanatar, D. Hawthorn, R. Hill, F. Ronning, M. Sutherland, L. Taillefer, C. Petrovic and P. Canfield, *Heat transport as a probe of electron scattering by spin fluctuations: the case of antiferromagnetic CeRhIn₅*, Phys. Rev. Lett. 94 (21), p. 216602 (2005)

7

Conclusions and further work

During the course of this work, the first magnetometer in a liquid helium free dilution refrigerator has been built. In the SQUID-based magnetometer a base temperature of a hundred milliKelvins have been achieved and tools to measure up to MHz frequencies in the SQUID open-loop operation mode provided. It is demonstrated that the slew rate of the flux-locked loop circuit used to linearise the SQUID response hinders susceptibility measurements beyond a few hundred of kHz. Instead, a versatile and exchangeable system of flux transformers were fabricated to reduce the magnetic flux from the sample to the SQUID down to the linear range of the SQUID open-loop mode, removing the frequency limitations. A comprehensive study of the noise sources made it possible to properly shield the magnetometer and isolate it from electromagnetic interferences in such a way that the final design exhibits a noise level similar to the bare SQUID. An almost flat noise per root Hertz were achieved beyond 50 kHz providing a sensitivity up to five orders of magnitude in

the locked-loop mode and two-three orders of magnitude in the open-loop mode used at high frequencies. The $\text{Dy}_2\text{Ti}_2\text{O}_7$ spin ice was chosen to calibrate and test the sample thermalisation thanks to the high-dependence of the freezing transition with the frequency. Thermalisation issues related to heating effects at high frequencies were identified and solved by a measurement protocol that was also optimised to improve the sensitivity and remove Eddy currents generated in the Copper holder at high frequencies. Further works should be focused on solving the sample thermalisation issues and to carry out high frequency measurements. The calibration of a new thermometer with a larger temperature range and less noisy response are required. The next step should be orientated to remove the temperature gradient between the sample and fridge base temperature. For that purpose, a new design of the sample holder, thermally linked to the MXC on both ends might be the best solution. It may also provide a lower base temperature as the base temperature of the fridge including the magnetometer was 14 mK. It will give access to investigate quantum critical transition or other exciting physics such as the superconducting transition in CeRhIn_5 claimed to appear at ~ 90 mK. To test the high-frequency magnetometer capabilities, samples with relevant physics within that range of frequencies and temperatures should be analysed. A pure Sapphire rod already designed may be used instead of the diamagnetic Copper. The paramagnetic Sapphire crystal is an electrical insulator that would avoid Eddy currents with a relatively good thermal conductivity.

$\text{Nb}_{1-y}\text{Fe}_{2+y}$ belongs to a family of ferromagnetic metallic alloys where theoretical considerations suggest that the second order quantum phase transition from a metallic paramagnet to an itinerant ferromagnet in the absence of quenched disorder is avoided by one of two escape routes, either the transition becomes discontinuous induced by fluctuations or a new ground state emerges forming a spatially modulated magnetic phase or spin density wave. Whereas first order quantum critical points have been observed in many systems, spin density wave has proven to be more challenging to experimentally investigate. Stoichiometric NbFe_2 has been investigated by bulk magnetic techniques and muon spin relaxation, as the $\text{Nb}_{1-y}\text{Fe}_{2+y}$

composition series is a good candidate to study ferromagnetic criticality. The control parameter y leads the magnetic transition to a quantum critical point around which a spin density wave has been reported close to stoichiometry. The past failure to detect magnetic order by neutron scattering, the ferrimagnetism found by Compton scattering in Fe-rich samples and theoretical studies suggesting several magnetic ground states with similar energy motivated the μ SR study that is able, in principle, to differentiate commensurate and incommensurate magnetic arrangements. The μ SR lineshape was only well-fitted by a phenomenological Kubo Toyabe relaxation function. It describes a magnetic order dominated by randomly-orientated static moments at muon sites with magnitudes homogeneously distributed from 0 to an effective field, Δ_{eff} , equivalent to $M \sim 0.0075\mu_B/\text{Fe}$ at 2K where fluctuations remain in the slow fluctuation limit. The field distribution may be explained by two possible scenarios: a new magnetic ground state controlled by short-range correlations or a SDW with helical and incommensurate modulation. The sensitivity of μ SR to the field distribution in the vicinity of the quantum critical point was clearly demonstrated. Further measurements around criticality might reveal details of the field distribution and fluctuations in the $\text{Nb}_{1-y}\text{Fe}_{2+y}$ series.

CeRhIn_5 is a heavy fermion that orders into an antiferromagnetic phase at $T_N \simeq 3.8$ K and becomes superconductor under pressure. The pressure-induced superconductivity exhibits a region of intermediate pressures where superconducting and antiferromagnetic order coexist. The nature of the superconductivity is still under debate due to a disagreement in the T_c found by different techniques and works. Either bulk or filamentary superconductivity have been claimed but the superconductivity onset at ambient pressure in specific heat, susceptibility and resistivity measurements with similar $T_c \simeq 90$ K were suggested to be an evidence of bulk superconductivity. The CeRhIn_5 ground state has been investigated by μ SR in the zero and transverse field geometry down to 50 mK and complemented by resistivity measurements down to 20 mK. The antiferromagnetic phase produces an oscillating ZF- μ SR lineshape associated with four frequencies. Neither the frequencies or the initial asymmetry displayed any temperature dependence around the expected

transition temperature, even though volume fraction lower than 5% were detected. Moreover, the large proportion of muons that do not depolarise supports the assignment of induced and short-range magnetic moments in Rh atoms along the c axis. TF- μ SR was investigated in the time and frequency domain for three different fields chosen below and above the highest internal field at the muon sites. Magnetic field in a superconductors is expelled by the Meissner effect forming an internal vortex line lattice that spreads the field distribution asymmetrically. The precessional frequency of the muon polarisation therefore undergoes a Gaussian relaxation proportional to the width of the field distribution that is inversely proportional to the penetration depth and directly proportional to the superconducting carrier density. The temperature dependence of the relaxation rate does not reveal any change below 1 K. Furthermore the field distribution were investigated in the frequency domain to detect any evidence of the vortex line lattice. The field distribution displayed a Gaussian lineshape centred on the applied fields, all below the field in which the reported bulk superconductivity vanishes, without any signature of a superconducting transition. Resistivity measurements exhibited a magnetic transition at $T \sim 38$ K never been observed before. The resistivity peak is independent of the contacts used and disappears by applying field, suggesting an intrinsic character. Below 1 K, resistivity remains constant. No signature of superconductivity were found in any of the analysis carried out, but the large residual resistivity and the contact effects in the low temperature resistivity motivates further investigations. Measurements of the sample quality and a systematic study of the resistivity with different geometries avoiding sample treatment that might add impurities are recommendable. It would clarify the unusual residual resistivity and would detect extrinsic contributions to the resistivity. Effects of the applied current in the sample temperature must be also investigated. Magnetic susceptibility measurements in the new magnetometer would provide another tool to investigate the CeRhIn₅ ground state.



Appendices

A.1 Refrigerators

Before choosing a refrigerator a few requirements should be considered:

- the refrigerator must get colder than the experiment temperature.
- it must have enough cooling power to absorb the power dissipated by the measurements and the thermal links.
- the sample must cool in a reasonable time.

Historically, liquid cryogenics have been used to maintain the experiment temperature. Liquid Nitrogen and Helium are the two most common refrigerants in cryogenic applications with 77 K and 4.2 K boiling point, respectively. The liquid Helium cost, the inefficient cryogenics transfer processes and the need to reach lower temperatures encouraged the developing of new technologies that will be detailed in this appendix.

A.1.1 Cryocoolers

Mechanical coolers or cryocoolers with ^4He closed circuits such as pulse-tube coolers, Stirling coolers or Gifford-McMahon coolers are widely used in to cool or pre-cool experiments. These cryocoolers are based on the cooling provided by the compression and expansion of Helium gas. Fig. A.1 (a) outlines a two-stage pulse-tube cooler (PT) whose thermal cycle consists of four steps [1]: firstly, the piston compresses the gas at room temperature, the pressure increases and the heat of compression is rejected from the compressor. During this step very little gas is transferred to the cold part, as the initial pressure difference across the orifice is small. As the piston compresses further, more working gas passes through the orifice into the reservoir in a quasi-isochoric process. The net effect is that the working gas is displaced across the high capacity regenerating material with heat transfer between the gas and the regenerator. The gas pressure and the temperature decrease. Then, the compressor reaches the limit, expansion takes place because the gas continues to flow into the reservoir. Pressure keeps dropping in the PT. In this step, the PT absorbs heat from the environment that cools down. Finally, the gas exits the reservoir. The expansion of the compression space results in another quasi-isochoric process. The pressure and the temperature of the cryogenic gas increases until the cycle is completed.

A PT can reach the gas boiling point at the working pressure. To optimize its cooling power and reduce the thermal load two stages are used, one at 45 K and another at 4 K. Although the PT efficiency is lower than a Sterling cooler, the cooling power is larger and the absence of moving parts in the cold part reduces vibrations and therefore it is more suitable for low temperature experiments. If it is compared with liquid Helium refrigerators, the cost saving and to avoid the arduous work of transfer the Helium regularly make worthy the high electrical power consumption. The magnetometer was developed in a refrigerator that includes the Cryomech PT415 model depicted in Fig. A.1 (b) with a cooling power of 40W at the 45 K stage and 1.5 W at the 4 K stage.

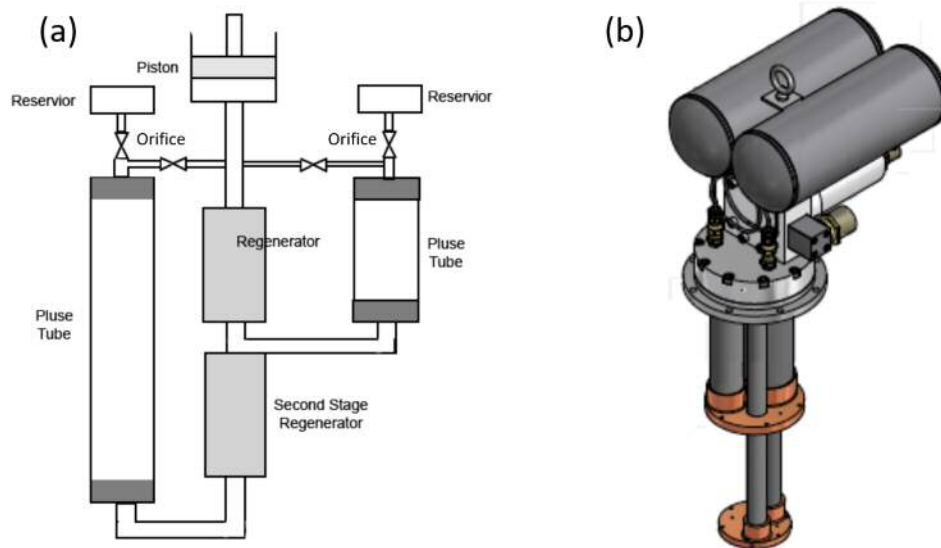


Figure A.1: (a) Two stage PT scheme. (b) Drawing of the Cryomech PT-415 used in the Bluefors dilution refrigerator.

A.1.2 Cooling below 4 K

Helium has the lowest latent heat of evaporation. The reasons are: the weak Van der Waals forces between the atoms because of the shielding effect of the closed electronic s-shell; and the small atomic mass that gives a large zero point energy with a large vibration amplitude being atoms less confined. If Helium is pumped, the boiling point decreases and it remains liquid down to the absolute zero. Temperatures between 4 and 1.2 K are achieved by pumping ^4He . Below this temperature the vapour pressure becomes too small and hence, the latent heat and the cooling power as well. Liquid ^4He has another peculiar property that it needs to bear in mind if it is used as a refrigerator. Below 2.17 K it becomes a superfluid and different properties show up. For instance, the thermal conductivity dramatically increases hampering the cooling. To minimise the refrigerant that is cold below 4 K is desirable to save time and cooling power. Otherwise, the cooling power will be unnecessarily wasted since Helium has a very high heat capacity.

The ^3He isotope is another cryogen candidate. It is even lighter and, therefore, the boiling point is lower (3.2 K at ambient pressure). The larger vapour pressure

(see Fig. A.2 (a)) allows one to reach temperatures lower than 300 mK when it is pumped. ^3He is produced from the tritium decay in nuclear reactors or from oil wells. Unfortunately, the cost (£2500 per STP litre of gas) constrains its use to closed circuits.

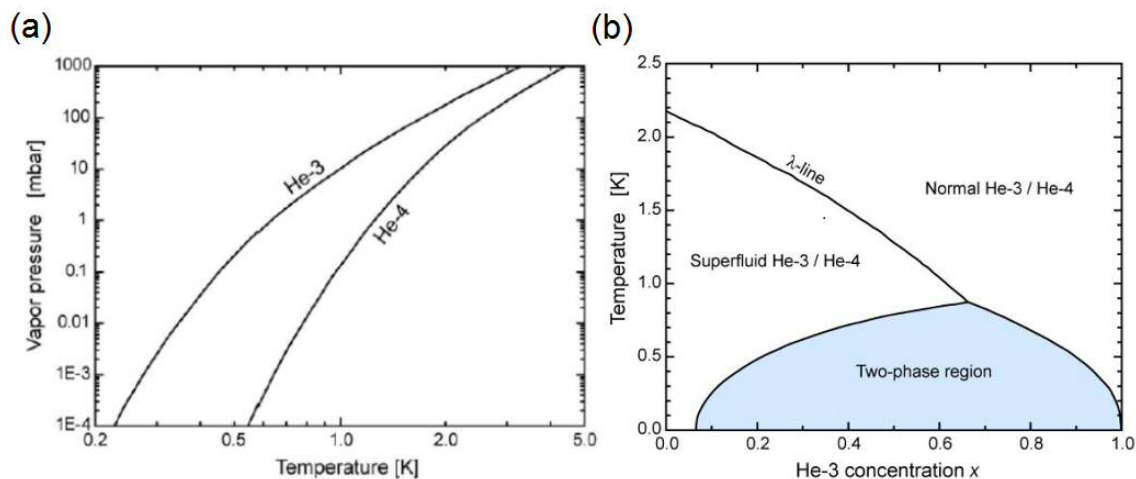


Figure A.2: (a) ^3He and ^4He vapour pressure as a function of temperature. (b) ^3He - ^4He mixture phase diagram from [2].

A.1.2.1 Sorption refrigerators

Another method to achieve temperatures below 4 K is using the pumping properties of sorbents. Sorption refrigerators are based on the sorbents physical properties to retain gases at low temperatures. The sorbent, normally charcoal, adsorbs Helium at low temperatures but the Helium is released when the charcoal is heated up. Complete desorption is reached at around 25 K. To operate a sorption refrigerator it must be thermalised to the refrigerant boiling point temperature (at ambient pressure, 4.2 K for ^4He and 3.3 K for ^3He). A scheme of a ^3He - ^4He sorption cooler is shown in Fig. A.3. The heat switch links the sorption pump to the refrigerant by a thermalised flange and controls its temperature. When the switch is off the charcoal warms up, desorbing the gas and increasing the vapour pressure. The gas drives off the pump and liquifies when it passes through the condenser that is linked to the thermal bath. Gravity makes it fall to the evaporator.

Then, the switch is turned on and the pump thermalises to the Helium bath. The charcoal cools down and the gas is absorbed, working as a pump. The vapour pressure decreases and hence, the boiling point of the liquid also drops. As a result, the evaporator cools down until the lowest temperature whilst the charcoal remains at the thermal bath temperature. If ${}^3\text{He}$ is used as a refrigerant the vapour pressure phase diagram (Fig. A.2 (a)) is different and lower temperature can be achieved. 800 mK and 300 mK are the common lowest temperature of ${}^4\text{He}$ and ${}^3\text{He}$ sorption pumps, respectively.

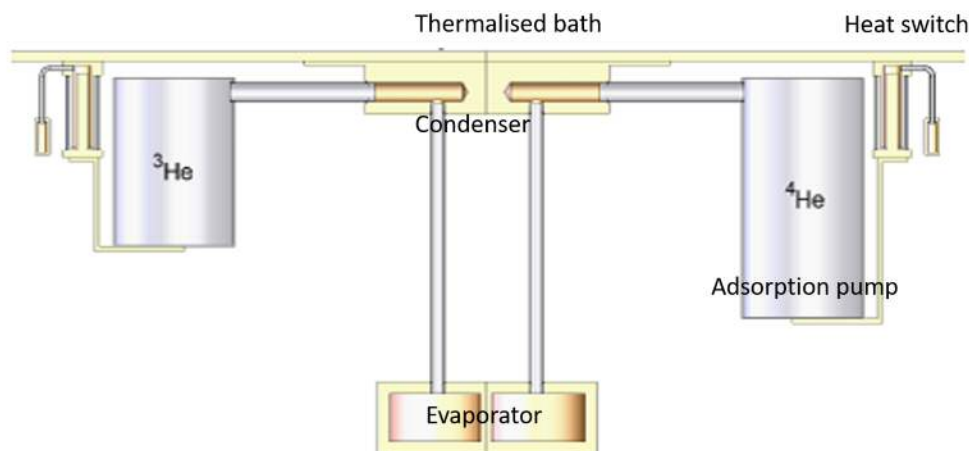


Figure A.3: Modified ${}^3\text{He} - {}^4\text{He}$ sorption cooler scheme from [3].

To optimize the cooling power a combination of ${}^3\text{He} - {}^4\text{He}$ sorption pumps (Fig. A.3) is normally used. The ${}^4\text{He}$ sorption cooler works as a pre-cooling pump that provides the starting temperature to the ${}^3\text{He}$ pump, since pumping the ${}^4\text{He}$ reservoir to 2 K involves to boil off a large amount of the liquid with the resulting waste of cooling power. A third ${}^3\text{He}$ stage was developed [4] to improve the pump performance and to reduce the base temperature to ~ 250 mK. The cooling power is given by the phase transition parameter

$$\dot{Q} = \Delta H \dot{n} \quad (\text{A.1})$$

where ΔH is the difference of molar enthalpy between the gas and the liquid phases. \dot{n} is the number of Helium atoms per unit of time that evaporates from the liquid

surface and it depends directly on the vapour pressure whose temperature dependence can be explained from the Clausius-Clapeyron equation $\frac{dP}{dT} = \frac{\Delta S}{\Delta V}$. As the liquid volume is negligible compared with the volume of the gas, the ideal gas approximation can be used. As a result, the vapour pressure decays exponentially with the temperature limiting the lowest temperature to above 0.2 K.

Sorption coolers present several advantages: they are simple to use and easy to automate; reliable, as they can work without external pumping; relatively cheap; and their pumping speed is high. These properties make them very popular in low temperature fridges. Unfortunately, the lowest temperature is limited and they do not run continuously, as the helium needs to be re-liquefied. To overcome this inconvenience, a design to keep an almost steady base temperature was recently built [5]. It consists of two parallel fridges running alternatively to provide a constant cooling power.

A.1.2.2 Adiabatic demagnetization refrigerator

Another technique to reach low temperatures is the Adiabatic Demagnetization Refrigerators (ADRs) that are based on the adiabatic demagnetization of some paramagnetic salt. A superconducting magnet produces a field that orientates the spins of the salt pill. The heat produced during the magnetization is removed by linking the salt thermally to a reservoir, and therefore the salt temperature remains constant. After that, the thermal link or heat switch is disconnected isolating the salt. When the magnetic field is reduced, the demagnetization cools the salt pill and temperatures down to 100 mK can be achieved. Finally, the salt pill is heated up and the cooling cycle close, so the system does not operate continuously. Again, complicated systems with salts in parallel have been developed to provide continuous operation [6]. The temperature is easily controlled by the magnetic field with low time consumption, and the absence of gas handling systems avoid leak problems. In contrast, ADRs provides low cooling power (0.1 mW at 0.1 K [6]), and the magnet makes them heavier than sorption coolers. The thermal load in the Helium bath is

high due to the large current needed to feed the magnet and the high magnetic field may hamper the experiment thus special care is needed to shield the sample space.

A.1.3 Dilution refrigerators

Dilution refrigerators (DR) are the most reliable method to achieve continuous cooling below 300 mK and base temperature of several mK may be reached. Enough continuous cooling power at these temperatures is possible thanks to the special properties of ${}^3\text{He} - {}^4\text{He}$ mixture. The mixture undergoes a phase transition below 700 mK, (temperature depends on concentration, see Fig. A.2 (b)). The mixture separates into two phases. A concentrated phase, with a rich proportion of ${}^3\text{He}$, floats on the top of a poor ${}^3\text{He}$ phase or dilute phase, where ${}^3\text{He}$ and ${}^4\text{He}$ co-exists. As temperature decreases, more isotopes cross the phase boundary but even at $T=0$ K, a 6% of ${}^3\text{He}$ remains in the dilute phase due to the different statistics of bosons and fermions.

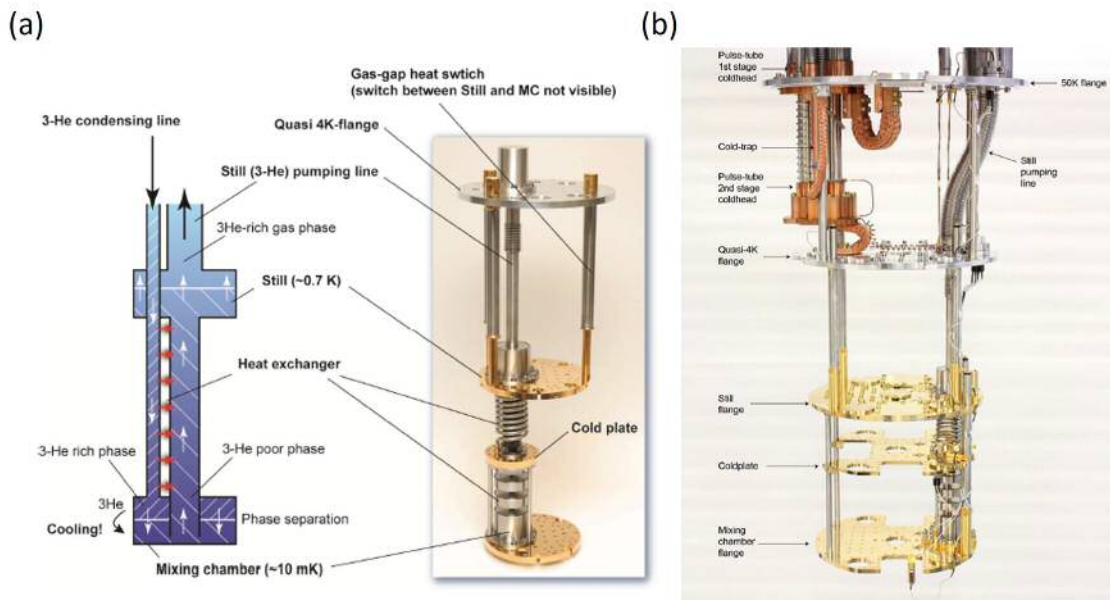


Figure A.4: (a) Bluefors DR Helium cycle. (b) DR Bluefors picture [2].

A DR consists of a mixing chamber (MXC), where the phase separation takes place and the lowest temperature is reached, and a still or evaporator, at higher

temperature, that pumps the Helium out. The mixture circulates from the external tanks to the MXC through heat exchangers that thermalise the incoming mixture with the outgoing gas. The Helium flow controls the cooling power so a gas handling system with a turbomolecular pump is required. The cooling cycle is quite similar in all the DR, so this section will cover the details of the Bluefors DR (See Fig. A.4). Pre-cooling may be provided by a ^4He bath or by a two stages PT as it is the case with the Bluefors DR. The 45 K and the 4 K stage are thermally anchored to the cryostat plates by Copper braids that damp vibrations from the PT. The 4 K plate is quasi-radiation shielded and thermally isolated from its surrounding by the 4 K can. The mixture is pushed into the cryostat from the external tanks and cleaned of contamination by the cold traps. The first trap remains in a Nitrogen bath and freezes undesirable particles before the mixture enters into the cryostat. The second one is thermally linked to the 50 K plate. It works also as a heat exchanger and together with the others heat exchangers condense the mixture before arriving to the MXC. The pillars, that keep apart the MXC from the still, works also as a heat exchanger. A sorption pump on the top of the pillars controls the Helium gas that thermally links, or not, the plates.

The bottom of the MXC is connected to the still that pumps the gas out of the MXC providing the circulation. A pressure difference is created between them and the vapour pressure in the MXC and the boiling temperature drops, cooling the MXC. At temperatures below 700 mK the mixture separates into the two phases at the MXC. At that point, the dilute phase falls to the bottom of the MXC by gravity and only the Helium from the concentrated phase is pumped out. As the vapour pressure of the ^3He is larger than the ^4He , almost only ^3He is evaporated from the still that remains in a quasi-constant temperature between 0.8-1 K.

The cooling power in the MXC depends on the ^3He atoms that cross the boundary from the dilute to the concentrated phase according to the Eq. A.1. In this case, the enthalpy difference is between pure ^3He in the two phases and is given

by the heat capacity:

$$H(T) = H(0) + \int_0^T C(T)dT$$

with $C \propto T$ as ${}^3\text{He}$ is a Fermi particle. The resulting cooling power

$$\dot{Q} = \dot{n}(T^2 - T_b^2) \tag{A.2}$$

varies now quadratically with the temperature and makes the cooling more efficient at low temperature than in sorption coolers. Base temperature, T_b , of few mK can be achieved.

Although a few details, like the pumping method or the heat exchangers may vary from one model to another, the technique is very similar in all the commercial DR available.

Low temperature experiments were carried out in a Bluefors LD-400 dilution refrigerator (DR) . It combines a two-stage Pulse Tube, that makes the fridge “cryogen-free” with a significant cost saving, and a DR with a cooling power of 15 μW at 20 mK and 450 μW at 100 mK. The DR provides a continuous operation with a better cooling power than ADR [6]. These features give a pioneering position to build a novel low temperature and high frequency magnetometer in a dry dilution fridge.

A.2 SQUID electronics

A.2.1 Flux-locked loop circuit (FLL)

Although the SQUID can operate in an open-loop mode around the working point (WP), the transfer coefficient only remains unchanged for small $\delta\phi$ and a non-linear output is obtained if the flux amplitude exceeds the linear flux range Φ_0/π . The dynamic range is considerably increased, $\Phi_{max} \gg \Phi_0$, if the voltage-to-flux response is linearised by using a flux-locked loop (FLL) feedback circuit, an electronic circuit located at room temperature together with an amplifier. The FLL is depicted in Fig. A.5. The SQUID output is amplified, integrated and fed back via

a resistor R_f and a feedback coil that apply a magnetic flux Φ_f in such a way that the working point WP in Fig. 4.5 remains stable, keeping a null flux in the SQUID. The feedback flux Φ_f will be equal and the output voltage proportional to the input flux induced in the SQUID and, then, the characteristic periodic flux-to-voltage linearised. At this point, the transfer coefficient does not depend on the working point of the SQUID, but only on the circuit components R_f . In the particular device used in this work, the voltage-to-flux transfer coefficient can be reduced 10 or 100 times by modifying the resistance and the capacitor included in the circuit via software.

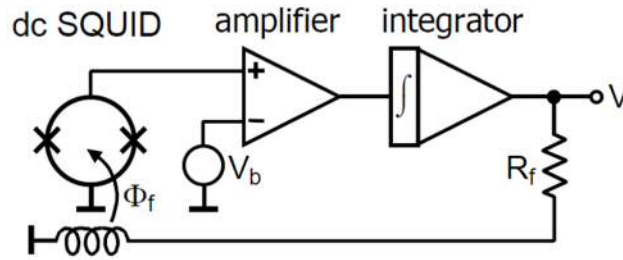


Figure A.5: Scheme of a Flux-Locked Loop circuit taken from Thomas Schurig work [7].

A.2.2 Two-stage SQUID amplifier

The programmable Feedback Loop Model PFL-102 is designed to operate a two-stage SQUID amplifier. Originally developed by Welty et al. [8], a scheme of the two-stage amplifier is shown in Fig. A.6. The low-noise SQUID consists of an input stage and an output stage. The former is a voltage-biased SQUID via a resistor $R_b \approx 100 \text{ m}\Omega$ and a bias current I_1 . R_b may be calculated by the rms voltage noise given by $V_n = \sqrt{4K_B T / R_b}$, being K_B the Boltzmann constant and T the SQUID temperature. The induced superconducting current in the gradiometer by the sample magnetic moment is coupled to the SQUID by an input coil as it was explain in Sec. 4.2.2. The coupling is characterised by the self-inductance L_i and the mutual inductance M_i . The input SQUID is coupled in series through the modulation coils to an array of $N=32$ identical, non-hysteretic SQUIDs in the output stage. The

total inductance of the array modulation coils is NL_m .

In the same way, the output SQUID array is current biased using bias current I_2 . A changing signal coupled to the input SQUID will produce a current through the input SQUID that coherently modulates the series SQUID array in the output stage. Finally, the output stage is directly coupled to a low-noise preamplifier in the

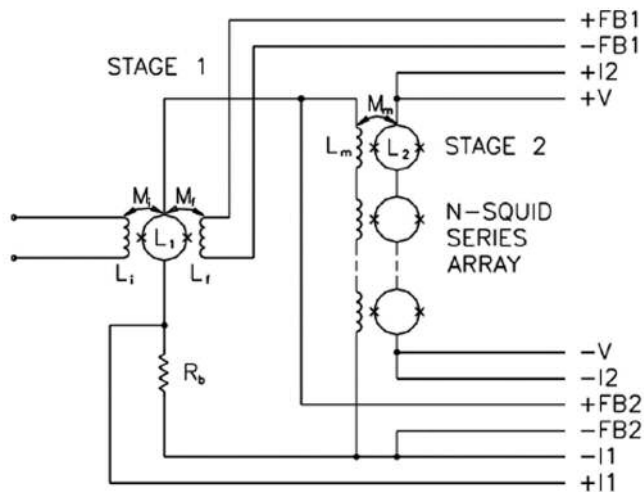


Figure A.6: Schematic diagram of a typical two-stage SQUID amplifier from Star Cryoelectronics SA632s user's manual.

room-temperature feedback electronics. The design is made in such a way that the output noise is dominated by the amplified noise of the input SQUID and exceeds the noise of the room-temperature preamplifier.

To operate the SQUID amplifier, firstly the output array is optimised by obtaining the largest output voltage. A test signal is applied to the modulation coils through the FB2 circuit. The generated flux, ϕ , in the array and a bias current I_2 between 40-60 μA will produce the standard $V-\phi$ SQUID response. An offset voltage is used to adjust the steepest part of the flux-to-voltage transfer function at zero Volts. The array working point is, then, optimised and ready for locked-loop operation.

The SQUID array operating in a locked mode works as a low-noise preamplifier for the input SQUID. The small signal voltage of the input SQUID of around $100 \mu V / \Phi_0$ is amplified to the final voltage-to-flux transfer function depicted in Fig. 4.5. In a similar way than the array, the voltage bias across the input SQUID is set by the SQUID bias current I_1 . The test signal is now coupled to the input SQUID and the SQUID output signal ΔI maximised. The array operates as an amplifier when the FLL is used to lock the input SQUID. The linearity is enhanced having a maximum current on the input SQUID lower than the current required to induce a quantum flux in the output array.

The Star Cryoelectronics SQUIDs are fabricated using a robust and reliable $Nb/Al - AlO_x/Nb$ trilayer Josephson junction technology and mounted in a printed circuit board. Two Niobium pads connect the gradiometer or the flux transformer to the input SQUID. The magnetic shielding is provided by a threaded Niobium cylinder and a mu-metal hollow tube that avoids trapped flux in the flux vortices of the type II superconducting Niobium.

References

- [1] S. W. K. Yuan and H. Jung, *Thermal management of computer systems using active cooling of pulse tube refrigerators Stirling Cooler Pulse Tube Cooler*, Pacific Rim / ASME International, Electronic Packaging Technical (1999)
- [2] B. Cryogenics Ltd, *BF-LD400 Cryogen-Free Dilution Refrigerator System–User Manual* (2013)
- [3] G. Teleberg, *Sorption Cooled Miniature Dilution Refrigerators for Astrophysical Applications*, Ph.D. thesis, Cardiff University (2006)
- [4] <http://www.chasecryogenics.com/3h-coolers.html>
- [5] G. M. Klemencic, P. A. R. Ade, S. Chase, R. Sudiwala and A. L. Woodcraft, *A continuous dry 300 mK cooler for THz sensing applications*, Rev. Sci. Instrum. 87 (4), p. 045107 (2016)

- [6] T. Numazawa, K. Kamiya, P. Shirron and K. Mitsuda, *Development of continuous ADR system for weak gravity missions*, J. Phys. Conf. Ser. 150 (1), p. 012032 (2009)
- [7] T. Schurig, *Making SQUIDs a practical tool for quantum detection and material characterization in the micro-and nanoscale*, J. Phys. Conf. Ser. 568 (3), p. 032015 (2014)
- [8] R. P. Welty and J. M. Martinis, *Two-stage integrated SQUID amplifier with series array output*, IEEE Trans. Appl. Supercond. 3 (1), p. 2605 (1993)

